PHYSICS OF MASS LOADED PLASMAS

KÁROLY SZEGÖ[1], KARL-HEINZ GLASSMEIER[2], ROBERT BINGHAM[3], ALEXANDER BOGDANOV[4], CHRISTIAN FISCHER[4], GERHARD HAERENDEL[4], ARMANDO BRINCA[5], TOM CRAVENS[6], EDUARD DUBININ[7], KONRAD SAUER[7], LEN FISK[8], TAMAS GOMBOSI[8], NATHAN SCHWADRON[8], PHIL ISENBERG[9], MARTIN LEE[9], CHRISTIAN MAZELLE[10], EBERHARD MÖBIUS[11], UWE MOTSCHMANN[12], VITALI D. SHAPIRO[13], BRUCE TSURUTANI[14] and GARY ZANK[15]

[1]*KFKI Research Institute for Particle and Nuclear Physics, H-1525 Budapest, P.O. Box 49, Hungary*

[2]*Technische Universität Braunschweig, Institut für Geophysik und Meteorologie, Mendelssohnstrasse 3, D-38106 Braunschweig, Germany*

[3]*Rutherford Appleton Laboratory, 202 The Avenue, Kennington, Oxford OX1 5RN, U.K.*

[4]*Max-Planck-Institut für Extraterrestrische Physik, Giessenbachstrasse, D-85740 Garching, Germany*

[5]*Centro de Fisica de Plasmas, Instituto Superior Tecnico, P-1096 Lisboa Codex, Portugal*

[6]*Department of Physics and Astronomy, University of Kansas, Lawrence, KS 66045, U.S.A.*

[7]*Max-Planck-Institut für Aeronomie, Postfach 20, D-37189 Katlenburg-Lindau, Germany*

[8]*University of Michigan, 1416 Space Res. Bldg., 2455 Hayward St., Ann Arbor, MI 48109-2143, U.S.A.*

[9]*Space Science Center, Morse Hall, University of New Hampshire, Durham, NH 03824, U.S.A.*

[10]*CNRS-CESR, 9, Avenue du Colonnel Roche, BP 4346, F-31028 Toulouse cedex 4, France*

[11]*Space Science Center, Morse Hall, University of New Hampshire, Durham, NH 03824, U.S.A.*

[12]*Technische Universität Braunschweig, Institut für Theoretische Physik, Mendelssohnstrasse 3, D-38106 Braunschweig, Germany*

[13]*Department of Physics, University of California San Diego, La Jolla, CA 92093-0319, U.S.A.*

[14]*Jet Propulsion Laboratory 169-506, 4800 Oak Grove Dr., Pasadena, CA 91109, U.S.A.*

[15]*The Bartol Research Institute, The University of Delaware, Newark, DE 19716, U.S.A.*

(Accepted 9 March 2000)

Abstract. In space plasmas the phenomenon of mass loading is common. Comets are one of the most evident objects where mass loading controls to a large extent the structure and dynamics of its plasma environment. New charged material is implanted to the fast streaming solar wind by planets, moons, other solar system objects, and even by the interstellar neutral gas flowing through our solar system. In this review we summarize both the current observations and the relevant theoretical approaches. First we survey the MHD methods, starting with a discussion how mass loading affects subsonic and supersonic gasdynamics flows, continuing this with single and multi-fluid MHD approaches to describe the flow when mass, momentum and energy is added, and we finish this section by the description of mass loaded shocks. Next we consider the kinetic approach to the same problem, discussing wave excitations, pitch angle and energy scattering in linear and quasi-linear approximations. The different descriptions differ in assumptions and conclusions; we point out the differences, but it is beyond the scope of the paper to resolve all the conflicts. Applications of these techniques to comets, planets, artificial ion releases, and to the interplanetary neutrals are reviewed in the last section, where observations are also compared with models, including hybrid simulations as well. We conclude the paper with a summary of the most important open, yet unsolved questions.

Space Science Reviews **94:** 429–671, 2000.

Table of Contents

1. Introduction

In space plasmas the phenomenon of mass loading is common. Comets are one of the most evident objects where mass loading controls to a large extend the structure and dynamics of the interaction of the cometary nucleus and the fast streaming solar wind plasma. When approaching the Sun vast amounts of cometary neutral gas evaporate from the nucleus surface due to increasing temperatures. EUV ionization, charge exchange, and collisional ionization lead to the generation of ions which are picked up by the solar wind plasma. The incorporation of these pickup ions into the solar wind causes a loading of the wind with particles, mass, momentum, and energy. Most important for the cometary case is the addition of mass. In a collision dominated gas such an accretion of mass is easily accomplished by collisions between the newly born or donator particles and the host gas particles. However, in the collision free magnetized plasma of the solar wind the pickup of newborn ions is a rather complex process which owes much consideration.

Further examples for mass loaded flows are the interaction of the solar wind with planetary atmospheres and exospheres or with artificially released ions as

well as the interaction of ions from the local interstellar medium with the solar wind plasma. Though very different in their respected details important aspects of a general theory of the physics of mass loaded flows have emerged during the past twenty years. Here we are trying to summarize the current status of the understanding of such mass accreting flows. Both, macroscopic flow effects as well as microscopic processes required to incorporate a donator particle population into a collisionless magnetized plasma will be reviewed. The specific conditions and experimental as well as observational results at comets, planets, artificial ion releases, and the interstellar case are discussed, too.

Section 2 is devoted to the fluid description of mass loading. We begin this section with a discussion on how gases react to loading, and then we explain how this process can be accounted for in the framework of magnetohydrodynamics. We consider in detail the role of source terms, and how we can generalize the single fluid model to trace individually more fluid components. This treatment has an important impact on the structure of the bow shock; this is analyzed in depth as well.

In Section 3 we review the kinetic approach to mass loading, investigating first the different wave excitation mechanisms in linear approximations, including processes due to nongyrotropic distribution as well. As we do not have a theoretical framework for nonlinear wave processes, they are described later, in the section devoted to observations. Pitch angle scattering and particle energization are considered in the quasilinear approximation.

Section 4 is devoted to observational evidences, and their interpretation. This is where some of the open questions are also emphazised. We review first the observation of mass loading at comets, then at planets, following it with the description of the interplanetary pickup processes. The artificial ion release experiments do shed light to many of the fine details, these are summarized at last. This section concludes with an overview of numerical simulations.

Finally, we briefly comment the open issues and questions that require further studies.

2. The Fluid Description of Mass Loading

The physics of mass loading can be described on different levels of sophistication. The easiest picture is that of gas dynamics, a more evolved one is in terms of magnetohydrodynamics, a picture which also allows to incorporate important effects emerging for a magnetized plasma. As space plasmas usually consist of electrons and several ion species the next level of sophistication is a multi-ion or a bi-ion fluid description. All three models as well as their possible applications will be described in the following.

2.1. THE GAS DYNAMIC PICTURE

There exist many practical situations where the understanding of the modification of a gaseous flow is very important. Typical examples are the area change in rocket nozzles, changes of phase by e.g. evaporation or condensation of water, or changes in molecular weight and specific heat occasioned by combustion, evaporation, gas injection etc. Due to their practical applications in combustion chambers for gas turbines and turbojet engines, moisture condensation shocks, moving flame fronts, or detonation waves the physics of such gas flow modification is well understood, and reference is made to the still very readable two volume book by Shapiro (1959) on the dynamics and thermodynamics of compressible fluid flow.

Mass loading of a gas stream as it occurs during the interaction of an evaporating comet with the interplanetary medium is a phenomenon of the same kind as the above mentioned gas flow modifications. Some major effects of mass loading on the flow may well be understood within the framework of a simple gas dynamic picture. The following discussion is based on Shapiro's (1959) treatment as well as work by Biermann et al. (1967) and Wallis (1971, 1973). In the one-dimensional situation the conservation laws for particle, mass, momentum, and energy density of a steady, laminar gas flow are given by

$$\frac{\mathrm{d}(nu)}{\mathrm{d}s} = \mathcal{N} \,, \tag{2.1.1}$$

$$\frac{\mathrm{d}(nmu)}{\mathrm{d}s} = \mathcal{G} \,, \tag{2.1.2}$$

$$\frac{\mathrm{d}(nmu^2)}{\mathrm{d}s} = \mathcal{I} \,, \tag{2.1.3}$$

$$\frac{\mathrm{d}\left(u\left[nm\dfrac{u^2}{2} + \dfrac{\gamma}{\gamma-1}\right]p\right)}{\mathrm{d}s} = \mathcal{E} \,, \tag{2.1.4}$$

respectively. Here, n denotes the particle number density, m the particle mass, and u the flow velocity; ds is the line element. Gas pressure p and temperature T are connected with the particle number density via the ideal gas equation $p = nk_{\mathrm{B}}T$, with k_{B} the Boltzmann number. The polytropic index γ is defined via $\gamma = (F+2)/F$, with F the number of degrees of freedom of the gas atoms or molecules. The right hand sides of equations (2.1.1)–(2.1.4), $\mathcal{N}$, $\mathcal{G}$, $\mathcal{I}$, and $\mathcal{E}$ denote particle, mass, momentum, and energy source terms, respectively. Here, we are not specifying the precise form of these source terms, but only assume that any donator gas is immediately coupled to its host gas by collisions. Loading the interplanetary medium, with, for example, a dense, hot, and streaming gas would correspond to adding particles, mass, momentum, and energy to the flow. The consequences of these sources on the flow velocity are described by

$$\mathrm{d}u = \frac{M_s^2}{1-M_s^2}\left(\frac{\gamma-1}{2}\mathcal{N}_\mathrm{R} + \gamma\mathcal{G}_\mathrm{R} - \gamma\mathcal{I}_\mathrm{R} - \frac{\gamma-1}{2}\mathcal{E}_\mathrm{R}\right)\mathrm{d}s\ , \tag{2.1.5}$$

where $M_s = u/c_\mathrm{s}$ is the sonic Mach number with $c_\mathrm{s} = \sqrt{\gamma p/nm}$. Source terms have been normalized and read $\mathcal{N}_\mathrm{R} = \mathcal{N}/m$, $\mathcal{G}_\mathrm{R} = \mathcal{G}/nm$, $\mathcal{I}_\mathrm{R} = \mathcal{I}/nmu$, and $\mathcal{E}_\mathrm{R} = 2\mathcal{E}/nmu^2$, respectively. Corresponding pressure modifications are given by

$$\begin{aligned}\mathrm{d}p = nmu\Bigg(&-\mathcal{N}_\mathrm{R}\left[1+\frac{\gamma-1}{2}\frac{M_s^2}{1-M_s^2}\right]- \\ &-\gamma\mathcal{G}_\mathrm{R}\frac{M_s^2}{1-M_s^2}+\gamma\mathcal{I}_\mathrm{R}+\mathcal{E}_\mathrm{R}\frac{\gamma-1}{2}\frac{M_s^2}{1-M_s^2}\Bigg)\mathrm{d}s\ ,\end{aligned} \tag{2.1.6}$$

Equations (2.1.5) and (2.1.6) exhibit a remarkable dependence on the sonic Mach number. At the transition from subsonic to supersonic flow the factor $(M_s^2/1-M_s^2)$ changes sign. Depending on the source terms, the flow changes from decelerating (accelerating) to accelerating (decelerating). A similar behavior is well known for a one-dimensional flow in a nozzle with changing cross section.

In the cometary case a cold gas consisting of heavy, almost non-streaming water-group particles is added to the fast streaming solar wind flow. Thus, only the mass source term is of importance (e.g., Wallis, 1971). In this mass loading case the incremental velocity and pressure changes (2.1.5) and (2.1.6) reduce to

$$\mathrm{d}u = \gamma\frac{M_s^2}{1-M_s^2}\mathcal{G}_\mathrm{R}\,\mathrm{d}s \tag{2.1.7}$$

and

$$\mathrm{d}p = -\gamma\frac{M_s^2}{1-M_s^2}\cdot nmu\mathcal{G}_\mathrm{R}\,\mathrm{d}s\ . \tag{2.1.8}$$

With the definition of the pressure, $p = nk_\mathrm{B}T$, also the incremental temperature change can be determined. For the special case discussed here one gets

$$\mathrm{d}T = \frac{\gamma M_s^2 - \gamma^2 M_s^4}{1-M_s^2}\frac{T}{u}\mathcal{G}_\mathrm{R}\,\mathrm{d}s\ . \tag{2.1.9}$$

Thus, mass loading of a supersonic flow leads to deceleration and heating of the flow, while mass loading of a subsonic flow causes acceleration and cooling.

Flow deceleration has been confirmed observationally during, e.g., the flyby of the GIOTTO spacecraft (Grensemann and Schwehm, 1993) at comet P/Grigg–Skjellerup (Johnston et al., 1993). Figure 2.1.1 displays solar wind velocity as well as number density of water group ions and solar wind protons. Here the water group ions constitute the donator gas, while the protons represent the host gas. Neglecting the fact that the solar wind is a magnetized plasma allows to characterize the interplanetary medium as a supersonic flow. With decreasing distance to the comet the donator gas density increases and the flow velocity of the host gas diminishes,

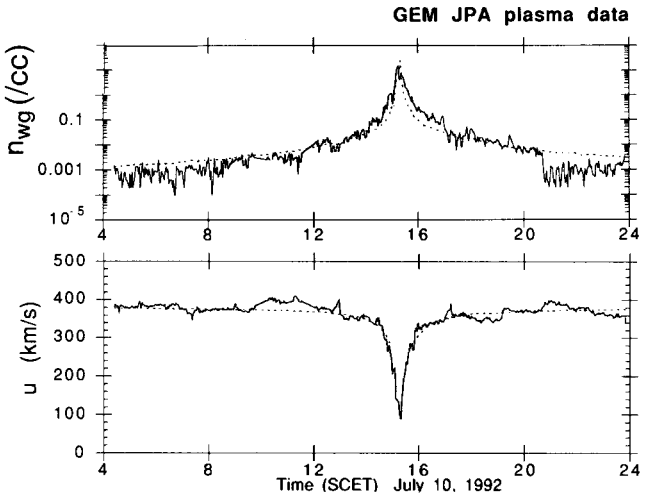

Figure 2.1.1. Water group ion density (*top*) and solar wind proton velocity (*bottom*) profiles observed by the Giotto JPA implanted ion sensor at comet P/Grigg-Skjellerup encounter on July 10, 1992 (after Huddleston et al., 1993).

much as expected from Equation (2.1.7). The observations at comets thus allow to confirm the simple gas dynamic picture outlined above and furthermore justify the early theoretical conjectures of Biermann et al. (1967).

Deceleration of the flow when adding mass is an expected behavior as one anticipates that energy and momentum from the host gas must be transferred to the donator gas, if both are mixing. Thus, equipartition of flow momentum between host and donator gas is expected. As the flow velocity decreases it eventually reaches a point where it changes from a supersonic into a subsonic flow. Equation (2.1.5) indicates that at this transition the denominator of the factor $M_s^2/(1 - M_s^2) \rightarrow \infty$. As discussed in detail by e.g., Biermann et al. (1967) and Wallis (1971) the transition of the sonic point is usually associated with a shock wave. Shock-free solutions of Equations (2.1.1)–(2.1.4) are only possible for very special profiles of the mass loading term $\mathcal{G}_R(s)$ as extensively discussed by Wallis (1971). Furthermore, the mass loading rate is limited to about 1–2% of donator particles in the cometary case, where the mass ratio of the donator particles (water group ions) to the host gas particles (protons) is about 17. This behavior of the flow in the gas dynamic description can easily be verified from the following considerations.

Mass loading of subsonic flows leads to acceleration and cooling under purely mass accretion conditions as Equations (2.1.7)–(2.1.9) exhibit. This result might not be guessed at first glance and needs some further discussion and consideration of the microscopic processes of mass loading. Adding a slowly moving, cold donator gas to the fast moving, hot host gas in the region $\{s, s + ds\}$ leads to rapid equipartition of the thermal energy between donator and host particles due to collisions (Figure 2.1.2). The resulting gas temperature, T_M, is less than the original

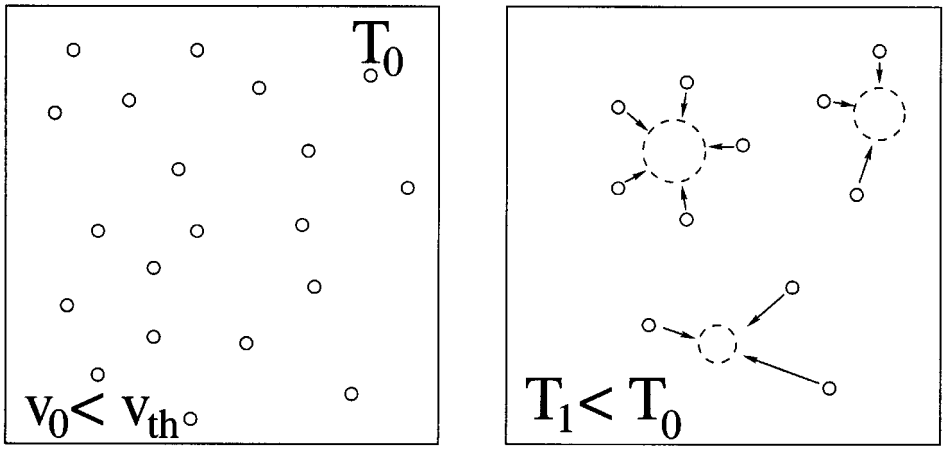

Figure 2.1.2. Illustration of the thermalization of donator particles in a host gas: Subsonic case.

host gas temperature, T_H, in the region $\{s, s + ds\}$: $T_M < T_H$. This furthermore causes a smaller pressure in the mass loaded region than outside: $p_M < p_H$. Thus, a local pressure gradient is created which accelerates the mass loaded flow.

This may also be viewed at in a somewhat different way. Mass loading requires to share energy and momentum between the donator and the host gas. Two energy reservoirs are available, a thermal energy and a flow kinetic energy one. In the subsonic case discussed the thermal energy reservoir is tapped by the donator particles, causing a local cooling of the flow and a pressure gradient accelerating the mass loaded flow. This acceleration not only provides the required momentum change of the donator particles, but furthermore drains thermal energy into the flow kinetic energy reservoir, thereby causing a further cooling of the flow below the temperature required by equipartition of the thermal energy of the two gases.

In the supersonic case a different picture emerges. Now, because of $M_s > 1$, the flow velocity is larger than the mean thermal velocity of the particles: $u > v_{th}$. This introduces an asymmetry into the velocity space. If $u = 0$ the donator particles exhibit collisions with host particles coming both from left and right (see Figure 2.1.2). This guarantees a rapid relaxation of the joint particle distribution towards equilibrium. However, if $u > v_{th}$ there are more host particles to hit a donator particle coming from the left than particles coming from the right (Figure 2.1.3). This implies a net momentum and flow kinetic energy transfer from the host to the donator particles with a reduced ability to reach thermal equilibrium.

The net momentum transfer leads to the discussed deceleration of the flow. The kinetic energy reservoir tapped to accommodate the donator particles is primarily the flow kinetic energy, not the thermal kinetic energy reservoir as in the subsonic case. The sonic Mach number as a measure of u/v_{th} serves to discriminate between the two different situations and serves as a parameter to describe the importance of the different microscopic processes leading to drainage of energy either from the

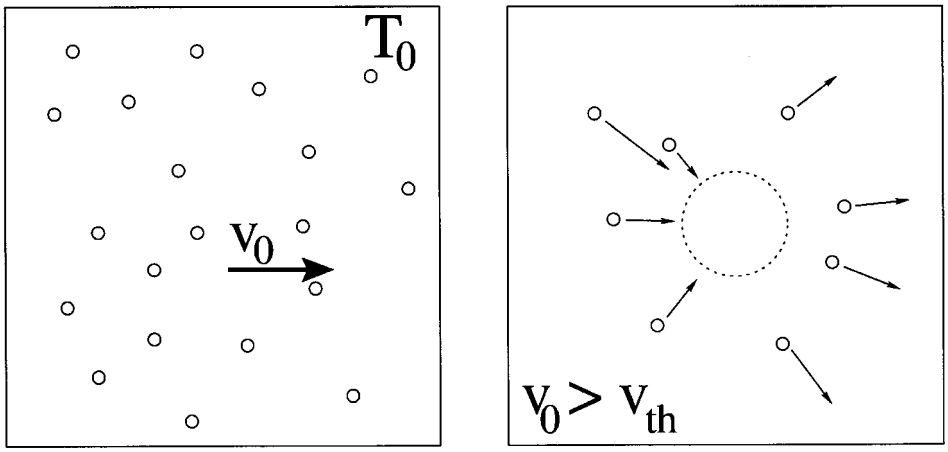

Figure 2.1.3. Illustration of the thermalization of donator particles in a host gas: Supersonic case.

thermal or the flow kinetic energy reservoir. For small values of M_s thermalization of the donator particles is very fast, while for large values of M_s flow processes are faster and more important.

In collisionless plasmas, however, the situation is more difficult due to the absence of collisions as an agent to thermalize the newborn ion distribution and to tap the thermal energy reservoir. As thermalization is a rather slow process in the collisionless case one may speculate that the collisionless case is better described as an always supersonic situation, that is the flow energy reservoir is easier to tap than the thermal one. An extreme case is the pickup of ions in cases where the flow velocity is perpendicular to the magnetic field. $\mathbf{E} \times \mathbf{B}$ pickup (e.g., Omidi and Winske, 1987) leads to a very rapid incorporation of the newborn ions or donator particles into the host gas. The characteristic time for the pickup process is the pickup ion gyroperiod. On this fast time scale flow energy is transferred from the host gas to the donator gas, while the thermal energy reservoir is nearly untapped. Thus, even if the magnetized plasma flow is sub-Alfvénic, the pickup process may be regarded as that in the supersonic case due to the flow energy reservoir tapped in a more efficient way than the thermal energy reservoir. This furthermore might indicate that a sonic or Alfvénic Mach number is not the ultimate parameter to characterize the mass loading situation; the sonic Mach number is only a good parameter in the gas dynamic, collision dominated case. Future work on a proper parameter is required.

Equation (2.1.5) allows to discuss other possible scenarios, for example, adding a warm or hot donator gas with $\mathcal{G}_R \neq 0$ and $\mathcal{E}_R \neq 0$. In such a case the incremental velocity change is given by

$$\mathrm{d}u = \frac{M_s^2}{1 - M_s^2} \left(\gamma \mathcal{G}_R - \frac{\gamma - 1}{2} \mathcal{E}_R \right) \mathrm{d}s \; . \tag{2.1.10}$$

It appears that the addition of a hot gas with large $\mathcal{E}_R$ may lead to an acceleration of the flow even if the flow is supersonic and mass loaded. Thermalization of the hot donator gas provides the required energy and resulting pressure gradients accelerate the flow. Accretion of such a hot gas leads to a much different behavior then expected in the cometary case. Furthermore, if a situation with $\mathcal{E}_R = 2\gamma/(\gamma - 1)\mathcal{M}_R$ emerges, no flow modification will happen at all.

Equation (2.1.10) can be used to discuss the importance of the polytropic index γ on the flow. A common value assumed for plasmas is $\gamma = \frac{5}{3}$ (e.g., Siscoe, 1983; Baumjohann et al., 1990). However, as pointed out by Belmont and Mazelle (1992) and Mazelle and Belmont (1993) different values for the polytropic index are required to describe pressure variations parallel and perpendicular to a background magnetic field. For the perpendicular index Belmont and Mazelle (1992) derive a value $\gamma_\perp \approx 0.5$, that is less than 1. Thomas and Lichtenberg (1997), studying the thermal properties of the Io plasma torus, derived empirically a value $\gamma \approx 0.5$.

The consequences of a polytropic index $\gamma < 1$ can be discussed with the help of Equation (2.1.10). Consider the mass loading due to a hot donator gas. With $\gamma < 1$ the energy loading diminishes the effect of the mass loading, that is a supersonic flow may well be accelerated as discussed above. However, if $\gamma < 1$ energy loading has the same effect on the flow as mass loading: the supersonic flow is decelerated, even for a hot donator gas. This indicates that a careful consideration of the polytropic index is required. A value $\gamma < 1$ means that during compression the temperature decreases which implies heat flows out of the compressed region. A possible scenario for such an unusual effect in a magnetized plasma is as follows: the plasma as the host gas is compressed, the compression is associated with a density increase, the increased density leads to an enhanced recombination rate, and the host plasma is deloaded with mass, momentum, and energy due to these newborn neutrals. Whether such a scenario is important is yet to be discussed and needs future work.

Furthermore, the usual closure of the momentum equations via a polytropic law is not always the most appropriate approximation. If strong heat flux effects are involved using the polytropic law closure introduces an approximation where the polytropic index becomes a parameter required to describe the neglected heat flux effects. Details of this effect also need further work.

The simple gas dynamic picture outlined here provides one with a very useful framework to discuss possible basic effects occurring under different mass loading conditions. It indicates the importance of knowing whether the flow is sub- or supersonic, it points toward the different roles particle number, mass, momentum, and energy loading play, and also points toward the importance of the polytropic index and its influence on loaded flows.

2.2. THE MAGNETOHYDRODYNAMIC MODEL

Only in a very limited way does the gas dynamic model allow to consider mass loading effects in a magnetized plasma such as the solar wind. Though this model may be extended by including the Lorentz forces via generalized pressure terms in the basic equations (2.1.1)–(2.1.4) a more advanced approach is required (e.g., Wallis, 1971). The model which received much attention and provided deep insight into the physics of mass loading is the magnetohydrodynamic model. In the following, we provide a comprehensive fluid description of the mass loading process and apply the results to several examples. Presently, most global scale 3D models of space plasmas use some kind of fluid approximation. This means that relatively low-order velocity moments are used to characterize the sometimes quite complicated velocity functions of the various neutral and charged particles species in the mass loaded flow. In such descriptions a large part of the underlying kinetic processes are completely neglected or at most characterized by some transport coefficients. In return for giving up some important aspects of the physics one gains a mathematical description which can be solved with the present generation of computers. These computer simulations are a very important part of the available research tools, and they significantly advance our understanding of the global scale dynamics of space plasma flows.

2.2.1. *The Plasma Kinetic Equation and General Considerations*

The governing equation for the phase-space distribution function of particles of type s, $F_s(t,\ \mathbf{r},\ \mathbf{v}_s)$, can be written in the following form (Gombosi, 1994):

$$\frac{\partial F_s}{\partial t} + (\mathbf{u}_s \cdot \nabla)\, F_s + (\mathbf{v}_s \cdot \nabla)\, F_s - \left[\frac{\partial \mathbf{u}_s}{\partial t} + (\mathbf{u}_s \cdot \nabla)\, \mathbf{u}_s + (\mathbf{v}_s \cdot \nabla)\, \mathbf{u}_s - \right.$$
$$\left. -\mathbf{g} - \frac{q_s}{m_s}\mathbf{E} - \frac{q_s}{m_s}\,(\mathbf{u}_s \times \mathbf{B}) - \frac{q_s}{m_s}\,(\mathbf{v}_s \times \mathbf{B})\right]\nabla_v F_s = \left(\frac{\delta F_s}{\delta t}\right)_{\text{coll}}, \tag{2.2.11}$$

where t = time, r = position, $\mathbf{u}_s(t,\ \mathbf{r})$ is the bulk velocity of particles s, $\mathbf{v}_s$ is the random velocity of particles s (with respect to $\mathbf{u}_s$). Other quantities are: $\mathbf{g}(t,\ \mathbf{r})$ = gravitational acceleration, q_s = charge of particles s (it can be zero for neutral particles), m_s = mass of particles s, $\mathbf{B}$ = magnetic field vector, $\mathbf{E}$ = electric field vector. The so-called collision term, $(\delta F_s/\delta t)_{\text{coll}}$, represents the rate of change of the phase-space distribution due to collisional physical processes, including ionization, recombination, charge transfer, elastic and inelastic collisions.

The collision term describes the rate of change of the distribution function. In our case we consider physical processes playing a significant role in mass loading. These processes are the following:

- elastic collisions,
- photoionization and impact ionization,
- charge transfer, and

– recombination.

To discuss the contributions of these processes to the collision term we make the following simplifying assumptions:

– all particles are assumed to lack any internal degrees of freedom,
– energy thresholds of various processes (such as chemical reactions, ionization thresholds, etc.) will be neglected,
– all neutral species are considered cold ($T_n = 0$) and are assumed to move with the same bulk velocity, $\mathbf{u}_n$.

Elastic collisions do not change the identity of particles, but do change the momentum and energy of individual particles. In the present approximation all particles are assumed to possess no intrinsic degrees of freedom, therefore all inelastic collisions change the identity of a particle. These reactions result in ionization, charge transfer, or recombination.

Collisional effects will be described in the general framework of the relaxation-time approximation (Bhatnagar et al., 1954; Burgers, 1969; Gombosi, 1994). The main idea behind this approximation is the recognition that collisions drive all gas components towards equilibrium. Since equilibrium phase-space distributions are Maxwellians, the cumulative effect of elastic collisions can be formally described by replacing the present distribution function F_s with the appropriate Maxwellians, $F_{s(st)}$:

$$\left(\frac{\delta F_s(t,\ \mathbf{r},\ \mathbf{v}_s)}{\delta t}\right)_{el} = -\sum_{t=\text{all}} \frac{F_s(t,\ \mathbf{r},\ \mathbf{v}_s) - F_{s(st)}(t,\ \mathbf{r},\ \mathbf{v}_s)}{\tau_{st}} \ . \tag{2.2.12}$$

In expression (2.2.12) the subscript t refers to all species other than s, and τ_{st} is a relaxation time characterizing how the distribution function F_s approaches equilibrium due to collisions between particles of types s and t. Equation (2.2.12) means that st and st' collisions may drive particles s towards two different equilibria. However, in steady-state equilibrium all species will reach the same bulk velocity and temperature.

The parameters of the Maxwellian, $F_{s(st)}$, are chosen in a way such that mass, momentum and energy are conserved while the gas is driven towards equilibrium (Burgers, 1969; Gombosi, 1994):

$$F_{s(st)} = n_s \left(\frac{m_s}{2\pi k_B T_{s(st)}}\right)^{3/2} \exp\left[-\frac{m_s}{2k_B T_{s(st)}} (\mathbf{v}_s + \mathbf{u}_s - \mathbf{u}_{st})^2\right] , \tag{2.2.13}$$

where

$$n_s = \int F_s(t, \mathbf{r},\ \mathbf{v}_s)\ \mathrm{d}^3 v_s \ , \tag{2.2.14}$$

$$\mathbf{u}_{st} = \frac{m_t \mathbf{u}_t + m_s \mathbf{u}_s}{m_s + m_t} \ , \tag{2.2.15}$$

$$T_{s(st)} = T_s + \frac{m_s m_t}{(m_s + m_t)^2}\left[2(T_t - T_s) + \frac{m_t}{3k_\mathrm{B}}(\mathbf{u}_t - \mathbf{u}_s)^2\right] . \tag{2.2.16}$$

Here, the kinetic temperature is defined as

$$T_s = \frac{m_s}{3k_\mathrm{B}} \int v_s^2 F_s(t,\ \mathbf{r},\ \mathbf{v}_s)\, \mathrm{d}^3 v_s . \tag{2.2.17}$$

Equations (2.2.14)–(2.2.16) describe the number density of species s, the drift velocity of species s with respect of the center mass of fluids s and t, and the stagnation temperature of species s. It should be noted that $m_s \mathbf{u}_{st} + m_t \mathbf{u}_{ts} = 0$ and in general $T_{s(st)} \neq T_{t(ts)}$.

Concerning ionization there are four primary ionization processes to be considered: photoionization, impact ionization by superthermal electrons, impact ionization by energetic ions, and finally impact ionization by energetic neutrals. These ionization processes create new charge, therefore we consider them separately from the charge transfer reactions.

The ionization process converts a particle from the thermal neutral population to one of the charged particle species. This is a mass loading process. Since the neutral gas is assumed to be cold ($T_n = 0$) the net ionization source can be approximated by the following expression:

$$\left(\frac{\delta F_s(t,\ \mathbf{r},\ \mathbf{v}_s)}{\delta t}\right)_{\mathrm{ion}} = \left(\nu_{ph} + \nu_{\mathrm{imp}}\right) n_{s'}\, \delta^3\left(\mathbf{u}_s + \mathbf{v}_s - \mathbf{u}_n\right) , \tag{2.2.18}$$

where ν_{ph} is the photoionization frequency, ν_{imp} is the total impact ionization frequency (including superthermal electrons, energetic ions and neutrals), $n_{s'}$ is the density of particles producing charged particles of type s. Here, we assume that the charge state of particles s' is always one less than the charge state of particles s.

Charge exchange transfers an electron from one particle to an other (an example is the accidentally resonant $\mathrm{O}^+ + \mathrm{H} \rightleftharpoons \mathrm{O} + \mathrm{H}^+$ reaction). Although there is a transfer of electrons between two heavy particles, in most cases each particle tends to retain its original kinetic energy. Here we limit our consideration to singly charged ions and we consider the following general charge exchange reaction:

$$\mathrm{S}^+ + \mathrm{M} \rightarrow \mathrm{S} + \mathrm{M}^+ . \tag{2.2.19}$$

The ion S^+ is referred to as species s, while particles S are species s'. In our approximation the neutral particles form a cold gas, therefore one can write the net rate of change of the phase-space distribution function of particles s as the following:

$$\begin{aligned}\left(\frac{\delta F_s(t,\ \mathbf{r},\ \mathbf{v}_s)}{\delta t}\right)_{cx} = &- \sum_{t=\mathrm{neutrals}} k_{st} n_t F_s(t,\ \mathbf{r},\ \mathbf{v}_s) + \\ &+ \sum_{t=\mathrm{ions}} k_{ts'}\, n_t\, n_{s'} \delta^3\left(\mathbf{u}_s + \mathbf{v}_s - \mathbf{u}_n\right) ,\end{aligned} \tag{2.2.20}$$

where $k_{ts'}$ and k_{ts} are charge exchange rates. The first term describe the loss of particles s due to charge exchange with neutral species, while the second term describes the creation of new s particles by charge exchange with s' type particles.

Recombination removes a positive and a negative charge from the system. It represents a sink for electrons and for particles s and a source for particles s'. This leads to the following loss rate for ions s:

$$\left(\frac{\delta F_s(t,\ \mathbf{r},\ \mathbf{v}_s)}{\delta t}\right)_{\text{rec}} = -\alpha_{\text{R}} n_e F_s(t,\ \mathbf{r},\ \mathbf{v}_s)\ , \tag{2.2.21}$$

where α_{R} is the recombination coefficient and n_e is the electron density. Equation (2.2.21) also gives the source term for species s' (naturally with positive sign).

Finally, we combine the collision terms for all processes discussed above and combine Equations (2.2.12), (2.2.18), (2.2.20) and (2.2.21) to obtain:

$$\begin{aligned}\left(\frac{\delta F_s}{\delta t}\right)_{\text{coll}} = & -\sum_{t=\text{all}} \frac{F_s(t,\ \mathbf{r},\ \mathbf{v}_s) - F_{s(st)}(t,\ \mathbf{r},\ \mathbf{v}_s)}{\tau_{st}} \\ & - \sum_{t=\text{neutrals}} k_{st} n_t F_s(t,\ \mathbf{r},\ \mathbf{v}_s) + \sum_{t=\text{ions}} k_{ts'}\, n_t n_{s'} \delta^3(\mathbf{u}_s + \\ & + \mathbf{v}_s - \mathbf{u}_n) + \left(\nu_{ph} + \nu_{\text{imp}}\right) n_{s'}\, \delta^3\,(\mathbf{u}_s + \mathbf{v}_s - \mathbf{u}_n) - \\ & - \alpha_{\text{R}} n_e F_s(t,\ \mathbf{r},\ \mathbf{v}_s)\ .\end{aligned} \tag{2.2.22}$$

This is the collision term we use with Equation (2.2.11). This collision term is capable of describing the basic features of mass loading in space plasmas.

We evaluate the collision terms for two important applications where mass loading of space plasmas plays a dominant role in the overall dynamics of the system. These two applications are the solar wind interaction with active comets and the interaction of the heliosphere with the local interstellar medium (LISM).

At comets it is assumed that escaping cometary neutrals move radially outward with a terminal gas velocity of $u_n \approx 1$ km s^{-1}. The neutral molecules are primarily water group particles, therefore in a good approximation one can take $m_n = 17$ amu. The flux of the expanding neutral gas gradually decreases due to a combination of increasing flux tube area and loss to ionization (cf., Section 2.1). Assuming a spherically symmetric neutral gas expansion geometry the neutral gas density at a cometocentric distance, r, can be written as

$$n_n = \frac{Q}{4\pi u_n r^2} \exp\left(-\frac{r}{\lambda}\right)\ , \tag{2.2.23}$$

where Q is the total gas production rate of the comet and λ is the ionization scale-length of cometary neutrals. It is assumed that all ionization processes are represented by λ. The plasma mass production rate is now

$$\mathcal{G} = \frac{m_n\, Q}{4\pi \lambda r^2} \exp\left(-\frac{r}{\lambda}\right)\ . \tag{2.2.24}$$

For recombination and charge transfer the electron density plays an important role in cometary physical and chemical processes. These processes are important primarily in the highly collisional inner coma, where the plasma is predominantly composed of heavy cometary pickup ions. This means that in the region where the electron density and temperature play a role the average ion mass is very close to the average neutral mass, $m_i \approx m_n$. In this approximation we use the following approximation of the electron density:

$$n_e = \frac{\rho}{m_n} , \tag{2.2.25}$$

where $\rho = nm$ is the mass density. This approximation grossly underestimates the electron density at large cometocentric distances where the extra ionization and recombination are negligible anyway. However, it is fairly accurate in the inner coma, where these processes do play an important role.

In general we have very little information about electron temperatures in cometary comae. The notable exception is comet P/Halley, where the electron temperature profile was directly measured (at larger cometocentric distances) and estimated (closer to the nucleus). For comet P/Halley one may use the following profile (Eberhardt, 1995; Gombosi, 1996):

$$T_e = \begin{cases} 100 & r \le 10^{3.2} \text{ km} , \\ 10^{(1.143 \log r - 1.667)} & 10^{3.2} \text{ km} < r \le 10^{3.84} \text{ km} , \\ 10^{(10.965 \log r - 39.3725)} & 10^{3.84} \text{ km} < r \le 10^{4} \text{ km} , \\ 10^{(0.5135 \log r + 2.4325)} & 10^{4} \text{ km} < r \le 10^{5} \text{ km} , \\ 10^{5} & 10^{5} \text{ km} < r , \end{cases} \tag{2.2.26}$$

where the cometary distance is r is given in units of km.

For comets other than P/Halley we have no direct information about the electron temperature and one may simply use the

$$p_e = \frac{p}{2} = n_e k_B T_e \tag{2.2.27}$$

approximation.

It is known from laboratory experiments that the recombination rate for polyatomic ions deviates significantly from the $T_e^{-0.5}$ dependence generally assumed. The ion density in a cometary coma can only be modeled correctly if this behavior is taken into account (Haberli, 1995; Eberhardt, 1995). A numerical approximation to the measured recombination rate has been given by Eberhardt (1995):

$$\alpha_R(T_e) = \begin{cases} \alpha_0 \sqrt{\dfrac{300}{T_e}} & T_e \le 200\ K \\ 2.342\, \alpha_0\, T_e^{(0.2553 - 0.1633 \log T_e)} & 200\ K < T_e , \end{cases} \tag{2.2.28}$$

where $\alpha_0 = 7.0 \times 10^{-7}$ cm^3 s^{-1}. We use this recombination coefficient for all ions. This is not a severe limitation, since H_2O^+ and H_3O^+ compose the majority of cometary ions.

In the inner cometary coma the collision terms are important and the mean molecular masses of the ions and neutrals are nearly the same. In this case we can combine the elastic collision terms with the charge transfer terms.

The reaction rate coefficient between H_2O^+ and water molecules at room temperature has been measured to be 1.85×10^{-9} cm^3 s^{-1} with an accuracy of $\pm 15\%$. In the coma of P/Halley, about 15% of the molecules have small dipole moments (CO and CO_2). These molecules will have a lower collision rate of only about 1×10^{-9} cm^3 s^{-1}. We therefore suggest a collision rate of $k_{\rm in} = 1.7 \times 10^{-9}$ cm^3 s^{-1}, which takes into account the percentage of molecules with small dipole moments. The reaction rate of H_2O^+ is actually only a lower limit to the collision rate, since it does not include nonreactive collisions. We also do not consider collisions with other minor species which might have a higher collision rate with ions than water molecules have (e.g., H_2CO). This results in an ion-neutral collision frequency of

$$\nu_{in} = k_{\rm in} n_n \; . \tag{2.2.29}$$

In addition, we use the present approximation $\mathcal{S}_i = 0$ and $\mathcal{L}_i = 0$, since charge transfer is taken into account by $\nu_{\rm in}$.

It should be noted that Equations (2.2.23), (2.2.24) and (2.2.29) can be combined to express the ion-neutral collision frequency with the help of the mass loading rate:

$$\nu_{\rm in} = \frac{k_{\rm in}\,\lambda}{m_n\,u_n} \mathcal{G} = \eta\,\mathcal{G} \; . \tag{2.2.30}$$

2.2.2. *The Multi-Fluid Approach*

To derive a multi-fluid approach we take the low-order velocity moments of Equation (2.2.11) with the collision term given by Equation (2.2.22). In order to do this we multiply the kinetic equation by $W_s(\mathbf{v}_s)$ and integrate over the entire velocity space. This results in the following general moment equation (Gombosi, 1994):

$$\begin{aligned}
&\frac{\partial}{\partial t}\left[n_s \langle W_s \rangle\right] + (\mathbf{u}_s \cdot \nabla)\left[n_s \langle W_s \rangle\right] + \nabla \cdot \left[n_s \langle \mathbf{v}_s W_s \rangle\right] + n_s \langle W_s \rangle \left(\nabla \cdot \mathbf{u}_s\right) + \\
&+ n_s \langle \nabla_v W_s \rangle \cdot \left[\frac{\partial \mathbf{u}_s}{\partial t} + (\mathbf{u}_s \cdot \nabla)\,\mathbf{u}_s\right] + n_s Tr\left[\langle (\nabla_v W_s)\,\mathbf{v}_s \rangle \cdot (\nabla \mathbf{u}_s)\right] - \\
&- n_s \langle \left(\mathbf{g} + \frac{q_s}{m_s}\left[\mathbf{E} + \mathbf{u}_s \times \mathbf{B}\right]\right) \cdot (\nabla_v W_s) \rangle - n_s \frac{q_s}{m_s} \langle (\mathbf{v}_s \times \mathbf{B}) \cdot (\nabla_v W_s) \rangle = \\
&= \int W_s(\mathbf{v}_s) \left(\frac{\delta F_s}{\delta t}\right)_{\rm coll} {\rm d}^3 v_s \; ,
\end{aligned} \tag{2.2.31}$$

where

$$\langle W_s \rangle = \frac{1}{n_s} \int W_s(\mathbf{v}_s)\, F_s(t,\ \mathbf{r},\ \mathbf{v}_s)\, \mathrm{d}^3 v_s \ . \tag{2.2.32}$$

The continuity equation for species s is obtained by substituting $W_s = m_s$ into Equation (2.2.31). This substitution yields the following:

$$\frac{\partial \rho_s}{\partial t} + (\mathbf{u}_s \cdot \nabla)\, \rho_s + \rho_s\, (\nabla \cdot \mathbf{u}_s) = \mathcal{G}_s + \sum_{t=\text{ions}} \mathcal{S}_{ts'}\, \rho_t - (\mathcal{L}_s + \alpha_{\mathrm{R}} n_e)\, \rho_s \ , \tag{2.2.33}$$

where the ionization and loss rates are defined as

$$\mathcal{G}_s = \left(\nu_{ph} + \nu_{\text{imp}}\right) m_s n_{s'} \ , \tag{2.2.34}$$

$$\mathcal{S}_{ts'} = \frac{m_s}{m_t} k_{ts'} n_{s'} \ , \tag{2.2.35}$$

$$\mathcal{L}_s = \sum_{t=\text{neutrals}} k_{st} n_t \ . \tag{2.2.36}$$

Here $\mathcal{S}_{ts'}$ and $\mathcal{L}_s$ characterize the mass addition and loss of particles s due to charge transfer reactions. It should be noted that even though charge transfer will not create new charge, it might act as a mass source/loss for the plasma. This is the standard continuity equation which describes particle sources due to ionization and charge exchange, and particle losses due to charge exchange and recombination.

The momentum equation for species s is obtained by substituting $W_s = m_s \mathbf{v}_s$ into Equation (2.2.31):

$$\begin{aligned} &\rho_s \frac{\partial \mathbf{u}_s}{\partial t} + \rho_s\, (\mathbf{u}_s \cdot \nabla)\, \mathbf{u}_s + \nabla \cdot \mathcal{P}_s - \rho_s \mathbf{g} - \rho_s \frac{q_s}{m_s} [\mathbf{E} + \mathbf{u}_s \times \mathbf{B}] = \\ &= \sum_{t=\text{all}} \nu_{st}\, \rho_s\ (\mathbf{u}_t - \mathbf{u}_s) + \mathcal{G}_s\ (\mathbf{u}_n - \mathbf{u}_s) + \sum_{t=\text{ions}} \mathcal{S}_{ts'} \rho_t\ (\mathbf{u}_n - \mathbf{u}_s) \ , \end{aligned} \tag{2.2.37}$$

where we have introduced the pressure tensor, $\mathcal{P}_s$, and the non-resonant (elastic) momentum transfer collision frequency, ν_{st}, as

$$\mathcal{P}_s = m_s n_s \langle \mathbf{v}_s \mathbf{v}_s \rangle \ , \tag{2.2.38}$$

$$\nu_{st} = \frac{m_t}{m_s + m_t} \frac{1}{\tau_{st}} \ . \tag{2.2.39}$$

The energy equation for species s is obtained by substituting $W_s = m_s v_s^2/2$ into Equation (2.2.31):

$$\begin{aligned}
&\frac{3}{2}\frac{\partial p_s}{\partial t} + \frac{3}{2}\left(\mathbf{u}_s \cdot \nabla\right) p_s + \frac{5}{2} p_s \left(\nabla \cdot \mathbf{u}_s\right) + \left(\nabla \cdot \mathbf{h}_s\right) \\
&\quad = \sum_{t=\text{all}} \nu_{st} \rho_s \frac{3k_\text{B}}{m_s + m_t} \left(T_t - T_s\right) + \\
&\quad + \sum_{t=\text{all}} \frac{m_t}{m_s + m_t} \nu_{st}\, \rho_s\, \left(\mathbf{u}_t - \mathbf{u}_s\right)^2 + \frac{1}{2} \mathcal{G}_s\, \left(\mathbf{u}_n - \mathbf{u}_s\right)^2 + \\
&\quad + \frac{1}{2} \sum_{t=\text{ions}} \mathcal{S}_{ts'} \rho_t\, \left(\mathbf{u}_n - \mathbf{u}_s\right)^2 - \frac{3}{2} \left(\mathcal{L}_s + \alpha_\text{R} n_e\right) p_s\ ,
\end{aligned} \tag{2.2.40}$$

where

$$\mathbf{h}_s = \frac{1}{2} m_s n_s \langle v_s^2 \mathbf{u}_s \rangle \tag{2.2.41}$$

is the heat flow vector and the scalar pressure, p_s, is defined as $p_s = \text{Tr}[\mathcal{P}_s]/3$.

In Equation (2.2.40) we have the divergence of the heat flow vector (the third velocity moment of the phase-space distribution function). The heat flow is either neglected in most calculations, or the Fourier approximation ($\mathbf{h}_s = -\kappa_s \nabla T_s$), is used to achieve a low-order closure of the moment equations.

Equations (2.2.33), (2.2.37) and (2.2.40) can be also expressed in conservative form:

$$\frac{\partial \rho_s}{\partial t} + \nabla \cdot \left(\rho_s \mathbf{u}_s\right) = \mathcal{G}_s + \sum_{t=\text{ions}} \mathcal{S}_{ts'} \rho_t - \left(\mathcal{L}_s + \alpha_\text{R} n_e\right) \rho_s\ , \tag{2.2.42}$$

$$\begin{aligned}
&\frac{\partial}{\partial t}\left(\rho_s \mathbf{u}_s\right) + \nabla \cdot \left(\rho_s \mathbf{u}_s \mathbf{u}_s + \mathcal{P}_s\right) = \\
&\quad = \rho_s \mathbf{g} + \rho_s \frac{q_s}{m_s} \left[\mathbf{E} + \mathbf{u}_s \times \mathbf{B}\right] + \\
&\quad + \sum_{t=\text{all}} \nu_{st}\, \rho_s\, \left(\mathbf{u}_t - \mathbf{u}_s\right) + \mathcal{G}_s\, \mathbf{u}_n + \\
&\quad + \sum_{t=\text{ions}} \mathcal{S}_{ts'} \rho_t\, \mathbf{u}_n - \left(\mathcal{L}_s + \alpha_\text{R} n_e\right) \rho_s\, \mathbf{u}_s
\end{aligned} \tag{2.2.43}$$

$$\frac{\partial}{\partial t}\left(\tfrac{1}{2}\rho_s u_s^2+\tfrac{3}{2}p_s\right)+\nabla\cdot\left(\tfrac{1}{2}\rho_s u_s^2\mathbf{u}_s+\tfrac{5}{2}p_s\mathbf{u}_s+\mathbf{h}_s\right)=$$

$$=\mathbf{u}_s\cdot\left[\nabla\cdot(p_s\mathcal{I}-\mathcal{P}_s)\right]+\rho_s\mathbf{u}_s\cdot\left(\mathbf{g}+\frac{q_s}{m_s}\mathbf{E}\right)+$$

$$+\sum_{t=\text{all}}\nu_{st}\rho_s\frac{3k_\text{B}}{m_s+m_t}(T_t-T_s)+$$

$$+\sum_{t=\text{all}}\nu_{st}\,\rho_s\left(\frac{m_t\mathbf{u}_t+m_s\mathbf{u}_s}{m_s+m_t}\right)\cdot(\mathbf{u}_t-\mathbf{u}_s)+ \tag{2.2.44}$$

$$+\frac{1}{2}\mathcal{G}_s\,u_n^2+\frac{1}{2}\sum_{t=\text{ions}}\mathcal{S}_{ts'}\rho_t\,u_n^2-$$

$$-(\mathcal{L}_s+\alpha_\text{R}n_e)\,(\tfrac{1}{2}\rho_s u_s^2+\tfrac{3}{2}p_s)\,.$$

We note that the momentum equation contains the divergence of the full pressure tensor and the divergence of the stress tensor (which is defined as $p_s\mathcal{I}-\mathcal{P}_s$) appears in the energy equation. This means that pressure anisotropies play a potentially important role in the dynamics of space plasma flows. Even though the contribution of the stress tensor (the deviation from isotropic pressure) is usually neglected in numerical simulations, we need to keep its effect in mind and we need to include it in future simulations.

We now have the basic ingredients for a self-consistent fluid description of multicomponent plasmas. For this purpose we will use Equations (2.2.33), (2.2.37), and (2.2.40). We note that in the derivation of these equations we never made any assumption about what happens to individual pickup ions. Equations (2.2.33), (2.2.37), and (2.2.40) simply express the conservation of mass, momentum and energy for the system. They are generalizations of Equations (2.2), (2.3), and (2.4). Naturally, these equations describe only the low-order velocity moments of the distribution function and significant information is lost about the plasma by limiting our consideration to these equations only. However, supplemented with Maxwell's equations, Equations (2.2.33), (2.2.37), and (2.2.40) provide a self-consistent framework for the description of the global dynamics of mass loaded plasmas in the solar system.

The multi-fluid description of space plasmas can be greatly simplified by making the following two very plausible assumptions about the electrons:

– The fluid is quasineutral and therefore the electron density can be expressed as the sum of the ion densities:

$$n_e=\sum_{s=\text{ions}}Z_s n_s\,, \tag{2.2.45}$$

where Z_s is the charge state of ion species s. This equation replaces the electron continuity equation.

– The electron mass is neglected and the electron gas is treated as a massless fluid (however, the collision terms are treated differently).

In this approximation the non-conservative form of the electron momentum equation can be written in the following form:

$$\nabla \cdot \mathcal{P}_e + e\, n_e\, [\mathbf{E} + \mathbf{u}_e \times \mathbf{B}] = m_e n_e\, \nu_{en}\, (\mathbf{u}_n - \mathbf{u}_e) + \\ + \sum_{t=\text{ions}} m_e n_e\, \nu_{et}\, (\mathbf{u}_t - \mathbf{u}_e)\ , \tag{2.2.46}$$

where

$$\nu_{en} = \sum_{t=\text{neutrals}} \nu_{et}\ , \tag{2.2.47}$$

is the total electron-neutral collision frequency. Electron collision frequencies with some important neutral species can be found in the literature (we refer to the classic review by Schunk and Nagy (1980)). The electron-ion collision frequency can be expressed as (Schunk and Nagy, 1980)

$$\nu_{es} = 54.5 \frac{Z_s^2 n_s}{T_e^{3/2}}\ . \tag{2.2.48}$$

In expression (2.2.48) the collision frequency is given in units of s^{-1}, the ion number density is measured in cm^{-3}, and the electron temperature is given in K. In Equation (2.2.46) we neglected the contribution of newly created electrons and separated the contribution of electron-ion and electron-neutral collisions. This equation can be used to express the electric field.

The only electron equation which needs to be solved in this approximation is the energy equation. Most models sidestep even this equation and either use an adiabatic equation of state ($p_e/\rho_e^\gamma = \text{const}$), or use a specified electron temperature profile. In general a somewhat modified version of Equation (2.2.40) needs to be solved for the electron temperature, since one needs to take into account additional heating and cooling terms due to photoelectron heating and inelastic collisions. The electron energy equation now becomes the following:

$$\frac{3}{2}\frac{\partial p_e}{\partial t} + \frac{3}{2}\,(\mathbf{u}_e \cdot \nabla)\, p_e + \frac{5}{2} p_e\, (\nabla \cdot \mathbf{u}_e) + (\nabla \cdot \mathbf{h}_e) = \\ = Q_e + m_e\, n_e\, \nu_{en}\, (\mathbf{u}_n - \mathbf{u}_e)^2\ , \tag{2.2.49}$$

$$+ \sum_{t=\text{ions}} \frac{m_e\, n_e\, \nu_{et}}{m_t} 3 k_\mathrm{B}\, (T_t - T_e) + \sum_{t=\text{ions}} m_e\, n_e\, \nu_{et}\, (\mathbf{u}_t - \mathbf{u}_e)^2 - \\ - \frac{3}{2} p_e \left(2\nu_{en}^{(e)} + \alpha_\mathrm{R} n_e\right)\ , \tag{2.2.50}$$

where Q_e is a net electron heating rate and

$$\nu_{en}^{(e)} = \sum_{t=\text{neutrals}} \nu_{et} \frac{m_e}{m_t} \,. \tag{2.2.51}$$

In general one can solve Equations (2.2.33), (2.2.37) and (2.2.40) for each ion species together with Equation (2.2.46) for the electric field and Faraday's law for the magnetic field. Here, we consider a simplified model which can serve as the basis of 3D global simulations.

In order to further simplify the transport equations we make the following assumptions about the ion fluids:

- All ion species move with the same bulk velocity, $\mathbf{u}_i$.
- We solve for the total ion pressure, p_i, and not for the pressures of the individual ions.

With these assumptions equation (2.2.46) becomes

$$\nabla \cdot \mathcal{P}_e + e\, n_e \left[\mathbf{E} + \mathbf{u}_e \times \mathbf{B}\right] = m_e n_e\, \nu_{en}\ (\mathbf{u}_n - \mathbf{u}_e) + m_e n_e\, \nu_{ei}\ (\mathbf{u}_i - \mathbf{u}_e)\ , \tag{2.2.52}$$

where

$$\nu_{ei} = \sum_{t=\text{ions}} \nu_{et}\ . \tag{2.2.53}$$

Next we recognize that the electron velocity can be expressed with the help of the current density, $\mathbf{j}$:

$$\mathbf{j} = -e\, n_e \mathbf{u}_e + e \sum_{t=\text{ions}} Z_t\, n_t\, \mathbf{u}_i = e\, n_e\, (\mathbf{u}_i - \mathbf{u}_e)\ . \tag{2.2.54}$$

Now one can combine Equations (2.2.52) and (2.2.54):

$$\begin{aligned} \mathbf{E} \ &= -\frac{1}{e n_e} \nabla \cdot \mathcal{P}_e + \left(\frac{1}{e n_e}\mathbf{j} - \mathbf{u}_i\right) \times \mathbf{B} \\ &\quad + \frac{m_e}{e^2 n_e}\, (\nu_{en} + \nu_{ei})\, \mathbf{j} + \frac{m_e}{e} \nu_{en}\, (\mathbf{u}_n - \mathbf{u}_i)\ . \end{aligned} \tag{2.2.55}$$

In a quasineutral plasma Maxwell's equations are given as Poisson's equation

$$\nabla \cdot \mathbf{E} = 0\,, \tag{2.2.56}$$

the absence of magnetic monopoles, that is

$$\nabla \cdot \mathbf{B} = 0\,, \tag{2.2.57}$$

Faraday's law, which for an arbitrary vector field can be written as (e.g., Jackson, 1975)

$$\frac{\partial \mathbf{B}}{\partial t} = -\nabla \times \mathbf{E} - (\nabla \cdot \mathbf{B})\, \mathbf{u}\,, \tag{2.2.58}$$

and Ampère's law

$$\mu_0 \mathbf{j} = \nabla \times \mathbf{B} - \frac{1}{c^2} \frac{\partial \mathbf{E}}{\partial t} \,, \tag{2.2.59}$$

where c is the speed of light and μ_o is the permeability of vacuum.

We note that mathematically speaking Equations (2.2.56) and (2.2.57) represent initial conditions. This is important to point out, since Equations (2.2.58) and (2.2.59) represent six equations for six unknown functions. In the mathematical sense Equations (2.2.56) and (2.2.57) would overconstrain the system if they were enforced as a constraint. As it will be discussed later, the full system of MHD equations ensure the conservation of charge and $\nabla \cdot \mathbf{B}$ along plasma flow lines, therefore it is adequate to use Equations (2.2.56) and (2.2.57) as initial conditions. This distinction becomes very important in modern numerical methods for solving the MHD equations, since these methods are based on basic mathematical properties of the MHD conservation laws.

A consequence of the enforcement of $\nabla \cdot \mathbf{B} = 0$ as an initial condition is that we must formally keep the $\nabla \cdot \mathbf{B}$ term in Equation (2.2.58). It was pointed in the leading textbook on electromagnetism (Jackson, 1975) that for an unconstrained vector field (where $\nabla \cdot \mathbf{B} = 0$ is not enforced at all times) an extra term appears in Faraday's law, which is proportional to $\nabla \cdot \mathbf{B}$. We kept this term here, even though we know that there are no magnetic monopoles. The absence of magnetic monopoles is enforced in a more subtle way through the (2.2.58) initial condition and through the property of the MHD equations that $\nabla \cdot \mathbf{B}/\rho$ is a passively convected scalar (Godunov, 1972; Powell, 1994).

In the present approximation Equation (2.2.55) defines the electric field vector, therefore Equations (2.2.58) and (2.2.59) can be used to obtain the magnetic field vector and the electric current density. Now Equations (2.2.33), (2.2.37), and (2.2.40), (or alternatively Equations (2.2.42), (2.2.43), and (2.2.44)) together with Equations (2.2.55), (2.2.58), and (2.2.59) provide a self-consistent description of the plasma.

The continuity equations become the following (we have a separate continuity equation for each ion species):

$$\frac{\partial \rho_s}{\partial t} + (\mathbf{u}_i \cdot \nabla)\, \rho_s + \rho_s\, (\nabla \cdot \mathbf{u}_i) = \mathcal{Q}_s + \sum_{t=\text{ions}} \mathcal{S}_{ts'} \rho_t - (\mathcal{L}_i + \alpha_{\mathrm{R}} n_e)\, \rho_s \,, \tag{2.2.60}$$

where we have assumed that the charge exchange loss rate is about the same for all ions, $\mathcal{L}_s \approx \mathcal{L}_i$.

Substituting expression (2.2.55) into Equation (2.2.37) yields a new momentum equation for ion s:

$$\rho_s \frac{\partial \mathbf{u}_i}{\partial t} + \rho_s \left(\mathbf{u}_i \cdot \nabla\right) \mathbf{u}_i + \nabla \cdot \mathcal{P}_s + \frac{Z_s n_s}{n_e} \nabla \cdot \mathcal{P}_e - \rho_s \mathbf{g} - \frac{Z_s n_s}{n_e} \mathbf{j} \times \mathbf{B} =$$
$$= \frac{Z_s n_s}{n_e} \frac{m_e}{e} \left(\nu_{en} + \nu_{ei}\right) \mathbf{j} + \left(\mathcal{G}_s + \nu_{sn} \rho_s + \sum_{t=\text{ions}} \mathcal{S}_{ts'} \rho_t \right) \left(\mathbf{u}_n - \mathbf{u}_i\right) \ , \tag{2.2.61}$$

where

$$\nu_{sn} = \sum_{t=\text{neutrals}} \nu_{st} \ . \tag{2.2.62}$$

Since all ions are assumed to have the same velocity one can add together all ion momentum equations:

$$\rho_i \frac{\partial \mathbf{u}_i}{\partial t} + \rho_i \left(\mathbf{u}_i \cdot \nabla\right) \mathbf{u}_i + \nabla \cdot \left(\mathcal{P}_i + \mathcal{P}_e\right) -$$
$$-\rho_i \mathbf{g} - \mathbf{j} \times \mathbf{B} = \frac{m_e}{e} \left(\nu_{en} + \nu_{ei}\right) \mathbf{j} + \tag{2.2.63}$$
$$+ \left(\mathcal{G}_i + \sum_{s=\text{ions}} \nu_{sn} \rho_s + \sum_{t=\text{ions}} \mathcal{S}_t \rho_t \right) \left(\mathbf{u}_n - \mathbf{u}_i\right) \ ,$$

where

$$\rho_i = \sum_{t=\text{ions}} \rho_t \ , \tag{2.2.64}$$

$$\mathcal{G}_i = \sum_{t=\text{ions}} \mathcal{G}_t \ , \tag{2.2.65}$$

$$\mathcal{P}_i = \sum_{t=\text{ions}} \mathcal{P}_t \ , \tag{2.2.66}$$

$$\mathcal{S}_t = \sum_{s'} \mathcal{S}_{ts'} \ . \tag{2.2.67}$$

Finally, we add together all ion energy equations (Equation 2.2.40) to obtain:

$$\frac{3}{2} \frac{\partial p_i}{\partial t} + \frac{3}{2} \left(\mathbf{u}_i \cdot \nabla\right) p_i + \frac{5}{2} p_i \left(\nabla \cdot \mathbf{u}_i\right) + \left(\nabla \cdot \mathbf{h}_i\right) =$$
$$= - \sum_{s=\text{ions}} 3 p_s \sum_{t=\text{neutrals}} \frac{m_s}{m_s + m_t} \nu_{st} +$$
$$+ \left(\sum_{s=\text{ions}} \rho_s \sum_{t=\text{neutrals}} \frac{m_t}{m_s + m_t} \nu_{st} + \right. \tag{2.2.68}$$
$$\left. + \frac{1}{2} \mathcal{G}_i + \sum_{t=\text{ions}} \frac{1}{2} \mathcal{S}_t \rho_t \right) \left(\mathbf{u}_n - \mathbf{u}_i\right)^2 -$$
$$- \frac{3}{2} \left(\mathcal{L}_i + \alpha_{\text{R}} n_e\right) p_i \ ,$$

where

$$p_i = \sum_{t=\text{ions}} p_t \ , \tag{2.2.69}$$

$$\mathbf{h}_i = \sum_{t=\text{ions}} \mathbf{h}_t \ . \tag{2.2.70}$$

When deriving Equation (2.2.68) we made use of the well-known identity:

$$\rho_s \nu_{st} = \rho_t \nu_{ts} \ . \tag{2.2.71}$$

Most terms in Equation (2.2.68) contain only the individual ion densities, ρ_s, the ion bulk velocity, $\mathbf{u}_i$, or the total ion pressure tensor, $\mathcal{P}_i$. Equation (2.2.68) also contains the electron pressure tensor, $\mathcal{P}_e$, which is assumed to be a known physical quantity. There is, however, one term on the right-hand side, which explicitly depends on the individual ion pressures, p_s. These pressures can be combined into the total ion pressure by making an additional simplification.

We recognize that the elastic collision frequency between an ion s and a neutral t can be expressed as

$$\nu_{st} = \sqrt{\frac{m_s m_t}{m_s + m_t}} \frac{1}{m_s} C_t n_t \ , \tag{2.2.72}$$

where C_t is a numerical constant and n_t is the number density of species t (Schunk and Nagy, 1980). Next we introduce the following approximations:

$$\nu_{st} \approx \nu_{it} = \sqrt{\frac{m_i m_t}{m_i + m_t}} \frac{1}{m_i} C_t n_t \ , \tag{2.2.73}$$

$$\frac{m_s}{m_s + m_t} \nu_{st} \approx \frac{m_i}{m_i + m_n} \nu_{it} \ , \tag{2.2.74}$$

$$\frac{m_t}{m_s + m_t} \nu_{st} \approx \frac{m_t}{m_i + m_n} \nu_{it} \ , \tag{2.2.75}$$

where m_i and m_n are the average molecular masses of all ions and neutrals, respectively. We note that ν_{it} is independent of s, therefore Equation (2.2.68) can be rewritten as

$$\begin{aligned} &\frac{3}{2}\frac{\partial p_i}{\partial t} + \frac{3}{2}\left(\mathbf{u}_i \cdot \nabla\right) p_i + \frac{5}{2} p_i \left(\nabla \cdot \mathbf{u}_i\right) + \left(\nabla \cdot \mathbf{h}_i\right) = \\ &\quad = \left(\frac{1}{2}\mathcal{G}_i + \frac{m_n \nu_{in}\, \rho_i}{m_i + m_n} + \sum_{t=\text{ions}} \frac{1}{2}\mathcal{S}_t\, \rho_t \right) \left(\mathbf{u}_n - \mathbf{u}_i\right)^2 - \\ &\qquad - \frac{3}{2}\left(2\,\frac{m_i}{m_i + m_n}\,\nu_{in} + \mathcal{L}_i + \alpha_{\mathrm{R}} n_e \right) p_i \ , \end{aligned} \tag{2.2.76}$$

where

$$\nu_{in} = \sum_{t=\text{neutrals}} \nu_{it} \ . \tag{2.2.76}$$

In the multi-ion approximation one has to solve Equations (2.2.60), (2.2.63), and (2.2.76) together with Equations (2.2.55), (2.2.58), and (2.2.59). In addition, the electron pressure must be obtained from some assumption or by solving Equation (2.2.49).

2.2.3. *The One-Fluid MHD Approach*

In single-fluid MHD we make an additional set of simplifying assumptions:

- The distribution functions of all plasma components are assumed to be isotropic in the plasma frame. In this approximation there are no stresses or heat fluxes, therefore $\mathcal{P}_s = p_s \mathcal{I}$ and $\mathbf{h}_s = 0$ for all species.
- We consider the total mass density (ρ), average bulk velocity ($\mathbf{u}$), total scalar pressure (p), and magnetic field ($\mathbf{B}$) as state variables. The global fluid quantities are defined in the following way:

$$\rho = \rho_i + m_e n_e \approx \rho_i \ , \tag{2.2.78}$$

$$\mathbf{u} = \frac{\rho_i \mathbf{u}_i + m_e n_e \mathbf{u_e}}{\rho} \approx \mathbf{u}_i \ , \tag{2.2.79}$$

$$p = p_i + p_e \ . \tag{2.2.80}$$

  The small difference between the ion and electron velocities due the presence of electric currents is neglected, that is $\mathbf{j}/en_e \approx 0$, except when it is multiplied with a large collision frequency.

In this approximation the single-fluid transport equations become the following. The continuity equation reads

$$\frac{\partial \rho}{\partial t} + (\mathbf{u} \cdot \nabla)\, \rho + \rho\, (\nabla \cdot \mathbf{u}) = \mathcal{G} + (\mathcal{S}_i - \mathcal{L}_i - \alpha_{\mathrm{R}} n_e)\, \rho \ , \tag{2.2.81}$$

where $\mathcal{G}$ is the mass production rate due to new ionization, $\mathcal{S}_i$ and $\mathcal{L}_i$ describe the mass addition and loss rates due to charge exchange, and finally $\alpha_{\mathrm{R}} n_e$ characterizes the mass loss rate due to recombination. It should be noted again that the recombination rate needs some approximation of the electron number density.

The momentum equation in the one-fluid approach reads

$$\rho \frac{\partial \mathbf{u}}{\partial t} + \rho\, (\mathbf{u} \cdot \nabla)\, \mathbf{u} + \nabla p - \rho \mathbf{g} - \mathbf{j} \times \mathbf{B} = \left(\mathcal{G} + \nu_{in}\, \rho + \mathcal{S}_i \rho\right) (\mathbf{u}_n - \mathbf{u}) \ . \tag{2.2.82}$$

Here we neglect the current dissipation term, since it is multiplied by the electron mass.

The energy equation is given as

$$\frac{3}{2}\frac{\partial p}{\partial t} + \frac{3}{2}(\mathbf{u}\cdot\nabla)\,p + \frac{5}{2}p\,(\nabla\cdot\mathbf{u}) = Q_e +$$
$$+\left[\frac{1}{2}\mathcal{G} + \frac{m_n}{m_i+m_n}\,\nu_{in}\,\rho + \frac{1}{2}\mathcal{S}_i\,\rho\right](\mathbf{u}_n-\mathbf{u})^2 - \tag{2.2.83}$$
$$-3\,\frac{m_i}{m_i+m_n}\,\nu_{in}p_i - \frac{3}{2}\mathcal{L}_i\,p_i - \frac{3}{2}\alpha_{\mathrm{R}}n_e p\ ,$$

where we neglect the electron-neutral frictional heating (this is very inefficient) and the ion-electron heat exchange (this is irrelevant since this heat exchange will have no effect on the total pressure).

We note that the right hand side of the energy equation contains loss terms which are proportional to the ion pressure only (in addition to the recombination loss term which is proportional to the electron density). In many applications these loss terms can be neglected, but here we keep them for completeness.

In Ohm's law (2.2.55) we neglect the ambipolar field, the Hall term, and the collisional losses. These simplifications result in Ohm's law for the ideal MHD:

$$\mathbf{E} = -\mathbf{u}\times\mathbf{B}\ . \tag{2.2.84}$$

With the help of Equation (2.2.84) Faraday's law (2.2.58) reads as

$$\frac{\partial\mathbf{B}}{\partial t} = \nabla\times(\mathbf{u}\times\mathbf{B}) - (\nabla\cdot\mathbf{B})\,\mathbf{u}\ . \tag{2.2.85}$$

Finally, with the help of Equation (2.2.84) Ampère's law (2.2.59) becomes the following:

$$\mu_0\mathbf{j} = \nabla\times\mathbf{B} - \frac{1}{c^2}\frac{\partial(\mathbf{u}\times\mathbf{B})}{\partial t}\ . \tag{2.2.86}$$

We note that the displacement current is neglected in most cases. However, in situations when the Alfvén speed is high the displacement current must be kept, because it will limit the Alfvén speed to the speed of light. For the sake of simplicity here we neglect the displacement current and obtain the following expression for Ampère's law:

$$\mu_0\mathbf{j} = \nabla\times\mathbf{B}\ . \tag{2.2.87}$$

Now the non-conservative form of the single-fluid MHD equations can be written as follows:

$$\frac{\partial\rho}{\partial t} + (\mathbf{u}\cdot\nabla)\,\rho + \rho\,(\nabla\cdot\mathbf{u}) = \mathcal{G} + (\mathcal{S}_i - \mathcal{L}_i - \alpha_{\mathrm{R}}n_e)\,\rho\ , \tag{2.2.88}$$

$$\rho\frac{\partial\mathbf{u}}{\partial t} + \rho\,(\mathbf{u}\cdot\nabla)\,\mathbf{u} + \nabla p - \rho\mathbf{g} + \frac{1}{\mu_0}\mathbf{B}\times(\nabla\times\mathbf{B}) =$$
$$= \left(\mathcal{G} + \nu_{in}\,\rho + \mathcal{S}_i\rho\right)(\mathbf{u}_n-\mathbf{u})\ , \tag{2.2.89}$$

$$\frac{3}{2}\frac{\partial p}{\partial t} + \frac{3}{2}(\mathbf{u}\cdot\nabla)\,p + \frac{5}{2}p\,(\nabla\cdot\mathbf{u}) = Q_e +$$
$$+\left[\frac{1}{2}\mathcal{G} + \frac{m_n}{m_i+m_n}\,\nu_{in}\,\rho + \frac{1}{2}\mathcal{S}_i\,\rho\right](\mathbf{u}_n-\mathbf{u})^2 - \tag{2.2.90}$$
$$-3\,\frac{m_i}{m_i+m_n}\,\nu_{in}p_i - \frac{3}{2}\mathcal{L}_i\,p_i - \frac{3}{2}\alpha_{\mathrm{R}}n_e p\ ,$$

$$\frac{\partial \mathbf{B}}{\partial t} = \nabla\times(\mathbf{u}\times\mathbf{B}) - (\nabla\cdot\mathbf{B})\,\mathbf{u}\ . \tag{2.2.91}$$

The conservative form of the MHD equations can be written in the following form:

$$\frac{\partial\rho}{\partial t} + \nabla\cdot(\rho\mathbf{u}) = \mathcal{G} + (\mathcal{S}_i - \mathcal{L}_i - \alpha_{\mathrm{R}}n_e)\,\rho\ , \tag{2.2.92}$$

$$\tfrac{\partial(\rho\mathbf{u})}{\partial t} + \nabla\cdot\left(\rho\mathbf{u}\mathbf{u} + pI + \tfrac{1}{2\mu_0}B^2 - \tfrac{1}{\mu_0}\mathbf{B}\mathbf{B}\right) =$$
$$= -\frac{1}{\mu_0}(\nabla\cdot\mathbf{B})\,\mathbf{B} + \rho\mathbf{g} + \left(\mathcal{G}+\mathcal{S}_i\rho\right)\mathbf{u}_n + \tag{2.2.93}$$
$$+\,\nu_{in}\,\rho\,(\mathbf{u}_n-\mathbf{u}) - (\mathcal{L}_i+\alpha_{\mathrm{R}}n_e)\,\rho\mathbf{u}\ ,$$

$$\frac{\partial}{\partial t}\left(\frac{1}{2}\rho u^2 + \frac{3}{2}p + \frac{1}{2\mu_0}B^2\right) + \nabla\left[\left(\frac{1}{2}\rho u^2 + \frac{5}{2}p + \frac{1}{\mu_0}B^2\right)\mathbf{u} - \right.$$
$$\left. -\frac{1}{\mu_0}(\mathbf{B}\cdot\mathbf{u})\,\mathbf{B}\right] = Q_e + \rho\,(\mathbf{g}\cdot\mathbf{u}) - \frac{1}{\mu_0}(\nabla\cdot\mathbf{B})\,(\mathbf{B}\cdot\mathbf{u}) +$$
$$+\frac{1}{2}\left(\mathcal{G}+\mathcal{S}_i\,\rho\right)u_n^2 + \nu_{in}\left(\frac{m_n\mathbf{u}_n + m_i\mathbf{u}_i}{m_n+m_i}\right)\cdot(\mathbf{u}_n-\mathbf{u}) - \tag{2.2.94}$$
$$-\frac{1}{2}(\mathcal{L}_i+\alpha_{\mathrm{R}}n_e)\left(\rho u^2+3p\right) + \frac{3}{2}\mathcal{L}_i\,p_e - 3\,\frac{m_i}{m_i+m_n}\,\nu_{in}\,p_i\ ,$$

$$\frac{\partial\mathbf{B}}{\partial t} + \nabla\cdot(\mathbf{u}\mathbf{B} - \mathbf{B}\mathbf{u}) = -\,(\nabla\cdot\mathbf{B})\ \mathbf{u}\ . \tag{2.2.95}$$

On the right-hand sides of Equations (2.2.92) through (2.2.95) there are terms proportional to $\nabla\cdot\mathbf{B}$. These terms in arise solely from rewriting the magnetic-field terms in the governing equations in conservative form. Equations (2.2.92)–(2.2.95) (with the source term) are exactly equivalent to Equations (2.2.88) through (2.2.91).

Although for physical fields there are no magnetic monopoles, and the $\nabla\cdot\mathbf{B}$ source term is therefore zero, dropping the source term from the analysis changes

the character of the equations. This has been pointed out previously by Godunov (1972). He showed that a special class of systems, which includes the equations of gas dynamics, admit an additional conservation law that comes from multiplying each of the equations by a function and adding them up. For gas dynamics, the extra equation is the entropy conservation law, $\mathrm{d}S/\mathrm{d}t = 0$. It turns out that this actually helps to cast the conservation equations into symmetric forms. Note, that a symmetrizable system is one that can be written in a form (in 1D, for simplicity) $\mathrm{d}u/\mathrm{d}t + A\,\mathrm{d}u/\mathrm{d}x = 0$ where A is a symmetric matrix.

Godunov (1972) found that the ideal MHD equations written in their usual way (i.e., Equations (2.2.92)–(2.2.95) without the $\nabla\cdot\mathbf{B}$ source term) are not symmetrizable. He further found that the system could be rendered symmetrizable only by adding a factor of the constraint $\nabla \cdot \mathbf{B} = 0$ to each of the equations, and that the resulting symmetrizable form was that of Equations (2.2.92)–(2.2.95) with the source term. One property of the symmetrizable form of a system of conservation laws is that an added conservation law (neglecting all source terms other than the $\nabla \cdot \mathbf{B}$ terms)

$$\frac{\partial(\rho S)}{\partial t} + \frac{\partial(\rho u S)}{\partial x} + \frac{\partial(\rho v S)}{\partial y} + \frac{\partial(\rho w S)}{\partial z} = 0\,,$$

for the entropy S can be derived by multiplying each equation in the system by a factor and adding the resulting equations. Note, that in ideal MHD the entropy is simply $S = p/\rho^{\gamma}$, therefore the added conservation law ensures the conservation of a thermodynamic quantity.

Another consequence of symmetrizable system of conservation laws is that the system is Galilean invariant and all waves in the system propagate at speeds $u \pm a$ (for MHD, the possible values of a are the Alfvén, magnetofast and magentoslow speeds). Neither of these properties holds for the system if the $\nabla \cdot \mathbf{B}$ source term is ignored.

Equations (2.2.88)–(2.2.91), or Equations (2.2.92)–(2.2.95) with the source term, yields the following evolution equation for $\nabla \cdot \mathbf{B}$:

$$\frac{\partial}{\partial t}(\nabla \cdot \mathbf{B}) + \nabla \cdot (\mathbf{u}\,\nabla \cdot \mathbf{B}) = 0\,. \tag{2.2.96}$$

This is a statement that the quantity $\nabla \cdot \mathbf{B}/\rho$ satisfies the equation for a passively convected scalar ϕ, i.e.,

$$\frac{\partial}{\partial t}(\rho\phi) + \nabla \cdot (\rho\mathbf{u}\phi) = 0\,. \tag{2.2.97}$$

Thus, for a solution of this system, the quantity $\nabla \cdot \mathbf{B}/\rho$ is constant along particle paths and therefore, since the initial conditions satisfy $\nabla \cdot \mathbf{B} = 0$, the same will be true for all later times.

The approach taken in our simulations is therefore to solve the equations in their symmetrizable form, i.e., the form of Equations (2.2.92)–(2.2.95). As shown

previously (Powell, 1994; Powell, 1999), this form of the equations allows the derivation of an eight-wave approximate Riemann solver that can be used to construct an upwind solution scheme for multi-dimensional flows. The elements of the solution scheme are described by Powell (1999).

Finally, we substitute all our approximations for the collisions terms into the conservative form of the single-fluid MHD equations to obtain the governing equations of cometary MHD:

$$\frac{\partial \rho}{\partial t} + \nabla \cdot (\rho \mathbf{u}) = \mathcal{G} - \alpha_{\mathrm{R}} n_e \rho \,, \tag{2.2.98}$$

$$\begin{aligned} &\frac{\partial (\rho \mathbf{u})}{\partial t} + \nabla \cdot \left(\rho \mathbf{u}\mathbf{u} + p\mathcal{I} + \frac{1}{2\mu_0} B^2 \mathcal{I} - \frac{1}{\mu_0} \mathbf{B}\mathbf{B} \right) = \\ &\quad = -\frac{1}{\mu_0} (\nabla \cdot \mathbf{B})\ \mathbf{B} + \mathcal{G}\mathbf{u}_n + \eta\, \mathcal{G}\, \rho\ (\mathbf{u}_n - \mathbf{u}) - \alpha_{\mathrm{R}} n_e \rho \mathbf{u} \,, \end{aligned} \tag{2.2.99}$$

$$\begin{aligned} &\frac{\partial}{\partial t} \left(\frac{1}{2}\rho u^2 + \frac{3}{2} p + \frac{1}{2\mu_0} B^2 \right) + \nabla \cdot \left[\left(\frac{1}{2}\rho u^2 + \frac{3}{2} p + \frac{1}{2\mu_0} B^2 \right) \mathbf{u} - \right. \\ &\left. (\mathbf{B} \cdot \mathbf{u})\, \mathbf{B} \right] = -\frac{1}{\mu_0} (\nabla \cdot \mathbf{B})\, (\mathbf{B} \cdot \mathbf{u}) + \frac{1}{2} \mathcal{G}\, u_n^2 + \\ &+ \eta\, \mathcal{G} \left(u_n^2 - u^2 \right) - \frac{1}{2} \alpha_{\mathrm{R}} n_e \left(\rho u^2 + 3p \right) - \frac{3}{2}\, \eta\, \mathcal{G}\, p_i \,, \end{aligned} \tag{2.2.100}$$

$$\frac{\partial \mathbf{B}}{\partial t} + \nabla \cdot (\mathbf{u}\mathbf{B} - \mathbf{B}\mathbf{u}) = -\,(\nabla \cdot \mathbf{B})\ \mathbf{u} \,. \tag{2.2.101}$$

Needless to say that gravity was neglected for the cometary case.

2.2.4. *The Two-Fluid MHD Approach*

The two-fluid approximation can be obtained from the multi-ion approximation by adding together all ion continuity equations. In this approximation we only consider two fluids: ions and electrons. In order to simplify our transport equations to the two-fluid form we must make some additional assumptions about the charge transfer rates. The most typical charge exchange rates are given by Schunk and Nagy (1980). Here we make the following approximation:

$$\sum_{t=\text{ions}} \mathcal{S}_t\, \rho_t \approx \mathcal{S}_i\, \rho_i \,, \tag{2.2.102}$$

where $\mathcal{S}_i$ is the average charge exchange production rate. Using this simplification one can add together all ion continuity Equation (2.2.60) to obtain a single-ion continuity equation:

$$\frac{\partial \rho_i}{\partial t} + (\mathbf{u}_i \cdot \nabla)\, \rho_i + \rho_i\, (\nabla \cdot \mathbf{u}_i) = \mathcal{G}_i + \mathcal{S}_i \rho_i - (\mathcal{L}_i + \alpha_{\mathrm{R}} n_e)\, \rho_i \,. \tag{2.2.103}$$

The single-ion momentum equation (Equation (2.2.63)) becomes:

$$\rho_i \frac{\partial \mathbf{u}_i}{\partial t} + \rho_i \left(\mathbf{u}_i \cdot \nabla\right) \mathbf{u}_i + \nabla \cdot \left(P_i + P_e\right) - \rho_i \mathbf{g} - \mathbf{j} \times \mathbf{B} = \\ = \frac{m_e}{e} \left(\nu_{en} + \nu_{ei}\right) \mathbf{j} + \left(\mathcal{G}_i + \nu_{in}\, \rho_i + \mathcal{S}_i \rho_i\right) \left(\mathbf{u}_n - \mathbf{u}_i\right) \ . \tag{2.2.104}$$

The single-ion energy equation now becomes

$$\frac{3}{2} \frac{\partial p_i}{\partial t} + \frac{3}{2} \left(\mathbf{u}_i \cdot \nabla\right) p_i + \frac{5}{2} p_i \left(\nabla \cdot \mathbf{u}_i\right) + \left(\nabla \cdot \mathbf{h}_i\right) = \\ = \left(\frac{1}{2} \mathcal{G}_i + \frac{m_n}{m_i + m_n}\, \nu_{in}\, \rho_i + \frac{1}{2} \mathcal{S}_i\, \rho_i\right) \left(\mathbf{u}_n - \mathbf{u}_i\right)^2 - \\ - \frac{3}{2} \left(2 \frac{m_i}{m_i + m_n}\, \nu_{in} + \mathcal{L}_i + \alpha_{\mathrm{R}} n_e\right) p_i \ . \tag{2.2.105}$$

These equations are again supplemented by Equations (2.2.55), (2.2.58), and (2.2.59), describing the **E**, **B**, and **j**.

It should be pointed out that the two-fluid equation system explicitly contains the electron density and pressure. These quantities need to be obtained from auxiliary information, since Equations (2.2.103), (2.2.104), and (2.2.105) do not provide their solutions.

2.2.5. *The Bi-Ion Fluid Approach*

A special application of the general two-fluid MHD approach described above is the bi-ion fluid approach frequently used by Sauer et al. (1994, 1996a, b, 1997).

Combining the momentum equations with the continuity equations for protons and heavy ions, including Faraday's law and the energy equation, the following set of equations forms our basic system of bi-ion fluid equations describing the electromagnetic coupling between the proton and heavy ion fluid. The proton equations read:

$$\frac{\partial}{\partial t} n_{\mathrm{p}} + \nabla \cdot \left(n_{\mathrm{p}} \mathbf{v}_{\mathrm{p}}\right) = 0 \ , \tag{2.2.106}$$

$$\frac{\partial}{\partial t} \left(n_{\mathrm{p}} \mathbf{v}_{\mathrm{p}}\right) + \nabla \cdot \left(n_{\mathrm{p}} \mathbf{v}_{\mathrm{p}} \mathbf{v}_{\mathrm{p}} + \frac{p_{\mathrm{p}}}{m_{\mathrm{p}}}\right) = \tag{2.2.107}$$

$$\frac{1}{m_{\mathrm{p}}} \frac{n_{\mathrm{p}}}{n_{\mathrm{e}}} \left[e n_{\mathrm{h}} (\mathbf{v}_{\mathrm{p}} - \mathbf{v}_{\mathrm{h}}) \times \mathbf{B} - \nabla \left(\left(p_{\mathrm{e}} + \frac{B^2}{2\mu_0}\right) \mathbf{I} - \frac{\mathbf{B}\mathbf{B}}{\mu_0}\right)\right] \ . \tag{2.2.108}$$

The corresponding heavy ion equations are:

$$\frac{\partial}{\partial t} n_{\mathrm{h}} + \nabla \cdot \left(n_{\mathrm{h}} \mathbf{v}_{\mathrm{h}}\right) = \mathcal{N}_{<} \ , \tag{2.2.109}$$

$$\frac{\partial}{\partial t}(n_{\mathrm{h}}\mathbf{v}_{\mathrm{h}}) + \nabla\cdot\left(n_{\mathrm{h}}\mathbf{v}_{\mathrm{h}}\mathbf{v}_{\mathrm{h}} + \frac{p_{\mathrm{h}}}{m_{\mathrm{h}}}\right) = \tag{2.2.110}$$

$$= \frac{1}{m_{\mathrm{h}}}\frac{n_{\mathrm{h}}}{n_{\mathrm{e}}}\left[en_{\mathrm{p}}(\mathbf{v}_{\mathrm{h}} - \mathbf{v}_{\mathrm{p}})\times\mathbf{B} - \nabla\left(\left(p_{\mathrm{e}} + \frac{B^2}{2\mu_0}\right)\mathbf{I} - \frac{\mathbf{BB}}{\mu_0}\right)\right] . \tag{2.2.111}$$

Faraday's law now reads:

$$\frac{\partial\mathbf{B}}{\partial t} + \nabla\times\left[\frac{1}{n_{\mathrm{e}}}(n_{\mathrm{p}}\mathbf{v}_{\mathrm{p}} + n_{\mathrm{h}}\mathbf{v}_{\mathrm{h}})\times\mathbf{B} - \frac{\mathbf{B}\cdot\nabla\mathbf{B}}{\mu_0}\right] = 0 \tag{2.2.112}$$

and the electron energy equation is given as

$$\frac{\partial}{\partial t}p_{\mathrm{e}} + \nabla\cdot(\mathbf{v}_{\mathrm{e}}p_{\mathrm{e}}) + (\gamma - 1)p_{\mathrm{e}}\nabla\cdot\mathbf{v}_{\mathrm{e}} , \tag{2.2.113}$$

where $\gamma = \frac{5}{3}$ is assumed. For the ion pressures p_{p} and p_{h} isothermal conditions (often $T_{\mathrm{p}} = T_{\mathrm{h}} = 0$) are used.

The multi-ion nature of many space plasmas gives rise to new, interesting phenomena of collisionless momentum coupling between different ion species. The effect is revealed even in an unmagnetized plasma consisting of electrons, protons and a secondary ion population (heavy ions). As the simplest case of a coupling of two ion fluids, we consider a localized heavy ion source in a one-dimensional streaming plasma of protons without magnetic field. Then, the coupling is provided only by the ambipolar electric field caused by electron pressure gradients, a mechanism which drives ion-acoustic waves and is of electrostatic nature. Of course, this example has no direct relevance to real mass loading situations in space, where mostly magnetic effects dominate. But, nevertheless, it may give hints on principally new effects which arise in multi-ion plasmas due to the appearance of new wave modes and associated beam-like situations in case of a relative drift between the ion species.

To describe the interaction between two (cold) ion fluids in a warm electron plasma without magnetic field, we put $B = 0$ and $T_{\mathrm{p}} = T_{\mathrm{h}} = 0$ in Equations (2.2.106)–(2.2.113). For the heavy-ion source function $\mathcal{N}_{\mathrm{h}}$ a Gaussian profile, $\mathcal{N}_{\mathrm{h}} = \mathcal{N}_0\cdot\exp(-x^2/\mathcal{L}^2)$ is assumed. The coupled system of equations is solved numerically using the FCT code of Book et al. (1981). Results are shown in Figure 2.2.1 which represents a snapshot of the space-time evolution of the bi-ion system. The main feature observed is the coupling between the two fluids and, especially, the excitation of bi-ion acoustic waves on the downstream side of the source region, which is obviously caused by the relative streaming between the two fluids. Due to the absence of any damping effects in this fluid approach such as proton Landau damping strong wave amplification takes place. The basic wave modes existing in such a plasma with two ion populations in relative drift have been discussed by McKenzie et al. (1993) using linear dispersion analysis. Besides of the modified 'proton modes', the admixture of heavy ions to the proton plasma

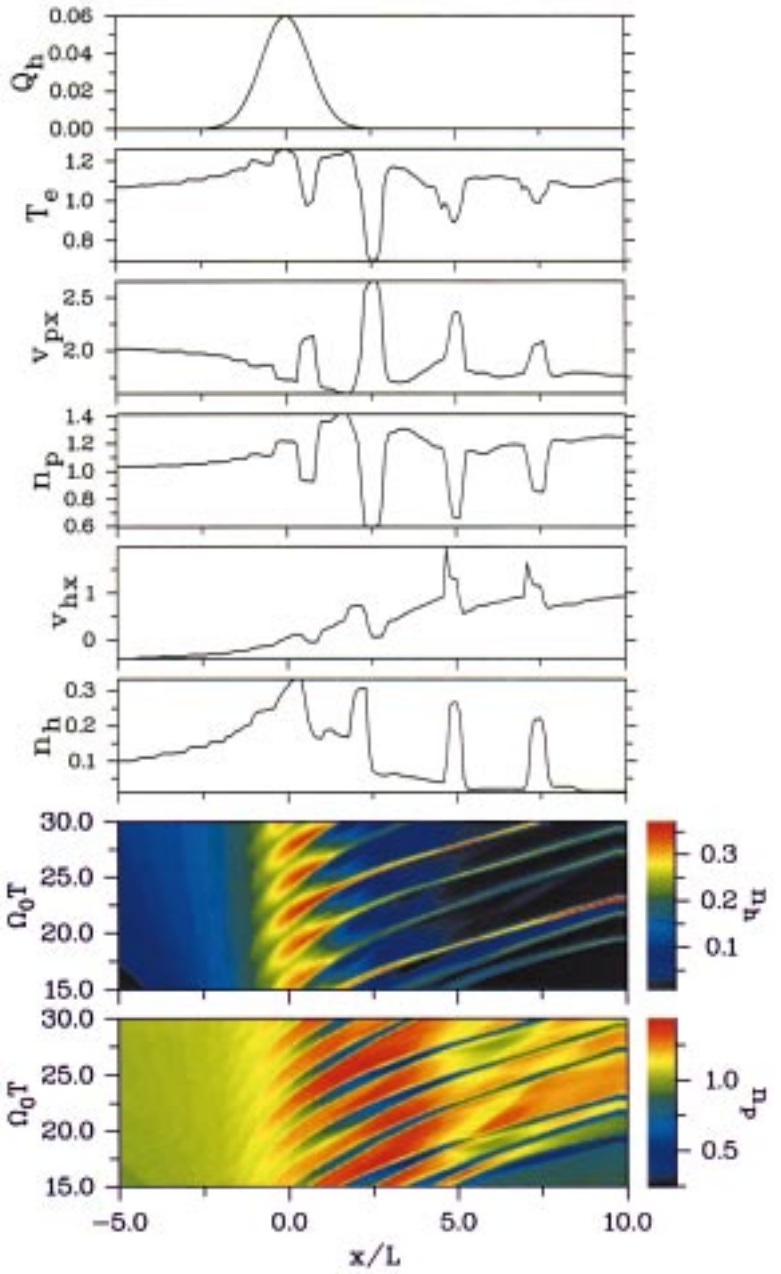

Figure 2.2.1. Non-stationary massloading in a plasma without magnetic field. A supersonic proton flow interacts with a heavy ion source ($Q_h = 0.06$, $m_h/m_p = 5$). x is normalized to the scale length L of the Gaussian source profile, T is normalized to $\Omega_o^{-1} = L/v_s$, where v_s is the proton sound velocity. Strong interaction starts at that point where $\Delta v = v_p - v_h \approx 1.7 v_s$ ($v_p = 1.9\ v_s$, $v_h = 0.2\ v_s$) is reached. As seen from the $x - T$ color plots, the heavy ion bunches move with about v_s.

results in an additional 'slow mode' which may resonate with a mode in the proton flow. In this mechanism, perturbations in both plasmas are coupled, resulting in period modulations of the whole bi-ion plasma. From the $x - T$ diagram of the heavy ion density displayed in the bottom part of Figure 2.2.1 one can clearly see that density striations are formed and move away with nearly constant velocity, which in this case is 0.5 of the ion-sound velocity $c_s = (T_e/m_p)^{1/2}$.

The frequency and wavelength of the unstable modes can be evaluated from the dispersion relationship of ion-acoustic waves in the bi-ion plasma ($T_p = T_h = 0$):

$$[(v_{ph} - v_p \cdot \cos\Theta_p)^2 - c_{sp}^2][(v_{ph} - v_h \cdot \cos\Theta_h)^2 - c_{sh}^2] = c_{sp}^2 \cdot c_{sh}^2 \quad (2.2.114)$$

where $c_{sp}^2 = (T_e/m_p)(n_p/n_e)$, $c_{sh}^2 = (T_e/m_h)(n_h/n_e)$, and Θ_p (Θ_h) is the angle between the wave number vector $\mathbf{k}$ and the ion flow velocity $\mathbf{u}_p$ ($\mathbf{u}_h$); u_{ph} is the phase velocity. Figure 2.2.2 shows the dispersion diagram: phase velocity (solid curve) and growth rate (dashed curve) – both values are normalized to the proton sound velocity c_{sp} – versus velocity of ion fluids for $\mathbf{u}_p$ and $\mathbf{u}_h$ parallel to $\mathbf{k}$. The upper part displays the relations in the proton reference frame, whereas the lower diagram gives results in the laboratory frame for the case in which the heavy ions gain the velocity of 0.5 c_{sp}. According to Figure 2.2.2 the instability is switched on where the proton velocity $v_p \sim 1.7\, c_{sp}$, and the mode with maximum growth rate has phase velocity $\sim 0.6\, c_{sp}$ which is in reasonable agreement with the simulation results presented in Figure 2.2.1.

In a magnetized plasma a similar magneto-acoustic type of two-fluid coupling can be considered for situations in which, due to limited scales (less than the proton gyroradius), the magnetization of protons and heavy ions can be neglected. In this case the Larmor-radius terms which are proportional to $\mathbf{u} \times \mathbf{B}$ on the right sides of the momentum equations can be neglected and the coupling is provided only by the magnetized electrons. Thus, the governing momentum equations for this case are the same, but differ in that in addition to p_e the magnetic pressure term $p_m = B^2/2\mu_0$ appears and $\mathbf{B}$ evolves in time according to

$$\frac{\partial}{\partial t} B_z + \frac{\partial}{\partial x}(B_z\, u_{ex}) = 0\,, \quad (2.2.115)$$

provided $\mathbf{u} \perp \mathbf{B}$ and the magnetic field $\mathbf{B}$ has a z-component only.

Dispersion analysis of the underlying bi-ion magneto-acoustic waves and one-dimensional simulations for this type of bi-ion fluid coupling at solar wind mass loading are described in detail by Sauer et al. (1996a, b). There it was shown that small-scale solar wind mass loading leads to plasma structuring by the excitation of magneto-acoustic waves behaving in a similar manner as the ion-acoustic case discussed above. In space, such effects may happen in the vicinity of weak heavy ion sources with characteristic scales smaller than the ion gyroradii, that is near weakly outgassing moons like Phobos and Deimos in the Martian system, or near Pluto.

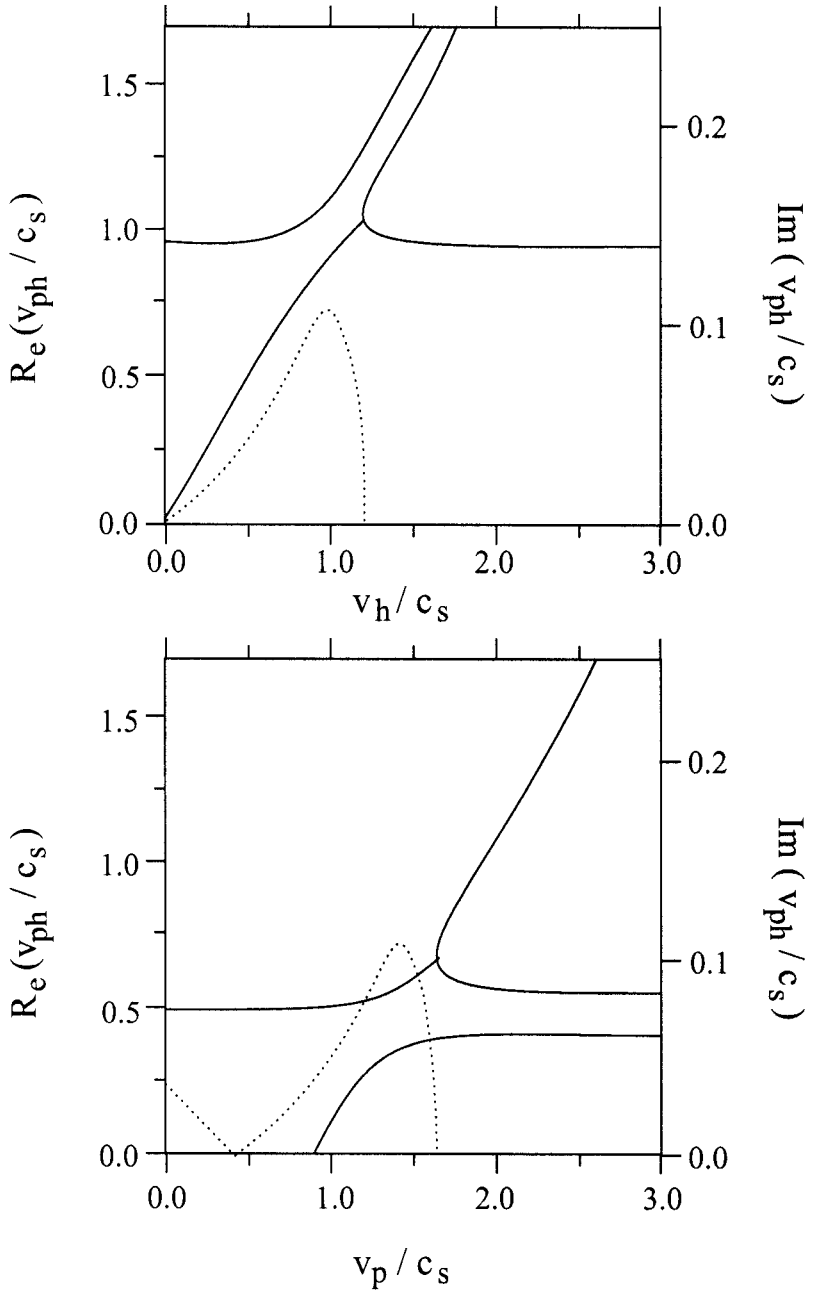

Figure 2.2.2. Dispersion relation of bi-ion acoustic waves. Upper panel: phase velocity v_{ph}/v_s (solid lines: real part, dashed lines: imaginary part) versus the drift velocity of heavy ions v_h/v_s in the proton reference frame; $n_h/n_p = 0.1, m_h/m_p = 20$. Maximum instability occurs at $v_h \approx v_s$. Lower panel: the same dependence in the laboratory frame changing v_p for a fixed heavy ion velocity of $v_h = 0.5\, v_s$.

To clarify the mechanism of two-fluid coupling and associated structuring in a plasma composed of two ion species, Lorentz forces $\Delta\mathbf{u} \times \mathbf{B}$ caused by the differential streaming of the two ion fluids have been neglected up to now. However, on medium scales ($l \leq r_h$, where r_h is gyroradius of heavy ions) when a relative streaming of ions is admissible, this force provides the main coupling between both ion fluids. Such Large Larmor Radius (LLR) configurations occur where the solar wind mass loading scale is smaller than the gyroradius of the pickup ions. Weak comets like P/Grigg–Skjellerup, unmagnetized planets with extended exospheres such as Mars and Venus, outgassing asteroids and moons, and possibly Pluto are typical candidates for this type of interaction.

If the heavy ions lag behind the protons, the Lorentz force ($\sim n_h/n_e\ \Delta\mathbf{u} \times \mathbf{B}$) decelerates the protons. The force which acts on the heavy ions ($\sim -n_p/n_e\ \Delta\mathbf{u}\times\mathbf{B}$) has the opposite sign and accelerates the ions to suppress their lag. As a result, both ion groups gyrate around each other with a cutoff frequency $\omega_{cf} = \Omega_p n_h/n_e + \Omega_h n_p/n_e$. A relative 'larmoring' of ion fluids occurs because each fluid in its own reference frame sees the motional electric field $\mathbf{E} = -\Delta\mathbf{u} \times \mathbf{B}$, which is supplied by the differential streaming. The interesting point is that even if the mass of heavy ions is very large (immobile ions), a cutoff frequency $\omega_{cf} = \Omega_p n_h/n_e$ remains as a characteristic frequency of the bi-ion plasma. Figure 2.2.3 shows the dispersion of low frequency electromagnetic waves in a cold bi-ion plasma of protons and unmagnetized heavies in the limit of massless electrons. It is seen that the L (left-hand) polarized mode evolves from the cutoff frequency and become coupled to the upper R (right-hand) mode which goes into the (ion) whistler branch at higher frequencies.

If protons move with respect to unmagnetized heavies which are nearby at rest, the beam-plasma configuration arising can lead to a bunching of the plasma flow. The mechanism of bunching is common in beam-plasma systems. If a 'slow' beam mode ($-\omega_b/k$) carried by the beam (Δv) is synchronized with a wave (ω/k) in the background proton plasma the instability occurs. Therefore, one can expect that the instability arises where the beam directed phase velocity intersects the beam velocity. Figure 2.2.3 gives frequencies of unstable modes in such a bi-ion configuration. For beam velocities higher than Alfvén velocity, at least, two intersections between the L/R mode and the beam velocity occur. The low frequency band falls between cutoff frequency $\omega_{cf} = \Omega_p n_h/n_e$ and proton gyrofrequency Ω_p. The whistler mode is another likely candidate for the instability in higher frequency range.

In the presence of a beam the dispersion relation becomes more complicated and could be derived either from bi-ion MHD equations discussed above (see also Baumgärtel et al., 1998), or by using the dispersion tensor of two-ion plasma (Sauer et al., 1998, 1999a). In the latter case, the dispersion relation is obtained from the condition $\det|\mathbf{D}(\omega, k)| = 0$, where $\mathbf{D}$ is the dispersion tensor.

Beam-plasma interactions in the low frequency range will result in plasma filamentation on meso-scales $\sim$20–30 L, where $L = v_A/\Omega_p$, corresponding to about 3000 km for typical solar wind conditions at $\sim$1 AU. Figure 2.2.4 displays the

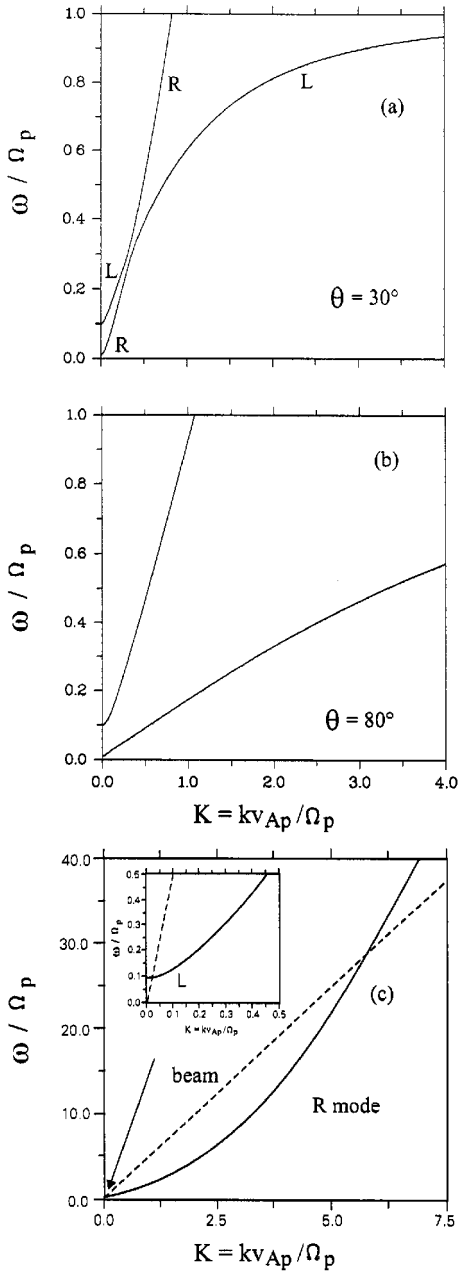

Figure 2.2.3. (a) The dispersion of LF electromagnetic waves in a cold bi-ion plasma, consisting of protons and unmagnetized heavy ions ($n_h/n_p = 0.1, m_h/m_p = 100$) for two angles of propagation: $\Theta = 30°$ (a), $\Theta = 80°$ (b). Two intersection points in the ω-k diagram between the 'beam mode' and the L/R plasma mode indicating a possible source of two wave emissions in a plasma-beam configuration (c).

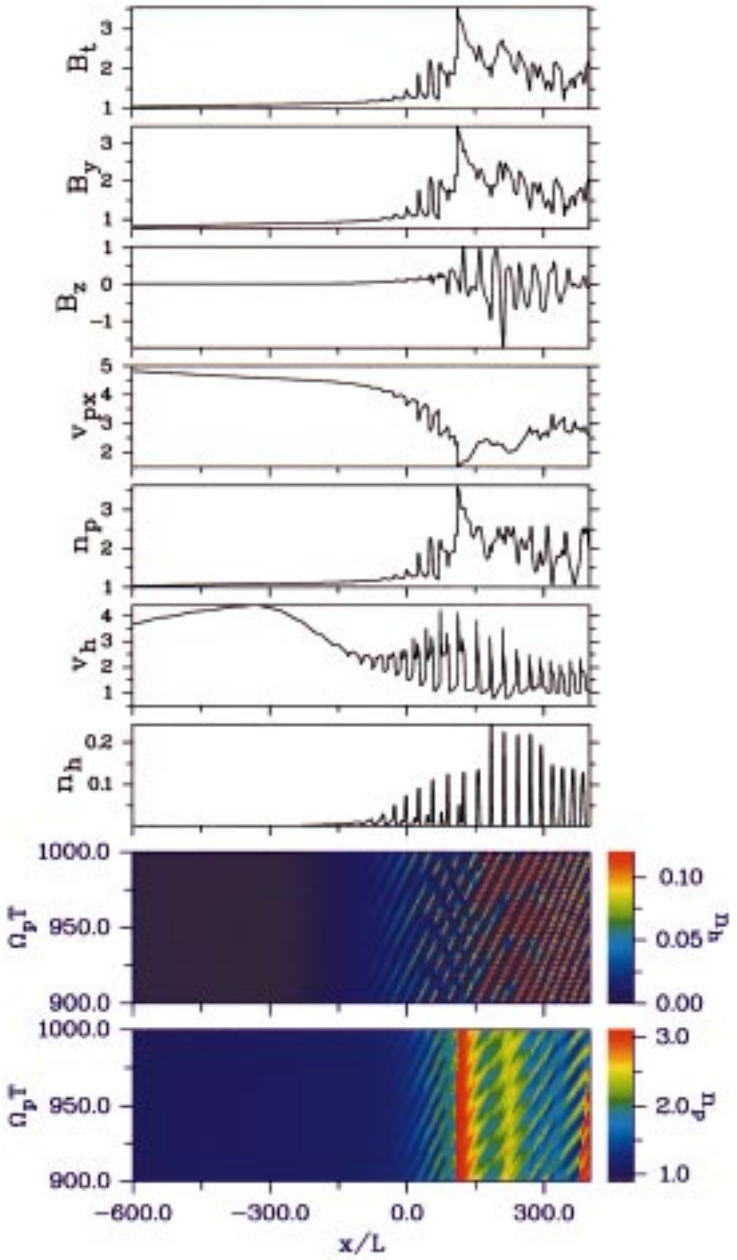

Figure 2.2.4. Dynamics of solar wind massloading on meso scales ($x \leq r_h$): $M_A = 5$, $\beta_e = 1.0$, $\angle(\mathbf{v_p}, \mathbf{B}) = \mathbf{50}°$. The parameters of the heavy ion source are: $m_h/m_p = 100$, $Q_h = 10^{-4}$ (normalized production rate $(n_o/n_p) \times (n/W_p)$, where n_o and n are the neutral gas density and the photoionization rate, respectively), $l = 200$ L (characteristic scale length). The upper seven panels show the spatial variation of the plasma parameters for a quasi-stationary state at $\Omega_p T = 800$. The lower color plots represent the $x - T$ variation of the heavy ion and proton density, respectively. As seen there, the phase velocity of the excited waves is near the Alfvén velocity. The characteristic time period is $\Omega_p T \approx 15$ or $\omega \approx 0.4\Omega_p$.

dynamics of a mass loaded solar wind plasma with $M_s = 5$, $\beta_e = 1$, $\varphi = 45°$, where φ is angle between the proton velocity and the magnetic field. A heavy ion source with a medium scale length of $l \sim 200\,L$ is assumed. The heavy ion gyroradius ($m_h/m_p = 10^2$) $r_h \sim 5 \times 10^2\,L$ is comparable to the characteristic size of the system.

Picked-up at large distances, the heavy ions are accelerated up to the velocity of protons. Approaching the center of the obstacle, the solar wind gradually slows down, but the heavy ions begin to lag behind the protons. When the differential streaming achieves $\Delta v \sim 1.5\,u_A$ the plasma motion becomes oscillatory. It is believed that the oscillations and a bunching of the plasma are related to the onset of the beam-plasma instability. It is seen that the relative streaming of both ion species occurs in an oscillating manner. The spatial separation between two bunches in the simulation run is about $30\,L$. An interesting feature is the double structure of the bunches clearly seen in the variations of n_h and u_h. In the $x - T$ diagram it can be seen that two modes travel with slightly different velocities. The generation of two modes is probably caused by both the normal and anomalous Doppler resonance. If the drift velocity of the heavy ion beam (in the proton reference frame) Δv is larger than the phase velocity of waves in the background proton plasma, the resonance condition for the instability is $\omega^{(p)} - k\Delta u = -\omega^{(h)}$ (anomalous Doppler effect). When the drift velocity occurs to be less than the phase velocity, the resonance can be met via the normal Doppler effect: $\omega^{(p)} - k\Delta u = \omega^{(h)}$, where $\omega^{(p)}/k$ and $\omega^{(h)}/k$ are phase velocities of waves in the proton plasma and in the beam. Therefore, $\omega^{(p)}/k = \Delta u \pm \omega^{(h)}/k$, where $\Delta u = -(u_p - v_h) < 0$, i.e., waves propagate in the upstream direction. Carried by the proton flow, the waves have velocities $\omega^{(p)}/k = u_p = u_h \pm \omega^{(h)}/k$ in the laboratory frame.

Figure 2.2.5 which shows the $\omega - k$ dispersion relation for a plasma composed of protons as the core ion component and a beam-minority of unmagnetized heavy ions, refers to the wavelength and the frequency of the unstable mode for a set of parameters according to the conditions in Figure 2.2.6 near the onset of the instability ($\Delta u \approx u_A$; $u_p = 3.5\,u_A$, $u_h = 2.5\,u_A$, $n_h/n_e = 0.05$, $m_h/m_p = 100$, and $\theta = 50°$, where θ is angle of wave propagation with respect to the magnetic field). The upper panel gives the $\omega - k$ relationship in the proton reference frame. The pattern contains several modes that are split due to beam-plasma interaction. The bottom panel presents the growth rate of the mode versus the wave number k. The frequency of the mode is about $0.2\,\Omega_p$. In the laboratory frame, the wave is Doppler shifted leaving behind a right-hand polarized one. The frequency in the laboratory reference frame (the middle panel) is $\omega^* \sim -0.4$ which corresponds to $T = 2\pi/\omega^* \sim 15\,\Omega_p^{-1}$. The characteristic wavelength is $\lambda \sim 20\,L$. Both values are in a reasonable agreement with the simulation in Figure 2.2.2.

The second intersection of a beam mode with a mode in the background plasma in the (ion) whistler frequency range gives rise to a small-scale structuring ($\sim u_{Ap}/\Omega_p$). Figure 2.2.6 shows the ω-k diagram near the intersection point for the proton velocity of $M_s = 3$ and oblique wave propagation ($\theta = 85°$, $\varphi = 45°$,

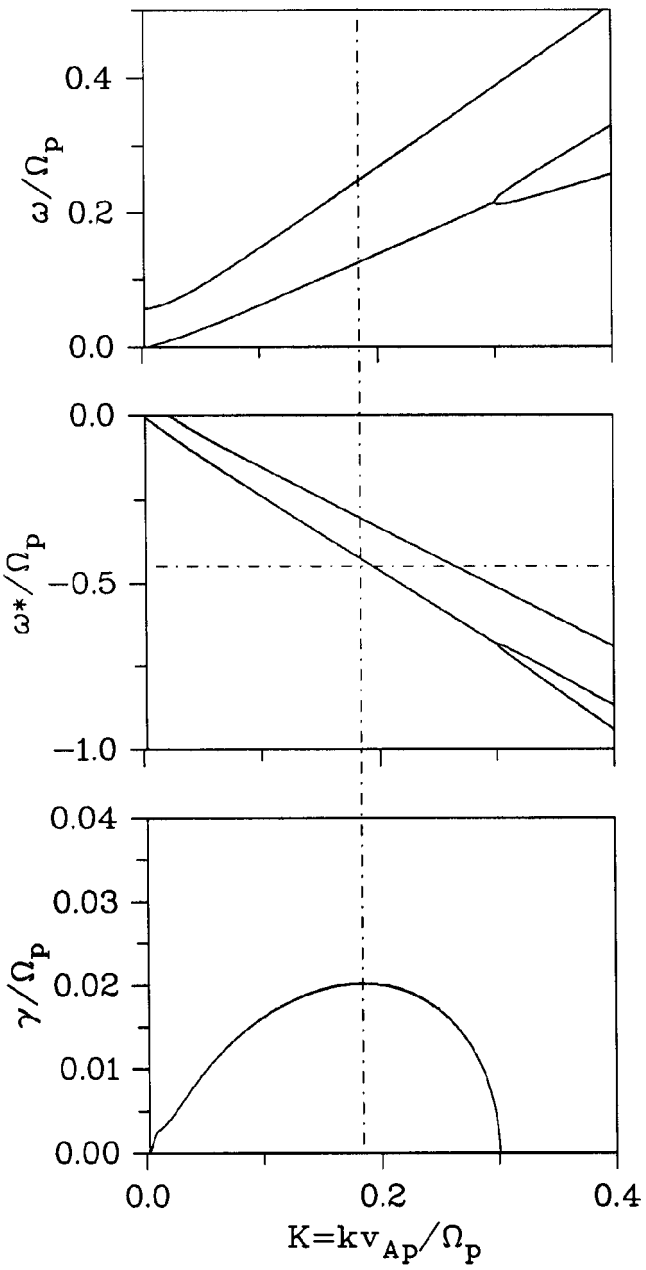

Figure 2.2.5. Dispersion relation of beam-excited ULF waves related to the conditions of Figure 2.2.4 near the onset of the instability: $n_h/n_p = 0.05$, $v_p = 3.0v_A$, $v_h = 1.9v_A$. The upper two curves show the frequency in the proton plasma (a) and laboratory frame (b), respectively, versus k. The lower curve gives the corresponding growth rate, which has its maximum at $\omega^* \approx 0.4\Omega_p$, in good agreement with the simulations.

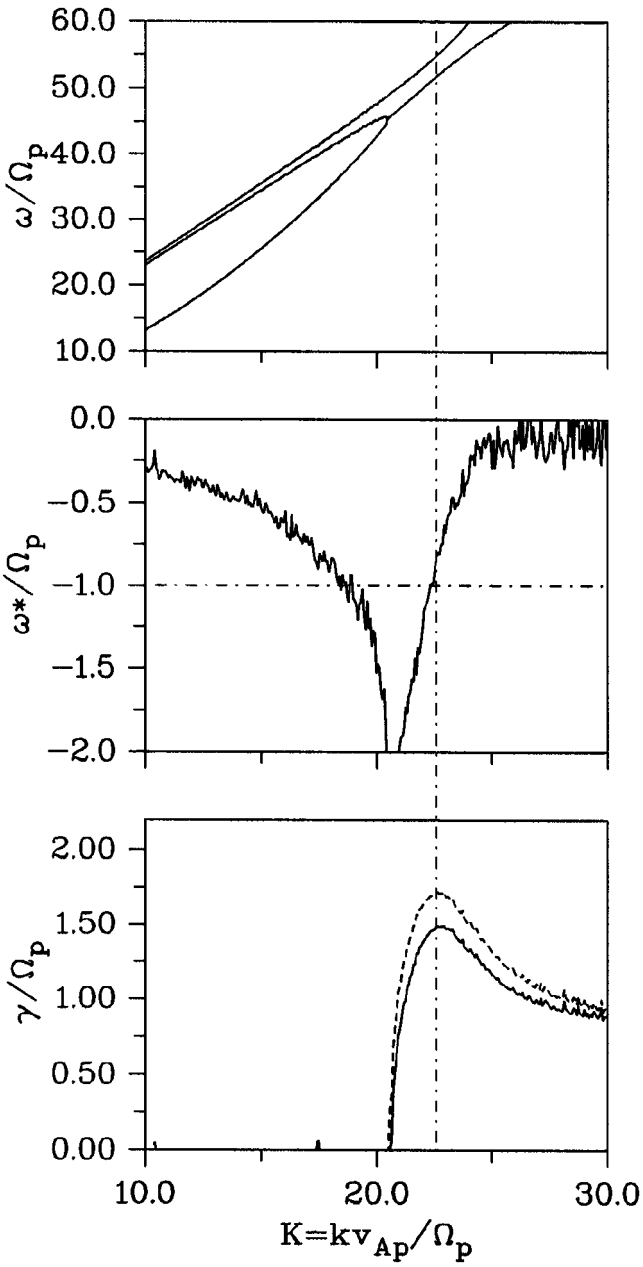

Figure 2.2.6. Dispersion relation for beam-excited whistlers. The $\omega - k$ diagram arises from the intersection of the beam mode ($\omega \approx \mathbf{k} \cdot \mathbf{v_h}$) with the whistler ($R$) mode of the background plasma; (a) in the proton reference system, (b) in the beam (laboratory) frame. (c) shows the growth rate. In the beam frame, waves near the proton cyclotron frequency Ω_p are the most unstable ones.

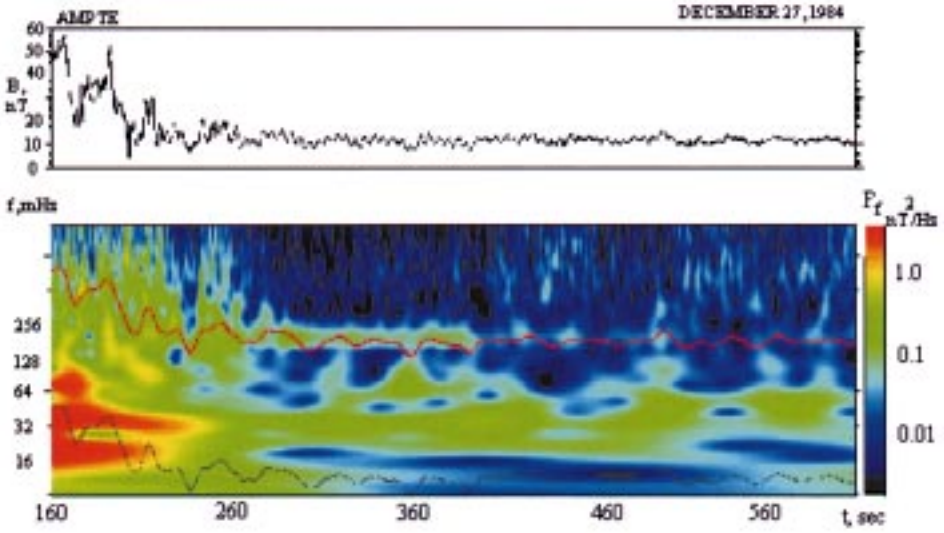

Figure 2.2.7. Wavelet diagram of magnetic field oscillations during the AMPTE/Ba release. Frequency bands at $f_{ULF} \approx 32$ mHz and $f_{LF} \approx 200$ mHz are clearly seen. The upper band is very close to the proton cyclotron frequency, which is marked by the red curve.

$n_h/n_e = 0.1$, $m_h/m_p = 100$). This pattern arises from the intersection of the beam mode ($\omega \approx \mathbf{k} \cdot u_h$) with the whistler ($R$) mode of the background plasma. As seen in Figure 2.2.6(c), there is a sharp threshold in the wave number k for the onset of the instability, and the maximum growth rate is attained just adjacent to it. The ω-k relation of unstable mode in the beam frame ($\omega^* = \omega - \mathbf{k} \cdot \mathbf{u}_h$), where the heavy ions are nearly at rest, is shown in Figure 2.2.6(b). It is evident that the wave near maximum growth is Doppler-shifted to the proton cyclotron band, that is $\omega - \mathbf{k} \cdot \mathbf{u}_h \approx -\Omega_p$ or $\omega^* \approx -\Omega_p$, leaving behind a left-hand polarized wave in the beam (laboratory) frame.

Emissions at $\Omega \sim \Omega_p$ were distinctly observed in the experiments with artificial comets (AMPTE; e.g., Haerendel et al., 1986) when Ba^+ ions formed a heavy ion cloud which expanded and interacted with the solar wind. Figure 2.2.7 gives the wavelet diagram of the magnetic field oscillations during the Ba-release. Two clear frequency bands at $f_{ULF} \sim 32$ mHz and $f_{LF} \sim 200$ mHz are observed. The lower frequency emission ($\sim 0.2\,\Omega_p$) has right-hand polarization and, probably, caused by the interaction process discussed in the previous paragraph. The upper band is very close to the proton gyrofrequency, which is marked by the red curve, and is believed to represent the Doppler-shifted R-mode excited in the (ion) whistler frequency range (Sauer et al., 1998).

Unlike ring-beam ion/ion instabilities which can give rise to modes near Ω_p for a proton beam (pickup protons) due to the normal or anomalous Doppler resonance $\omega - \mathbf{k} \cdot \mathbf{u}_b = \pm\Omega_p$, an unmagnetized heavy ion beam can excite only waves via $n = 0$ resonance ($\omega = \mathbf{k} \cdot \mathbf{u}_b$). A kinetic treatment by Baumgärtel et al. (1998) shows

that the frequency of unstable mode in the beam reference frame is not sensitive to the angle of wave propagation ($\omega^* \sim -\Omega_p$). Damping due to wave-particle interaction provides a gap in the $\theta - k$ space for unstable modes, which increases with β_e, leaving behind only wave modes propagating nearly parallel and almost transverse for $\beta_e \sim 1$ (Baumgärtel et al., 1998). Simulations made with small-scale heavy ion obstacle ($l = 5\,L$) demonstrate the generation of whistlers during the interaction with flow of proton-plasma. Figure 2.2.8 gives spatial variations of plasma parameters at time $T = 10$ and the $X - T$ diagram of wave propagation. The frequency and the wavelength of excited waves in the laboratory reference frame are $\sim 0.8\,\Omega_p$ and $\sim 0.6\,u_{Ap}/\Omega$, respectively, that is close to the predicted values.

The detection of proton cyclotron emission at comet P/Halley (Mazelle and Neubauer, 1993) and Mars (Russell et al., 1990), partly related to the so-called 'Phobos events' (Baumgärtel et al., 1998; Sauer et al., 1998, 1999a) may find an explanation by such a mechanism.

Studying the dynamics of mass loaded plasmas on scales which are larger than the heavy ion pickup gyroradius can be classified as large-scale mass loading. An important aspect of such a loading situation is to study what mechanism causes the coupling between both fluids. Here, the cone angle φ, that is the angle between the magnetic field and the velocity of protons, plays an essential role. Omidi and Winske (1987) in their 1D-hybrid simulations have distinguished two regimes of mass loading. For the quasi-perpendicular case, when the angle between flow velocity and the magnetic field $\varphi \geq 70°$, a deceleration of the solar wind occurs through macroscopic electromagnetic fields. For oblique angles $60° \geq \varphi \geq 20°$ microscopic fields associated with generation of low-frequency waves due to beam-ring distribution of heavies contribute essentially to the momentum exchange between solar wind protons and heavy ions. For the quasi-parallel case, microscopic coupling processes play the dominant role. Already then, we show that in a bi-ion MHD approach two different coupling mechanisms are clearly distinguished although they have different origins.

Figure 2.2.13 demonstrates coupling process in the upstream region with respect to the shock ($M_s = 3.5$, $m_h/m_p = 12$, $l = 2.5 \times 10^3\,L$, $\beta_e = 1$, $\varphi = 7°$, 25°, and 50°). The initial magnetic field is in the xy-plane. The fourth panel from the top gives the proton velocity u_{px} along the x-axis. The next panel contains the total velocity of heavies. The dashed line depicts the component of the proton velocity perpendicular to the magnetic field. For large cone angles ($\varphi \geq 50°$) the momentum coupling is controlled by the $\Delta\mathbf{u} \times \mathbf{B}$ forces with the evident trend to equalize the flow velocities. As clearly seen, both ion species move nearly with the same velocity in the whole mass loading region. Only small oscillations occur, caused by the initial gyration of heavy ions at the left border of the simulation box. They are standing structures in the laboratory frame. The main features look like that of one-fluid mass loading. But, this is valid only for our actual situation of weak mass loading. Even for quasi-perpendicular propagation increasing density

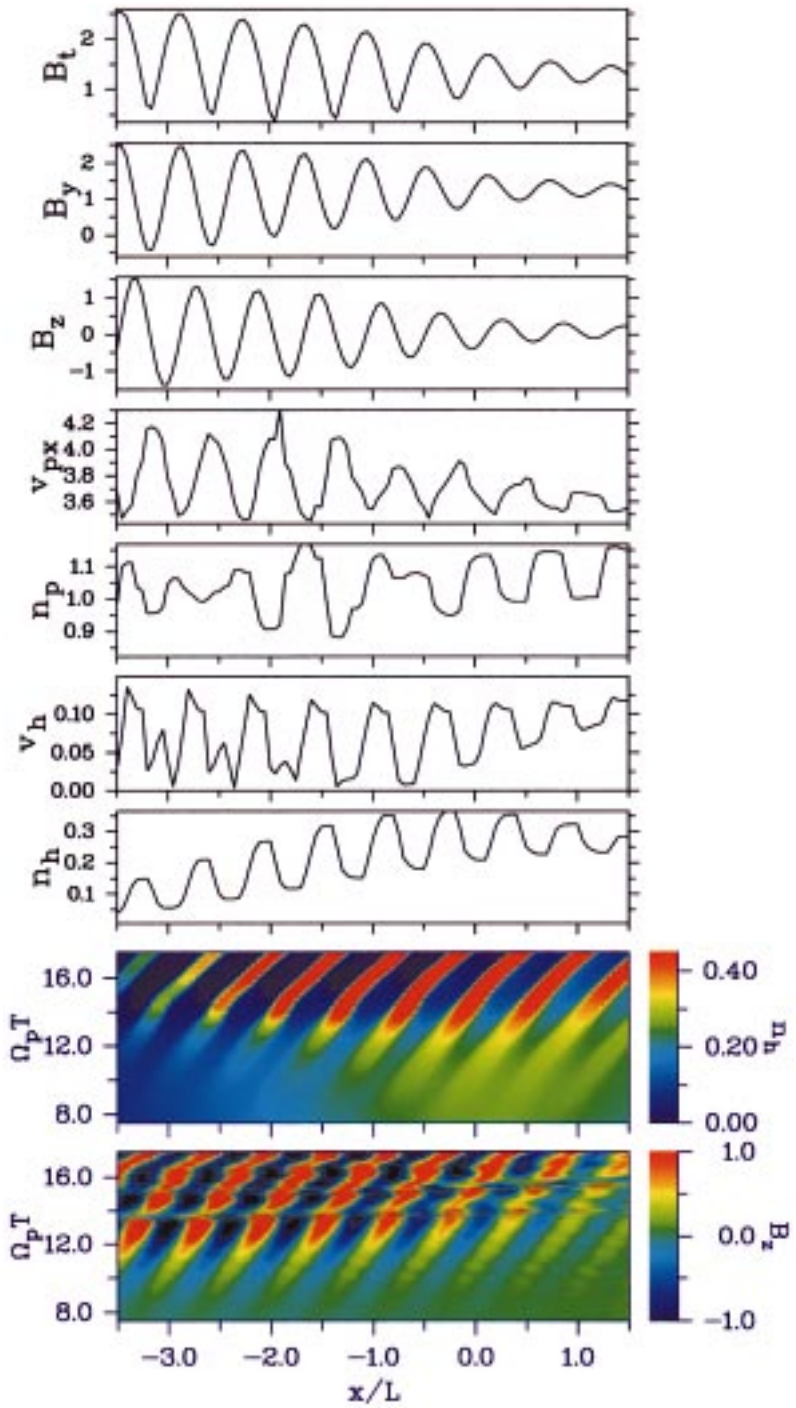

Figure 2.2.8. Massloading generated whistler waves: $M_A = 4.0$, $\angle(\mathbf{v_p}, \mathbf{B}) = \mathbf{500}$. The upper seven curves show the spatial variations of the plasma parameters at $\Omega_p T = 12$. Whistlers are excited causing the small-scale structuring of the plasma. As seen from the $x - T$ plots in the lower two panels, the waves move with low phase velocity ($v_{ph} \leq 0.2 v_A$), their frequency is slightly below Ω_p.

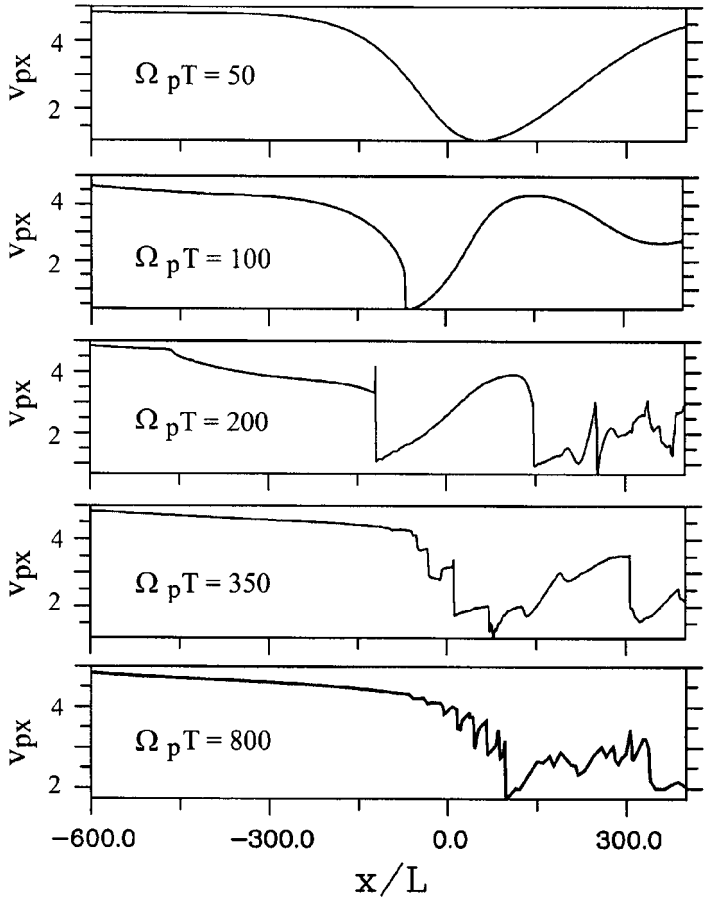

Figure 2.2.9. Time sequence showing the formation of a massloading shock for the parameters of Figure 2.2.4. Caused by massloading, the x component of the proton velocity decreases up to a point where the magneto-sound velocity is reached and a shock is formed which initially moves upstream. The onset of wave excitation by the relative drift between protons and heavies, obviously, leads to a quasi-stationary pattern which is shown in lowest panel.

of heavy ions, in the case of higher production rates or more extended sources, would lead to a relative streaming between both ion species, including related wave excitation, as described subsequently.

For smaller angles ($\varphi = 25°$) both fluids at first gain the same $u_\perp$ velocities and a quasi-stationary state of plasma flow is accomplished. The proton velocity in the x-direction slows down only slightly. However, with increasing mass loading, large amplitude electromagnetic waves are excited. Contrary to the previous case of linear polarization, these waves are elliptically polarized in the yz-plane due to a switch-on of the large amplitude B_z variations. Under the action of the $\Delta\mathbf{u} \times \mathbf{b}$ forces related with the wave magnetic field ($\mathbf{b}$ is the wave amplitude of the magnetic field) a 'macroscopic' mechanism, similar to the case of quasi-perpendicular

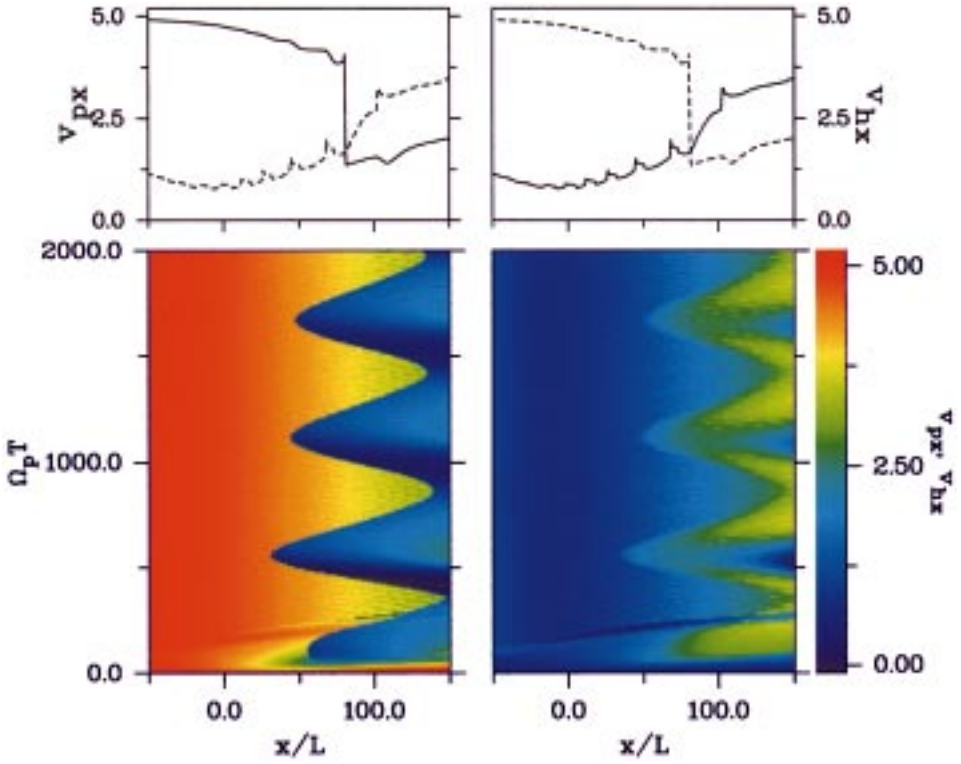

Figure 2.2.10. Example of an oscillating massloading shock. For the same parameters as in Figure 2.2.4 ($M_A = 5$, $m_h/m_p = 100$, $\beta_e = 1.0$, $\angle(\mathbf{v_p}, \mathbf{B}) = \mathbf{500}$), but smaller scale length ($l = 50L$) the shock position oscillates with a period of $\Omega_p T \approx 550$, which is close to the heavy-ion cyclotron period $\Omega_h T = 2\pi$. The left (right) two panels show the spatial variation at $\Omega_p T = 1000$ and the $x - T$ diagram of the proton velocity (heavy ion velocity). The coupling between the ion species, which causes periodic changes of their velocities, is the obvious reason for the shock oscillation.

propagation, is switched on and mass loading becomes more effective. The important difference with the quasi-perpendicular case is that the waves provide the cross flow component of the large-amplitude magnetic field. Another difference is that these waves are not standing, but they travel downstream. The interesting point is that both fluids begin to 'gyrate' in the yz- plane and the analogy with a nongyrotropic beam distribution, that is exploited for the kinetic description of mass loading near weak comets (Motschmann et al., 1997), becomes evident. The hodogram given on the top, shows the 'larmoring' of the protons. At first, the rotation in phase is uniform over the X, but then reveals the more phase-steepened fronts which give rise to arc-polarized waves similar to those observed by Tsurutani et al. (1997) in comet P/Halley's environment.

The left column comprises variations of the plasma parameters for quasi-parallel propagation ($\varphi = 7°$). Large-amplitude waves are generated at larger distances which indicates that the growth rate of the instability increases with decreasing

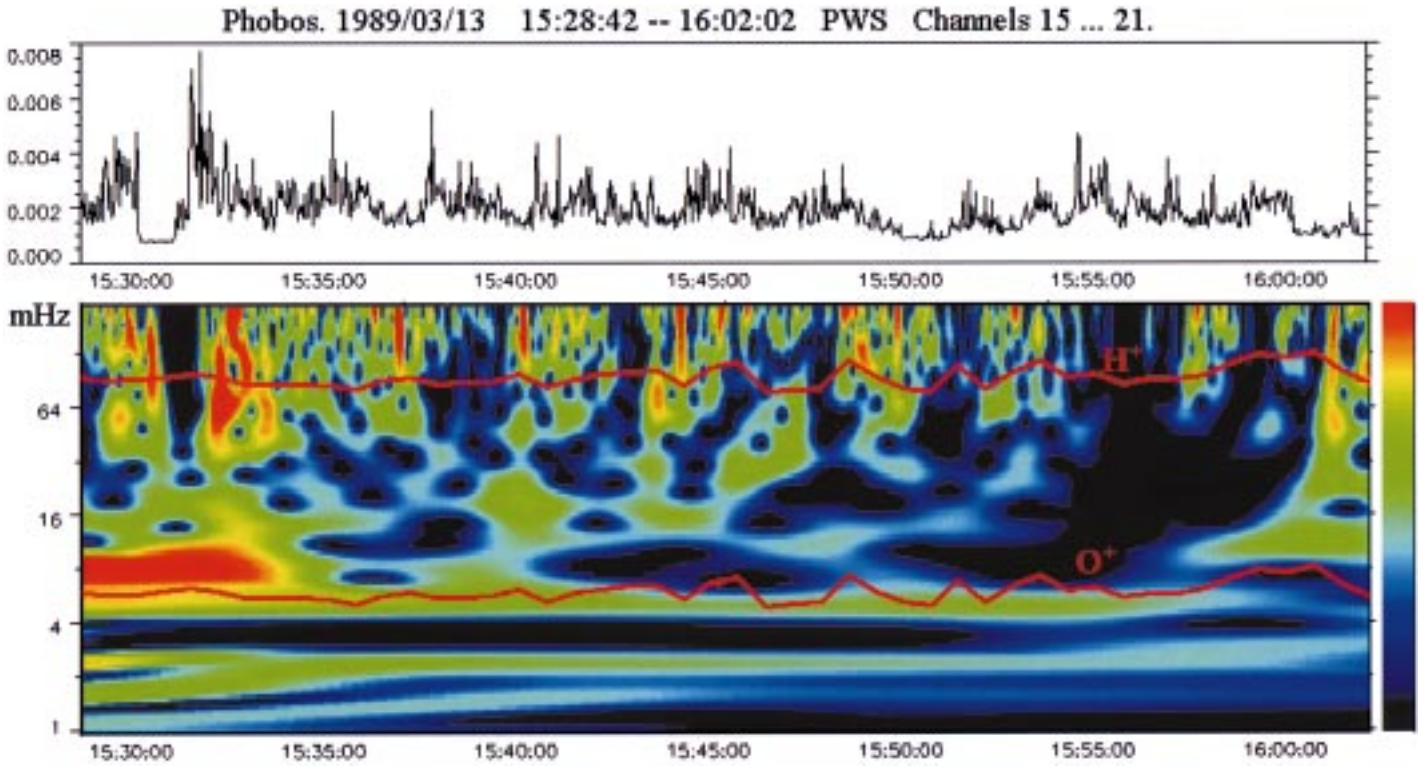

Figure 2.2.11. Wavelet diagram of intensity variations of electron plasma waves in the foreshock region of Mars. A distinct frequency band near the O^+ cyclotron frequency (lower red line) is seen which may be caused by oscillations of the shock front with the same frequency.

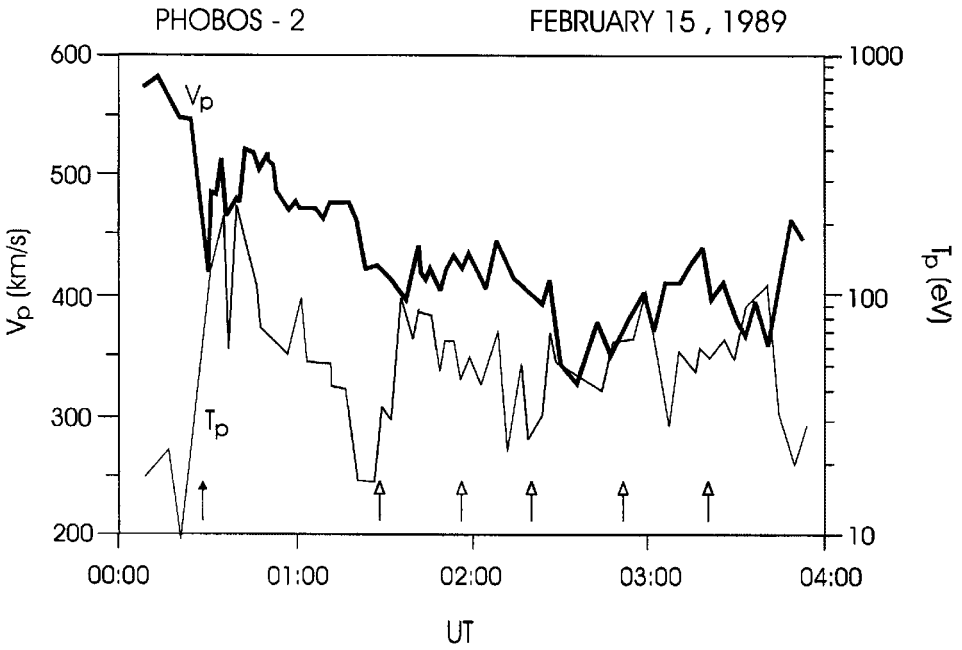

Figure 2.2.12. Multiple shocks at Mars. Bulk velocity and temperature of protons for the pass through the magnetosheath of Mars on February 15, 1989. Step-like deceleration of the protons accompanied by their heating indicates the presence of multiple shocks (after Dubinin et al., 1998).

cone-angle. The polarization of waves is circular. A rigid phase relation in the waves is important feature which distinguishes them from Alfvén waves with random phases expected from a quasi-linear evolution of a ring-beam distribution of heavies. The observed frequency is close and slightly below the gyrofrequency of the heavies. All these features strikingly resemble the characteristics of low frequency waves observed in the upstream region of comet P/Grigg–Skjellerup (Neubauer et al., 1993).

2D simulations allow us to trace wave structures and shocklets which are observed in the 1D simulations. For a weak localized source of heavy ions the newly born particles move along cycloidal trajectories. Therefore, one can expect that bunches in heavy ion flow will be formed along the 'cycloidal' beam. 2D bi-ion MHD simulations confirm these expectations (Sauer et al., 1996a, b; Bogdanov et al., 1996). The right column in Figure 2.2.14 shows the example of the observed striations. The interesting feature of 2D simulations is that a beam emits waves at certain angles providing a peculiar pattern of multiple Mach cones (Dubinin et al., 1998). The analogy with a charged particle moving in a medium with a speed u higher than phase velocity $u_{\rm ph}$ and emitting waves at resonance angles $\cos\theta = u_{\rm ph}/v$ (Cherenkov radiation) is evident. 2D-hybrid simulations with the protons and the heavy ions treated as particles and the electrons as being massless have been performed for the same initial parameters give rise to similar signatures

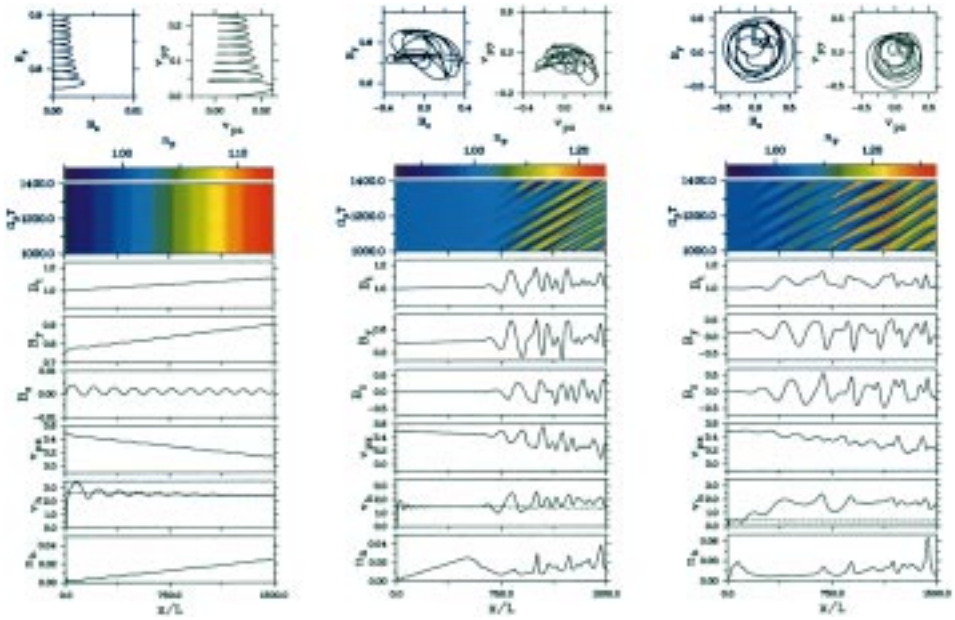

Figure 2.2.13. Large-scale massloading for three different orientations of the magnetic field relative to the proton flow, $\angle(\mathbf{v_p}, \mathbf{B}) = \mathbf{50}^\circ$ (a), 25° (b), 7° (c). The other parameters are $M_A = 3.5$, $m_h/m_p = 12$, $\beta_e = 1.0$. The heavy ion production rate is $Q_h = 3 \times 10^{-5}$ over the whole interval. The upper six panels show the spatial variation of the plasma parameters at $\Omega_p T = 1000$. From the $x - T$ diagrams it is seen that at the transition from large to small cone angles, massloading becomes more and more a non-stationary process accompanied by excitation of low-frequency waves. This is also evident from the hodograms on top of the figure.

of beam bunching (the left column). With increasing production rates of heavy ions, the flow of the heavy ions, which forms a 'beam' in the background proton plasma, becomes wider and covers more space. As a result, an interference pattern of multiple sets of emitted waves appears more complicated and resembles ray-structures often seen in photographs of comets (Figure 2.2.15, middle panels). The structures are moving downstream and new ones arise due to a continuous production of new heavy ions and repeated occurrence of differential streaming. The bottom panel of Figure 2.2.15 demonstrates a filamentary structure of the flow which is observed with a further increase of the strength of the heavy ion source. When approaching the center of the obstacle, the heavy ions gradually dominate over protons. It occurs that a response of bi-ion flow depends crucially on the Mach number. Critical heavy ion density (or critical column density) exists not only for 'supersonic' flows. It was shown (Sauer et al., 1992; Baumgärtel and Sauer, 1992) that for 'subsonic' flows critical points, that is points beyond which stationary spatially continuous mass loading is no longer possible, are met for $n_\mathrm{h} \leq n_\mathrm{p}$. This may result in a sudden stoppage of the proton flow and the formation of a 'proton cavity' around the obstacle. Such cavity is seen, for example, in the right bottom

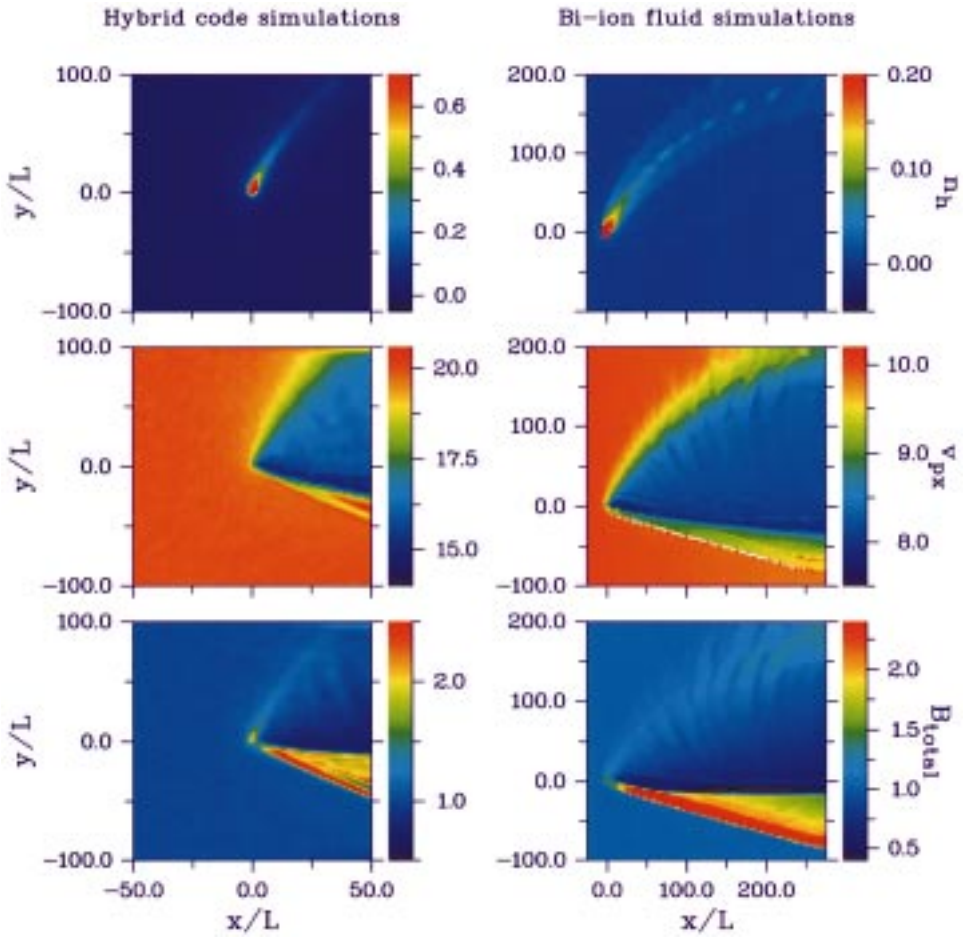

Figure 2.2.14. Solar wind interaction with a weak heavy ion source, comparison between 2D hybrid code and bi-ion fluid simulations. In both cases, the magnetic field is out of the simulation box. Although the flow parameters are not the same (left: $M_A = 20$, right: $M_A = 10$), the overall interaction pattern, showing the heavy-ion cycloid and multiple Mach cones, coincides well. Weak plasma structuring is already visible.

panel of Figure 2.2.15. The interesting point is that this 'obstacle boundary' does not coincide with the so-called ionopause, where the stagnation of the flow could be expected. In particular, the controversial debate about the obstacle boundary near Mars arose for a long time because of an ignorance of this argument. Only recent Mars Global Surveyor observations clearly demonstrate that the obstacle boundary for the solar wind flow and ionopause are two different boundaries. Figures 2.2.16 and 2.2.17 show the variations of plasma parameters measured by the Phobos-2 spacecraft near the '*proton obstacle boundary*' in comparison with results of 2D bi-ion MHD simulations (Sauer et al., 1997; Sauer and Dubinin, 1999). It is clearly seen that the termination of proton fluxes occurs at point where

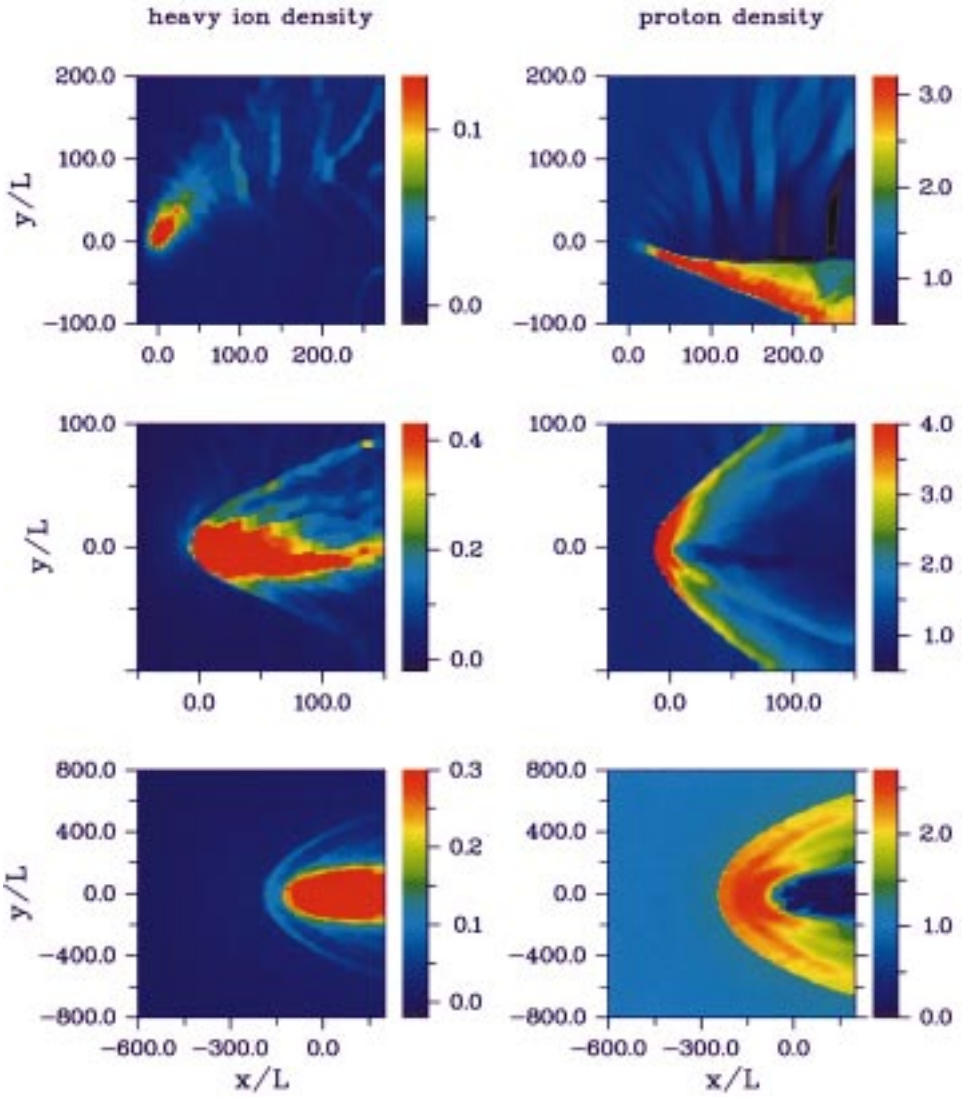

Figure 2.2.15. Plasma structures for three massloading regimes, $M_A = 5$. From one set of color pictures (heavy ion density, proton density) on the top, to that in the middle and below the production rate changes by about one order, beginning with $q_h \approx 10^{25}$ s^{-1}. For the simulation results shown on top and in the middle the magnetic field is directed along z. In the simulations below the magnetic field is in y direction. For the highest production rate a proton cavity is formed which is marked as dark region in the lower right plot.

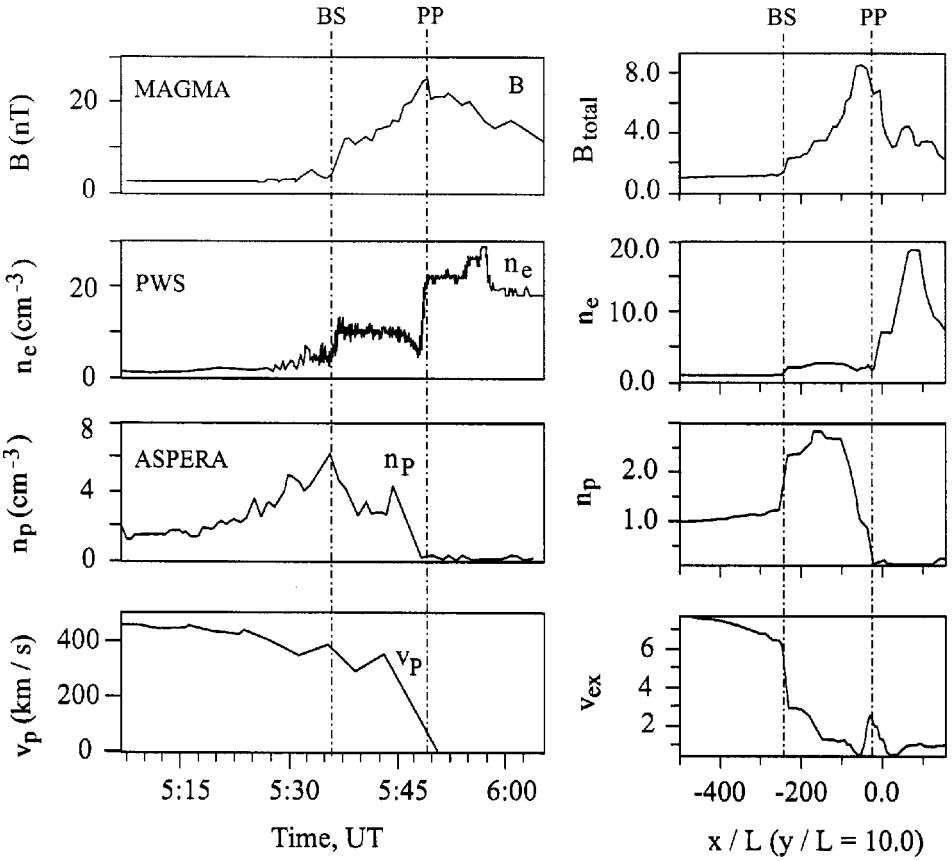

Figure 2.2.16. Phobos-2 observations (elliptical orbit) of the ion composition boundary (pile-up boundary, protonopause) at Mars compared with results of 2D bi-ion simulations (from Sauer et al., 1999b).

$n_h \sim n_p$. The boundary is characterized by a change of ion composition and pile-up of the magnetic field (Dubinin et al., 1997; Acuña et al., 1998). The magnetic field frozen to the electrons is carried across the boundary and piled-up due to the decrease of the electron velocity which is adjusted to a driven slow motion of the heavy planetary plasma in the boundary layer between the obstacle boundary and ionopause. Therefore, the magnetic pressure is not sufficient to balance the solar wind dynamic pressure, and a certain part of the momentum is transferred to the heavy ions.

So far we have investigated solar wind mass loading using a bi-ion fluid model which describes the electromagnetic coupling between the two ion fluids. One of them, the heavy ion component, contains a continuous, more or less extended source of new ions. Generally, it is found, that this process is very dynamic because of the different types of bi-ion low-frequency waves which are excited by the permitted relative streaming between both fluids. The characteristic frequency

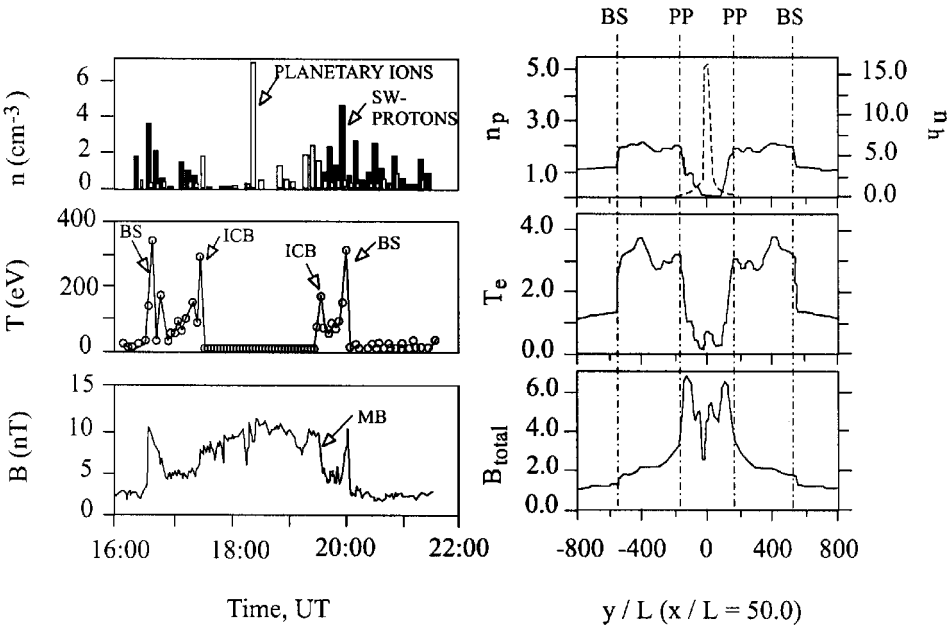

Figure 2.2.17. Phobos-2 observations (circular orbit) of the ion composition boundary (pile-up boundary, protonopause) at Mars compared with results of 2D bi-ion simulations (from Sauer et al., 1999b).

ranges are related to the cyclotron frequencies of protons (Ω_p) and heavy ions (Ω_h) and the bi-ion cut-off frequency $\Omega^* = n_p/n_e\Omega_h + n_h/n_e\Omega_p$. Wave steepening and associated plasma structuring appears as a characteristic signature and may explain the very dynamic features of the interaction with comets. Especially, tail rays and recently in the coma of Hale-Bopp observed moving ring-like O^+ bunches (Bonev et al., 1998) are thought to be a common phenomenon of comets, caused by two-fluid coupling. Other interesting observations in this respect were made in the plasma environment of Mars by the Phobos-2 and Mars Global Surveyor (MGS) spacecrafts. Many features seen in the plasma and magnetic field measurements (as multiple shocks, low-frequency wave emission, etc.) resemble a comet-type interaction, similar to that of comet P/Grigg–Skjellerup. Of course, a fluid description has its limitations, especially, the lack of heating effects caused by wave particle interaction. Therefore, it seems to be necessary to extend the fluid simulations, as partly carried out here, to include kinetic effects using hybrid code simulations, e.g. In any case, the fluid approach has the advantage of readily yielding information about essential macroscopic effects and forms a guideline for more detailed kinetic studies.

2.2.6. *Mass Loading and Shock Waves*

The problem of shocks in the mass-loaded solar wind is complicated because of the absence of a 'piston', as in the case of the solar wind interaction with magnetized planets. Here we shortly discuss the problem of cometary shock waves in the bi-ion fluid model. Observations and a different theoretical discussion is presented in Sections 4.1 and 2.3, respectively. The heavy ion plasma, mimicking the obstacle, influences the solar wind by continuous mass loading. Biermann et al. (1967) has shown that the continuous deceleration of the solar wind by mass loading occurs only up to a critical value of accumulated mass density. Then, as was shown in the one fluid MHD description, on the assumption that heavies are instantaneously assimilated into the solar wind, a singularity point is met where the Mach number of the flow is equal to two (Biermann et al., 1967; Schmidt and Wegmann, 1982; Galeev and Khabibrakhmanov, 1992). This happens with the contaminated solar wind before a critical mass-density is achieved, and results in shock formation.

One of the interesting points in Figure 2.2.4 is the compressive character of excited waves which suggests their nonlinear evolution with steepening and shock formation. These waves propagate upstream in the proton reference frame, carried by heavy ion beam and steepen in that direction, as is seen in Figure 2.2.4. A jump transition occurs at $X/L \sim 130$. The behavior of the waves also varies downstream of the transition. The amplitude of perturbations in the B_y-component decreases with a switch-on of the B_z-variations. Another interesting point is the behavior of the perturbations in the proton number density. Upstream of the shock fluctuations of n_p and B are in-phase. Downstream, the peaks in n_p and B are anticorrelated. Moreover, the wave form of the n_p perturbations changes drastically. Steepening features are observed in the downstream direction. The phase velocity of these waves in the proton reference frame is small which explains the smaller amplitudes of u_p variations as compared to n_p variations. It is suggested that generation of these waves occurs at lower values of the beam velocities ($\Delta u \leq u_\mathrm{A}$) when the intersection of a beam and R/L modes occurs (see Figure 2.2.3).

Figure 2.2.9 shows how a shock is formed in the bi-ion MHD simulations for the same parameters as in Figure 2.2.4. In the initial stage, the solar wind slows down and then is accelerated after the passage of the obstacle. With a increase of mass loading (the peak density of heavies gradually increases with time) deceleration reaches a value of $M_\mathrm{MS} = u/(u_\mathrm{A}^2 + c_\mathrm{s}^2)^1/2 \cong 1$ and the process of shock formation starts. A strong steepening is clearly seen at $\Omega_\mathrm{p}T = 100$. At $\Omega_\mathrm{p}T = 200$, the shock with trailing shocklets traveling in the upstream direction is observed. At later times, the shock goes back and stands at the quasi-stationary position where $M_\mathrm{MS} \cong 2$ (see also Figure 2.2.4). The interesting point is that the end position of the shock coincides with the 'start' point. It is assumed that forward and backward motions of the shock is controlled by coupling between heavies and protons.

Figure 2.2.10 gives the interesting example of an oscillating shock due to a feedback effect of heavy ions on dynamics of protons. The $x - T$ diagram contains variations of the velocities of protons and heavies across the shock which is formed

in the proton flow against the heavy ion obstacle $M_s = 5$, $m_h/m_p = 10^2$, $\beta_e = 1$, $\varphi = 50°$, $l = 50\,L$). An oscillating motion of the shock is evident. The cause is in a different behavior of protons and heavies across the shock. The proton flow abruptly slows down, therein the heavies maintain on their acceleration due to the pickup mechanism. The velocity of heavies exceeds the downstream proton velocity and the Lorentz force ($\Delta\mathbf{u} \times \mathbf{B}$) provides the acceleration of protons to suppress their lag. As a result, jump relations vary and the shock comes into a motion to adjust the ratio u_{up}/u_{down} to the jump condition. In the upstream region, where the heavies lag behind the protons, the ($\Delta\mathbf{u} \times \mathbf{B}$) force decelerates the proton flow. As a result, the shock starts to travel in the opposite direction. This leads to periodical oscillations of the shock with the bi-ion cut-off frequency $\omega_{cf} \sim 10^{-2}\,\Omega_p$. In order to address the question whether such oscillating motion of the bow shock occurs in space we present the interesting observations made near Mars. Figure 2.2.11 gives the wavelet diagram of variations of the intensity of the electron plasma waves in the Martian foreshock. 'Emission band' at the frequency near the oxygen gyrofrequency (red curve) is clearly seen. One of the probable interpretations for the observed modulations of the electron plasma oscillations at $\Omega_{O^+}$is that the position of the bow shock and the electron foreshock oscillate with a frequency $\omega_{cf} = \Omega_p n_{O^+}/n_e + \Omega_{O^+} n_p/n_e \approx \Omega_{O^+}$ (for $n_{O^+}/n_e, m_{O^+}/m_e$). Further study and kinetic simulations are necessary to answer the questions whether the shock position is stationary and determined by the point where the local Mach number is equal 2 or not, and whether a shock is replaced by a series of multiple shocklets moving in the plasma frame toward the sun with velocity of $2-3\ V_A$, or a concept of a single shock is realized.

The concept of shocklets which evolve from steepened magnetosonic waves, was suggested by Omidi and Winske [1988, 1990]. These shocklets are strikingly similar to the steepened magnetosonic waves observed at Giacobini–Zinner (Tsurutani et al., 1987). The pattern of shocklets observed downstream of the Martian bow shock is shown in Figure 2.2.11 (Dubinin et al., 1996, 1998). A periodical heating of the solar wind protons that replicates subsequent drops of the bulk velocity is followed by a plasma cooling. The state of plasma does not recover after crossings of these shocklets, emphasizing an analogy with multiple shocks with step-like transition to the downstream state.

2.3. MASS LOADED SHOCK WAVES

Observations made in situ at the three comets P/Giacobini–Zinner, P/Halley, and P/Grigg–Skjellerup reveal the presence of bow shocks/waves well ahead of a very small active cometary nucleus along with numerous other apparent discontinuities (see Section 4.1). The difficulty in deciding whether an observed transition corresponds to a shock or not has been well documented and, together with the sometimes confusing observations made from the different cometary encounters, has led to a reassessment of the theory of shock waves in a cometary environment. This

reassessment has taken two routes: one approach (Galeev and Khabibrakhmanov, 1993) has been to develop particle simulations of mass-loaded environments in the solar wind and to then try and develop a reasonably tractable kinetic model for shock formation and structure. A second approach, which draws on both observations and simulations, is the development of more sophisticated conservation laws which take into account the effects of mass-loading via photoionization and charge exchange. An advantage of the second approach lies in its comparative simplicity and its predictive capabilities (at least on sufficiently large scales) although it suffers of course from being unable to treat detailed kinetic effects properly.

The encounters with comets P/Halley and P/Grigg–Skjellerup have provided a wealth of information regarding the interaction of the solar wind with a diffuse cometary coma. In particular, the expectation that a cometary bow shock exists was confirmed. It was found that the formation, structure, nature, and properties of the cometary shock differ from their better studied planetary counterparts in a number of important ways:

1. The sublimation and subsequent pickup of cometary ions well ahead of the cometary nucleus produces an extended and diffuse obstacle to the incoming supersonic solar wind.
2. Since cometary ions (typically water group ions, e.g., O^+) add mass to a supersonic flow, the solar wind decelerates before encountering a weak shock (Biermann et al., 1967; Wallis, 1971).
3. The initial ring beam associated with the ionization of cometary neutrals is highly unstable (Wu and Davidson, 1972), generating significant levels of low-frequency MHD turbulence. The newborn cometary ions subsequently scatter strongly in pitch angle and are transported diffusively at a speed close to that of the solar wind flow speed (Coates et al., 1989, 1990a).
4. The cometary shock is dominated energetically by the minority (although massive) cometary ions (Coates et al., 1990b, 1991). Indeed, it was observed that at some distance before the cometary shock, the cometary ion pressure and the combined solar wind pressure (protons, electrons, and magnetic field) were approximately equal but that downstream of the shock, the cometary ion pressure could be as much as $\approx$3 times that of the solar wind pressure (Section 2.3.1).
5. The number density of the cometary ions in the vicinity of the shock is very low ($<$10% of the solar wind number density) (Coates et al., 1987, 1990b).
6. The cometary bow shocks were observed to be extremely broad for both quasi-perpendicular and quasi-parallel configurations. The quasi-perpendicular shock observed by *Giotto* on the inbound encounter measured some 40 000–50 000 km thick, while the quasi-parallel shock observed on the outbound Giotto encounter was broader yet at some 120 000 km. In terms of the oxygen ion gyroradius, such shock thicknesses correspond to about 5 and 20 r_{g,O^+} for the magnetic fields observed. Given the thickness of the cometary bow shock and the possible existence of solar wind disturbances, particularly during the *Giotto* inbound pass, it is difficult to identify the shock location precisely.

7. Some evidence for the existence of an abrupt discontinuity whose thickness is of the order of a thermal solar wind proton gyroradius has been published (e.g., the S2 feature pointed out by Coates et al. (1990b)). This could be consistent with a proton subshock. However, we cannot determine whether this is an intrinsic feature of the shock structure or an effect due to the highly variable local medium. This variability is thought to be due to a combination of pickup instabilities, which could steepen into 'shocklets' according to some simulations (Omidi and Winske, 1987), and convected solar wind features (Neubauer et al., 1990; Kessel et al., 1994).
8. The reflection of solar wind protons or cometary ions by the quasi-perpendicular shock does not appear to be an important factor in determining the structure of the shock.
9. The level of low-frequency MHD turbulence generated by the pickup of cometary ions is very high, and some fraction of the available or free wave energy density is damped away, resulting in the heating of the solar wind plasma (Johnstone et al., 1991; Huddleston and Johnstone, 1992; Zank et al., 1994)

Point 6 above distinguishes the cometary shock from ordinary nonreacting gas dynamical or MHD shocks in that mass-loading is important within the shock itself. It was pointed out (Neubauer et al., 1990; Zank et al., 1991) that, using typical cometary gas production rates and dissociation lifetimes (Krankowsky et al., 1986), the ratio of the newly ionized cometary mass flux injected within the shock to the convected incident mass flux can easily achieve values of ≈ 0.01, which suggested that the Rankine–Hugoniot (RH) relations should include a source term to account for mass-loading within the body of the shock. However, this procedure raised questions concerning the admissibility of certain solutions to the Rankine–Hugoniot relations. In general, the simple thermodynamical arguments used in gas dynamics and MHD are inappropriate for complex reacting flows experiencing mass-loading (Zank, 1991). To understand shocks subjected to significant mass injection, Lax's formulation of the 'entropy condition' (Lax, 1973) is necessary to isolate the physically relevant solutions to the RH conditions.

2.3.1. *Gas Dynamic Mass-Loaded Shock Waves*

Frequently, the pickup ion velocity distribution is shell-like due to rapid pitch-angle scattering and a common velocity for the plasma components is soon established. This ensures that an MHD description of the solar wind loaded by cometary ions is justified and that the specific heat ratio $\gamma = \frac{5}{3}$. However, the comments in chapter 2.1 on the sonic Mach number and the γ should be noted. To include the injection of cometary ions within the shock, one needs an 'averaged' source term for the mass in the Rankine–Hugoniot (RH) conditions. Thus the conservation of mass jump condition becomes (Neubauer et al., 1990; Zank and Oughton., 1991; Zank et al., 1991)

$$[\rho u_x] \equiv \rho u_x - \rho_0 u_{x0} = \alpha \equiv q m_c d \ , \tag{2.3.116}$$

where q denotes the average volume production rate of cometary ions, m_c the cometary ion mass, d the observed shock thickness, ρ the fluid density, and u_{x0} the normal upstream fluid velocity. The magnitude of the mass-loading source term in Equation (2.3.116) is easily inferred from in situ observations. The thickness of the 'outbound' P/Halley shock observed by Giotto in the normal direction is $d = 120\,000$ km. Then, using a 10^6 second lifetime for the dissociation products of cometary neutral molecules implies an injected mass-loaded mass flux within the shock of the order of 1.4×10^7 amu cm^{-2} s^1. The upstream mass flux is found to be 2.3×10^8 amu cm^{-2} s^{-1} (Coates et al., 1990a), giving a conservative shock mass-loading to upstream mass flux ratio of $\approx$0.06. For the slightly thinner inbound P/Halley shock, the ratio is not very different. Why this at most 10% term is important in the flow dynamics is discussed explicitly below. The remaining RH conditions are given by

$$[\rho u_x^2 + p] = 0 \,, \tag{2.3.117}$$

$$[\rho u_x u_y] = 0 \,, \tag{2.3.118}$$

$$[(e + p)u_x] = 0 \,, \tag{2.3.119}$$

where $e = \rho u^2/2 + \rho\epsilon$, ϵ is the internal energy of the fluids, $\mathbf{u} = (\mathbf{u_x}, \mathbf{u_y})$ is the velocity field, and p is the gas pressure. Let $m = \rho_0 u_{x0}$, and introduce the specific volume $\tau = \rho^{-1}$ together with $\alpha^* = \alpha/m$ and $\tau^* = (1 + \alpha^*)\,\tau$. Then, rearranging 2.3.116 - 2.3.119 yields the mass-loaded form of the Hugoniot function

$$\begin{aligned} H(\tau^*, p) = \; & \epsilon^*(\tau^*, p) - \epsilon(\tau_0, p_0) + \frac{p + p_0}{2}(\tau^* - \tau_0) - \\ & - \frac{\alpha^*}{2} m^2 \tau_0 \tau^* - \frac{1}{2}\frac{\alpha^*}{1 + \alpha^*} u_{y0}^2 \,, \end{aligned} \tag{2.3.120}$$

where $\epsilon^* \equiv (1 + \alpha^*)\epsilon$. Expression (2.3.120) differs from the standard gas dynamic Hugoniot function, in the terms ϵ^*, u_{y0}, and $\alpha^* m^2 \tau_0 \tau^*/2$. Three important points are immediately apparent from (2.3.120): (i) The mass-loaded Hugoniot is a function of the upstream Mach number through m^2 since $M_0^2 \equiv u_{x0}^2/C_s^2 = u_{x0}^2/(\gamma p_0 \tau_0)$ for an ideal gas. Thus, even though α^* is a rather small term, its associated momentum contribution in the shock frame can be significant. (ii) The mass-loaded Hugoniot is not invariant with respect to tangential flows. The true significance of this point is to be found in MHD with mass-loading because this invariance causes a rotation of the magnetic field downstream of a mass-loaded front (Neubauer et al., 1990; Zank et al., 1992). The lack of invariance arises from the fact that the tangential velocity components in front of and behind the shock are unequal unless $\alpha^* = 0$, that is $u_{y1} = (1/(1 + \alpha^*)u_{y0}$ which implies that a mass-loaded front is subjected to shearing stresses - something that sets it apart from both ordinary non-reactive gas dynamical shocks and combustion shocks. (iii) Finally, a state cannot

be connected to itself by a mass-loaded front since $H(\tau_0, p_0) \neq 0$. This provides a different perspective on the "physical" entropy condition used normally to select the physically relevant RH solutions (Zank, 1991). For a given α^*, $H(\tau^*, p) = 0$ is the locus of all possible states that can be connected to the given state (τ_0, p_0).

For an ideal gas, $H(\tau^*, p) = 0$ reduces to

$$\frac{p}{p_0} = \frac{1-\mu^2\tau^*/\tau_0}{\tau^*/\tau_0-\mu^2} + \alpha^*\mu^2\gamma M_0^2\frac{\tau^*/\tau_0}{\tau^*/\tau_0-\mu^2} + \\ +\mu^2\gamma M_0^2\frac{\alpha^*}{1+\alpha^*}\frac{\tan^2\theta}{\tau^*/\tau_0-\mu^2}\,, \tag{2.3.121}$$

where $M_0^2 = u_{x0}^2/(\gamma p_0\tau_0)$ is the square of the Mach number normal to the shock, θ is the angle the incident flow makes with the shock normal and $\mu = (\gamma-1)/(\gamma+1)$. Depending on the upstream supersonic Mach number, the $\tau^*/\tau_0 \to \infty$ asymptote can lie either in the $p > 0$ or the $p < 0$ half-plane and the initial state $(\tau_0, p > 0)$ can also lie above, on, or below the Hugoniot. In determining the downstream state corresponding to a prescribed upstream state, one must solve the momentum equation, now rewritten as

$$m^2 = (p - p_0)/[\tau_0 - (1 + \alpha^*)\tau^*]\,, \tag{2.3.122}$$

simultaneously with the Hugoniot. This can be done explicitly, so enabling one to identify different sections of the Hugoniot (2.3.121) with different flow transitions. Thus we may summarize the properties of the RH conditions (2.3.116)–(2.3.119) conveniently in terms of a general representation of the mass-loaded Hugoniot, depicted in Figure 2.3.1. The dashed section from A to B is not physically relevant since the states it represents requires that $m^2 < 0$ if the Rayleigh line (2.3.122) is to intersect the Hugoniot (2.3.121). The Hugoniot can be separated into two branches – the upper corresponds to compressive fronts ($p > p_0$); the detonation branch of combustion theory and the lower portion to expansion fronts ($p < p_0$); the deflagration branch for combustion. The lines through $[\tau_0/(1 + \alpha^*)^2, p_0]$ tangent to the Hugoniot at points I and II are mass-loaded versions of the 'Rayleigh' lines and the points I and II correspond to the 'Chapman–Jouguet' points of combustion theory.

The points I and II serve to further divide the Hugoniot curve. The strong compression branch above I corresponds to flows that are subsonic downstream of the discontinuity. The weak compression regime between I and A corresponds to downstream states with supersonic flows. The branch between B and II describes the weak expansion regime and the flow is subsonic downstream of the front. The final branch, the dot-dashed segment from II onward, represents the strong expansion regime with supersonic downstream flows.

Shock solutions lie on the Hugoniot above B provided $u_{x0} > C_0$ and below B if $u_{x0} < C_0$. Thus, the strong compression branch describes supersonic-subsonic

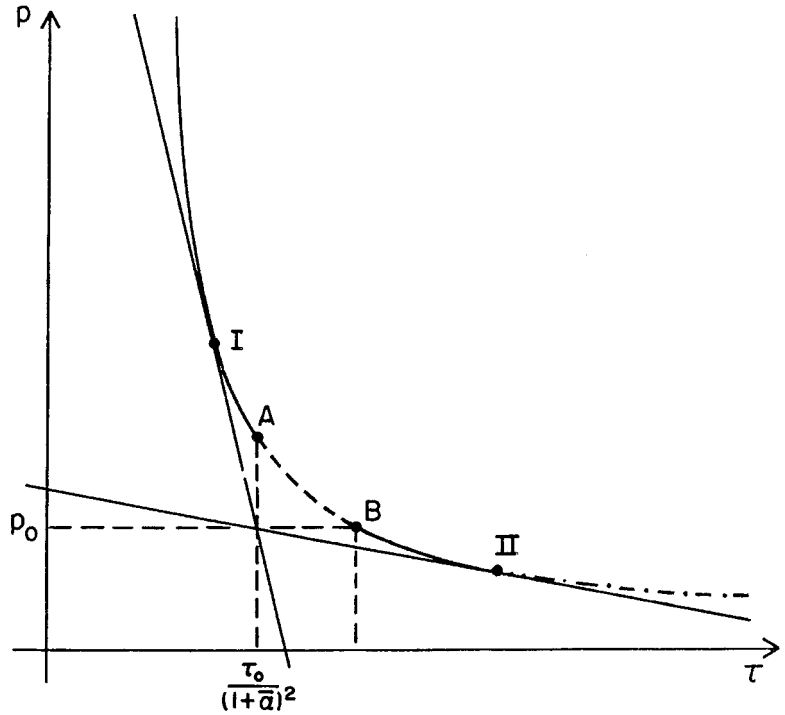

Figure 2.3.1. The classification of the gas dynamic mass-loaded Hugoniot. Only the solid lines correspond to admissible downstream states.

transitions and, notably, the weak compression branch corresponds to supersonic-supersonic, but nonetheless decelerated, transitions. On the basis of the Lax entropy criterion, Zank et al. (1991) showed that all compressive solutions to the mass-loaded gas dynamic RH condition are physically admissible, including those transitions that lie on the weak compression branch. The weak compression branch is interesting in that it demonstrates that the mass-loaded system of equations is nonconvex. It can be shown that weak compressive transitions possess a compound structure, consisting of an initial deceleration such that the flow speed equals the sonic speed followed by a recovery in the flow speed to the final downstream state. It should be noted that, since the shock structure problem was not solved explicitly, no estimate of the various length scales appropriate to a compound shock can be given. For this, a more sophisticated model is necessary (Section 3 below). The compound shock represents, however, a quite new form of shock transition that has no counterpart in nonreacting hydrodynamics. It has been suggested that a train of such compound shocks was observed at P/Halley on the inbound shock encounter.

In concluding this section, consider the properties of mass, loaded fronts as a function of the upstream Mach number. This further clarifies aspects of the above analysis. The downstream and upstream Mach numbers can be related via a simple relation $f(M_1^2, M_0^2, \alpha^*)$. Figure 2.3.2(a) illustrates the classical hyperbolic relation

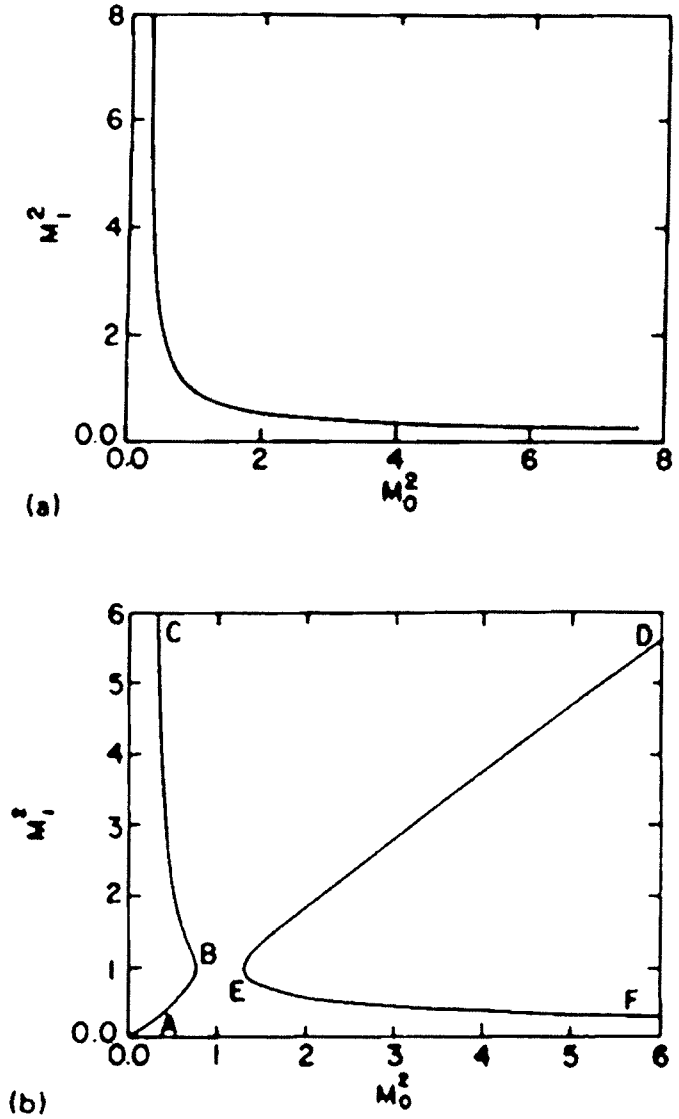

Figure 2.3.2. Solutions of the gas dynamic Rankine–Hugoniot conditions in which the square of the downstream Mach number M, is plotted as function of the incident Mach number M. (a) Solutions for the case $\alpha^* = 0$. (b) The same except that $\alpha^* = 0.01$.

when $\alpha^* = 0$, and Figure 2.3.2(b) shows the RH solutions when $\alpha^* = 0.01$. The change in topology wrought by mass loading is profound. Figure 2.3.2(b) reveals (i) that there is a range of M_0^2, for which no steady downstream mass-loaded transitions can exist; (ii) the region EF corresponds the usual gas dynamic shock solutions; (iii) the locus ED corresponds to the region of compound mass-loaded

fronts; and (iv) B = I and E = II are the mass-loaded 'Chapman–Jouguet' points, therefore E corresponds to a 'Chapman–Jouguet' mass-loaded front.

2.3.2. *MHD Mass-Loaded Shock Waves*

The model used to investigate shocks experiencing mass loading in a magnetofluid is an appropriate extension of the gas dynamic model and much of the physics described already continues to hold for MHD. An important assumption which is well corroborated by observations at P/Halley (Neubauer et al., 1990) is that the coplanarity theorem holds at MHD shocks experiencing mass-loading. The RH conditions are now given by

$$[\rho u_x^2 + p + B_y^2/2\mu_0] = 0\,, \tag{2.3.123}$$

$$[\rho u_x u_y - B_x B_y/\mu_0] = \alpha V_y\,, \tag{2.3.124}$$

$$[\rho u_x(\epsilon + u^2/2) + u_x p + 1/\mu_0(\mathbf{E}\times\mathbf{B})_{\mathbf{x}}] = \alpha \mathbf{V}_{\mathbf{y}}^{\mathbf{2}}/\mathbf{2}\,, \tag{2.3.125}$$

$$[B_x] = 0, \quad [u_x B_y - u_y B_x] = 0\,, \tag{2.3.126}$$

where **E** denotes the electric field, **B** the magnetic field, and V_y the transverse velocity of the newly ionized cometary particles. It is simplest to work in the normal incidence frame of the flow $u_y^* = u_y - u_{y0}$, $V_y^* = V_y - u_{y0}$, so that $u_{y0} = 0$ and V_y^* can be positive, negative, or zero. Equations (2.3.123)–(2.3.126) are effectively unchanged except that we now use u_y^* and, V_y^* instead. We omit the asterisk hereafter. It should be recognized that V_y can be significant because of translation and should not therefore be neglected. The V_y term is important because the RH conditions are no longer invariant with respect to tangential flows, and observationally, we might expect V_y to be sizable (Coates et al., 1990a).

Equations (2.3.123)–(2.3.126), together with (2.3.116), yield the mass-loaded form of the MHD Hugoniot function:

$$\begin{aligned} H(\tau^*, p) = {} & \epsilon^* + \frac{1}{2}\langle p\rangle\alpha^* + \frac{1}{4\mu_0}\tau^*[B_y]^2 - \frac{\alpha^*}{2}m^2\tau^*\tau_0 + \\ & + \frac{1}{2}\frac{\alpha^*}{1+\alpha^*}\frac{B_x}{\mu_0 m}[B_y]V_y - \frac{1}{2}\frac{\alpha^*}{1+\alpha^*}u_{y0}^2 \end{aligned} \tag{2.3.127}$$

and the Hugoniot equation is $H(\tau_1^*, p_1) = 0$. Equation (2.3.127) is, in many respects, very similar to the Hugoniot of classical MHD (Cabannes, 1970) except that the jump condition contains the effects of mass-loading and shearing. Here $\langle Q\rangle \equiv Q_0 + Q_1$, and $a^*b = (1+\alpha^*)a_1b_1 - a_0b_0$. The fourth term in (2.3.127) was found in the gas dynamical example and the remaining two terms arise through the lack of tangential invariance in oblique mass-loaded flows.

Observe that the tangential magnetic field component in (2.3.127) can be written in terms of τ^* as

$$[B_y] = \frac{\tau_0 - \tau^*}{\tau^* - \tau_A} B_{y0} + \frac{\alpha^*}{1+\alpha^*} \frac{B_x}{m} \frac{V_y}{\tau^* - \tau_A} , \tag{2.3.128}$$

where

$$\tau_A \equiv \frac{1}{1+\alpha^*} \frac{B_x^2}{\mu_0 \rho_0^2 u_{x0}^2} = \frac{\tau_0}{1+\alpha^*} M_{A0}^{-2} . \tag{2.3.129}$$

Thus the sheared flow drags the magnetic field within the shock so that even a parallel shock (i.e., $B_{y0} = 0$) has its downstream magnetic field rotated. Mass-loading will, therefore, always 'switch on a shock' regardless of the magnitude of the plasma beta, and this represents yet another important difference between reacting and nonreacting MHD shocks.

As before, use of the mass-loaded form of the Rayleigh line (Zank et al., 1991b, 1992) indicates that those segments of the Hugoniot bounded by

$$\tau^- < (>) \frac{1}{1+\alpha^*}, \quad p^- > (<) 1 - \frac{1}{\beta_{p0}} (B_y^{-2} - \tan^2\theta_0) \cos^2\theta_0 , \tag{2.3.130}$$

in the (τ^-, p^-) plane map to a downstream state for which $m_2 > 0$. Here, $B_y^- = B_y/B_x$, $\tau^- = \tau^*/\tau_0$, $B_{y0}/B_x = \tan\theta_0$ and β_{p0} denotes the upstream plasma beta. Solutions to the RH conditions are located at the points of intersection of the Hugoniot equation (2.3.127) and the generalized Rayleigh curve. Unlike classical MHD, the Hugoniot and Rayleigh line need not intersect, indicating that one cannot connect a state to itself by means of a mass-loaded front. However, as with the hydrodynamical case, distinguished points exist at which the Hugoniot and Rayleigh curves touch. At these points of common tangency, one can show (Zank et al., 1992) that the downstream normal fluid velocity u_x must satisfy

$$u_x^2 - \left(\frac{\gamma p}{\rho} + \frac{B^2}{\mu_0 \rho} \right) u_x^2 + \left(\frac{\gamma p}{\rho} \right) \left(\frac{B_x^2}{\mu_0 \rho} \right) = 0 , \tag{2.3.131}$$

which is equivalent to the magnetosonic dispersion relation. Thus, when the Rayleigh curve is tangent to the Hugoniot, the downstream fluid velocity u_x is equal to either the fast or slow magnetosonic speed. This important result enables one to distinguish between submagnetosonic and sub-Alfvénic downstream flow speeds.

Two examples that illustrate the possible topological features of the Hugoniot are illustrated in Figure 2.3.3. At the point I, the downstream flow speed equals the fast magnetosonic speed, i.e., $u_x = V_f$, and at II, $u_x = V_s$ the slow magnetosonic speed. The region IM corresponds to transitions with downstream flow speeds satisfying $u_x < V_f$. The shock polar relations appropriate to Figure 2.3.3 are illustrated in Figure 2.3.4. The segment ID of Figure 2.3.4 may be identified with fast-mode mass-loaded shocks, the section IC with a new form of MHD shock (fast-mode compound shocks), AII is inadmissible, and BII identifies subsonic-subsonic expansion flows which may or may not be admissible (Zank et al., 1991b). The fast-mode compound mass-loaded fronts possess the same structure as the gas

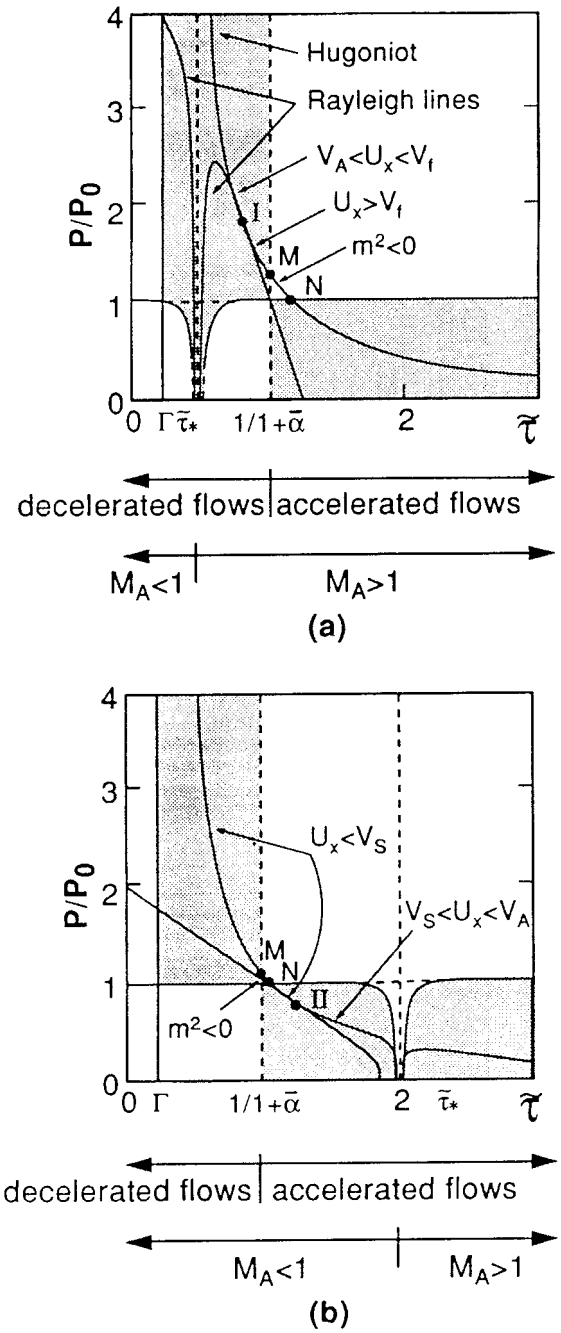

Figure 2.3.3. Illustrative examples of the Hugoniot and Rayleigh curves for a parallel shock $\theta_0 = 0$, $\gamma = 5/3$, $V_y^- = 4$, $\beta_{p0} = 1$, $\alpha^* = 0.01$. (a) Corresponds to incident flows satisfying $u_{x0}\ V_{f0}$, and (b) to $V_{f0}\ u_{x0}\ V_{s0}$.

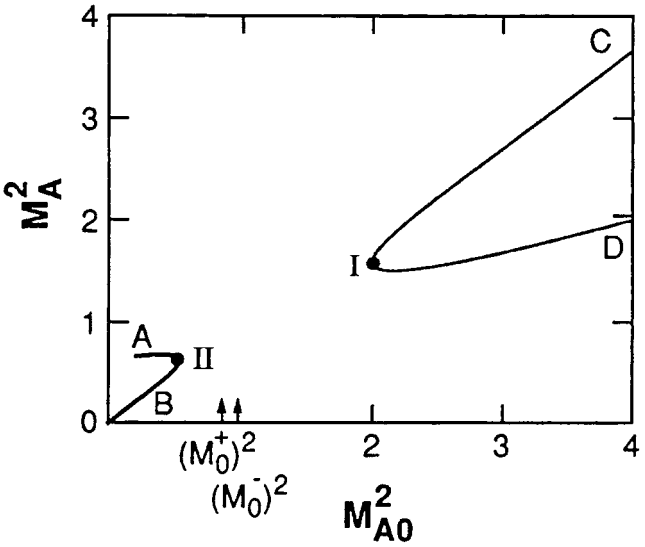

Figure 2.3.4. Plot of the Alfvén Mach number shock polar for parameters appropriate to Figure 2.3.3. $(M_0^+)^2$ and $(M_0)^2$ locate the normalized fast and slow magnetosonic speeds. Only real solutions for which the pressure $p0$ are plotted.

dynamic compound shock except that the initial deceleration of the flow is now to the fast magnetosonic speed, after which the fluid accelerates back to its final downstream state. Note the rather large parameter regime in Figure 2.3.4 for which stable (parallel) mass-loaded transitions do not exist.

Although the magnetic field is always 'dragged' on passage through the shock by the shearing mass-loaded flow, stable slow-mode mass-loaded fronts need not always exist for quasiparallel shocks. Consider now $\theta_0 = 45°$. In this case, the shock polar topology changes significantly from the classical structure (e.g., Zank et al., 1992) to that illustrated in Figure 2.3.5 (although only the slow mode section is plotted here, the fast mode section resembling that of Figure 2.3.4). The most interesting section is the segment D-III-E-F, III the point at which $u_x = V_s$. Here, E identifies the mass-loaded switch-off shock, i.e., the downstream $B_y = 0$, and differs from the classical switch-off shock in that $M_{A0} \neq l$. Here, F corresponds to the point at which the upstream normal flow speed matches the upstream slow magnetosonic speed. Careful use of the Lax entropy criterion reveals that those sections of the shock polar satisfying either (i) $V_{f0} > u_{x0} > V_{A0} > V_{s0}$, and $u_x < V_s < V_A$; or (ii) $V_{f0} > u_{x0} > V_{A0} > V_{s0}$ and $u_x = V_s$ do not represent physically sensible solutions to the RH conditions (Zank et al., 1992). An interesting class of shocks, labeled in Figure 2.3.5 exists for which $M_{A0} < 1$ and yet the magnetic field is rotated in such a way that it is consistent with an intermediate shock. These structures have been called 'slow-intermediate' shocks.

The segment from F to E corresponds to the mass-loaded version of MHD slow-mode shocks. Although not present in this particular case, for smaller θ_0

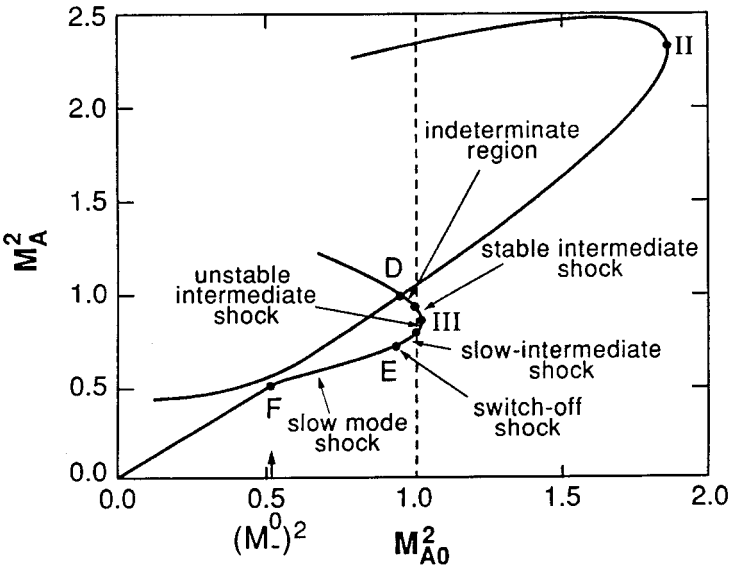

Figure 2.3.5. Detail of the 'slow' section of the $\theta_0 = 45°$ shock polar curve. The different classes of shock corresponding to each section of the shock polar are marked.

values (e.g., $\theta_0 = 30°$), the existence of slow-mode compound shocks can also be established under certain circumstances. Thus, mass loading in a shock leads to an extraordinary richness of different transitions.

2.3.3. *Quasi-Perpendicular Shock Waves*

Consider the implications of mass loading at quasi-perpendicular shocks. The quasi-perpendicular shock observed by *Giotto* during the P/Halley encounter was much narrower than its parallel counterpart and so, at first sight, mass loading within the shock should be relatively modest. This conclusion, however, needs to be considered more carefully within the context of the conventional theory of quasi-perpendicular shocks.

At a perpendicular shock, the electrostatic potential Φ satisfies

$$e\Phi = \int_{-\infty}^{x} \frac{\mathrm{d}}{\mathrm{d}x}\left(\frac{B^2}{8\pi} + p\right)\mathrm{d}x + \overbrace{\int_{-\infty}^{x} u_x B_z \,\mathrm{d}x}\ , \tag{2.3.132}$$

where the (over)bracketed term can assume particular importance because of the net ion cross-field drift u_y which results from the gyromotion of particles reflected at the shock. As the reflected particles (in our case, the solar wind protons) begin to dominate the incident u_y an overshoot in develops which in turn further enhances the efficiency of particle reflection. Thus, in this case, one also has a 'shear' in u_y across the transition. This theory is borne out very nicely by simulations. Accompanying the downstream overshoot in Φ is an overshoot in the magnetic pressure.

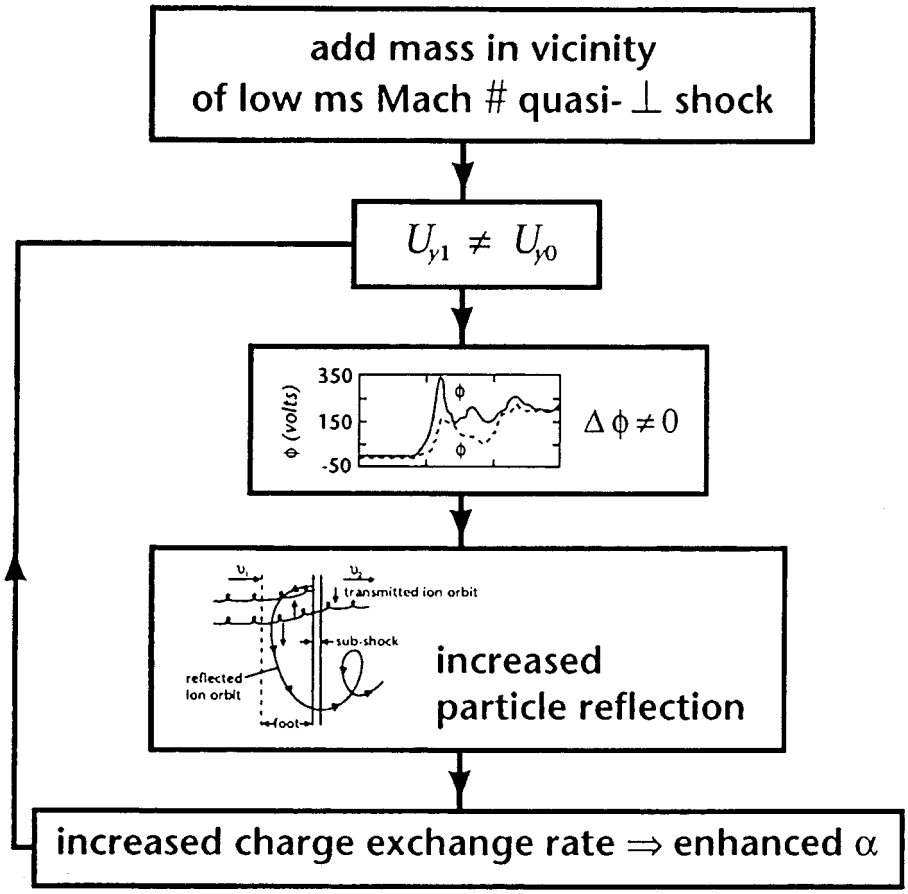

Figure 2.3.6. A scenario for low magnetosonic Mach number mass loaded shocks.

Although the correlation between the magnetosonic Mach number, the plasma beta β_p and the theory is not completely clear, it does appear that low magnetosonic Mach number shocks remain laminar. How might mass-loading in the vicinity of a perpendicular shock change this picture?

A possible scenario for low magnetosonic Mach number mass-loaded shocks is depicted in the flow chart of Figure 2.3.6. Even a modest addition of cometary ions in the immediate vicinity of a low magnetosonic Mach number shock induces a jump in the tangential flow velocity across the mass-loaded front. From Figure 2.3.6, the electrostatic potential Φ is enhanced thereby proving a more effective barrier to inflowing solar wind protons, hence increasing the number of ions reflected from the shock. Besides further enhancing the shear (the jump in u_y), the proton number density should increase somewhat immediately ahead of the discontinuity. However, increasing the solar wind proton number density increases their rate of charge exchange with cometary neutrals, a rate which compares to the

photoionization rate in the whole outer coma of comet P/Halley at 1 AU (Galeev, 1989). If a significant fraction of the reflected solar wind protons charge exchange with neutral cometary particles, then the mass density associated with the one-fluid description will increase significantly through the enhanced α, which in turn increases the shear and the entire cycle then repeats itself, perhaps at a more efficient level. Thus, even at the narrower quasi-perpendicular transition, we expect mass loading, via both photoionization and charge exchange, to play a key role in determining the properties of the transition. From the flow chart of Figure 2.3.6, it is not clear whether a quasi-perpendicular mass-loaded front can settle into a steady or even quasi-periodic state. A similar argument has been advanced for the cometopause (Khabibrakhmanov and Zank, 1993).

2.3.4. *The Structure of Cometary Shock Waves*

To gain some insight into the structure of a shock in a mass-loaded environment, it is necessary to utilize at least some form of a multi-fluid model if not a direct kinetic description. In Section 2.2.7 a bi-ion fluid model is explored in which electromagnetic fields couple the various fluids, but the effect of particle scattering in the highly turbulent magnetofluid is neglected entirely (Sauer et al., 1990; Motschmann et al., 1991). By contrast, in this chapter the latter effect is regarded as intrinsic to the physics of the cometary coma-solar wind interaction, and a somewhat different approach is taken (Zank et al., 1993, 1994, 1995; Story and Zank, 1996). They assume 'momentum exchange' between the solar wind protons and the cometary ions (facilitated by the Alfvén turbulence intermediary) and adopt a simple mean free path to describe 'collisions'. By taking moments of the collisional Boltzmann equation (with a source term) and assuming that the total momentum of the system is conserved, a system of multi-fluid equations similar to those of Sauer et al. (1991) is derived, except that additional 'frictional' terms are present. The cometary ion pressure is assumed to be isotropic (which is quite reasonable) and thermal conduction is neglected (which is perhaps less reasonable).

The salient features of the Zank et al. (1993a, b, 1994, 1995) approach are summarized here. The model consists of a distinct cometary ions fluid (taken to be composed of oxygen ions typically with a density ρ_c, pressure p_c and velocity $\mathbf{u_c}$) and a solar wind fluid (composed of thermal protons and massless electrons). The corresponding solar wind plasma parameters are density ρ_s, bulk flow velocity $\mathbf{u_s}$, and isotropic pressure P_s, and magnetic field $\mathbf{B}$. Since the plasma beta is observed to be very high at comet P/Halley (Coates et al., 1991; Table 2.3.1), the magnetic pressure is dominated by P_s. Finally, thanks to the strong scattering of cometary ions by self-generated and *in situ* MHD turbulence, Zank et al. assume that the cometary ion pressure is described reasonably well by an isotropic tensor in the vicinity of the bow shocks.

The cometary ion-scattering centers are assumed to be effectively embedded in the supersonic solar wind frame so that momentum exchange, although facilitated by the MHD turbulence-Alfvén wave intermediary, occurs essentially between the

TABLE 2.3.1

Pressure contribution from the various plasma components upstream and downstream of the shock. The solar wind plasma beta β_{sw} and total plasma beta β_{total} are also included

Pressure component	Upstream (eV cm^{-3})	Downstream (eV cm^{-3})
Electrons	200	400
Protons	50	110
Magnetic field	90	300
Cometary ions	800	1400
β_{sw}	2.8	1.7
β_{total}	11.7	6.4

cometary ions and the solar wind. Then, as was shown by Zank et al. (1993a), the strongly scattered cometary ions convect and diffuse in the solar wind fluid frame. Thus, to leading order, the cometary ion streaming or mass flux can be approximated as

$$\rho_c \mathbf{u_c} = \rho_\mathbf{c} \mathbf{u_s} - \kappa \cdot \nabla(\mathbf{P_c}/\mathbf{u_0^2}) \; . \tag{2.3.133}$$

The spatial diffusion tensor κ has components which can be expressed in coordinates parallel and perpendicular to the mean magnetic field **B** as

$$\kappa_\parallel = \tau u_0^2, \quad \kappa_\perp = \frac{\kappa_\parallel}{1 + \Omega_c^2 \tau^2}, \quad \kappa = \kappa_\perp \Omega_c \tau \; . \tag{2.3.134}$$

Here τ is the effective scattering time of the cometary ions, Ω_c is the cometary ions cyclotron frequency, κ_D are the off-diagonal elements of the diffusion tensor, and u_0 is a normalizing hydrodynamic flow speed which provides the appropriate dimensional units for the spatial diffusion tensor. As was discussed by Isenberg and Jokipii (1979), the diffusion coefficients (2.3.134) can be derived equally easily at a kinetic level. The scattering time τ must scale with the cometary ion cyclotron frequency, and from (2.3.134) it is apparent that the diffusion scale can differ significantly from perpendicular to parallel magnetic field geometries. Equation (2.3.133) represents the hydrodynamic formulation of the widely used transport equation for cometary ions (e.g., Gombosi et al., 1991). It should be recognized that τ is effectively averaged over particle speeds and is therefore a somewhat simplistic representation of the full complexity of the expected scattering term, a term which should contain the effects of both resonant scattering and wave-turbulence power. Nonetheless, one can, in principle, include macroscopic wave power effects, for example.

Approximation (2.3.133) reduces the complexity of the full multifluid equations significantly by introducing self-consistent dissipation coefficients into the fluid description. Such dissipation is analogous to the inclusion of heat conduction in the Euler equations. It follows therefore that the inclusion of cometary ion scattering and momentum exchange with the solar wind enables one to resolve, at least partially, the structure of the cometary shock. It transpires that under typical solar wind conditions, cometary ion spatial diffusion is sufficient to smooth all cometary shocks completely. A notable exception to this result may be the outbound shock observed at comet P/Grigg–Skjellerup. The nature of the P/Grigg–Skjellerup shocks and bow waves has been discussed by Neubauer et al. (1993) and Reme et al. (1993). An important paper for the analysis presented here is that of Mazelle et al. (1994), who have synthesized the electron and magnetometer data obtained at P/Grigg–Skjellerup to compare P/Grigg–Skjellerup boundaries with those observed at P/Halley. They conclude that despite the smaller scale of the P/Grigg–Skjellerup plasma environment, it possesses many regions and boundaries that are common with P/Halley. Consequently, the results of Zank et al. (1995) may well have interesting applications for smaller comets such as P/Grigg –Skjellerup.

The hypersonic solar wind limit (i.e., for a cold solar wind) is most instructive, as it reveals the basic properties of the diffusive multifluid model very clearly and illustrates the close correspondence between the Zank et al. model and the original one-fluid model of Biermann et al. (1967). The hypersonic model may be expressed as (Zank et al., 1994),

$$\frac{\partial \rho_s}{\partial t} + \nabla \cdot (\rho_s \mathbf{u_s}) = \mathbf{0} \,, \tag{2.3.135}$$

$$\frac{\partial \rho_c}{\partial t} + \nabla \cdot (\rho_c \mathbf{u_s} - \kappa \cdot \nabla_\mathbf{c}) = \mathbf{m_c Q_c} \,, \tag{2.3.136}$$

$$\rho \left(\frac{\partial}{\partial t} + \mathbf{u}_s \cdot \nabla \right) \nabla \mathbf{u}_s - (\kappa \nabla p_c) \cdot \nabla \mathbf{u}_s = -\nabla p_c - m_c \mathbf{u}_s Q_s \,, \tag{2.3.137}$$

$$\begin{aligned} \nabla \cdot \left(\frac{\rho u_s^2}{2} \mathbf{u}_s - \frac{u_s^2}{2} \kappa \cdot \nabla p_c + \frac{\gamma_c}{\gamma_c - 1} p_c \mathbf{u}_s - \frac{\gamma_c}{\gamma_c - 1} \frac{p_c}{\rho_c} \kappa \cdot \nabla p_c \right) + \\ + \frac{\partial}{\partial t} \left(\frac{\rho u_s^2}{2} + \frac{p_c}{\gamma_c - 1} \right) = 0 \,. \end{aligned} \tag{2.3.138}$$

Here $\rho \equiv \rho_s + \rho_c$, ρ_i is the species density, and γ_c the adiabatic index of the cometary ions. In the case of a warm solar wind, a critical Mach number exists for which certain solutions require a subshock (Story and Zank, 1996).

In the steady-state limit, the diffusive multifluid equations can be combined as single ordinary differential equation in terms of the mass-loaded inverse compression ratio $Z_s \equiv (1 + \alpha) y_s$, $y_s \equiv u_s / u_s(-\infty)$, $\alpha \equiv \int_{-\infty}^{x} Q(x')\, \mathrm{d}x'/m$:

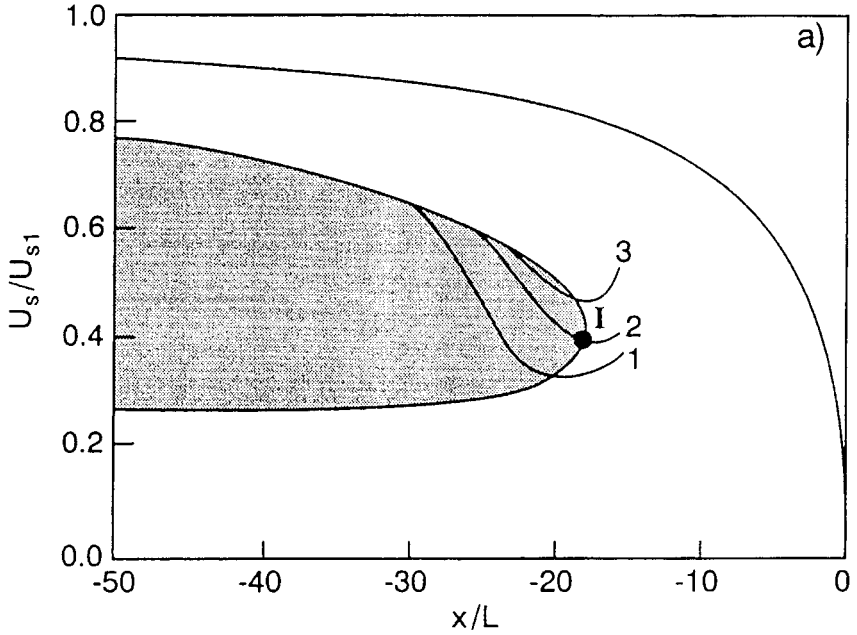

Figure 2.3.7. Solutions to the steady one-dimensional (1-D) shock structure equation in the hypersonic limit. velocity (normalized to the undisturbed solar wind velocity) is plotted as a function of normalized distance x/L from the cometary nucleus (where L is the diffusive length scale κ/u_1). The curve bounding the shaded region corresponds to the choked single-fluid 1-D solution of Biermann et al. (1967), and this curve bounds the region of physically admissible shock layer solutions. Curves 2 and 3 correspond to Chapman–Jouguet solutions, whereas curve 1 is analogous to a gasdynamics shock. See Zank et al. (1994) for details regarding the classification of the various solution curves.

$$\frac{\mathrm{d}Z_s}{\mathrm{d}x} = \frac{\gamma_c + 1}{\gamma_c - 1}\alpha^* \frac{Z_s^2 + \mu_c^2(1+\alpha^*) - 2\gamma_c/(\gamma_c+1)Z_s}{(1+\alpha^*) - Z_s^2}\,, \tag{2.3.139}$$

where $\mu_c^2 = (\gamma_c - 1)/(\gamma_c + 1)$. After normalizing x by $u_s\kappa$, the only free parameter in (2.3.139) is the ratio of the mass-loading to the cometary ions diffusion length scale.

Examples of different solutions are illustrated in Figure 2.3.7. The heavy curve bounding the shaded region corresponds to the well-known one-dimensional (1-D) hypersonic solution of Biermann et al. (1967). It also corresponds to the zero cometary ion pressure gradient solution of our multifluid equations, that is, $\nabla P_c = 0$. Thus, as illustrated in Figure 2.3.7, the shock layer solutions follow the Biermann et al. (1967) curve closely (a gradual deceleration due to mass loaded) before diverging strongly in the neighborhood of a shock transition. From (2.3.133), we see that $u_c = u_s$ exactly on the Biermann et al. (1967) solution. A suitable boundary condition would determine the location and strength of a subshock in the single-fluid Biermann et al. (1967) formulation of the mass loading problem. In the Zank et al. formulation the same boundary condition also determines the shock loca-

tion, but the transition, as illustrated in Figure 2.3.7, now has structure. Physically, Figure 2.3.7 shows that the incoming solar wind is decelerated via mass loading while momentum exchange in the nonuniform flow between cometary ions and the solar wind (via the wave-turbulence intermediary) initiates the formation of a decelerating pressure gradient. Eventually, the cometary ion pressure gradient dominates and forces the solar wind to decelerate smoothly and abruptly through a shock layer whose thickness is several times the diffusive length scale κ/u_1, of the cometary ions, where u_1 is the upstream flow velocity.

By assuming a warm i.e., non-hypersonic solar wind, the multi-fluid equations (2.3.137) are complicated significantly, although the basic physics described above is unchanged. In addition, Zank et al. (1994) include a non-polytropic description of the solar wind. As discussed by Johnstone et al. (1991) and Huddleston and Johnstone (1992), one can readily estimate the wave energy density of the low-frequency turbulence generated by the newborn cometary ions. Although the various processes are not yet fully understood, the self-generated wave intensity is limited by nonlinear effects, effects that must lead to the damping of the scattering waves into the background solar wind plasma eventually. Some will also be dissipated into the cometary ions via second-order Fermi acceleration. If it is assumed that some fraction ν of the available free energy in waves is used to heat the solar wind plasma, then the solar wind pressure equation acquires a source term which is proportional to the mass loading rate (Zank et al., 1994). It transpires that wave damping is necessary to account for the observed solar wind pressure. Its importance lies in the fact that since the cometary bow shock can be smoothed by the large-gyroradius O^+ ions, the solar wind is heated only adiabatically. In the absence of wave damping (Zank et al., 1995) solar wind pressures can be as much as 3 times too low.

Zank et al. (1994, 1995) use a 1-D model for the supersonic solar wind and the shock itself, but it was shown that a quasi 1-D formulation changed the 1-D results but little in this regime (Zank et al., 1994). Obviously, in the subsonic flow regime, a 1-D model is quite inapplicable.

One has to be particularly careful in applying the 1-D diffusive model to the quasi-perpendicular shock. From (2.3.134), diffusion is much more effective along the magnetic field than perpendicular to it. Consequently, unlike at the quasi-parallel shock, cometary ions that manage to diffuse far upstream or downstream of the perpendicular shock are likely to diffuse into neighboring flow tubes, thereby invalidating the 1-D hypothesis. Thus, even were the solar wind flow velocity normal to the shock, the cometary ions would possess a large lateral diffusive drift due to their greater mobility along the field. Thus, for a quasi-perpendicular diffusive shock, one should really account for geometric effects.

Plotted in Figure 2.3.8(a) are the observed solar wind and cometary ion number densities and the predicted solar wind and cometary ion number densities. The cometary ion number density has been multiplied by a factor of 10 for display purposes. Following Huddleston et al. (1990), Zank et al. (1995) used a mass

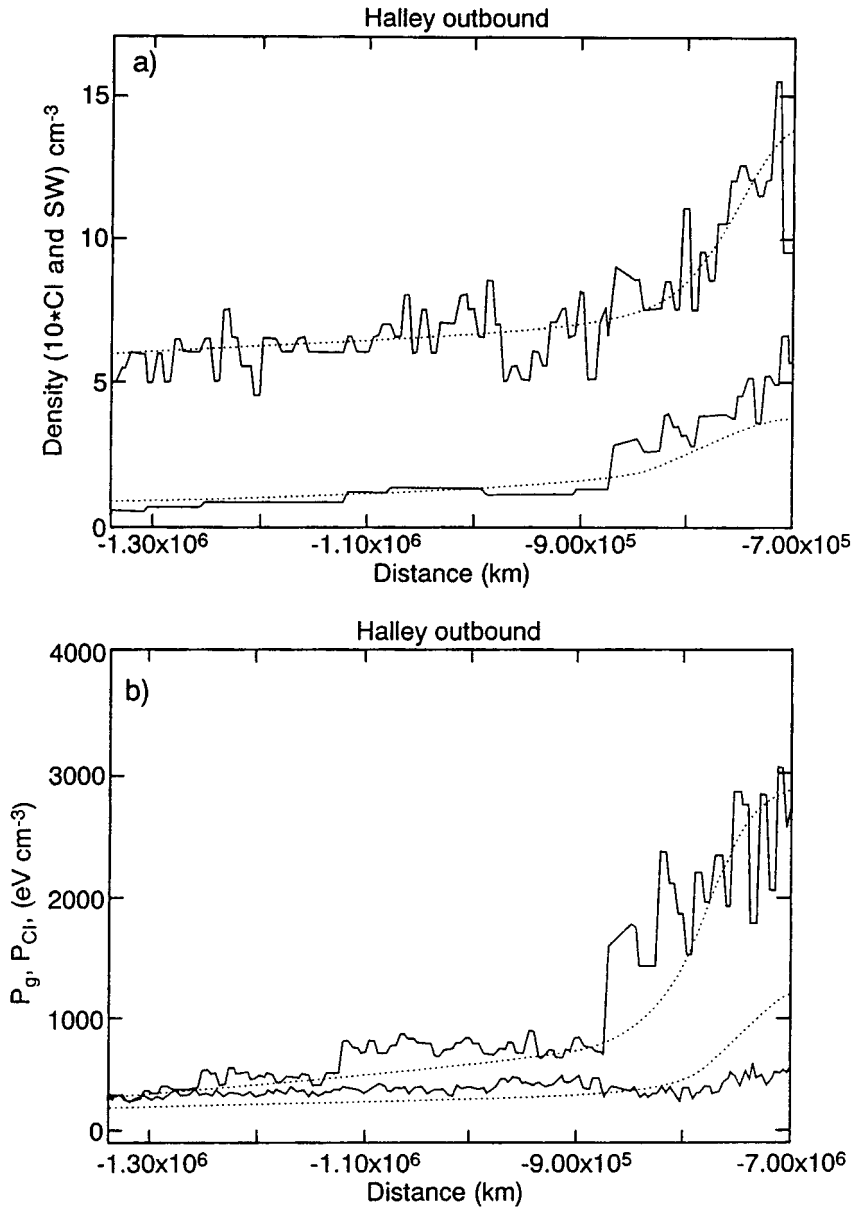

Figure 2.3.8. (a) Overplots of the theoretical and observed solar wind and cometary ion number densities for the quasi-parallel cometary bow shock observed by *Giotto* at P/Halley. The top plot, and its associated smoother theoretical curve (dotted), correspond to solar wind protons. The remaining two curves correspond to 10× the cometary ion number density. (b) Plots of the theoretical and observed cometary ion (top curves) and solar wind (bottom curves) pressures.

loading rate of $Q = 10^{30}$ s^{-1}, a newborn cometary ion velocity of 1 km s^{-1}, and an ionization time $\tau_{ph} = 4.2 \times 10^{-7}$ s^{-1}. Normalizations were chosen to match the model to observations well upstream of the shock. The model depicted in Figure 2.3.8 assumes that 10% of the self-generated wave energy is available to heat the wind dissipatively. Zank et al. (1995) find that the model is not very sensitive to assumptions regarding the magnitude of the wave damping term in the vicinity of the shock. An important parameter that remains to be specified, and for which we have little guidance from observations, is the diffusive length scale κ/u_1. To fit the data and theoretical curves of Figure 2.3.8 required a value of $\kappa/u_1 = 2.97 \times 10^4$ km which corresponds to a scattering time of $\tau = 74.25$ s. For an oxygen ion gyrofrequency of $\Omega_0 = 2 \times 10^{-2}$ s^{-1} then $\tau = 1.5\Omega_0^{-1}$ s. Thus, the scattering time and the oxygen gyrofrequency are comparable, which seems reasonable for cometary ions that are scattered resonantly by the pickup-ion-excited cyclotron waves.

It is evident from Figure 2.3.8(a) that the observed solar wind number density compares well with theory. Even when using the smooth calculated curves, it is difficult to identify the shock location precisely. From the model curve for the solar wind density, the head of the shock is found at approximately 8.25×10^5 km from the cometary nucleus. Thereafter, the solar wind is abruptly but smoothly decelerated until about 7×10^5 km, which has been identified as the point immediately downstream of the shock. The theoretical steady state shock thickness for the quasi-parallel mass-loaded shock is therefore approximately 1.25×10^5 km. The theoretical compression ratio r is $r = 13.8/7.4 \approx 1.9$. Hence, using standard gasdynamics relations, $M_u = 1.6$ and $M_d = 0.7$, where $M_{u,d}$ refer to the theoretically inferred Mach numbers immediately upstream and downstream of the cometary bow shock. The data derived (Coates et al., 1990b, 1991) and model derived Mach numbers fall into the same 1.6–1.7 range.

Figure 2.3.8(b) illustrates that the cometary ion pressure can be modeled accurately, both upstream of and through the shock itself. The thermal solar wind pressure is modeled better ahead of the shock than through it where the theoretical values appear to be somewhat high. It is possible that Zank et al. (1994, 1995) have not included the electron pressure component adequately. The most striking result, as discussed by Coates et al. (1990b), is the complete dominance of the cometary ion pressure component at the shock. Ahead of the shock, the two pressures are comparable. The diffusive transport term $\kappa \cdot \nabla P_c$ can be identified with the spatial diffusion term in the kinetic transport equation for cometary ions (Gombosi et al., 1991) and it is this term that describes first-order Fermi energization in a nonuniform flow and at shocks. The Zank et al. model neglects any energization associated with second-order Fermi acceleration far upstream of the shock. From Figure 2.3.8(b), the energization of cometary ions at the shock (as expressed by their pressure) is due to a first-order Fermi mechanism entirely. Indeed, without such a mechanism, one would be unable to account for either the structure of the shock or the downstream cometary ion pressure. Clearly, first-order Fermi

acceleration of cometary ions at the cometary bow shock is important and may be responsible for the bulk energization of cometary ions at the shock, which, by implication, plays the key role in determining the structure of the shock itself.

The best agreement between observation and theory is found for the quasi-parallel bow shock. The models of Zank et al. (1995) appear to support the growing consensus that the inbound shock was not in equilibrium because of the interaction of the shock with local interplanetary disturbances. Nonetheless, their results suggest that the quasi-perpendicular P/Halley bow shock, like the parallel shock, is a cometary ion-modified shock, albeit in a nonequilibrium state. The overall structure and density profiles of the theoretical quasi-perpendicular shock agree well with observations, but the cometary ion pressure is less well modeled. This, Zank et al. (1995) suggest, is a consequence of the nonstationarity of the shock.

In concluding this section, the cometary bow shock appears to be an excellent example of an energetic-particle-mediated shock where the energetic population comprises less than 10% of the total number density. In addition, it offers an opportunity to study parallel and perpendicular examples of such shocks in situ and possibly even steady and unsteady examples. Thus, cometary shocks may provide valuable insight into the physics of other astrophysical shocks where a minority species (e.g., cosmic rays) might dominate energetically. One particularly topical example is the heliospheric termination shock.

3. The Kinetic Description

3.1. General considerations

The focal point of this section is to answer what is the microphysics of mass loading, especially: what is the microphysics of ion pickup including the subsequent wave generations and wave particle interactions, and how does the loaded flow develop? In the kinetic description the pickup is not instantaneous, different time scales are attached to the 'subprocesses'. Whereas the kinetic approach is appropriate to clarify many details, it is too complicated to discuss global flow properties. First let us consider the motion of a freshly ionized test particle in the solar wind frame of reference. If the neutral particle had a velocity $\mathbf{u}$ with respect to the Sun, then the newborn ion starts to gyrate around $\mathbf{B}$ with a velocity $u_\perp = |(\mathbf{u} - \mathbf{u}_{sw}) \times \mathbf{b}|$, and keeps moving along $\mathbf{B}$ with a velocity (called 'parallel velocity') $u_\parallel = (\mathbf{u} - \mathbf{u}_{sw})\mathbf{b}$; here $\mathbf{b}$ denotes the unit vector along $\mathbf{B}$. The cases when either $u_\parallel$ or $u_\perp$ is zero are special, we neglect them for the time being. When the plasma environment is stable for a long period of time relative to the gyroperiod $2\pi/\Omega = 2\pi mc/eB$, and the volume available is large relative to the Larmor radius, (this is generally the case in the cometary upstream region, or in the interplanetary space), the distribution of the ions in the velocity space forms a ring, moving along $\mathbf{B}$ with a fixed velocity, i.e. the distribution function has the form, as first given by Wu and Davidson (1972):

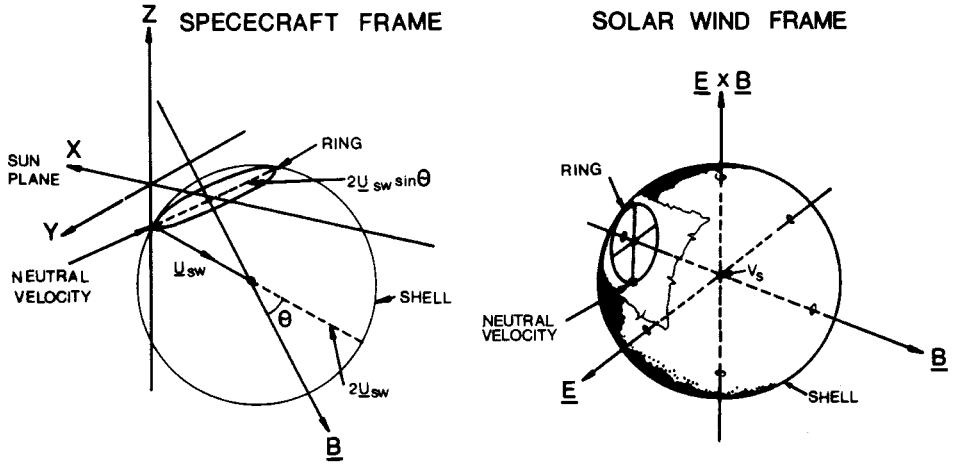

Figure 3.1.1. Two schematic views of the pickup process in velocity space. Newborn ions appear first as a ring then as a simple shell distribution left: in the spacecraft frame, right: in the solar wind frame.

$$f(\mathbf{v}) = \frac{1}{2\pi u_\perp}\delta(u_\perp - v_\perp)\delta(\mathbf{u}_\parallel - \mathbf{v}_\parallel)\ . \tag{3.1.140}$$

A distribution of such ions is then scattered in pitch angle, predominantly by transverse hydromagnetic waves, onto a sphere in velocity space of radius $|\mathbf{u} - \mathbf{u}_{sw} - V'_A\mathbf{b}|$ centered on $\mathbf{v} = V'_A\mathbf{b}$, here V'_A is the average phase wave velocity component parallel to **B**. If, for example, the waves are propagating outwards parallel to **B**, then $V'_A = V_\mathrm{A}$, the Alfvén speed. This sequence is known as the pickup of newborn ions by the solar wind.

This 'simple' picture is not always valid. Around terrestrial planets neither the time, nor the volume is adequate for a ring distribution to form, both the velocity and the magnetic field variations take place in a smaller scale. In the vicinity of Io the pickup ring immediately interacts with the complex plasma environment. In other cases, such as newborns at (the weak comet) P/Grigg–Skjellerup, the velocity distribution in the perpendicular plane depends on the gyrophase ϕ of the particles and thus the newborns will have nongyrotropic distributions (cf., Section 4.3.2). In all cases the recently ionized cometary particles have free energy in the solar wind frame and can feed a wide panoply of instabilities.

Several frames of reference are used in the literature to discuss the pickup process. In Figure 3.1.1, taken from Coates (1991), the ring and shell distribution functions are shown in the spacecraft frame and in the SWB frame (this is a solar wind frame with **B** parallel to the **z**-direction). If $V_{sw} \gg V_\mathrm{A}$ then the 'ring-beam' intersects the origin and the sphere intersects the origin and $\mathbf{v}' = 2\mathbf{V}_{sw}$. It is also practical to visualize the pickup ion motion in the configuration space, in the ecliptic (or planetary) frame of reference: the particle path is a cycloid with a guiding

centre drift velocity $(\mathbf{E} \times \mathbf{B})/B^2$, in the plane perpendicular to the magnetic field if the injection velocity is negligible.

3.2. WAVE EXCITATION

3.2.1. *Gyrotropic Particle Populations*

3.2.1.1. *On the wave generation mechanism.* In this section we discuss wave excitation processes in linear approximation (Davidson, 1983). The plasma we consider comprises of the passive solar wind (Maxwellian protons and electrons) with β around unity, and the newborn populations; the magnetic field can assume arbitrary orientations. The cometary species include also newborn electrons that are usually ignored in stability analyzes because their much lighter mass brings on fast pickup and ensuing integration in the solar wind (in the time scale of the ion gyromotion). In the planetary case the planetary electrons play an important role, cf., Section 4.3. The newborn ions are assumed to be either protons (arising from hydrogen ionization) or heavier water group ions. In the solar wind frame, the free energy available to feed wave growth thus lies in the newborn ions; however, the properties of the stimulated instabilities depend on the characteristics of both the newborn ions (densities, distributions) and the background medium (solar wind and IMF).

There are two basic types of instability resulting from solar wind interactions with newly implanted ions: (a) the electromagnetic ion cyclotron instability that propagates parallel to the magnetic field, (b) the electrostatic lower hybrid instability that propagates perpendicular to the magnetic field. The non-resonant firehose instability is a special case of propagation parallel to **B**.

The dispersion relation for (a) corresponding to circularly polarized electromagnetic waves has the form

$$D^{\pm}(k_{\parallel}, \omega) = 1 - \frac{c^2 k_{\parallel}^2}{\omega^2} + \sum_j \frac{\omega_{pj}^2}{\omega} \int \mathrm{d}^3\mathbf{v} \frac{v_{\perp}}{2} \frac{1}{\omega \pm \Omega_j - k_{\parallel} v_{\parallel}} Gf = 0 \,, \quad (3.2.141)$$

where

$$G = \frac{\partial}{\partial v_{\perp}} + \frac{k}{\omega} \left(v_{\perp} \frac{\partial}{\partial v_{\parallel}} - v_{\parallel} \frac{\partial}{\partial v_{\perp}} \right) \,. \quad (3.2.142)$$

The ion-cyclotron instability is driven by resonance between ions and waves

$$\omega - k_{\parallel} v_{\parallel} = \pm \Omega_i \,. \quad (3.2.143)$$

In Equation (3.2.143) ω and $k_{\parallel}$ are the frequency and the parallel components of the wave number, $v_{\parallel}$ is the ion parallel velocity, and Ω_i is the ion gyrofrequency. The upper sign (+) corresponds to the normal Doppler wave-particle resonance, i.e., the case when the wave is polarized in the direction of ion gyration; the lower sign (−) is the so-called anomalous Doppler resonance, i.e., when the wave polarization is opposite to the direction of ion gyration. This instability excites

Alfvén waves (Tsurutani and Smith, 1986); the fastest growth is for parallel wave propagation. For newborn ions, having approximately ring-beam distribution, the cyclotron resonance condition takes a particularly simple form. If $v \ll V_{sw}$, then $\omega - k_\parallel v_\parallel + \Omega = \omega + \mathbf{k}\mathbf{V}_{sw} + \Omega$. However, $\omega + \mathbf{k}\mathbf{V}_{sw}$ is simply the wave frequency in the inertial (~spacecraft) frame, ω_{sc}. The cyclotron resonance condition then becomes $\omega_{sc} = -\Omega$. The minus sign implies that the resonant waves are left-hand circularly polarized in the spacecraft frame.

The dispersion relation for electrostatic wave excitation, nearly perpendicular to **B**, for strongly magnetized electrons and unmagnetized ions has the form (Davidson, 1989) (for simplicity we give it for a two-component plasma):

$$D(\mathbf{k}, \omega) = 1 + \left(\frac{\omega_{pe}^2}{\Omega_e^2} - \frac{k_\parallel^2}{k^2} \frac{\omega_{pe}^2}{\omega^2} \right) + \frac{\omega_{pi}^2}{k^2} \int \mathrm{d}^3\mathbf{v} \frac{\mathbf{k} \dfrac{\partial f}{\partial \mathbf{v}}}{\omega - \mathbf{k}\mathbf{v}} = 0 \,. \tag{3.2.144}$$

This was further analyzed by (Rosenbluth and Post, 1965) for a loss cone instability driven by the Landau resonance

$$\omega = k_\perp v_\perp \tag{3.2.145}$$

between an ion ring distribution and the so-called lower hybrid waves, almost transversely polarized with respect to the magnetic field. These waves are indeed ion plasma oscillations developing on the background of strongly magnetized electrons with a dielectric constant $\epsilon_{\perp e} = 1 + (\omega_e^2/\Omega_e^2)$. If these waves are slightly oblique ($k_\parallel \neq 0$), then longitudinal electron Langmuir oscillations with a frequency $\Omega_e(k_\parallel/k)$ are also permitted, finally resulting in the following relationship for the lower hybrid wave frequency

$$\omega = \sqrt{\frac{\omega_p^2 + \omega_e^2 \dfrac{k_\parallel^2}{k^2}}{\epsilon_{\perp e}}} = \sqrt{\frac{\Omega_e^2 \left(\omega_p^2 + \omega_e^2 \dfrac{k_\parallel^2}{k^2} \right)}{\omega_e^2 + \Omega_e^2}} \tag{3.2.146}$$

In (3.2.146) the plasma frequencies are defined with $n = n_0$.

An important property of the lower hybrid waves is that their frequency, as determined by (3.2.146) is always between electron and proton gyrofrequencies $\Omega_p \ll \omega \ll \Omega_e$. Therefore, while ions and protons participating in the lower hybrid oscillations do not feel the presence of the magnetic field, and their interaction with waves is described by the unmagnetized Landau resonance conditions (3.2.145), electrons are strongly magnetized and experience Landau resonance

$$\omega = k_\parallel v_\parallel \tag{3.2.147}$$

only in their field aligned motion. Since $k_\parallel \ll k$, the lower hybrid waves can be in simultaneous Landau resonances with both plasma components (electrons and ions) transferring energy from slow ions to fast electrons and serving as a

powerful tool of electron energization accompanying the mass-loading process. This mechanism of electron energization will be discussed in more details later.

In order to clarify the role of the two instabilities in mass-loading process, it is necessary to compare the corresponding growth rates. The ion cyclotron instability for parallel propagating Alfvén waves, derived from (3.2.141) can be written as (e.g., Galeev et al., 1987):

$$\begin{aligned}\gamma_A &= -\frac{\mathrm{Im}D(\omega_r)}{\dfrac{\partial \mathrm{Re}D}{\partial \omega_r}} = \\ &= -\frac{\pi^2}{2}\frac{\omega_i^2\omega^2}{c^2k^2}\int \mathrm{d}v_\parallel\, \mathrm{d}v_\perp v_\perp^2 \delta(\omega \pm \Omega - k_\parallel v_\parallel) G f_i = \\ &= -\frac{\pi^2}{2}\frac{\omega_i^2\Omega_p^2}{\omega_p^2}\frac{k}{|k|\omega}\int_0^\infty \mathrm{d}v_\perp v_\perp^2 \frac{\partial f_i}{\partial \Theta}|_{v_\parallel = \frac{\mp\Omega_i}{k}} ,\end{aligned} \tag{3.2.148}$$

where f_i is the pickup ion distribution function, ω_r denotes the real part of the solution of the dispersion relation, the relation $\Omega_p^2/\omega_p^2 = V_\mathrm{A}^2/c^2$ was used, in G we assumed that $v \gg \omega/k$, and the derivative over pitch angle variable θ is calculated along the diffusion lines in the velocity space being close to the lines of the constant energy $v_\perp^2 + v_\parallel^2$ (see below). If the original ions were implanted into solar wind around $\theta = \alpha$ (here and further α is the angle between $\mathbf{u}_{sw}$ and $\mathbf{B}$), then $\partial f_1/\partial\theta > 0$ for $\theta < \alpha$, and the waves with $k < 0$ (propagating to the comet) are unstable due to the normal Doppler resonance. For $\theta > \alpha \partial f_1/\partial\theta$ is negative, waves with $k > 0$ are unstable due to anomalous Doppler resonance. The growth rate (3.2.149) can be estimated, using $ku_{sw} \sim \Omega_p$ as

$$\gamma_A \approx \frac{\pi n_i}{2n_0}\frac{u_{sw}\,\tan\alpha}{V_\mathrm{A}(\Delta\theta)^2}\Omega_p , \tag{3.2.149}$$

where $\Delta\theta$ is a typical width over pitch angle of the ion distribution function.

The growth rate of the electrostatic lower hybrid waves, similarly, can be written following Rosenbluth and Post (1965) as:

$$\gamma_{LH} = \frac{\pi}{2}\frac{\omega^2\omega_{LH}^2}{k^2}\frac{m_p}{n_p m_i}\int \mathrm{d}v_\perp^2 \frac{\dfrac{\partial g}{\partial v_\perp^2}}{\sqrt{k_\perp^2 v_\perp^2 - \omega^2}} , \tag{3.2.150}$$

here $g(v_\perp^2) = \pi \int \mathrm{d}v_\parallel f(v_\perp^2, v_\parallel)$. Whereas the ion-cyclotron instability is driven by an inversion over pitch angle for an implanted ion distribution, a loss cone instability of the lower hybrid waves is driven by an inversion of the ion ring distribution over $v_\perp$, that is there is an interval of $v_\perp > \omega/k$ for which $\partial f_i/\partial v_\perp > 0$.

Inserting the ring beam distribution function of the implanted ions, and approximating $k_\perp v_\perp \sim kV_{sw}$, because the radius of the ring is proportional to V_{sw}, the growth rate for the lower hybrid waves can be written as:

$$\gamma_{LH} = \frac{\pi}{2}\omega_{LH}\left(\frac{V_{\rm A}}{u_{sw}}\right)^3 \frac{m_p n_i}{m_i n_p}\,. \tag{3.2.151}$$

Then the ratio of two growth rates for Alfvén and lower hybrid waves is

$$\frac{\gamma_{LH}}{\gamma_A} \approx \frac{\omega_{LH} m_p}{\Omega_p m_i}\left(\frac{V_A}{u_{sw}}\right)^4\,. \tag{3.2.152}$$

Well upstream of cometary bow shock the deceleration of the solar wind induced by mass loading is not yet significant and the Alfvén speed, $V_{\rm A}$, is usually much smaller than the solar wind speed, u_{sw}, Accordingly, those linear instabilities whose growth rates are proportional to $(V_{\rm A}/u_{sw})^n$ (with $n > 1$), such as the electrostatic, almost perpendicular propagating lower hybrid waves, can be ignored in the far upstream phenomenology, whereas inside the comet's bow shock, or inside planetary magnetospheres they can contribute significantly to particle energization. Furthermore, having wave phase velocities much smaller than u_{sw} in the solar wind frame implies that the (Lorentz) force exerted on the newborns by the wave electric field is also much smaller than the one generated by the wave magnetic field; this means that pitch angle scattering of newborns shall be a faster process than (particle) energy diffusion, cf., Section 3.4 for details.

Numerous theoretical investigations of wave generation by gyrotropic cometary newborns have been reviewed by Lee (1989), Scarf (1989), Gary (1991), Brinca (1991), Roberts and Goldstein (1991), therefore here only the basic characteristics of the linear gyrotropic instabilities will be cursory highlighted. The role of nongyrotropy in cometary wave generation, first speculated upon by Lee (1989), and suggested by Glassmeier and Neubauer (1993) for the P/Grigg–Skjellerup case, is not yet fully understood.

In the general gyrotropic case, the velocity distribution of the newborn ions in the solar wind frame is a parallel-drifting ring (realistically with velocity spreads, 'temperatures', in the $\parallel$ and $\perp$ directions) that can evolve in extreme cases to a nondrifting ring ($\alpha = \pi/2$) or beam ($\alpha = 0$), where α is the angle between $\mathbf{B}$ and $\mathbf{u}_{sw}$. Even restricting the water group ions to one species, modification of the parameters that define the model medium yield a huge variety of instabilities covering parallel and oblique propagation, electrostatic, electromagnetic and hybrid waves, and resonant and fluid growth, as shown in the reviews cited above.

In order to place some perspective into this potential profusion, the observations of wave activity at comets (as reviewed, for example, in Glassmeier et al. (1997)) suggest that a sizeable part of the waves generated by newborn ions originated in resonant wave instabilities, and most of them seem to imply (nearly) parallel propagation (wave numbers closely aligned with the IMF). Notice, however, that there are both direct (wave spectral features at multiples of the newborn cyclotron frequency) and indirect (observation of wave steepening) evidences of oblique wave generation briefly mentioned below, and that the possible occurrence of fluid instabilities (mirror mode, firehose) cannot be excluded. The emphasis on parallel

resonant instabilities thus has these caveats; the interested readers can study the original investigations in other domains of (comet stimulated) instabilities. Wave modes involved in resonant parallel instabilities include

- longitudinal (wave electric field parallel to the wave number) electrostatic waves and
- transverse electromagnetic waves with (a) right-hand (magnetosonic, whistler, RH) or (b) left-hand (ion cyclotron, Alfvén, LH) circular polarization. As an example, in Figure 3.2.1 we show circularly polarized waves, LH polarized in the spacecraft frame, consistent with a RH wave that has been anomalously Doppler shifted to LH polarization by the solar wind convective flow.

The parallel electrostatic wave should (Landau) resonate with the newborns, that is its phase velocity should closely match the parallel velocity of the resonant particles and thus ensure that they sense a stationary wave electric field resulting in a strong wave-particle interaction. Albeit electrostatic wave activity has been reported (e.g. Gurnett et al. (1986) in the AMPTE ion releases and Richardson et al. (1989) at Giacobini–Zinner) and attempts at their interpretation have been made (e.g., Brinca et al. (1986) and Brinca et al. (1989)), most observational and theoretical results are focused on the electromagnetic modes. The particles that resonate with these circularly polarized waves have to feel also stationary wave fields; because a LH wave (fields rotating in the same sense as the perpendicular ion gyromotion) with a frequency ω close to the ion cyclotron frequency Ω_b would be heavily damped, resonance implies that the frequency Doppler shift due to the parallel drift of the particles, $kv_{b\|}$, has to match the difference between ω and Ω_b (bearing in mind the two possible types of polarization), that is, the resonance condition $\omega - kv_{b\|} = \Omega_b$ should be satisfied. For example, newborn ions can resonate with (i) LH waves with $\omega < \Omega_b$ if their parallel motion carries them against the wave (increasing the sensed frequency), (ii) LH waves with $\omega > \Omega_b$ if they move in the parallel direction with the wave (reducing the effective wave frequency), and (iii) with RH waves if they overtake the wave (phase velocity) in their parallel motion (thus sensing a LH, and not RH, wave circular polarization). Clearly, newborn ions are unable to resonate with counterstreaming RH waves and with costreaming RH waves whose phase velocity is larger than their parallel drift speed.

Two issues should be discussed in the context of resonant wave interaction: (i) identification of the potential wave dispersion domains where strong wave-particle interactions might occur and (ii) the determination of the energy balance of the interaction, namely whether the energy flows from the particles to the wave (meaning instability) or vice-versa (implying wave damping). These matters shall be addressed below.

3.2.1.2. *Wave-particle resonances and the Brillouin plane.* Analysis of the parallel wave-particle resonances requires the knowledge of the sign of the particle charge that determines the sense of rotation of the gyromotion, the dispersion and

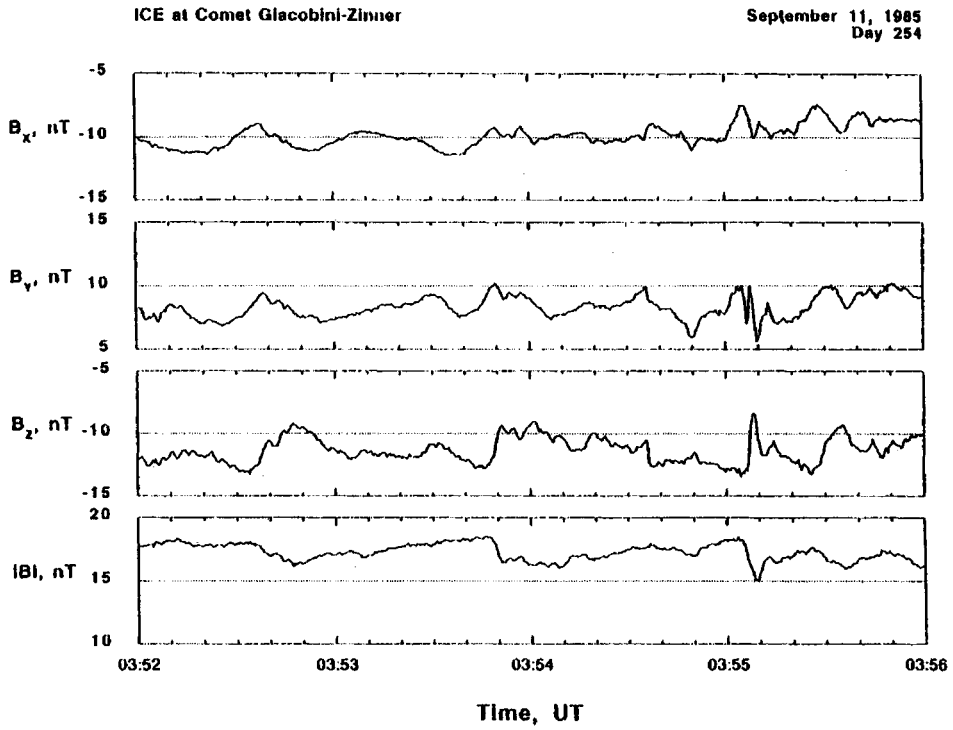

Figure 3.2.1. Waves observed at a distance of 4.5×10^5 km from the nucleus, and the corresponding hodograms for one of the waves (taken from Tsurutani et al., 1997).

polarization of the waves, and the parallel velocity of the particle (moving with, or against, the waves). This information can be integrated into a single plot that, adopting the parallel velocity of the particle beam as a reference direction, represents (i) the real dispersion of the costreaming (F), or counterstreaming (B) parallel modes of left (L) or right (R) hand circular polarization in the four quadrants (LF, LB, RF, RB) of the Brillouin (ω, k) plane, and (ii) the resonance condition $\omega - kv_{b\|} = \Omega_b$ for the newborn species under consideration.

Because the density of the cometary particles is usually much smaller than the density of the background (solar wind) plasma, it is a good approximation to plot the wave dispersion as being defined by the characteristics of the solar wind. Figures 3.2.2(a) and 3.2.2(b), taken from Brinca (1991) and repeated here for the reader's convenience, sketch the dispersion curves and the electron ($\Omega_e < 0$) and ion resonance lines for a hydrogen magnetoplasma (Figure 3.2.2(a) and a similar medium with an additional heavy ion (oxygen) species (Figure 3.2.2(b)). The intersections of the dispersion and resonance curves identify domains of strong wave-particle interaction that correspond to wave growth or damping, depending on the net energy flow between the particles and the waves. Simple considerations can then infer the energy flow direction for the resonant interactions with parallel

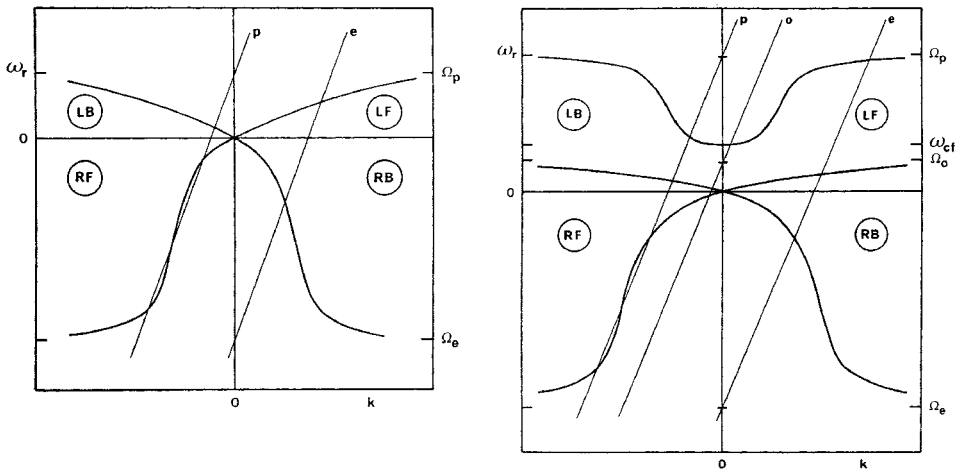

Figure 3.2.2. (a) *Left*: Sketch in the Brillouin plane of the real dispersion of parallel electromagnetic modes in a hydrogen magnetoplasma, and (straight lines) resonance conditions for protons (p), and electrons (e) with arbitrary common velocity. The quadrants correspond to (LF) left hand circularly polarized waves costreaming with respect to the particles, (LB) counterstreaming left-hand waves, (RF) costreaming right-hand waves, and (RB) counterstreaming right-hand waves. The intersection of the straight (cyclotron resonance) lines with the dispersion curves locate domains of strong wave-particle interactions. The particle masses (and, hence their cyclotron frequencies, Ω_s are fictitious to facilitate the depiction. (b) *Right*: Same as on the left, for hydrogen magnetoplasma with a heavy (oxygen) ion species and an additional resonance condition for the oxygen ion particles.

electromagnetic waves in the velocity space $(v_{b\perp}, v_{b\parallel})$ of the newborns using the relative positions of three families of curves: diffusion, isodensity, and constant kinetic energy (Gendrin, 1981).

Because the wave electric field is inductive in the given case, moving into the wave frame we get rid of this field. Sensing only magnetic field in the wave frame, the particles cannot change their kinetic energy in this frame. Hence, the diffusion curves in velocity space must satisfy $(v_{b\parallel} - \omega/k)^2 + v_{b\perp}^2 = \text{constant}$. The direction in which diffusion occurs is determined by the isodensity curves of the distribution function of the resonant species: it goes from higher density to lower density regions. The energy flow direction is then obtained from the position of the curves associated with the particles kinetic energy, $K_b = v_{b\parallel}^2 + v_{b\perp}^2 = \text{constant}$. If the diffusion motion leads to regions with higher (lower) K_b, the wave-particle resonance contributed to wave damping (growth). (This reasoning can also be adapted to more general circumstances where the wave electric field is not purely inductive, see Dungey (1997). In the wave frame particles may feel also an electrical potential together with the wave magnetic field, so the conserved particle's energy also includes the potential energy. For quasi-linear resonant effects increasing with time, where the potential is limited by the wave amplitude, the kinetic energy can still be taken to be conserved.)

3.2.1.3. *On the characteristics of gyrotropic instabilities.* The results of linear stability analysis for parallel propagation in the model medium described above for several α values and different cometary densities can be found, for example, in Brinca and Tsurutani (1988b). Each of the coexisting newborn ion (protons and water group) beams excites resonant instabilities without undue influence from the other species in most dispersion domains (for small α and sufficiently high newborn densities the (fluid) firehose instability is also stimulated). However, if the coexisting ions have similar masses, they tend to enhance strongly (weakly) nonresonant (cyclotron resonant) growth (Brinca and Tsurutani, 1989a).

The drifting proton rings generate stronger parallel wave growth than water group ions with similar (large) density, albeit, interestingly, observations of proton cyclotron waves are rare at comets, in contrast to water group cyclotron waves. As the newborn densities decrease, the hierarchy of growth rates is modified. Resonant instabilities in the RF quadrant of the Brillouin plane (ion beams overtaking the costreaming RH parallel mode) usually have the largest growth rates and α-range. Particle replenishment, viz. continuous generation of newborns, tends to favor nonresonant instabilities: ion recycling benefits fluid, but not kinetic, growth (McKean et al., 1992).

If the wave activity observed in spacecraft originated in resonant growth, it can occupy easily anticipated spectral positions. The resonance condition generalized to arbitrary directions of propagation reads $\omega - \mathbf{k}\mathbf{v}_{b\|} = n\Omega_b$, with $n = 1, 2, 3, \ldots$, meaning that the resonant ion must feel wave fields rotating in the proper (left, for positive newborns) sense with frequencies that are multiples of its cyclotron frequency. As it was pointed out first by Tsurutani and Smith (1986), because usually the newborns are almost at rest in the spacecraft frame, the resonant wave frequencies detected by the spacecraft instrumentation should also be centered at multiples of the particles cyclotron frequencies. And indeed, wave spectra during cometary encounters usually display maxima in the neighborhood of the water group ions cyclotron frequency (e.g., Glassmeier et al., 1997), although the missing of humps at the proton cyclotron frequency, or multiples thereof, is not yet fully understood (Glassmeier et al., 1989). However, caution is needed in using this result. Leaving aside obvious situations of cases of non-applicability, such as nonresonant instabilities and non negligible relative velocities between the particles and the spacecraft, there exist other situations when the observed resonant wave frequencies require careful interpretation. For example, resonant water group ions can excite modes with spacecraft frequencies of the order of the proton cyclotron frequency if the thermal spread in the newborn velocities is taken into consideration (Brinca and Tsurutani, 1988a); also, bearing in mind that oblique instabilities in the solar wind frame stimulate modes with a common frequency ω_r and wave vectors lying on a conical surface with semiaperture θ, apex and axis on and along the IMF, the corresponding spacecraft observation yields a frequency spectrum centered at $\omega_r + ku_{sw} \cos\alpha \cos\theta$ (the expected multiple of the appropriate cyclotron

frequency for resonant instabilities) but with a bandwidth of $2ku_{sw}|\sin\theta\ \sin\alpha|$ (despite assumedly being monochromatic in the solar wind frame).

Oblique ($\theta \neq 0$) propagation is necessary for the occurrence of mass density and wave magnetic field compression, and hence wave steepening. It may be excited by oblique instabilities or by refraction of originally parallel modes. The free energy of the newborns can stimulate waves whose growth is not always maximal at parallel propagation, and exploration of the waves vector plane discloses the frequent occurrence of islets of oblique (resonant and fluid) growth unrelated to the unstable parallel modes (Brinca and Tsurutani, 1989b). Observation of wave activity with spectra centered at multiples of the newborn cyclotron frequencies (Glassmeier et al., 1989) implies oblique propagation, and its basic features can be interpreted in terms of oblique cyclotron resonances (Brinca and Tsurutani, 1989c; Goldstein et al., 1990).

3.2.2. *Nongyrotropic Particle Populations.*
The model described in the previous subsection is now modified to allow for the existence of newborn species with nongyrotropic distributions. After a brief review of nongyrotropy in space plasmas, typical results of the stability of parallel and perpendicular propagation in homogeneous (stationary and time-varying) nongyrotropic environments are presented, showing that gyrophase bunched particles can enhance previously existing (gyrotropic) instabilities or destabilize an otherwise passive medium.

3.2.2.1. *Characterization of the nongyrotropic distributions.* A particle population is nongyrotropic when its unperturbed velocity distribution (by the wave fields) in the plane perpendicular to the ambient magnetic field depends on the gyrophase angle $\phi = \arctan(v_z/v_y)$. The first space observations that reported particles exhibiting gyrophase organization described nongyrotropic ions in the Earth's foreshock region (Eastman et al., 1981) and several Earth radii upstream (Gurgiolo et al., 1981). Since that time many other observations have confirmed the frequent occurrence of nongyrotropic populations in several regions of the geoplasma (upstream and downstream of the Earth's bow shock, solar wind, magnetosphere, magnetotail, space shuttle vicinity, AMPTE ion releases in the solar wind) and in cometary environments (Coates et al., 1993). Mechanisms capable of generating nongyrotropy include the gyrophase filtering associated with particle reflection and transmission at the Earth's bow shock (Burgess, 1987), nonlinear wave-particle interactions (Hoshino and Terasawa, 1985), inhomogeneous ionization (Neubauer et al., 1993), magnetized double layers (Borovsky, 1988), substorm dipolarization (Delcourt et al., 1997) and inhomogeneous current sheets (Motschmann and Glassmeier, 1997; Delcourt and Belmont, 1998). Nongyrotropic distributions were also observed at discontinuities of the interplanetary magnetic field (Astudillo et al., 1996).

Studies on the stability of homogeneous nongyrotropic magnetoplasmas with respect to parallel and perpendicular wave propagation used both analytic and simulation approaches; we shall use results from both. Introduction of gyrophase bunching in a species of a magnetoplasma generates coupling among the eigenmodes of gyrotropic propagation that can destabilize an otherwise thoroughly stable medium or, all the more, enhance previously existing gyrotropic instabilities. The free energy associated with gyrophase organization can thus feed distinct types of wave activity.

Adopting cylindrical coordinates in velocity space, the unperturbed (zero wave fields) distribution function of a nongyrotropic particle population identified by the subscript b, $F_{bo}(v_\perp, v_x, \mathbf{r}, t)$ in a collisionless magnetoplasma with (open phase space) or without (closed phase space) source (S) and loss (L) terms satisfies the Vlasov equation,

$$\left(\frac{\partial}{\partial t} + \mathbf{v}\frac{\partial}{\partial \mathbf{r}} - \Omega_b \frac{\partial}{\partial \phi}\right) F_{bo} = rhs \ , \tag{3.2.153}$$

where Ω_b is the signed angular cyclotron frequency of the nongyrotropic species, $rhs = 0$ (closed phase space) or $rhs = S_o - L_o$, and the subscript o identifies unperturbed terms.

In the case of nongyrotropic distribution the pressure tensor which has the general form

$$\Pi_{ij} = \int (v_i - \langle v_i \rangle)(v_j - \langle v_j \rangle) F_{bo} \, \mathrm{d}v^3 \tag{3.2.154}$$

gets nonvanishing off-diagonal elements. In a Cartesian frame with $v_y = v_\perp \cos \phi$ and $v_z = v_\perp \sin \phi$ the component

$$\Pi_{zy} = \int v_\perp^2 \cos \phi \sin \phi \, F_{bo}(v_\parallel, v_\perp, \phi) \, \mathrm{d}\phi \, v_\perp \, \mathrm{d}v_\perp \, \mathrm{d}v_\parallel \tag{3.2.155}$$

obviously does not vanish in general. The other off-diagonal elements behave in an analogous way. Surely these additional components of the pressure tensor bring about several new effects which have not been studied in detail up to now.

3.2.2.2. *Stationary and time-varying distributions.* Restricting the discussion to homogeneous media, it becomes clear that nongyrotropic unperturbed distributions (depending on ϕ) in closed phase spaces have to be time-varying rotating, $F_{bo} = F_{bo}(v_\perp, v_x, \phi + \Omega_b t)$. We shall use the acronym TNG to identify these distributions, where 'T' stands for 'time-varying' an 'NG' for 'non-gyrotropic'.

Consideration of open phase spaces (finite source and/or loss terms) leads to the inclusion of $S_o - L_o$ on the rhs of the above (transport) equation. Now F_{bo} can be both homogeneous in space and constant in time: $F_{bo}(v, v_x, \phi)$. We refer to these solutions as SNG distributions, where 'S' stands for 'stationary'. Other possibilities may also occur (viz. also homogeneous and time-varying nongyrotropies

in media with source and, or, loss terms); specific examples can be found in the literature (Motschmann et al., 1997).

As already stressed, TNG and SNG distributions do not constitute a complete set of nongyrotropic populations. For example, both in closed and open phase spaces it is possible to find inhomogeneous unperturbed distributions exhibiting gyrophase organization. The TNG and SNG models are adopted here for the sake of simplicity, with the further proviso that the gyrophase dependence is separable and (necessarily) 2π periodic, $F_{bo} = G_{bo}(v_\perp, v_x)\Phi(\Delta)$, where $\Delta = \phi + \Omega_b t (\Delta = \phi)$ for the TNG (SNG) model, with

$$\Phi(\Delta) = \sum_{n=-\infty}^{\infty} \Phi_n e^{-in\Delta}, \quad \Phi_n = \frac{1}{2\pi} \int_{2\pi} \Phi(\Delta) e^{in\Delta} \, \mathrm{d}\Delta \,, \tag{3.2.156}$$

$$\Phi \geq 0, \quad \Phi_n = (\Phi_{-n})^*, \quad \int_{2\pi} \Phi(\Delta) \, \mathrm{d}\Delta = 1 = 2\pi\phi_0 \,.$$

Extreme examples of gyrophase organization are the monochromatic (gyrophases share a common value), $\Phi_b(\Delta) = \Phi_m(\Delta) = \delta(\Delta)$, $\phi_n = (2\pi)^{-1}$, or dichromatic (gyrophases are evenly distributed between two values differing by π)

$$\Phi_b(\Delta) = \Phi_d(\Delta) = \tfrac{1}{2}[\delta(\Delta) + \delta(\Delta - \pi)] \,, \tag{3.2.157}$$

$\phi_n = (2\pi)^{-1} (n = 0, \pm 2, \pm 4, \ldots)$, $\phi_n = 0 (n = \pm 1, \pm 3, \ldots)$, distributions (defined in the interval $-\pi/2 < \Delta < 3\pi/2$, and 2π periodic elsewhere). Their use facilitates the following analysis, but the consequences of adopting more realistic distributions can usually be anticipated (Brinca and Romeiras, 1998).

3.2.2.3. *Balanced and unbalanced distributions.* The amplitude of the perpendicular current density, $J_{\perp b}$ carried by the nongyrotropic species is proportional to

$$\int_{2\pi} \mathrm{d}\phi e^{i\phi} \int_{-\infty}^{\infty} \mathrm{d}v_x \int_0^{\infty} \mathrm{d}v_\perp v_\perp^2 F_{bo} \,. \tag{3.2.158}$$

If the coefficients of the first harmonic of the Fourier expansion of the gyrophase distribution are zero, then this perpendicular current density is null ($J_{\perp b} = 0$) and we have a *balanced* nongyrotropic population (TNG^b or SNG^b); when the first harmonic is finite we have $J_{\perp b} \neq 0$ and the nongyrotropy is *unbalanced* (TNG^u or SNG^u).

3.2.2.4. *External and internal sources and sinks.* Standard linearization procedures assume that the relevant quantities in the system under consideration can be decomposed into unperturbed and first order components, $(\,) = (\,)_0 + (\,)_1$. In the

case of open phase spaces, and hence for stationary nongyrotropies, we assume that the source and sink mechanisms are *external* to the system if $S_1 = L_1 = 0$, that is $S = S_o$ and $L = L_o$: the characteristics of the sources and sinks do not affect the linear dispersion properties of the SNG plasma (SNG_e). The source and/or sink become *internal* when $S_1 \neq 0$ and/or $L_1 \neq 0$; these terms enter the linearized Vlasov equation of the nongyrotropic species and influence the dispersion of the SNG_i medium.

3.2.2.5. *Stability of parallel propagation.* Parallel propagation in TNG magnetoplasmas was first studied by Sudan (1965); more recently Brinca et al. (1992, 1993a, b) and Motschmann and Glassmeier (1993) pursued the analysis further. Cao et al. (1995), Motschmann et al. (1997) and Brinca and Romeiras (1998) investigated the parallel stability of the 'external' SNG model. In both media the existence of a nongyrotropic species can couple the characteristic modes of parallel propagation (+ and −: left- and right-hand circularly polarized transverse electromagnetic modes; ×: longitudinal electrostatic mode).

3.2.2.6. *Dispersion equation.* The dispersion and stability study is based on the standard linearization and the Laplace-in-time and Fourier-in-space transformation of the Maxwell and Vlasov equations. Our homogeneous magnetoplasma is neutral, parallel-current free (parallel drifts are not precluded) and, besides the nongyrotropic population, contains electrons (subscript e) and protons (subscript p) with unperturbed distribution functions $F_{ol}(v_\perp, v_x)$, $l = e,\ p$. Adoption of 'gyrating' coordinates,$(\ )_\pm = \frac{1}{2}[(\ )_y \pm i(\ )_z]$, yields the matrix wave equation

$$\begin{pmatrix} m_{++} & m_{+x} & m_{+-} \\ m_{x+} & m_{xx} & m_{x-} \\ m_{-+} & m_{-x} & m_{--} \end{pmatrix} \begin{pmatrix} \overline{E}_+(\overline{\omega}_1, k) \\ \overline{E}_x(\omega, k) \\ \overline{E}_-(\overline{\omega}_{-1}, k) \end{pmatrix} = 0\,, \tag{3.2.159}$$

with $\overline{\omega}_n = \omega + n\Omega_b (\overline{\omega}_n = \omega)$ for TNG (SNG) media; the matrix elements m_{rs} are defined in the Appendix. The spectral electric field components in the matrix wave equation for the TNG model are frequency shifted by $+\Omega_b$ with respect to results presented elsewhere (e.g., Brinca et al., 1993a) and similar shifts occur in the expressions of the matrix elements. Both versions are correct and the interpretation of the associated dispersion is given in Brinca (1996).

Whereas $m_{rr} = 0$ defines the dispersion equations associated with the eigenmodes of parallel gyrotropic propagation ($r = +$: left-hand circularly polarized electromagnetic waves; $r = \times$: longitudinal electrostatic waves; $r = -$: right-hand circularly polarized electromagnetic waves), the off-diagonal elements generate coupling among these eigenmodes. More exactly, m_{+-} and m_{-+} allow for the interaction between the two electromagnetic modes; $m_{+\times}$ $m_{\times+}$, $m_{\times-}$ and $m_{-\times}$ create coupling between the electrostatic and the electromagnetic modes. Bearing in mind that the matrix elements depend on the Fourier expansion coeffi-

cients of the gyrophase distribution (shown in the Appendix), it becomes clear that the interaction between electrostatic and electromagnetic modes requires the existence of the first harmonics in $F(\phi)$, that is, the unperturbed nongyrotropic species must carry a finite perpendicular current (unbalanced distributions), while the second harmonic coefficients mediate the interaction between the right- and left-hand electromagnetic modes. For parallel propagation, the linear dispersion of nongyrotropic environments is independent of the third, and higher harmonic terms of the gyrophase distribution.

The dispersion equation is obtained allowing for the occurrence of nontrivial solutions of the wave dispersion equation and is defined by $\det(mrs) = D(\omega, k) = 0$ where (initial value problem) k is real and $\omega = \omega_r + i\omega_i$.

3.2.2.7. *Illustrations.* The introduction of gyrophase bunching in a particle species generates coupling among the characteristic modes of parallel propagation; these interactions depend on the values of the first two Fourier coefficients of the gyrophase distribution. If other conditions are identical, a rough assessment of the intensity of the nongyrotropic effects can be made from the magnitudes of these Fourier coefficients. The coupling between the electrostatic and electromagnetic modes requires the existence of a finite first harmonic ($\phi_1 = (\phi_{-1})^* \neq 0$), whereas the left and right electromagnetic modes interact when there exists a second harmonic ($\phi_2 = (\phi_{-2})^* \neq 0$); the remaining harmonics of the gyrophase distribution do not influence the linear behavior of parallel propagation. If $\phi_1 = (\phi_{-1})^* \neq 0$ is satisfied, a finite unperturbed perpendicular current density, $\mathbf{J}_{bo} \neq 0$, exists that generates an additional magnetic field and thus, strictly speaking, invalidates the assumed unperturbed state. The (ir)relevance of this effect to the ensuing analysis is discussed elsewhere (Brinca and Romeiras, 1998).

Parallel propagation in TNG media were studied extensively. The appropriate dispersion relations were solved by Brinca et al. (1992, 1993a, b), and by Motschmann and Glassmeier, (1993); numerical simulations with hybrid codes were used by Brinca et al. (1993a), Motschmann et al. (1997); Brinca et al. (1993b) used kinetic codes. It was shown that time-varying gyrophase bunching can (i) enhance pre-existing gyrotropic instabilities and (ii) destabilize otherwise thoroughly passive magnetoplasmas, albeit the later effect (ii) requires the existence of unbalanced gyrophase organization ($\phi_1 = (\phi_{-1})^* \neq 0, \mathbf{J}_{bo} \neq 0$). The numerical simulations confirmed the linear characteristics determined by the dispersion equation (bearing in mind the frequency shifts caused by the time-varying unperturbed state and their appropriate interpretation (e.g., Brinca, 1996)), and proved that the nonlinear evolution of the system is accompanied by diffusion in velocity space that gradually smears the initial gyrophase bunching.

To date, investigations of parallel stability in SNG plasmas (Cao et al., 1995; Motschmann et al., 1997; Brinca and Romeiras, 1998; Motschmann and Glassmeier, 1998) have always (implicitly or explicitly) assumed that the necessary source and/or sink terms in the Vlasov equation for the distribution of the nongy-

rotropic species were 'external' to the system, that is, those terms did not influence the small perturbations of the medium and thus did not affect its linear dispersion. The study of the solutions of the $SNG_e^{b,u}$ parallel dispersion equation ('external' sources and sinks) has shown that the stationary gyrophase bunching can also, as in the TNG case, (i) enhance pre-existing gyrotropic instabilities and (ii) destabilize otherwise passive media. However, in the SNG gyrophase bunching, and in contrast to the TNG case, the destabilizing effect (ii) also occurs for balanced distributions ($SNG^b : \phi_1 = (\phi_{-1})^* = \mathbf{J}_{bo} = 0$). This means that the interaction between the two parallel electromagnetic modes (originated in $\phi_2 = (\phi_{-2})^* \neq 0$) can be sufficient to produce wave growth in an otherwise stable magnetoplasma; and as it was shown in Brinca and Romeiras (1998), stationary balanced gyrophase organization can stimulate nonoscillatory, pure growth (positive growth rates with zero real frequencies within a finite range of wave numbers). Simulation results for stationary gyrophase organization are not available: the eventual particle recycling necessary to generate SNG, seems to be too intense to provide reliable results.

3.2.2.8. *Stability of perpendicular propagation.* Even in gyrotropic media, the dispersion of oblique (perpendicular, in particular) propagation, when compared to the parallel case, is considerably more complicated. Introduction of species with gyrophase organization complicates the problem and yields such dispersion equations for nongyrotropic warm magnetoplasmas that, in general, can only be solved (numerically) with the adoption of extreme simplifications.

In contrast to the nongyrotropic parallel dispersion where only the first two harmonics of the gyrophase distribution influence the behavior of the system, at oblique propagation all the harmonics can appear in the dispersion equation. Whereas in parallel propagation there exist, at most, three interacting modes with (TNG) or without (SNG) frequency shifts in their spectral field components, oblique propagation in TNG plasmas couples all the frequency shifted ($\omega - n\Omega_b$) field components yielding a dispersion equation that results from the annulment of an infinite order determinant whose elements contain infinite sums. The study of TNG characteristics under these circumstances is easier via appropriate numerical simulations. Oblique dispersion in SNG plasmas is somewhat simpler, and as described below, even tractable analytically in special cases.

The difficulties arising from gyrophase bunching can be traced back to the transformed structure of the perturbed current density associated with the nongyrotropic species in oblique propagation, $\overline{\mathbf{J}}_b(\omega, \mathbf{k})$. In general, all the harmonics of the gyrophase distribution contribute to the elements of the generalized conductivity tensor; in SNG media this current density spectral component is stimulated by similar spectral components of the wave fields (allowing for a conductivity tensor of order 3), whereas for TNG plasmas $\overline{\mathbf{J}}_b(\omega, \mathbf{k})$ is obtained from the contributions of all the frequency shifted spectral components $(\omega - n\Omega_b, \mathbf{k})$ of the wave fields (generating an infinite order conductivity tensor).

When requiring a nontrivial solutions for the wave matrix equation to obtain the dispersion equation, the associated determinant is of order 3, as in gyrotropic oblique propagation for SNG plasmas, but it is of infinite order for the TNG case. In both situations the elements of the determinants depend, in general, on all the Fourier coefficients of the gyrophase distribution. Not surprisingly, studies of oblique (perpendicular, in particular) propagation in nongyrotropic magnetoplasmas are scarce.

3.2.2.9. *Illustrations.* Investigations of perpendicular propagation in TNG magnetoplasmas started with Eldridge (1970) who derived the electrostatic dispersion equation and discussed its solutions for very weak nongyrotropies. Brinca et al. (1994, 1998) reported (preliminary and comprehensive) results of the first numerical simulations of perpendicular propagation in TNG media. Cao et al. (1998) looked at oblique propagation in cold SNGe media, and Motschmann and Glassmeier (1998) discussed the oblique dispersion in SNG_e and TNG environments albeit presenting numerical (perpendicular propagation) solutions only for the cold plasma approximation. Romeiras and Brinca (1999) derived the dispersion equation satisfied by perpendicular electrostatic waves in SNG media (external sources and sinks) with monochromatic or dichromatic gyrophase distributions, and demonstrated analytically the occurrence of a strong instability (growth rates of the order of the real frequencies) for large wavelengths (as compared to the thermal gyroradii) below a certain critical value.

Motschmann and Glassmeier (1998) presented numerical solutions for perpendicular propagation in a magnetoplasma comprised of gyrotropic electrons and protons, and unbalanced gyrophase bunched alpha particles, in the cold plasma approximation. They obtained extraordinary-mode instabilities excited by the nongyrotropic species, though in the TNG model the parameters were outside of the range of validity of the adopted approximation. Perpendicular electrostatic propagation in SNG_e media with extreme (monochromatic or dichromatic) gyrophase organization satisfies a reasonably simple dispersion equation (Romeiras and Brinca, 1999), that demonstrates that the SNG free energy can feed strong perpendicular electrostatic wave growth; other instabilities may be found through the full numerical solution of the dispersion equation.

In general, numerical simulations are used to study perpendicular propagation in TNG environments (Brinca et al., 1994, 1998). In this approach the influence of more realistic gyrophase distributions can be easily assessed, and it provides information on the nonlinear evolution of the instabilities encountered. The results obtained for perpendicular electrostatic stability show that both balanced and unbalanced time-varying nongyrotropies can destabilize an otherwise passive medium. The application of an electromagnetic code shows that this electrostatic instability may coexist with the growth of the extraordinary mode (the ordinary mode was found to be stable). The evolution towards saturation is accompanied by a gradual gyrotropization of the initial gyrophase bunching; and the wave growth

is reasonably resilient with respect to the degree of gyrophase organization. It is interesting to note that for parallel propagation the TNG environment can only destabilize an otherwise passive media for unbalanced gyrophase distributions.

3.2.2.10. *Wave excitation by nongyrotropic distribution functions.* Usually isotropic particle distribution functions are stable and do not excite unstable waves. However, it should be noted that spherical shell distributions are unstable against cyclotron harmonic waves and oblique propagation. By breaking the isotropic symmetry the distribution may become unstable. A well-known example is the anisotropy instability occurring in a magnetoplasma if the perpendicular temperature exceeds the parallel temperature. A special case of the anisotropy instability is the ring instability as the ring corresponds to a high perpendicular kinetic temperature. This distribution contains excess energy which may drive unstable waves. Further symmetry breaking with respect to the gyrophase angle provides us a nongyrotropic distribution. It opens an additional source of excess energy and thus it may excite new wave modes. As already described open nongyrotropies are of major interest for the mass-loading by particle pickup.

Open nongyrotropies are studied by Motschmann and Glassmeier (1998a). An instability is found as for waves propagating parallel to the ambient magnetic field as for perpendicular propagating waves. Furtheron, for parallel propagation the nongyrotropy provides a coupling of the right-hand polarized (R mode), the left-hand polarized (L mode) and the electrostatic (P mode) modes which are decoupled in the corresponding gyrotropic plasma (Brinca et al., 1992). The nongyrotropy excites the R mode at frequencies well below the ion gyrofrequency where the R mode and the L mode have comparable phase velocities. Coupling with the P mode was studied by Brinca and Romeiras (1998). They found that by mode coupling the modified electrostatic P mode and the modified R mode may become unstable.

Now we compare the growth rates of the instabilities caused by a pure nongyrotropy (without any ring contribution) with that of a nongyrotropic distribution which includes a ring contribution. A pure nongyrotropy was studied by Motschmann and Glassmeier (1998a) and a nongyrotropic ring was discussed by Motschmann et al. (1997). In both cases a plasma of nongyrotropic ions (alpha particles in the examples discussed) and a stable proton-electron basic plasma is regarded. Whereas for the pure nongyrotropy any excess energy is contained only in the phase organization of the particles for the nongyrotropic ring a remarkable amount of excess energy is also contained in the anisotropy of the configuration. The corresponding growth rates are shown in Figures 3.2.3 and 3.2.4. Figure 3.2.3 depicts the dispersion and growth rate for a nongyrotropic distribution without the contribution of an anisotropy. The maximum growth rate is about $\gamma/\Omega_p = 0.03$. With the contribution of the anisotropy one gets $\gamma/\Omega_p = 0.18$ as depicted in Figure 3.2.4. Thus the anisotropy is obviously the stronger source of excess energy and the nongyrotropy contributes to the instability as an additional but weaker source.

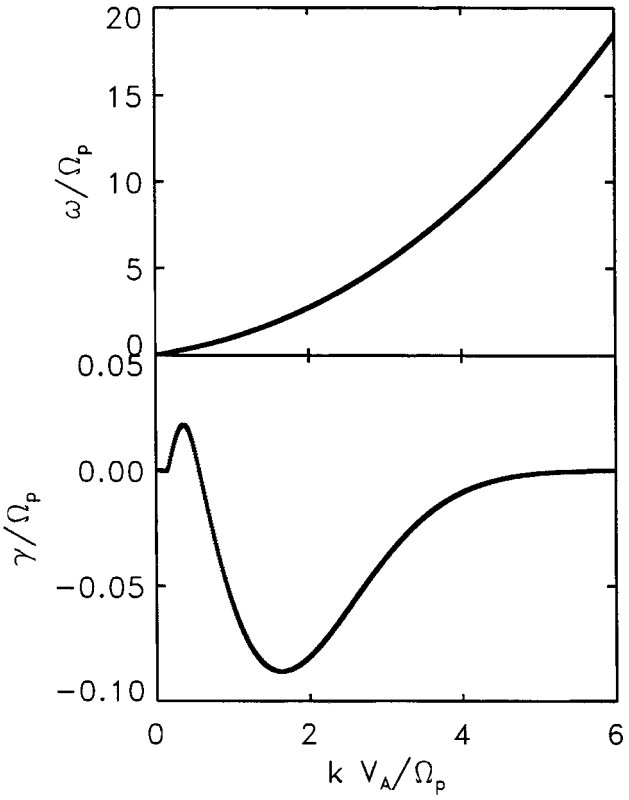

Figure 3.2.3. Dispersion and growth rate of the pure nongyrotropy instability for wave propagation parallel to the ambient magnetic field. The nongyrotropic alpha particle abundance is 50% of the particle density of the gyrotropic proton-electron background. The nongyrotropy drives the *R* mode unstable.

3.2.2.11. *Saturation of the nongyrotropic instability and phase space diffusion.* When nongyrotropic particles move in phase space for several gyration periods and interact with the excited waves they can take part at different diffusion processes. Finally they approach a thermal equilibrium. Nongyrotropic distributions diffuse especially along the phase angle ϕ. Of course there is also diffusion along the other phase space coordinates as pitch angle diffusion and energy diffusion. A suitable method to study these diffusion processes is a hybrid code simulation as applied by Motschmann et al. (1997) and Brinca et al. (1993). Here we continue the work of Motschmann et al. (1997) and study especially the time scales of the different diffusion mechanisms. We focus to nonstationary nongyrotropies (type (b)) assuming that the pickup of new particles is finished and the mass-loading is now dominated by the particle diffusion. The particle dynamics is studied by a $2\frac{1}{2}$-dimensional hybrid code.

Nongyrotropic ions (protons or alpha particles) and gyrotropic protons are described as particles and the electrons are modeled as neutralizing massless fluid.

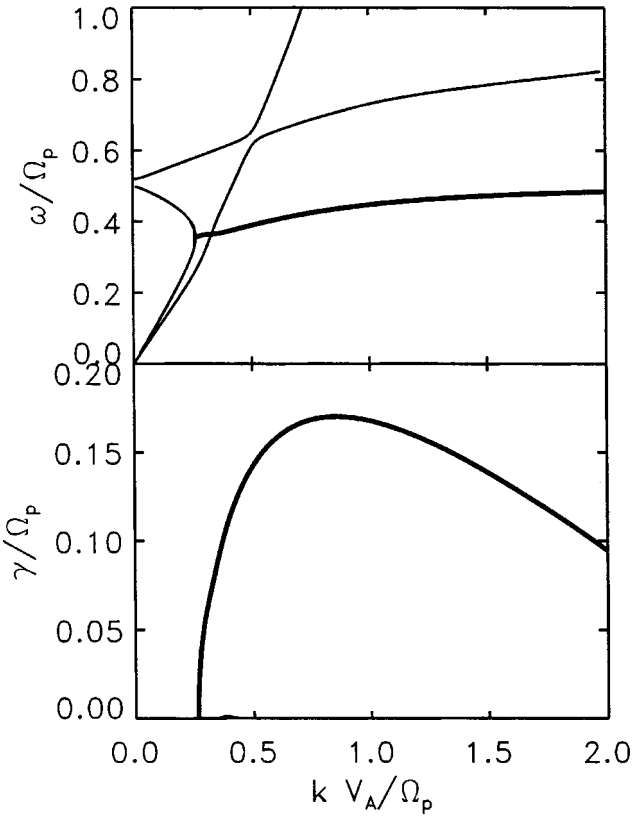

Figure 3.2.4. Dispersion and growth rate of a nongyrotropic ring instability. The nongyrotropic alpha particle abundance is 5% of the number density of the gyrotropic electron-proton background. The anisotropy instability drives the lower branch of the L mode (fat line) unstable. The nongyrotropy splits the crossing point of the upper branch of the L mode and the R mode.

We simulate two situations which are analogous to the examples discussed in the previous section. The first simulation is initialized by a pure nongyrotropic distribution whereas the second simulation is initialized by a nongyrotropic ring, that is there is additional anisotropy besides the nongyrotropy. Furtheron we assume symmetric distributions of the form $F_0(\phi) = F_0(\phi + \pi)$. This symmetry guarantees a vanishing current of zeroth order. The simulation results are shown in Figures 3.2.5 and 3.2.6. In Figure 3.2.5 the panels show the distribution function in a thin slice for three different simulation times. The ambient magnetic field is perpendicular to the plane. With respect to $v_\parallel$ and $v_\perp$ the distribution is initialized Maxwellian without any anisotropy. The simulation shows the diffusion of the particles along the gyrophase angle. As in this example the nongyrotropic particles are chosen as protons the thermalization is completed at about 24 gyrations. The diffusion is forced by the scattering of the particles at waves excited by the nongyrotropy instability. The waves propagate preferred perpendicular to the ambient magnetic

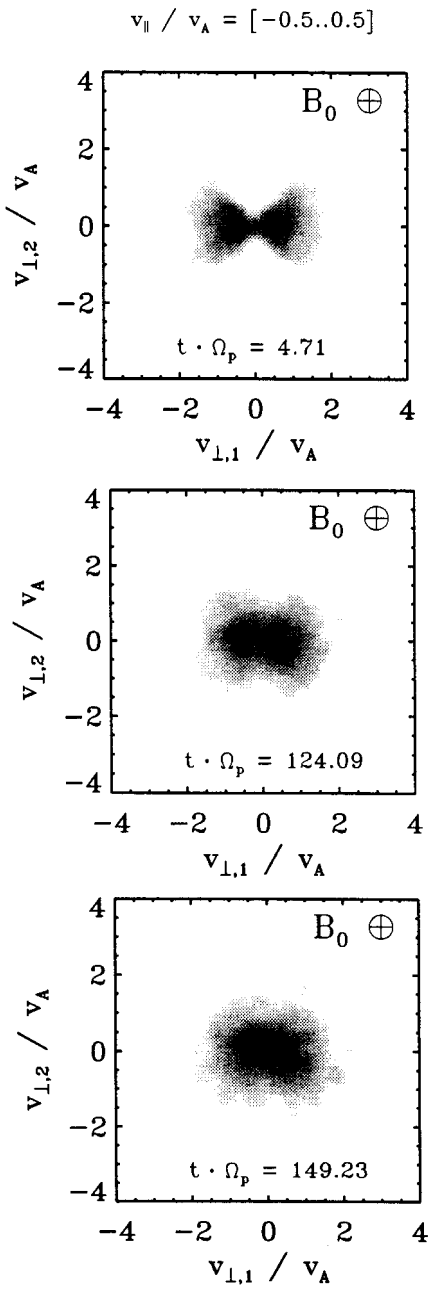

Figure 3.2.5. Evolution of the phase space density of a pure nongyrotropic distribution. The nongyrotropic proton abundance is 100% of the gyrotropic background. The particles diffuse into the undercrowded gyrophase sectors.

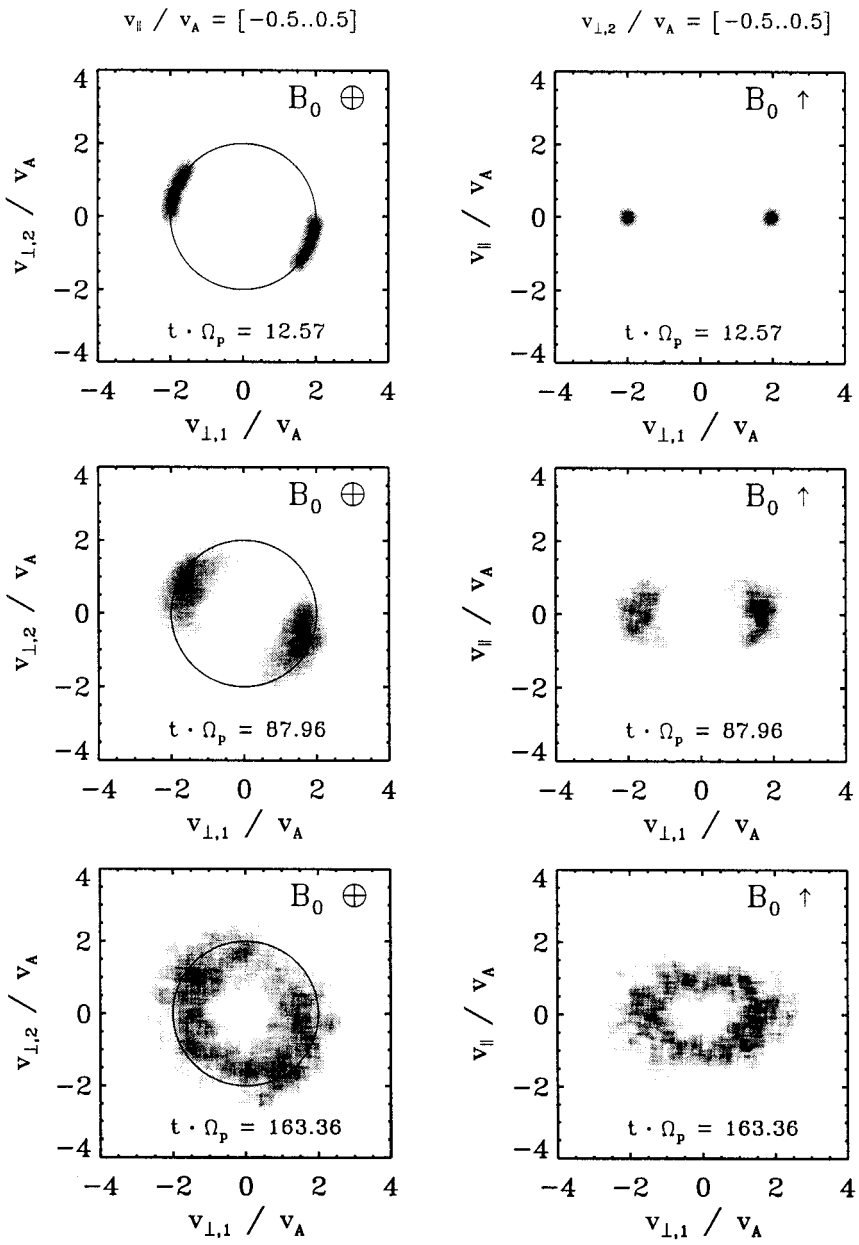

Figure 3.2.6. Evolution of the phase space density of a nongyrotropic ring distribution. The nongyrotropic alpha particle abundance is 20% of the number density of the gyrotropic proton-electron background. The particles diffuse along the phase angle and along the pitch angle. The final spherical configuration is stable within acceptable simulation times.

field. This is in agreement with the results of Motschmann and Glassmeier (1998a) who found that a pure nongyrotropy may excite the perpendicular extraordinary mode and their growth rate is somewhat bigger than the growth rate of the parallel excited R mode. Figure 3.2.6 shows the results when the simulation is initialized by a nongyrotropic ring. In this example alpha particles are used as nongyrotropic species. The left panels represent slices of the distribution perpendicular to the ambient magnetic field whereas the at the right panels the ambient magnetic field lays in the plane. The top panels are snapshots from the early beginning of the simulation. At simulation times shown in the bottom panels a quasistationary regime is reached. To the end of the simulation the alpha particles completed about 13 gyrations. The cuts at the left panels demonstrate the diffusion process along the gyrophase angle ϕ. Starting at $t = 0$ with an arc length of $\Delta\phi = 2\frac{\pi}{4}$ at the end a closed ring is reached and the nongyrotropy is completely vanished. The right panels demonstrate that the phase diffusion is accompanied by the pitch angle diffusion. The characteristic diffusion time is in the same order as for the phase angle diffusion. In this simulation the diffusion is forced by the scattering at parallel propagating waves. As studied by Motschmann et al. (1997) the anisotropy instability exceeds the nongyrotropy instability. Thus the unstable L mode is excited propagating with about Alfvén velocity v_A parallel and antiparallel with respect to $\mathbf{B}_0$. Therefore the lower right picture is not one sphere but the upper part of a sphere centered around $v_\parallel/v_A = -1$ and the lower part of a sphere centered around $v_\parallel/v_A = +1$. This quasistationary spherical configuration is stable at least for time scales we can cover by the simulation. Energy diffusion is rather small and the extension of the simulation up to complete thermalization was not reached.

3.3. PITCH-ANGLE SCATTERING OF PICKUP IONS

3.3.1. *The Pitch-Angle Transport*

The pitch-angle transport of the pickup ions is described by the quasilinear equation for diffusion in velocity space (Kennel and Engelmann, 1966; Lee, 1971; Lee and Ip, 1987)

$$\frac{\partial F}{\partial t} = \frac{\pi}{2}\left(\frac{q}{m}\right)^2 \frac{1}{v_\perp} \int_{-\infty}^{\infty} \mathrm{d}k \sum_{\rho=\pm} \left(\frac{V_A}{c}\right)^2 G_\rho [v_\perp \delta(\omega_\rho - k v_z + \\ + \Omega) I_\rho(k)(G_\rho F)] \,, \tag{3.3.160}$$

where $F(v_z, v_\perp, t)$ is the gyrotropic phase-space distribution function of the pickup ions, G is defined by Equation (3.2.142), $\mathbf{v}$ is velocity in the solar wind frame, $v_z = \mathbf{v} \cdot \mathbf{e}_B$, $\Omega = qB/mc$, q is the proton charge, m is ion mass, k is wavenumber, $\omega_\pm$ is the frequency of waves propagating in the ($\pm$)-direction along $\mathbf{e}_B$, and $I_\rho(k)$ is the wave intensity.

$$\langle |\delta \mathbf{B}|^2 \rangle = \sum_{\rho=\pm} \int \mathrm{d}k \; I_\rho(k) \,. \tag{3.3.161}$$

For our purposes it is adequate to take F to be spatially homogeneous. Equation (3.3.160) is based on the assumption that the waves have phase speed V_A (dispersion is neglected) and propagate parallel or antiparallel to $\mathbf{e}_B$, the unit vector parallel to $\mathbf{B}$. This assumption is supported by the fact that the instability addressed below maximizes for parallel propagation. Even when the assumption is not valid, Equation (3.3.160) provides an instructive model for pickup ion evolution. For parallel propagation the waves are circularly polarized: with $\mathbf{B} = B\mathbf{e}_B$, right-hand circularly polarized waves have $\omega >$, < 0 for $B >$, < 0, and left-hand circularly polarized waves have $\omega <$, > 0 for $B >$, < 0.

The operator G_ρ is proportional to the derivative with respect to pitch angle in the wave frame. Therefore, Equation (3.3.160) describes the effect on the ion distribution of pitch-angle scattering in the wave frame by a superposition of transverse hydromagnetic waves. Only waves which satisfy the cyclotron resonance condition, $\omega_\rho - kv_z + \Omega = 0$, affect the ions. This condition states that the (signed) wave frequency in the frame of the ion guiding center ($\mathbf{v} = v_z\mathbf{e}_B$) must equal the cyclotron frequency, so that the ion and wave rotate with the same frequency and the same sense. Within quasilinear theory, which is based on small wave amplitudes, nonresonant wave-particle interactions do not have a secular effect on the evolution of $F(v_z, v_\perp, t)$.

The waves responsible for scattering the pickup ions may be unstable, grow to larger amplitudes, and enhance the scattering rate. Observed properties of these nonlinear waves are discussed in Section 4.2. Under the same assumptions employed in the derivation of Equations (3.3.160) and (3.3.161), the growth rate of the Alfvén (left-hand) and fast (right-hand) waves is

$$\gamma_\rho = 2\pi^3 \left(\frac{V_A}{c}\right)^2 q^2 m^{-1} \int \mathrm{d}v_z \, \mathrm{d}v_\perp v_\perp^2 \delta(\omega_\rho - kv_z + \Omega)(G_\rho F) \qquad (3.3.162)$$

(this is equivalent to Equation (3.2.148)) where now F is normalized to satisfy $\int \mathrm{d}^3\mathbf{v}F = n$, the pickup ion number density. The instability is driven by ion anisotropy ($G_\rho F > 0$), and occurs only for cyclotron resonant waves. The instability rate decreases for oblique propagation (Hada et al., 1987; Gary et al., 1984; see Section 3.2). Thus, equation (3.3.162) for parallel propagation gives the maximum growth rate. This feature of the instability strengthens the assumption of parallel propagation, on which Equations (3.3.160) and (3.3.161) are based.

Under the further assumption that

$$v \gg |\frac{\omega_\rho}{k}|, \quad G_\rho \cong \left(\frac{v_\perp}{v}\right)\left(\frac{k}{\omega_\rho}\right)\frac{\partial}{\partial\mu} ,$$

where μ is the cosine of the ion pitch angle. Then in spherical coordinates in velocity space Equations (3.3.160) and (3.3.162) become

$$\frac{\partial F}{\partial t} = \frac{\pi}{2}\left(\frac{q}{mc}\right)^2 \frac{1}{v}\int \mathrm{d}k \sum_{+,-} \frac{\partial}{\partial\mu}\left[(1-\mu^2)\frac{1}{|\mu|}\delta\left(k - \frac{\Omega}{v\mu}\right) I_\pm(k)\frac{\partial F}{\partial\mu}\right] , \qquad (3.3.163)$$

$$\gamma_{\pm} = \pm 2\pi^3 V_{\rm A} \frac{q^2}{c^2} \frac{1}{|k|m} \int \mathrm{d}\mu \, \mathrm{d}v v^2 (1-\mu^2) \delta \left(\mu - \frac{\Omega}{kv} \right) \frac{\partial F}{\partial \mu} \, . \tag{3.3.164}$$

Equation (3.3.163) describes pitch-angle diffusion in the solar wind frame. Equation (3.3.164) describes instability if $\partial F/\partial \mu$ has the same sign as that of the wave propagation. Instability occurs if the pitch-angle scattering in the wave frame leads to loss of ion energy in the solar wind frame. Since in the latter frame the high density solar wind cannot gain or lose energy, the energy appears as increased wave intensity. If $\partial F/\partial \mu$ has the opposite sign as that of the wave propagation, the wave damps. From the cyclotron resonance condition, it can be seen that if the resonant ion and wave propagate in the same (opposite) direction along the magnetic field, then the wave is right (left) circularly polarized. Thus a beam distribution ($\partial F/\partial \mu$ and v_z of the same sign) excites right-circularly polarized waves, while a ring distribution ($\partial F/\partial \mu$ and v_z of opposite sign) excites left-circularly polarized waves. It must be noted, however, that the polarization signature is not as definitive for oblique propagation, for which the waves are elliptically polarized and can resonate with both helicities of ion trajectories. A hydromagnetic wave transition from circular to linear polarization occurs when $\Omega_p^2 \sin^4 \theta \sim 4\omega^2 \cos^2 \theta$ where Ω_p is the proton cyclotron frequency and θ is the angle between $\mathbf{k}$ and $\mathbf{e}_{\rm B}$ (Stix, 1992).

The wave intensity satisfies the wave kinetic equation

$$\frac{\partial I_{\pm}}{\partial t} = 2\gamma_{\pm} I_{\pm} \, . \tag{3.3.165}$$

Both Equations (3.3.163) and (3.3.165) may be integrated from $t = 0$ to $t \to \infty$. Noting that F evolves from a ring-beam with say $v = v_o$ and $\mu = \mu_o$, to near isotropy with $v = v_o$, the integrated equations may be manipulated to yield (Lee and Ip, 1987)

$$I_{\pm}^{\infty} = \tfrac{1}{2}[(C^2 + 4I_+^0 I_-^0)^{1/2} \pm C] \, , \tag{3.3.166}$$

$$C = I_+^0 - I_-^0 + 2\pi V_{\rm A} \frac{1}{k^2} |\Omega| mn \left(\frac{\Omega}{kv} - \left[2S \left(\frac{\Omega}{kv} - \mu_0 \right) - 1 \right] \right) \, , \tag{3.3.167}$$

where $I_{\pm}^0(k)$ are the initial wave intensities, $I_{\pm}^{\infty}(k)$ are the time asymptotic wave intensities, and $S(x)$ is the standard step function. The wave intensity spectra described by Equation (3.3.166) of course require for their validity that the timescale for pitch-angle scattering is small compared to the timescale of interest, say, for variations in the ionization rate. This is true for wave excitation by interstellar pickup ions, but not for cometary pickup ions.

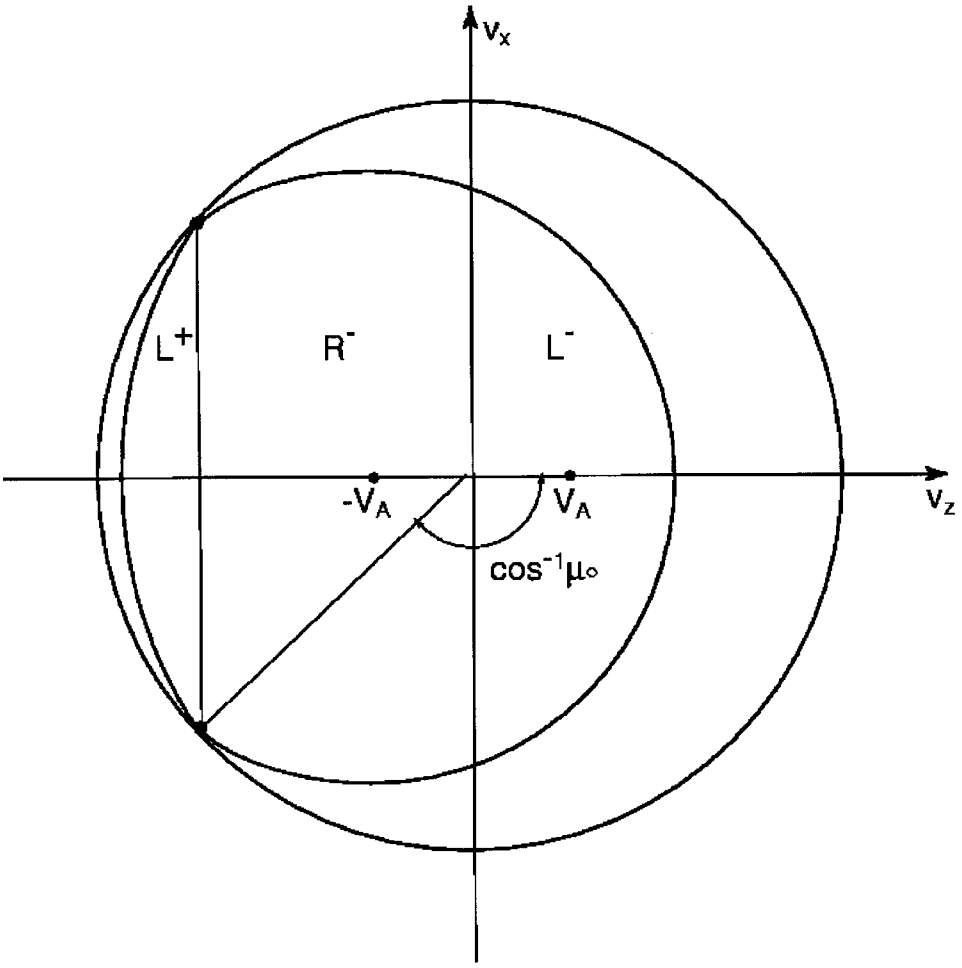

Figure 3.3.1. The pickup ion bispherical distribution (thick solid line) in the frame of the solar wind. The initial ring beam (solid dots) and the spherical shell centered on v = 0 are also shown. The polarization and wave propagation direction of waves resonant with the ions in the three ranges $\mu < \mu_0$, $\mu_0 < \mu < 0$, and $\mu > 0$ are also shown.

3.3.2. *The Bispherical Distribution*

Although for the purpose of calculating the wave intensities in Equations (3.3.166) and (3.3.167) F is assumed to evolve toward isotropy, the time-asymptotic distribution exhibits anisotropy of order $V_A/v \ll 1$. In the special case that the initial wave intensities are small ($I_\pm^0 \ll |C|$), the unstable waves dominate the wave intensity. Since the condition for instability is $(\omega/k)(\partial F/\partial\mu) > 0$, ions with $\mu > \mu_0$ scatter toward uniform density on a shall centered on $\mathbf{v} = -V_A\mathbf{e}_B$, and ions with $\mu < \mu_0$ scatter toward uniform density on a shell centered on $\mathbf{v} = V_A\mathbf{e}_B$. The resulting time-asymptotic distribution shown in Figure 3.3.1 is called a bispherical distribution (Galeev and Sagdeev, 1988; Rowlands et al., 1966). The polarizations

and propagation directions (in the solar wind frame) of the waves resonant with the ions in each domain of $\mu(\mu < \mu_0, \mu_0 < \mu < 0, \mu > 0)$ are shown. Also shown is the spherical distribution which would obtain if the ions scattered from the initial ring-beam to isotropy in the frame of the solar wind. The difference in the ion kinetic energy between the spherical and the bispherical distributions appears as wave energy, with equal amounts in magnetic fluctuations, specified by Equation (3.3.166), and in kinetic plasma oscillations. Based on the shape of the bispherical distribution and respecting the cyclotron resonance condition, Huddleston and Johnstone (1992) and Williams and Zank (1994) also calculated wave intensity (3.3.166) and (3.3.167) in the case $I_{\pm}^{0} \to 0$.

If the ambient wave intensities are negligible, the bispherical distribution is the evolutionary endpoint. There is then only one wave resonant with a given ion v_z. For that wave $G_\rho F = 0$, and, according to Equation (3.3.162), $\gamma = 0$ (marginal stability). If the ambient wave intensities are not small, then the time-asymptotic state involves two waves resonant with each v_z. Stochastic acceleration, or energy diffusion, will then occur on a slower timescale (see Section 3.4.) and the ions will generally gain energy at the expense of the waves (Bogdan et al., 1991). For $v \gg V_A$ the bispherical distribution is approximate to an isotropic shell distribution, which was shown by Freund and Wu (1988) to be stable to parallel-propagating waves. However, an isotropic shell is weakly unstable to waves propagating oblique to the magnetic field (Wu and Yoon, 1990; Isenberg, 1993). Presumably this weak instability allows the wave intensity to increase if diffusion in energy initially fills in the shell distribution and leads to a loss of ion energy. Once the shell is partially filled the waves decay (Isenberg, 1993), in response to stochastic acceleration of the pickup ions to higher energies.

Figure 3.2.6 is not completely correct. From the cyclotron resonance condition it is clear that for $v_z \sim V_A$, $\omega \sim \Omega$. If the pickup ions are protons then the waves are dispersive with $\omega/k \neq V_A$. Figure 3.3.2 shows the cold plasma dispersion relations for $B > 0$ and wave propagation parallel to **B**, with the four branches marked with the wave polarization and propagation direction. For the Alfvén (L) branch $\omega \to -\Omega_p$ as $|k| \to \infty$; for $|\omega| \ll \Omega_p$ the modes satisfy $\omega = \pm k V_A$. The resonant waves follow from the cyclotron resonance condition and are specified by the intersection of $\omega(k)$ and $kv_z - \Omega_p$, shown for two values of v_z in Figure 3.3.2. For $|v_z| \gg V_A$ there are two points of intersection representing two resonant waves, one of which according to Equation (3.3.164) is always unstable unless $\partial F/\partial \mu \cong 0$. For $|v_z| <\sim V_A$, however, there is only one intersection. This may imply that there is no unstable mode, or that there is a resonance 'gap' with no resonant mode (if, for example, waves only propagate in the z-direction and $|v_z| \sim V_A$). Furthermore, the Alfvén (L) waves with $\omega \sim -\Omega_p$ probably have low intensity (indicated by the dotted extension of the Alfvén branch as $|k| \to \infty$) due to their dissipation by thermal protons. This feature almost ensures the existence of a 'gap' for pickup protons with $v_z \cong 0$ (Rowlands et al., 1966; Dusenbery and Hollweg, 1981). Dispersion therefore implies that the bispherical distribution for

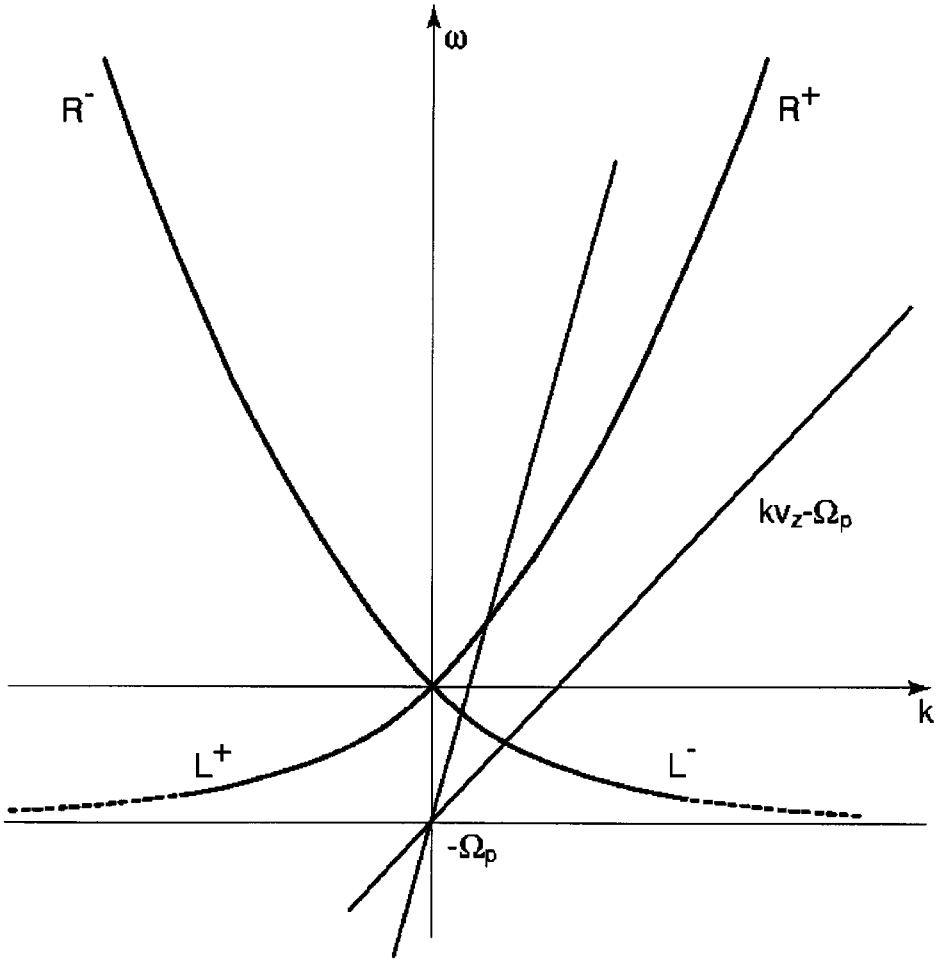

Figure 3.3.2. The dispersion relations for the four transverse low-frequency waves for wave propagation parallel to **B**, B $>$ 0, and a cold thermal plasma. The four curves are specified by their polarization and propagation direction in the solar wind frame. Cyclotron resonance occurs at the intersection of $\omega(k)$ and $kv_z - \Omega_\rho$, shown schematically for two values of v_z.

pickup protons is not actually composed of spherical portions and in general has resonance 'gaps' (Isenberg and Lee, 1996). Dispersion can therefore modify the excited wave intensity. These effects are smaller for more massive pickup ions with $\Omega < \Omega_p$. Scattering in pitch angle through a resonance 'gap' is not possible within quasilinear theory. Nonlinear corrections to quasilinear theory may allow transport through the 'gap'. Nevertheless, a 'gap' should lead to increased values for the pickup ion scattering mean free path parallel to the magnetic field.

3.3.3. *Remarks*

3.3.3.1. *Interstellar pickup ions.* Interstellar pickup ions are observed to have spherical shell distributions as anticipated by pitch-angle scattering on hydromagnetic turbulence in the solar wind. However, within the inner heliosphere the shell is often not uniformly populated, presumably due to scattering rates reduced from those anticipated from straightforward application of Equation (3.3.163). The scattering mean free paths parallel to **B** are inferred from *Ulysses* (Fisk et al., 1997) and AMPTE (Möbius et al., 1998) observations to be ∼1 AU. The incomplete scattering may be due to the resonance 'gap' which occurs for outward-propagating field-aligned waves as described above. In addition the spherical shell distribution is partially filled in by adiabatic deceleration of the pickup ions, an effect not addressed here. The interpretation of the interstellar pickup ion distribution is presented in Section 4.4.

The isotropization of the interstellar pickup ions should excite hydromagnetic waves as described by Equations (3.3.166) and (3.3.167). Lee and Ip (1987) calculate substantial enhancements of solar wind turbulence at about the proton gyrofrequency and beyond about 5 AU due to the isotropization of pickup hydrogen. These enhancements have not been observed at the anticipated levels. However, Murphy et al. (1995) document sporadic enhancements at about the local proton cyclotron frequency, which they attribute to interstellar pickup hydrogen. Certainly several effects would reduce the intensity level predicted by Lee and Ip (1987) (Equations (3.3.166) and (3.3.167)): incomplete pitch angle scattering, dispersion, and the fact that the initial ring-beam is broadened by fluctuations in the direction of **B** at the time of ionization (Isenberg, 1996). However, nonlinear wave coupling may also contribute to reducing wave anisotropy in wavevector space, which in turn reduces the 'free-energy' in the initial pickup ion ring-beam since the ions pitch-angle scatter in an average wave frame which is more nearly equivalent to the plasma frame with little change in energy.

3.3.3.2. *Cometary pickup ions.* In spite of the smaller spatial and temporal scales at comets, cometary pickup ions are scattered in pitch angle and excite hydromagnetic waves. At the smaller comets, P/Giacobini–Zinner and P/Grigg–Skjellerup, pitch-angle scattering is not as effective and the ion distributions retain their ring-beam structure. At Comet P/Halley, however, those ions ionized far from the comet are scattered to near isotropy within $\sim 10^6$ km of the cometary bow shock (Coates et al., 1990). At all comets very large-amplitude waves/turbulence are observed to be excited by the cometary water group ions. At the smaller comets with little pitch-angle scattering, the waves are observed as expected with $\omega_{sc} \sim -\Omega_{\mathrm{OH}}$ (left-hand circular polarization), where Ω_{OH} is the cyclotron frequency of H_2O^+, OH^+ or O^+. Far from Comet P/Halley the waves are also left-hand circularly polarized with $\omega_{sc} \sim -\Omega_{OH}$. However, closer to the comet where the pickup ions are nearly isotropic, the transverse field fluctuations are more turbulent although a signature at the cyclotron frequency remains [Glassmeier et al., 1989]. The fluctuation power

spectrum is proportional to k^{-2} at large k, as anticipated from Equation (3.3.167) (if $I_{\pm} \gg I_{\pm}^{0}$, then $I \propto C \propto k^{-2}$). The k^{-2} dependence was first predicted by Sagdeev et al. (1986) in a calculation of the spatial evolution of the waves and ions from far upstream of the comet to the bow shock, which is equivalent to the temporal evolution presented here. In view of the dominance of the unstable waves and the nearly isotropic ion distribution within $\sim 10^6$ km of P/Halley's bow shock, the ion distribution is expected to be bispherical. Coates et al. (1990) showed that the bulk flow velocity of the pickup ion distribution is consistent with that of a bispherical distribution. Huddleston and Johnstone (1992) calculated the expected wave intensity associated with a bispherical ion distribution (essentially Equations (3.3.166) and (3.3.167) with $I_{\pm}^{0} \to 0$) and found excellent agreement with the observed wave power spectra.

3.4. Pitch angle diffusion and ion energization

3.4.1. *General Considerations*

The driver for the ion cyclotron instability is an inversion of pitch angle distribution of the resonant ions. The nonlinear evolution of the instability results, first of all, in a pitch angle ion diffusion, which restricts the driver and stabilizes the instability. Diffusion lines of the resonant ions at $v_{\perp}$, $v_{\parallel}$ plane can be easily calculated using a 'quantum mechanical' approach described below. In the plane perpendicular to the magnetic field ions can be considered as 'oscillators' with an eigen-frequency Ω_i and quantized energy levels $\epsilon_m = (h/2\pi)\Omega_i(m + \frac{1}{2})$, here h is a Planck constant, and m is an integer.

Therefore, a change of the transverse particle energy is equal to $(h/2\pi)n\Omega_i$, $n = \pm 1$. Along the field lines ions are participating in a free motion and the radiation of a wave quantum ω, k changes the momentum with $\Delta p_{\parallel} = (h/2\pi)k$ and the change of the longitudinal energy is $\Delta\epsilon_{\parallel} = (h/2\pi)kv_{\parallel}$. Therefore, the relative changes of the transverse and longitudinal energy along the diffusion line can be written as:

$$\frac{mv_{\perp}\Delta v_{\perp}}{mv_{\parallel}\Delta v_{\parallel}} = \frac{n\Omega_i}{kv_{\parallel}} \,. \tag{3.4.168}$$

At the same time, energy conservation law in wave quantum radiation has a form

$$\omega = kv_{\parallel} + n\Omega_i \tag{3.4.169}$$

(the energy lost by the resonant particle is transferred to a wave quantum). Combining Equation (3.4.168) and (3.4.169) it is possible to write the following equation for the diffusion lines:

$$m(v_{\perp}\Delta v_{\perp} + v_{\parallel}\Delta v_{\parallel}) - m\frac{\omega}{k}\Delta v_{\parallel} = 0 \,. \tag{3.4.170}$$

In (3.4.169) $n = 1$ corresponds to normal Doppler resonance. In this case the radiation of a wave quantum means that a particle fall to lower energy level; the

energy source for wave radiation is in the transverse particle motion. The value $n = -1$ corresponds to anomalous Doppler resonance. In that case wave radiation is accompanied by the excitation of an upper energy level of the transverse motion and the free energy source for that type of radiation is in a field aligned particle motion. Substituting the phase velocity of the Alfvén waves, $\omega/k = \pm V_A$, into Equation (3.4.170), and integrating it, we can write the following equation for the diffusion lines:

$$\frac{m}{2}v_\perp^2 + \frac{m}{2}(v_\parallel \mp V_A)^2 = \text{constant} , \tag{3.4.171}$$

where the upper sign correspond to waves with $k > 0$ (sunward propagation), and the lower sign corresponds to $k < 0$ (propagation towards the comet). This result has an obvious physical interpretation. Since for Alfvén waves the electric field is of inductive nature, it is equal to zero in the wave reference frame, and, in accordance with Equation (3.4.171), particle energy is conserved in this frame of reference. Particle diffusion lines are sketched in Figure 3.4.1. For $\theta < \alpha$, the source for wave excitation and particle diffusion is in the transverse particle motion. The instability is normal Doppler resonance, $v_\parallel \approx -\Omega_i/k$, since $\omega \ll \Omega_i$. Excited waves have $k < 0$, and the diffusion lines are determined by Equation (3.4.171) with the lower sign inside the brackets. For $\theta > \alpha$ (region II in Figure 3.4.1) the free energy source is in the longitudinal particle motion, and wave radiation is accompanied by the increase of particle transverse energy. The instability is anomalous Doppler resonance, $v_\parallel \approx \Omega_i/k$, waves are excited with $k > 0$, and the diffusion lines are determined by Equation (3.4.171) with upper sign in the brackets. Finally, for $\theta > \pi/2$ (region III in Figure 3.4.1), the source of energy is again in the transverse motion, the driver instability is normal Doppler resonance, $v_\parallel \approx -\omega_{ci}/k$. However, now the resonant particle velocity is negative, waves are excited with $k > 0$, and the diffusion lines remain the same as in a region II. A combination of pitch angle diffusion along the two diffusion lines described above leads to the so-called bispherical distribution (Galeev et al., 1987; Galeev and Sagdeev, 1988; Lee, 1989).

3.4.2. *Acceleration by MHD Waves*

Particle acceleration by MHD turbulence is equivalent to the so-called stochastic or second order Fermi acceleration. The change of energy of a particle moving along the diffusion line corresponding to bispherical distribution is small, $\sim V_A/u$, and there is no energy diffusion accompanying the evolution of this distribution. The only possibility to obtain energy diffusion in the turbulent regime is to have an interval of pitch angles, in which simultaneous resonance takes place with waves having different phase velocities ω/k. In this case, a resonant particle has the possibility to drift along the intersecting diffusion lines. This process can be described as diffusion in the magnitude of the velocity.

Next we derive the appropriate diffusion coefficient. Instead of analyzing Equation (3.3.160), we follow a simple and straightforward method, starting from the

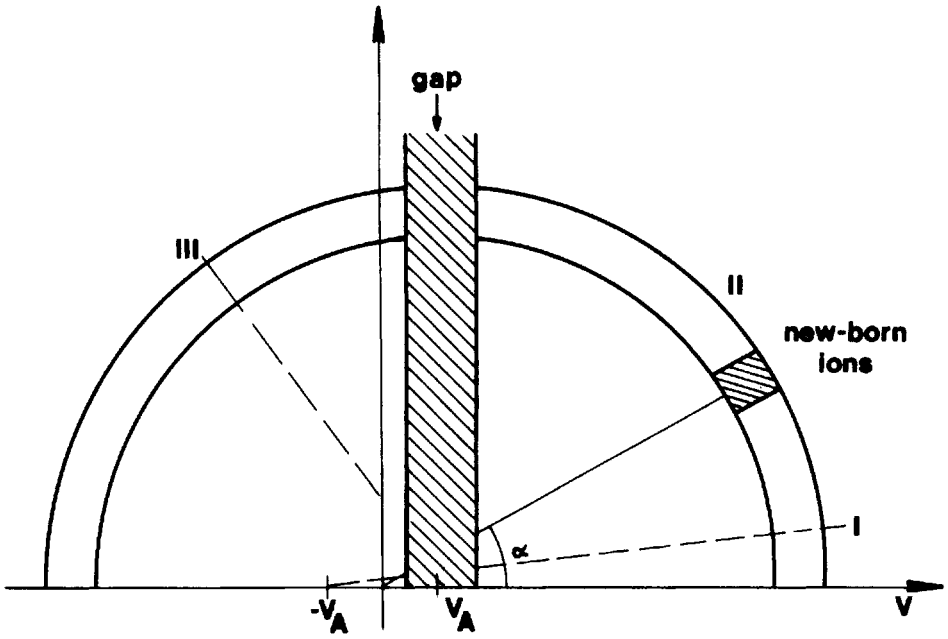

Figure 3.4.1. Diffusion lines on $v_\perp$, $v_\parallel$ plane.

equation of the diffusion line (3.4.171); because it is sufficient to calculate the diffusion coefficient along these lines. The diffusion develops in the parallel component of the particle velocity $v_\parallel$, and it is driven by the corresponding component of the Lorentz-force $F_\parallel = (e/c\alpha(v_x B_y - v_y B_x)$, where $v_x = v_\perp \cos\theta$, $v_y = v_\perp \sin\theta$. The magnetic field components can be expressed by left and right hand circularly polarized fields $B^\pm$, that are superpositions of wave harmonics: $B^\pm = \sum B_k^\pm e^{i(kz-\omega t)}$. Substituting these back into the Lorentz-force equation, we have

$$F_\parallel = \frac{e}{2c} v_\perp \sum_k B_k^\pm e^{i(kz-\omega t\pm\theta)} \,. \tag{3.4.172}$$

The diffusion coefficient for $v_\parallel$ along the diffusion lines can be written as

$$D_{v_\parallel v_\parallel} = \frac{\mathrm{d}}{\mathrm{d}t}\langle v_\parallel^2\rangle = \left\langle \frac{F_\parallel}{m} v_\parallel \right\rangle \,. \tag{3.4.173}$$

Brackets denote averaging over wave phase. From the equation of force (3.4.172) using the non-relativistic Newton equation we obtain

$$v_\parallel = \frac{e}{2c} v_\perp \sum_k B_k^\pm \frac{e^{i(kz-\omega t\pm\theta)}}{i(kv_\parallel - \omega \pm \Omega_i)} \,. \tag{3.4.174}$$

Substituting the expressions for $v_\parallel$, $F_\parallel$ into (3.4.173), and performing the averaging, we get at last:

$$D_{v_\parallel v_\parallel} = \frac{\pi}{4}\frac{e^2 m_i^2}{c^2} v_\perp^2 \sum_k |B_k^\pm| \delta(k v_\parallel - \omega \pm \Omega_i) \; . \tag{3.4.175}$$

This form of $D_{v_\parallel v_\parallel}$ yields the following equation for the evolution of the particle distribution function, after having used the δ-function to perform the summation over k:

$$\frac{\partial f}{\partial t} = \frac{e^2}{4 m_i^2 c^2} \sum_\rho \frac{\partial}{\partial v_\parallel} \left[\frac{v_\perp^2 |B_k^\rho|^2}{|v_\parallel - \dfrac{\mathrm{d}\omega_k^\rho}{\mathrm{d}k}|} \right] \frac{\partial f}{\partial v_\parallel}\bigg|_{\text{at } v_\parallel = \mp \frac{\Omega_i}{k}} \; . \tag{3.4.176}$$

The derivatives over $\partial v_\parallel$ are calculated along the diffusion lines

$$\omega^\lambda = v_\perp^2 + v_\parallel^2 - 2 v_\parallel \left(\frac{\omega^\lambda}{k} \right) = \text{constant } (\lambda) \; ,$$

where λ denotes the different lines; accordingly

$$\begin{aligned} \frac{\partial}{\partial v_\parallel}\bigg|_{\text{at } \omega^\lambda = \text{constant}} &= \frac{1}{v_\perp} \left[v_\perp \frac{\partial}{\partial v_\parallel} - \left(v_\parallel - \frac{\omega}{k} \right) \frac{\partial}{\partial v_\perp} \right] = \\ & \frac{-1}{v} \left(\frac{1}{\sin\theta} \left(1 - \frac{\omega}{k v} \cos\theta \right) \frac{\partial}{\partial \theta} - \frac{\omega}{k} \frac{\partial}{\partial v} \right) \end{aligned} \tag{3.4.177}$$

and the diffusion equation can be rewritten as

$$\begin{aligned} \frac{\partial f}{\partial t} = \; & \frac{e^2}{4 m_i^2 c^2} \sum_\rho \frac{1}{v} \left(\frac{1}{\sin\theta} \frac{\partial}{\partial \theta} + \frac{\omega^\rho}{k} \frac{\partial}{\partial v} \right) \left[\frac{\sin^2\theta |B_k^\rho|^2}{v |\cos\theta|} \right] \times \\ & \times \left(\frac{1}{\sin\theta} \frac{\partial f}{\partial \theta} + \frac{\omega^\rho}{k} \frac{\partial f}{\partial v} \right)\bigg|_{\text{at } -k = \pm \frac{\Omega_i}{v} \cos\theta} \; . \end{aligned} \tag{3.4.178}$$

In this equation V_A/v is a small parameter, in zero order (3.4.178) gives back the pitch-angle diffusion equation:

$$\frac{\partial f}{\partial t} = \frac{e^2}{4 m_i^2 c^2} \sum_\rho \frac{1}{\sin\theta} \frac{\partial}{\partial \theta} \left[\frac{\sin\theta |B_k^\rho|^2}{v |\cos\theta|} \right] \frac{\partial f}{\partial \theta}\bigg|_{\text{at } -k = \pm \frac{\Omega_i}{v} \cos\theta} \; . \tag{3.4.179}$$

As a consequence, the diffusion over pitch angle is the fastest process, and the time scale of isotropization is

$$\tau_\Theta \sim \Omega_i^{-1} \left(\frac{\Omega_i^2}{\Xi_i^2} \right) \; ,$$

where

$$\Xi_i^2 = e^2 \frac{(\delta B)^2}{m^2 c^2} = \Omega_i^2 \frac{(\delta B)^2}{B_0^2} \tag{3.4.180}$$

is the cyclotron frequency corresponding to the wave magnetic field.

To obtain D_{vv}, the velocity diffusion coefficient, we shall expand (3.4.178) in the small parameter V_A/v; to do that first we decompose the distribution function as

$$f(t, v, \theta) = f_0(t, v) + f_1(t, v, \theta) ,$$

where $f_1 \sim V_A/v$; it easily follows that $\partial f_0/\partial t = 0$.

In the next order of V_A/v from (3.4.178), – assuming spatially homogeneous case – we obtain

$$\frac{\partial f_1}{\partial \theta} = -\frac{\sin\theta}{v} \frac{\sum_\rho \frac{\omega^\rho}{k} |B_k^\rho|^2}{\sum_\rho |B_k^\rho|^2} \frac{\partial f_0}{\partial v}\bigg|_{\text{at } -k=\pm\frac{\Omega_i}{v}\cos\theta} . \tag{3.4.181}$$

Finally, substituting (3.4.181) back into (3.4.178), collecting all the second order terms in V_A/v, and averaging over θ, the following equation describes the evolution of f_0:

$$\frac{\partial f_0}{\partial t} = \frac{1}{v}\left(\frac{\partial}{\partial v} + \frac{1}{v}\right) D_{vv} \frac{\partial f_0}{\partial v} = \frac{1}{v^2}\frac{\partial}{\partial v}\frac{D_{vv}}{v} v^2 \frac{\partial f_0}{\partial v} . \tag{3.4.182}$$

The v^{-1} term has come from the $(1 + (\omega/kv)\ \cos\theta)\frac{\partial}{\partial\theta}$ term in the external derivative after doing the averaging and partial integration over θ. In (3.4.182)

$$D_{vv} = \frac{e^2}{8m_i^2c^2} \int_0^\infty \mathrm{d}\theta \frac{\sin^3\theta}{|\cos\theta|} \frac{(\sum |B_k^\rho|^2)(\sum \left(\frac{\omega^\rho}{k}\right)^2 |B_k^\rho|^2) - (\sum \frac{\omega^\rho}{k}|B_k^\rho|^2)^2}{\sum |B_k^\rho|^2} \tag{3.4.183}$$

$$\text{calculated at } -k = \pm\Omega i/v\ \cos\theta . \tag{3.4.184}$$

If there are only two branches of MHD waves present, the velocity diffusion coefficient corresponding to (3.4.182) can be written in the form (Skilling, 1975; Forman and Webb, 1985):

$$D_{vv} = \frac{\pi e^2}{8m_i^2c^2}\frac{1}{v}\int_0^\pi \mathrm{d}\theta \left(\left(\frac{\omega}{k}\right)^{|} - \left(\frac{\omega}{k}\right)^{\|}\right)^2 \frac{\sin^3\theta}{|\cos\theta|} \frac{|B_k^||^2 |B_k^\||^2}{|B_k^||^2 + |B_k^\||^2} . \tag{3.4.185}$$

Here $|B_K^||^2$, $|B_k^\||^2$ are the magnetic energy spectral densities for two branches of MHD waves with phase velocities $(\omega/k)^|$, $(\omega/k)^\|$, respectively. Both branches are in simultaneous resonance with ions having velocity $v = \omega_{ci}/k_\| \cos\theta$. In the case of oppositely propagating Alfvén waves, the bracket in (3.4.185) is simply $4V_A^2$.

Comparing the time of velocity diffusion to the pitch angle diffusion time, it is not difficult to see that it is smaller by V_A^2/v^2, i.e., diffusion in velocities is a much slower process than pitch angle diffusion:

$$\tau_v \sim \left(\frac{v}{V_A}\right)^2 \tau_\Theta \ .$$

It is quite easy to formulate the physical interpretation of this result: the energy change along every line of the pitch angle diffusion is small $\sim \epsilon = V_A/v$. As usual for a stochastic process, the diffusion rate due to particle random walk between those lines is proportional to ϵ^2.

It is very important and not always recognized that in order to have velocity diffusion by waves, it is necessary to have such an interval of the particle velocities $v_\parallel$, where simultaneous resonance takes place with different branches. As a consequence, a stochastic, second-order Fermi acceleration by Alfvén waves is impossible in the solar wind, because the accelerating waves are propoagating only in one direction, outward; and similarly, it is impossible in all cases when there is only one wave direction, outward, or inward present.

3.4.3. *Examples of Ion Energization by MHD Turbulence*

Observations carried out by Tsurutani et al. (1987) during an encounter with comet P/Giacobini–Zinner demonstrated that in parallel with Alfvén waves, a compressional MHD wave component is also excited comprised by obliquely propagating magnetosonic waves. A theoretical explanation of this result has been proposed by Kotelnikov et al (1991). In the case of a solar wind plasma with $\beta \sim 1$, excitation of oblique magnetosonic waves is usually suppressed by a strong Landau damping ($\omega = k_\parallel v_\parallel$) due to wave interaction with the solar wind protons. However, quasilinear proton diffusion over $v_\parallel$ suppresses Landau damping, and allows the excitation of such waves. Their phase velocity along the magnetic field is equal to $\omega/k_\parallel = V_A(k/k_\parallel)$, and acting together with Alfvén waves, having a phase velocity V_A, they are able to organize energy diffusion of the resonant ions, because the intersection of the corresponding diffusion lines. Using the magnetic energy spectral density power law $|B_k|^2 \sim k^{-2}, k \geq \Omega_i/u$, (Galeev et al, 1987; Shapiro, 1989), it is easy to find a scaling law for the velocity diffusion coefficient:

$$D_{vv} \sim v \int_0^\pi |\cos\,\theta|\,\mathrm{d}\theta \sim \frac{1}{v} \ ,$$

where we have taken into account that accelerated ions remain in a resonance with waves in a narrow interval of pitch angles near $\pi/2$, namely $\cos\,\theta \sim u/v \ll 1$.

Then the diffusion equation for ion acceleration

$$u\frac{\partial f}{\partial x} = \frac{1}{v^2}\frac{\partial}{\partial v}\left(v^2 D_{vv}\frac{\partial f}{\partial v}\right) \tag{3.4.186}$$

has an automodel solution (Kotelnikov et al., 1991)

$$f \sim e^{-\lambda(x)v^3/u^3} \tag{3.4.187}$$

describing the tail formation of the accelerated ions. This tail descends rapidly with growing v.

More effective stochastic ion acceleration can be produced by the so-called firehose instability (Sagdeev and Vedenov, 1959; Gary et al., 1984). It is a non-resonant instability, and its driver is an anisotropy of the kinetic pressure of the pickup ions. In the solar wind reference frame ion kinetic pressure along the magnetic field is $p_\parallel = n_i m u_\parallel^2$ and across it $p_\perp = n_i m u_\perp^2$. The condition to set on the instability is

$$p_\parallel - p_\perp > \frac{B_0^2}{4\pi} \,. \tag{3.4.188}$$

Sufficiently close to the source of pickup ions, their kinetic pressure exceeds the magnetic pressure. In the cometary case, it happens even outside the cometary bowshock. Then, there is a wide range of angles between the solar wind flow and the magnetic field, when condition (3.4.188) is fulfilled. Due to the firehose instability waves, propagating in the opposite directions and polarized oppositely, are excited (Gary et al., 1987). Then, accelerated particles being in a simultaneous resonance with both types of waves are drifting along the intersecting diffusion lines and are accelerated stochastically, as it has been explained above.

Numerical simulation of the firehose instability (Quest and Shapiro, 1996) demonstrated a strong cascading of the wave energy to the large scales $k \ll \Omega_i/u$. In that case the resonance is possible between the accelerated particles having velocities $v \gg u$, and waves, in a whole interval of pitch angles between 0 and π, leading to more effective acceleration than it has been described above. The diffusion coefficient now scales as $D_{vv} \sim v$, and an automodel solution of the diffusion equation (3.4.186) is essentially more flat in comparison with (3.4.187), as the tail of the accelerated ions is:

$$f_i(v) \sim e^{-\beta(x)v} \,. \tag{3.4.189}$$

As an interesting example we discuss below a peculiarity both in wave excitation and diffusion of the mass-loaded particles, following Shevchenko et al. (1995), that was observed during the encounter with comet P/Grigg–Skjellerup (Neubauer et al., 1993). This comet is characterized by a relatively low gas production rate $Q \approx 7 \times 10^{27}$ mol s^{-1}, by two orders of magnitude less than for comet P/Halley. During the encounter with P/Grigg–Skjellerup, the solar wind magnetic field was anomalously large, corresponding to $u/V_\mathrm{A} \sim 3$, and it was oriented at almost normal angles to the wind flow, $\alpha \sim 75°$–$85°$. As it was explained before, there are two types of wave resonances with the mass-loaded particles:

(a) anomalous Doppler resonance: for a finite value of ω/Ω_i ratio and $\omega = |k|V_\mathrm{A}$ it can be written as

$$k = \frac{\Omega_i}{V_\mathrm{A}} \frac{1}{\dfrac{v_\parallel}{V_\mathrm{A}} - 1} \,, \tag{3.4.190}$$

(b) normal Doppler resonance:

$$k = -\frac{\Omega_i}{V_A}\frac{1}{\frac{v_\parallel}{V_A} - \frac{k}{|k|}} \,. \tag{3.4.191}$$

It follows from the resonant condition that for anomalous Doppler resonance the wave vector k is obligatory positive. Usually due to normal Doppler resonance waves with $k < 0$ are excited. However, if resonant particles are in the region $v_\parallel < V_A$, excitation of waves with $k > 0$ is also possible.

Due to the much smaller gas production rate for P/Grigg–Skjellerup mass-loading is essentially weaker than for comet Halley, the growth rate of an ion cyclotron instability is smaller and less space is available for its development. Therefore, excitation of a broad spectrum of MHD waves and evolution of bispherical distribution are impossible. Instead, a regular quasi-monochromatic spectrum is excited, and the particle distribution remains sufficiently narrow in pitch angle. In that case the instability growth rate is given by:

$$\gamma \sim \left(\frac{\Delta\rho}{\rho} \frac{\left(\frac{u}{V_A}\right)^2}{\left(\frac{u}{V_A}\cos\alpha \pm 1\right)} \sin^2\alpha \right)^{1/3} \cdot \omega \,. \tag{3.4.192}$$

that is valid if $\Delta\theta < \gamma/\Omega_i$; and $\Delta\rho/\rho = n_i m_i / n_p m_p$ is the relative mass-loading value of the solar wind. For $\Delta\rho/\rho \approx 10^{-2}$, and for typical solar wind parameters, the value of γ is about $(10^{-2}\text{–}3 \times 10^{-3})$ s^{-1}. The distance, at which Alfvén waves are excited and can be observed is equal to $r_0 \approx 10u/\gamma \sim (3\text{–}5) \times 10^5$ km (compare it with $(5\text{–}10) \times 10^6$ km for P/Halley).

In the quasi-monochromatic regime the saturation of ion cyclotron instability is due to the trapping of the resonant particles in the direction of wave propagation. This trapping is caused by a longitudinal component of the Lorentz force $(e/c)v_\perp \times \Delta B_\perp$ and produces phase oscillations of the resonant ions with respect to the wave. The condition for saturation is $\Omega_{TR} \sim \gamma$, where $\Omega_{TR} \approx ((\Delta B/B)\Omega_i\, k\, u\, \sin\alpha)^{1/2}$ is the trapping frequency. Saturation is reached when the relative level of the magnetic field modulation by the transverse Alfvén wave is $\Delta B/B \approx (\Delta\rho/\rho)^{2/3} \sim (0.1\text{–}0.3)$. Time evolution of the amplitude of the left hand polarized wave, as obtained in numerical simulation, is shown in Figure 3.4.2. Initially, the excitation of Alfvén wave with $k < 0$ can be observed, propagating towards the comet. Later on, in the nonlinear stage, bounce oscillations transport resonant particles to the small $v_\parallel < v_A$, a left hand polarized wave with $k > 0$ is also excited. The diffusion lines corresponding to these two types of waves are intersecting, so when they are interacting simultaneously with the resonant particle, it drifts from one diffusion line to another, i.e., participates in the diffusive energy growth.

This theoretical analysis agrees well with the evolution of the ion phase space, obtained in the numerical simulations, and shown in Figure 3.4.3. It is important

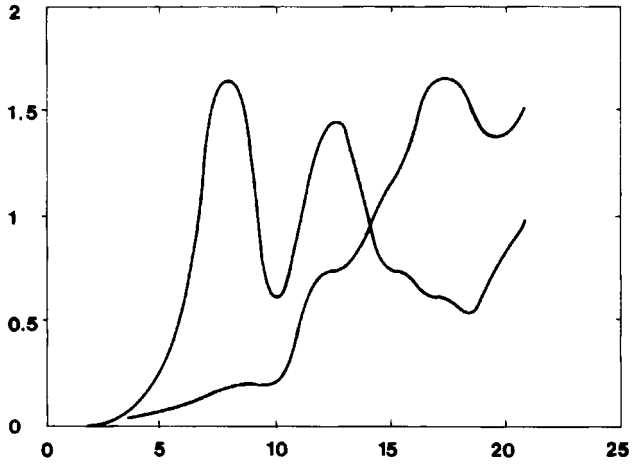

Figure 3.4.2. Time evolution of the amplitude of left hand polarized waves: thick line, k <0 (cometward direction); thin line, k>0 (sunward direction).

to note that the energization mechanism illustrated in Figure 3.4.3 is effective only in the quasi-monochromatic regime when the broadening of the wave-particle resonance due to the bounce oscillations is important, and it is negligibly small for a broad spectrum of the Alfvén wave turbulence.

3.4.4. *Particle Energization by the Lower Hybrid Waves*

Inside the bowshock, where in the shocked solar wind flow $V_A/u \sim 1$, lower hybrid waves dominate the wave activity accompanying the mass-loading process. These waves are very efficient to couple via Landau resonance to the fast, field aligned electrons and to the slow, unmagnetized ions. In the case when the free energy source is in plasma electrons, excitation of the lower hybrid waves energizes ions. A classical example of this situation is connected with the aurora, where precipitation of fast electrons along magnetic field lines excite so-called electrostatic whistler waves close to lower hybrid frequency (Kintner et al., 1991). Absorption of these waves by ions causes them to get accelerated across the magnetic field and to form ion conics. For the mass-loading process the opposite situation is typical: Ions implanted into the host plasma due to mass-loading excite lower hybrid waves, this leads to a significant energization of plasma electrons. Such energization takes place at the front of the planetary bowshock, where the reflected solar wind protons play the role of implanted ions exciting lower hybrid waves (see, e.g., Vaisberg et al., 1983). Another important example is the so-called critical velocity ionization phenomenon first described by Alfvén (1960). Plasma flowing through neutral gas initiates discharge when the proton flow energy exceeds the ionization potential. Currently it is a widespread opinion that the discharge is initiated by plasma electrons obtaining energy from protons via excited lower hybrid waves (Galeev et al., 1982).

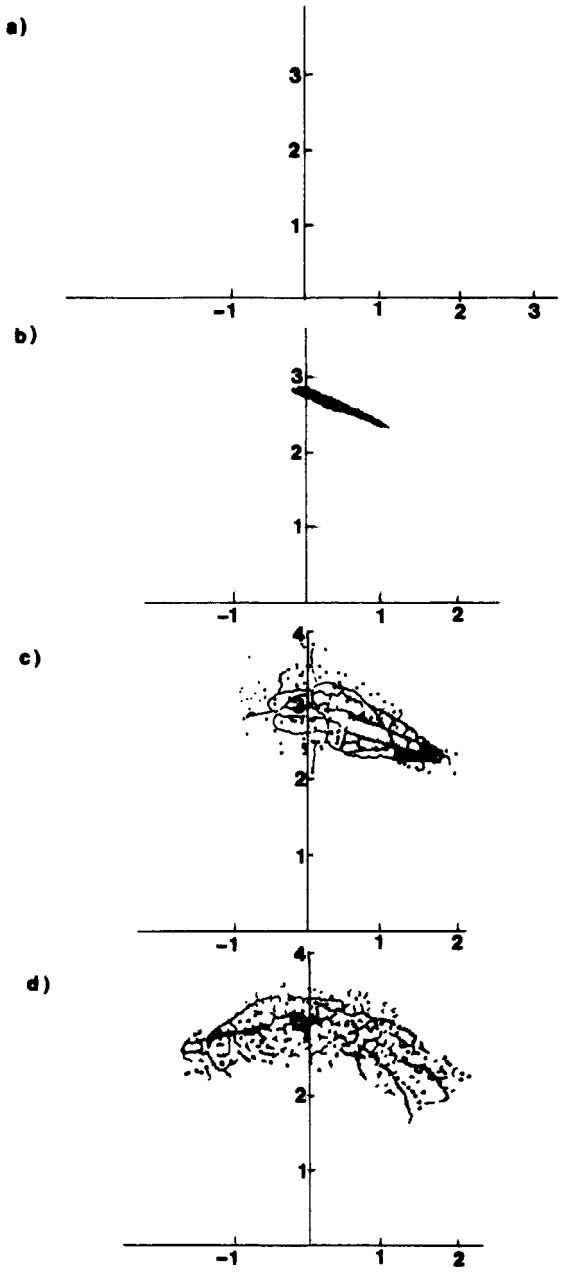

Figure 3.4.3. The dynamics of cometary ions phase space: (a) initial state, (b) only waves with $k > 0$ are excited, pitch angle diffusion, (c) and (d) waves propagating in both directions are excited resulting in energy diffusion.

In what follows we will discuss in detail particle energization due to lower hybrid waves excited in solar wind/comet interaction, the planetary case is treated in Section 4.3. As discussed previously, newly born cometary ions, forming a ring, excitate lower hybrid waves via loss cone instability. The growth rate of this instability is given by Equation (3.2.150). In the space physics it is more common to call this instability type modified two stream instability (MTSI) (Shapiro et al., 1995); such instability can be generated without a ring formation as well, cf., Section 4.3.

The distance from comet needed to develop MTSI can be estimated as:

$$r_{LH} \approx \frac{10u}{\gamma_{LH}} .$$

From Equations (3.2.148 and 3.2.150) it follows that γ_{LH} is inversely proportional to the ion density, or it increases as r^2 at the large cometocentric distances. Detailed analysis show that the minimum value of the gas production rate needed for the development of MTSI is:

$$Q \geq 40\pi^2 n_0 u \frac{m_i}{m_p} \beta^{3/4} \frac{v_g \tau u}{\omega_{LH}} \left(\frac{u}{v_{Tp}} \right)^4 . \tag{3.4.193}$$

For typical solar wind parameters, $Q_{\min}$ is between $10^{27}-10^{28}$ mol s^{-1}. Therefore, encounter with such a strong comet as P/Halley, is always accompanied with strong lower hybrid wave activity, in accordance with observations.

Electrons gain energy from the lower hybrid waves along the magnetic field lines; this stochastic process is described by the diffusion equation

$$u \frac{\partial f_e}{\partial x} = \frac{\partial}{\partial v_\parallel} \left[D(v_\parallel) \frac{\partial f_e}{\partial v_\parallel} \right] , \tag{3.4.194}$$

where the diffusion coefficient is calculated from the lower hybrid wave energy spectral density at the resonant point $k_\parallel = \omega_k / v_\parallel$:

$$D(v_\parallel) = \frac{e^2}{m_e^2} \frac{|E_k|^2}{|v_\parallel - \dfrac{\partial \omega}{\partial k_\parallel}|} \frac{k_\parallel^2}{k^2}, \quad \left(v_\parallel = \frac{\omega_k}{k_\parallel} \right) . \tag{3.4.195}$$

There is a resonant enhancement of the diffusion coefficient because for the lower hybrid waves the phase velocity $v_{ph} = \omega / k_\parallel = v_\parallel$ is close to the group velocity $|v_\parallel - \partial\omega/\partial k_\parallel| \approx v_\parallel (k_\parallel^2 / k^2)$. In our calculations we used $\langle E^2 \rangle \approx 15 (mV/m^{-1})^2$ for the lower hybrid waves obtained from in-situ measurements at P/Halley, and the wave energy spectral density was approximated as:

$$|E_k|^2 = \frac{2T_p}{m_e u \Omega_e} \langle E^2 \rangle \frac{\epsilon^2 \Delta^3}{[(\epsilon - \epsilon_e)^2 + \Delta^2]^2} ,$$

where $\epsilon_e = 1$ is the average tail electron energy (in units of T_p), and $\Delta = 1$ is the spectrum width. The evolution of the electron energy distribution with changing

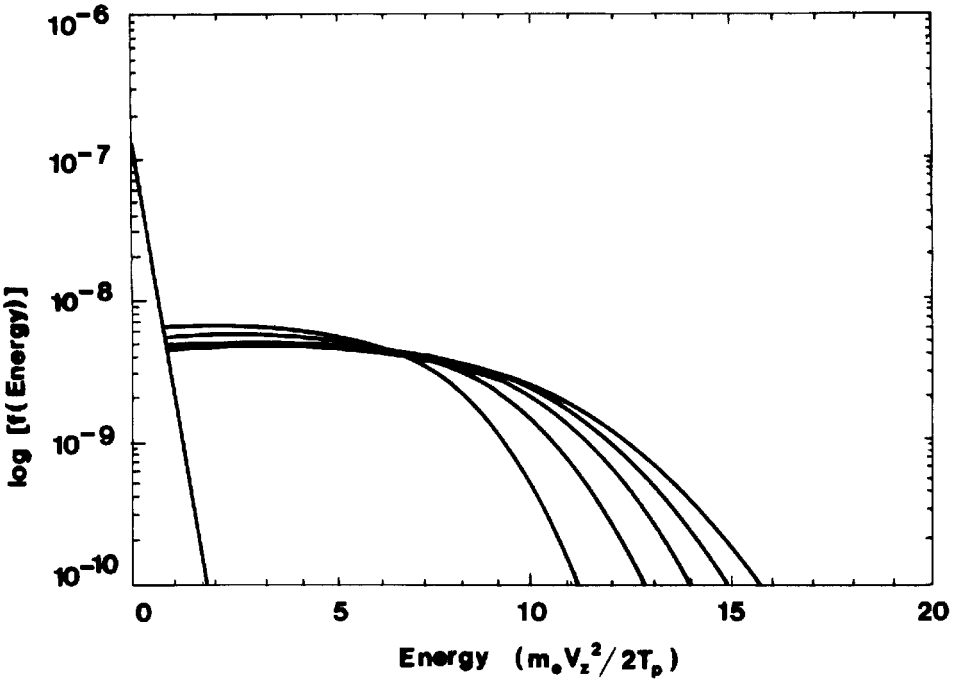

Figure 3.4.4. Evolution of the distribution function for the solar wind electrons accelerated by the lower hybrid waves.

cometocentric distance is shown in Figure 3.4.4. As the result shows, a plateau is formed in the electron velocity distribution in the energy interval 100–800 eV; and a power like tail stretches up to the energies ~1.5 keV. From numerical analysis it was obtained that sufficiently close to the cometopause approximately 10% of the solar wind electrons are accelerated to energies exceeding 100 eV. These energetic electrons penetrating into dense cometary atmosphere are capable of producing a strong soft X-ray emission by combination by bremsstrahlung and K-shell line radiation. This mechanism contributes significantly around the cometopause to the strong cometary x-ray emissions recently observed first at comet P/Hyakutake, and later on at many other active comets.

4. Observations of Mass Loading Processes

4.1. Mass loading at comets

In the realm of mass-loaded space plasmas of the solar system, cometary plasmas would certainly occupy the best place. Since the suggestion of a solar wind based on ground-based observations of comet tails (Biermann, 1951), the interaction mechanism of comets with the solar wind via pickup ions has attracted much in-

terest. The process of ion pickup and implantation into the solar wind flow, which loads the flow with additional mass, was expected to be the key to the comet-solar wind interaction (e.g., Wallis, 1973). Since 1985, *in situ* measurements were made thanks to several spacecraft flybys around three comets: P/Giacobini–Zinner, P/Halley, and P/Grigg–Skjellerup. These spacecraft investigations were directed toward studying plasma processes around active comets to learn more about what happens when a cloud of neutral gas (the comet's atmosphere) interacts with ionizing radiation (sunlight) and a flowing plasma (the solar wind). Active comets are excellent natural laboratories for studying such interactions, which must be ubiquitous throughout the universe.

This chapter lays the stress on the contribution of these in situ investigations to the knowledge of mass loading at comets. It attempts to be comprehensive on this topic but obviously cannot be exhaustive in its coverage of the literature. Particular emphasis will be placed on some unexpected observations.

4.1.1. *Characteristics of Solar Wind-Comet Interaction*

As well as the properties of the solar wind itself, the gas production rate of a comet is a vital parameter that determines the size and nature of the comet-solar wind interaction region. At large heliocentric distances the solar wind-comet interaction is directly dominated by the properties of the nucleus, its surface and near-surface layers (Figure 4.1.1, top). Sublimation of ice is negligible and the solar wind directly impinges onto the surface. The interaction with the almost 'bare' nucleus is comparable to that with an asteroid and is expected to be a wake-type interaction, probably similar to what observed as the Galileo spacecraft passed the asteroids Gaspra in 1990 and Ida in 1993 (e.g., Kivelson et al., 1995). It depends on the magnetic properties of the nucleus, the electrical conductivity of its surface region, or any near-surface dust layers. As the comet's orbit takes it to the Sun, neutral gas and dust are more and more driven away form its nucleus. The gas escapes supersonically into space because the comet is too small to retain a gravitationally bound atmosphere. The gas then ionizes due to photoionization and charge exchange with very large ionization mean free path. The increase of the outgasing will modify the type of interaction by the increasing mass-loading.

At smaller heliocentric distances the interaction is fully governed by the outgasing properties of the comet and associated solar wind mass-loading (Figure 4.1.1, bottom). New, pickup ions are produced on a much larger scale than the nucleus size, which can be tens of millions kilometers, forming an enormous region over which the comet-solar wind interaction occurs. Photoionization of cometary gas results in the addition of plasma to the solar wind, while charge exchange collisions replace fast solar wind ions with slow cometary ions and also add mass if the cometary ions are heavier than the solar wind ions they replace. Conservation of momentum requires that the solar wind therefore be decelerated by the ion pickup process. Biermann's original suggestion that momentum was transferred from the wind to comet tails by Coulomb collisions was superseded by Alfvén's (1957)

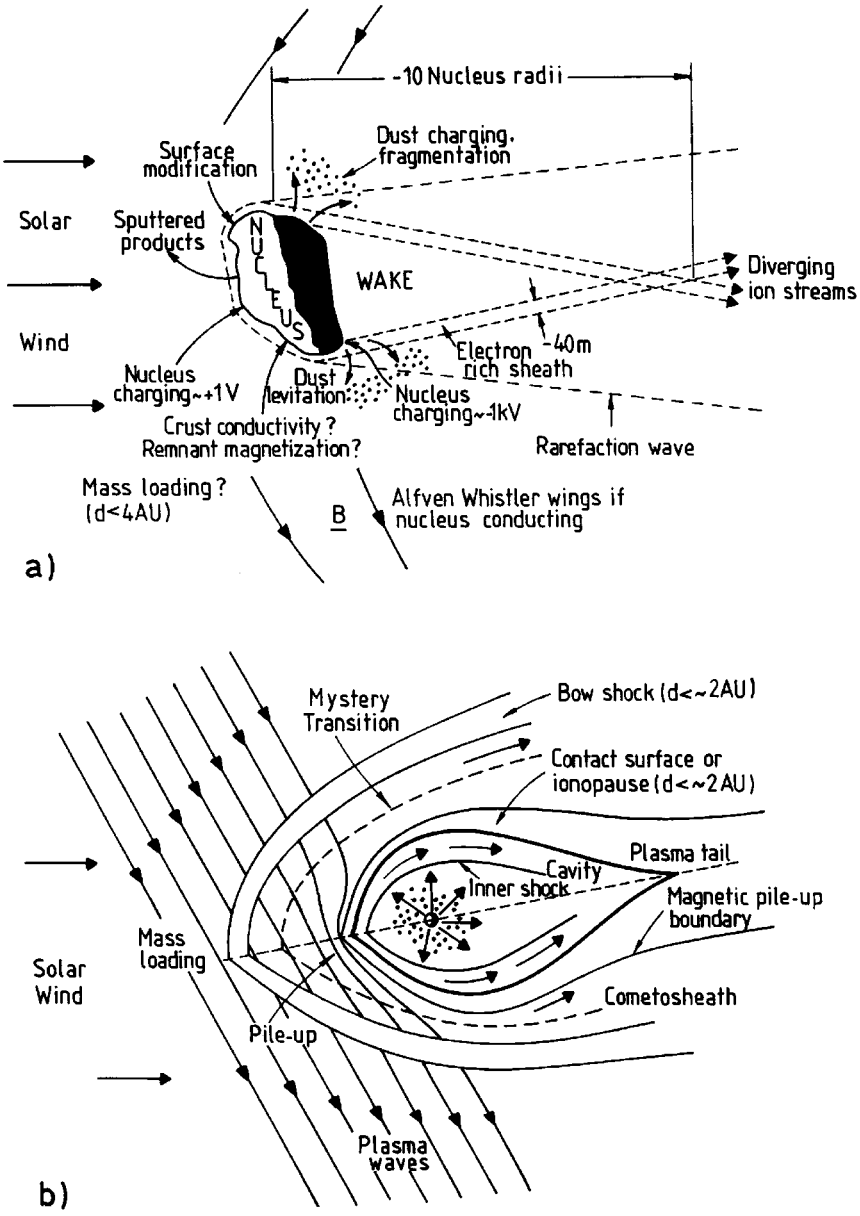

Figure 4.1.1. Top: solar wind low activity comet interaction, far from the Sun. *Bottom*: solar wind high activity comet interaction (not to scale).

proposal that the mass-loading of the solar wind would cause the interplanetary magnetic field to be draped around the comet tail and confine the plasma in a sort of magnetic bottle. The field draping occurs because the wind near the comet-Sun axis is more heavily mass loaded and therefore more strongly decelerated than is the wind at greater distances from the comet, while the high conductivity of the plasma keeps the IMF frozen into the wind, no matter what is its speed.

At the same time, the pickup ions slow down the solar wind, their high-speed gyration about the magnetic field increase the effective temperature of the wind and decrease its Mach number. A weak bow shock is expected to develop where the Mach Number reaches a value of ≈ 2 . Unlike the planets with a strong magnetic field (e.g., Earth) or unmagnetized planets with dense atmospheres (e.g., Venus), an active comet does not form a blunt obstacle with an impermeable boundary separating the solar wind from all the cometary material, but instead, the solar wind can interact with the expanding partially ionized atmosphere of the comet over a large distance. Thus at comets, the shock transition is formed through the mass loading process itself.

The dense pure cometary ionosphere which forms near to the comet is bounded by a contact surface. This boundary also often named 'ionopause' (which is a little incorrect since the ionosphere extends further away) marks the outer edge of a field-free cavity surrounding the nucleus which excludes the solar wind particles and fields. Inside the cavity boundary, the cometary plasma is cold and stagnant. The position of this boundary can be understood by a balance between inward magnetic gradient forces and outward ion-neutral drag (e.g., Cravens, 1991a). The bow shock and the contact surface were the two anticipated boundaries in the mass-loaded flow, separating plasmas with different properties.

4.1.2. *Overview of the Observations*

The ICE passage through the tail of comet P/Giacobini–Zinner on September 11, 1985, the flybys of comet P/Halley in March 1986 by a fleet of spacecraft (*Giotto, Vega-1* and *-2*, *Suisei, Sakigake*), and the *Giotto* flyby of comet P/Grigg–Skjellerup on July 10, 1992, have provided for the first time an *in situ* study of the interaction of the solar wind with a cometary plasma under various solar and cometary conditions. All these *in situ* measurements were made at about 1 AU from the Sun. It must be stressed that all the spacecraft trajectories occurred at nearly right angles to the comet-Sun line and only one went through the tail. Four encounters occurred close to the ecliptic plane and from the 'dusk' to the 'dawn' side defined by considering an arbitrarily direct rotating body, whereas the *Giotto* encounter at P/Grigg–Skjellerup occurred nearly perpendicular to the ecliptic plane from north to south and from 'dawn' to 'dusk'. These geometry considerations must be kept in mind when comparing observations from different data sets. Moreover, part of the well-known difficulty encountered in studying the interaction of the solar wind with a comet, or with any other extended object, is that the wind can change its properties during the time the spacecraft is inside the environment of the body

TABLE 4.1.1
Summary of the main parameters for the ICE flyby of P/Giacobini–Zinner, the Giotto flybys of P/Halley and P/Grigg–Skjellerup as well as the Vega flybys of P/Halley

Comet	P/Halley			P/Giacobini-Zinner	P/Grigg-Skjellerup
Encounter date	March 6, 1986	March 9, 1986	March 14, 1986	Sept. 10, 1985	July 10, 1992
Encounter time (UT)	7:20:06	7:20:00	00:03:01	11:02:03	15:18:40
Fly-by velocity (km s^{-1})	79.2	76.73	68.37	20.9	13.99
Fly-by distance (km)	8890	8030	596	7800	about 200
Heliocentric distance (AU)	0.79	0.83	0.90	1.05	1.01

being studied. Thus it is always difficult to separate spatial from temporal effects. Each high- or low-speed solar wind stream lasts for several days to weeks, but many smaller-scale fluctuations and waves are superimposed on the large-scale variations.

A large amount of literature about these three flybys and related studies can be found in Science, April 1986; *Geophysical Research Letters*, March and April, 1986; *Nature*, May 1986; ESA SP 250, December 1986; *Astronomy and Astrophysics*, 1987; *AGU Geophysical Monograph* 53, 1989; *AGU Geophysical Monograph* 61, 1991; *Journal of Geophysical Research* (*Space Physics*), December 1993, and ESA SP 1127, 1996. To illustrate some of these cometary encounters, Table 4.1.1 summarizes the main parameters of all the flybys. See also review papers by Neugebauer (1990) and Coates (1997).

Following the spacecraft encounters, the importance of pickup ions has been confirmed and much work has been done on the wave-particle interactions, particle distributions and wave properties which are key features of the deceleration of the solar wind in the cometary environment. The spacecraft observations on the mass-loaded flow are in qualitative agreement with the theoretical predictions made prior to the cometary encounters. The existence of a bow shocks is confirmed by all the spacecraft results. On the other hand, the contact surface was only penetrated by Giotto during the P/Halley flyby, the other spacecraft flying too far from the nucleus. Nevertheless, it confirms the existence of the field-free cavity.

However, the encounters have raised significant questions regarding the permanence of some of the boundaries and features in the various data sets, which have been the subjects of very lively debates. Sometimes there have been huge theoretical efforts to interpret a single specific feature reported from the observations made around only one comet by a single instrument on only one side of this specific spacecraft pass. Despite the possible intrinsic interest of such transient features for

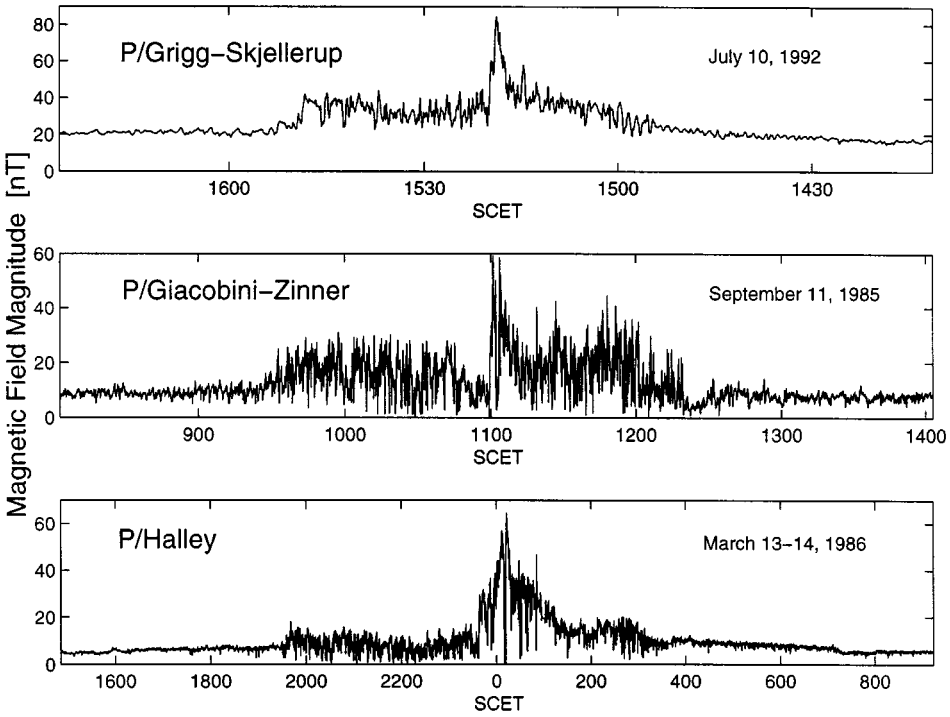

Figure 4.1.2. Comparison of the magnetic field magnitude observations at the three comets encountered so far. For details see text. (after Glassmeier et al., 1997).

cometary physics, it seems more reasonable to lay the stress on features reported from different instruments during different flybys around different comets.

The cometary encounters have also provided the opportunity to study the solar wind interaction with an active (P/Halley), an intermediate (P/Giacobini–Zinner), and a weakly active (P/Grigg–Skjellerup) comets. Due to 2 orders of magnitude difference in cometary neutral gas production rate, there is a large difference in the size of the plasma interaction regions between $\approx 2 \times 10^6$ km for Halley and $\approx 10^4$ km for P/Grigg–Skjellerup; however, many similarities have been found: bow shocks and/or bow waves and many and unexpected 'cometosheath' structures.

Figure 4.1.2 displays a comparison of the observations on the magnetic field magnitude around the three comets during the three chosen encounters of Table 4.1.1 for which full time coverage is available in the data. For each panel the time of closest approach is at the center of the time interval shown. At Halley and P/Giacobini–Zinner, the trajectories of the spacecraft were from the 'dusk' towards the 'dawn' and at P/Grigg–Skjellerup in the reversed way so that time axis has been inverted. Table 4.1.2 provides an overview of the parameter difference for the five encounters. The upstream water group ion gyroradius is a parameter of major importance for microscopic processes. Mean solar wind speed and interplanetary magnetic field are also given. For the three encounters the upstream flow direction

TABLE 4.1.2
Comparison of the main physical parameters for the three comet encounters of Table 4.1.1

Comet	P/Halley			P/Giacobini-Zinner	P/Grigg-Skjellerup
Gas production rate (s^{-1})	1.3×10^{30}	6×10^{29}	6.9×10^{29}	$2 - 5 \times 10^{28}$	$6.7 - 7.5 \times 10^{27}$
Shock distance (km): 'dawn'	$(4.5 - 6) \times 10^5$	–	$\approx 7.5 \times 10^5$	$\approx 7.5 \times 10^4$	$\approx 19\,000$
Shock distance (km): 'dusk'	1.05×10^6	1.3×10^6	$\approx 1.15 \times 10^6$	$\approx 1.2 \times 10^5$	$\approx 25\,000$
Upstream parameters					
H_2O^+ gyroradius (km)			10 000	10 000	5000
Interplanetary magnetic field (nT)	7	9	8	8	20
Solar wind flow speed (km s^1)	500	590	380	400	350
Alfvén velocity (km s^{-1})	37	70			
Alfvén Mach number			4–6	4–6	0.2–2

was predominantly away from the sun. The IMF was much more variable at Halley and P/Giacobini–Zinner than at P/Grigg–Skjellerup, which is not surprising taking into account the scale differences. At P/Grigg–Skjellerup, the encounter occurred inside a magnetic cloud with a very steady IMF pointing in the azimutal direction, always close to perpendicular to the solar wind flow. Since the gas production rate governs the macroscopic scale of the comet 'laboratory', we have used the most clearly defined 'dusk' shock distance crossing as a measure of this scale and have chosen appropriate time windows to enforce the coincidence of the 'dusk' shock crossings. The differences in the spatial resolutions linked to the different flyby velocities have been taken into account by appropriate averaging of the data.

The first evidence when looking at Figure 4.1.2 is the striking similarities between the three profiles. It must be however remembered that at comet P/Giacobini –Zinner the tail was traversed while the two other profiles were obtained on the dayside. Moreover, the closest approach at Halley correspond to the field-free cavity between to maximum of the pileup field magnitude while it corresponds to an observed maximum at P/Grigg–Skjellerup since the very small (estimated radius of some tens of kilometer) field-free cavity was not crossed. A local minimum is also observed at P/Giacobini–Zinner in the plasma sheet between the high tail lobe fields. The second evidence in Figure 4.1.2 is the general obvious asymmetries for the three profiles between the 'dawn' and 'dusk' sides.

4.1.3. *The Cometary Shock*

The existence of a bow shock at active comets was predicted well before any cometary encounter (e.g., Biermann et al., 1967). The idea was that mass-loading of the solar wind could occur quickly enough to cause a strong shock at a singularity in that one dimensional solution when the mean molecular weight of the flow reached a critical value of $\frac{4}{3}$. In contrast, a weak or nonexistent shock was anticipated by Wallis (1973). The current consensus among modelers is that a weak bow shock appears in two- and three-dimensional MHD calculations (e.g., Schmidt and Wegmann, 1982; Gombosi et al., 1996; Zank et al., 1995) and in some cases of kinetic simulations (e.g., Omidi and Winske, 1987).

The existence of bow shocks or bow waves is confirmed by all the spacecraft results. Where sufficient data were available, the bow shock was shown to occur at the predicted point in the mass-loaded flow. Also the Mach numbers of the features support the interpretation of a bow shock. But its observed properties place this mass-loading shock amongst the most complex in the solar system. In all cases the cometary ions dominates the dynamics in term of pressure (e.g., Coates et al., 1997). The cometary shock properties seemed to change dramatically between crossings at the same comet depending on the interplanetary magnetic field orientation. The 'dusk' shock crossings appear usually more clearly defined than the 'dawn' shock crossings. For *Giotto* at comet Halley, it has been pointed that the inbound ('dusk') shock occurred in quasi-perpendicular configuration while it was more quasi-parallel for the outbound ('dawn') crossing. The width of the feature

varies from a few water group ion gyroradii in the quasi-perpendicular case to many gyroradii in the quasi-parallel case (Coates et al., 1990). Neubauer et al. (1990) proposed to interpret this later feature a model of a 'draping' shock with a reversal of the transverse magnetic field component, not admissible in classical shock physics. The shock observations at *Vega-1* were more or less similar than for Giotto while *Vega-2* saw an inbound shock with significant parallel features but with a fairly perpendicular geometry and the ICE experimenters used the term 'bow' wave on both sides since there was no sharp signature on the field (e.g., Coates et al., 1997 and references therein). At comet P/Grigg–Skjellerup, kinetic effects were expected to dominate, possibly obscuring the weak shock signature because of the relatively large water ion gyroradius compare to the shock size. But the observations are surprisingly very similar to those at Halley (Neubauer et al., 1993; Rème et al., 1993; Mazelle et al., 1995). A sharp signature is observed on the 'dusk' side. Figure 4.1.3 displays the magnetic field and electron density observations (Mazelle et al., 1997) for a time interval including the inbound ('dawn') shock crossing (1455 SCET) or for distances between $\approx 2.6 \times 10^4$ km and $\approx 1.9 \times 10^4$ km from the nucleus. The field components are shown in the comet-centered solar ecliptic (CSE) coordinates, with the X-axis pointing from the comet to the sun and the Z-axis pointing towards the north pole of the ecliptic plane. Large amplitude low frequency waves generated by the cometary pickup ions are observed. No clear shock transition appears despite the quasi-perpendicular configuration as for the 'dusk' shock crossing. The crucial role of the heavy ion generated instabilities has also been mentioned for comet P/Giacobini–Zinner where there is some evidence that the observations can be explained in terms of reforming shock model (Omidi and Winske, 1990).

4.1.4. *The Contact Surface*

The contact surface or ionopause is relatively very close of the comet nucleus. From all the cometary missions only *Giotto* was able to fly inside the P/Halley ionopause thanks to its approach at 600 km from the nucleus. In the case of P/Grigg–Skjellerup *Giotto* approached at about 200 km from the nucleus but did not go through the ionopause showing that the magnetic cavity in this case was very small. For Halley the identification of the ionopause was very clear with the magnetometer data. Figure 4.1.4 shows magnetic field and cometary ion observations within 25 000 km from the nucleus from Neubauer et al. (1986) for the magnetic field results and from Balsiger et al. (1986) for the ion results. 16 400 km before Closest Approach (CA) the magnetic field magnitude (lower panel) reached a maximum of 57 nT (magnetic pile-up region). Afterwards the magnitude started to decrease rapidly, to essentially zero inside the contact surface, which was crossed at 4700 km before CA. The spacecraft was inside the magnetic cavity for about 2 min. On the outward bound pass the contact surface was crossed at 3800 km after CA and the magnetic field magnitude rose rapidly to reach an even higher maximum of 65 nT at 8200 km after CA. At the same time, a steadily decreasing ion temperature and

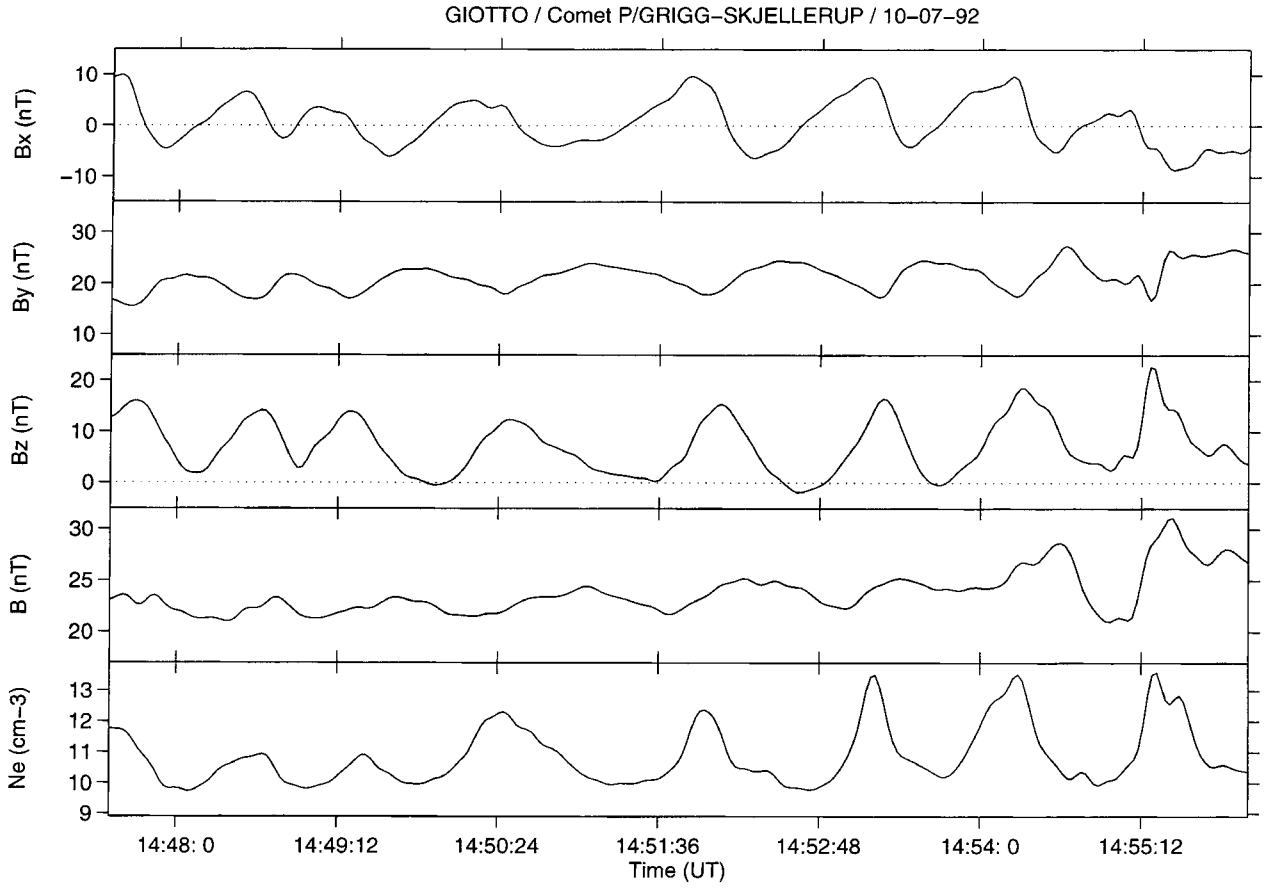

Figure 4.1.3. Magnetic field and plasma electron density observations upstream from the inbound ('dawn') shock crossing at comet P/Grigg-Skjellerup.

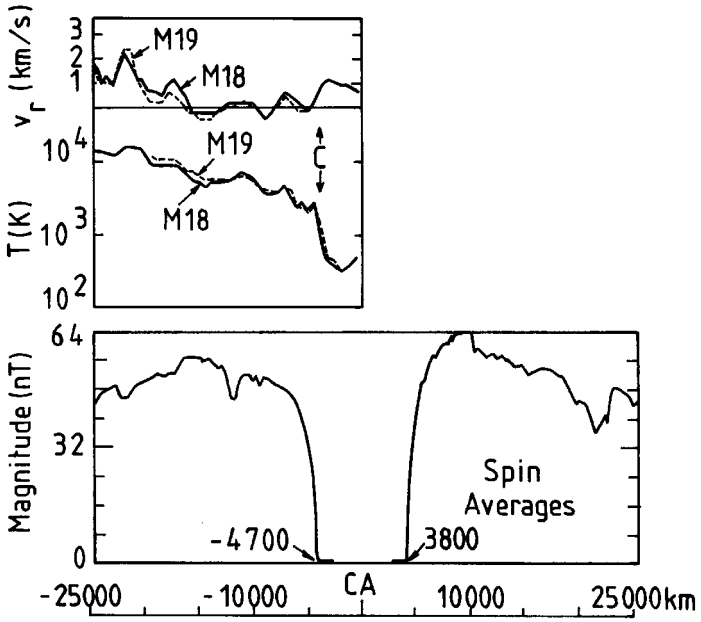

Figure 4.1.4. Bottom: Magnetic field magnitudes B based on spin-averaged components from 25 000 km before *Giotto* Halley encounter to 25 000 km after encounter showing the inner magnetic pile-up region inbound and outbound and the magnetic cavity region (CA Closest Approach) from Neubauer et al. (1986). *Top*: from Balsiger et al. (1986), with the same distance scale are the profiles of the ionospheric flow speed relative to the comet (v_r) and temperature (T_i) derived from the mass 18 (H_2O^+; bold line) and 19 (H_3O^+; thin line) data. v_r changes from near zero to about 1 km s^{-1} at the inbound of the magnetic cavity while T_i decreases rapidly from 2600 to about 450 K.

velocity (upper panel) were observed at 18 (H_2O^+) and 19 (H_3O^+) atomic mass units. When crossing the contact surface the temperature suddenly dropped from 2600 to less than 450 K. This drop in temperature coincided with a sudden onset of a (1 km s^{-1}) flow of ions outwards from the comet.

4.1.5. *The Unexpected 'Cometosheath' Observations*

The region of a cometary environment downstream from the shock has often been called the 'cometosheath'. For each cometary flyby the cometosheath displayed several important features that were not expected (e.g., Coates, 1997). A question which has given rise to much controversy is whether these features are non-stationary or permanent in the cometary plasma environment (Rème, 1991 and references therein). Even at the weakly active comet Grigg–Skjellerup, Giotto measurements have also revealed a highly structured plasma environment (Rème et al., 1993; Neubauer et al., 1993; Johnstone et al., 1993) and surprisingly despite the small scale it displays characteristic regions and boundaries very similar to those at Halley as also obviously shown on Figure 4.1.2. This is a priori surprising because while the characteristic length scales in the plasma (gyroradii, inertial

lengths, ionization mean free path, etc.) are similar, since they essentially depend on the solar wind parameters, the size of interaction region at P/Grigg–Skjellerup is comparable, as already mentioned, with a heavy (water ion) gyroradius. This should imply a stronger influence of the kinetic effects induced by the heavy ion pickup process on the properties of the plasma environment at comet P/Grigg–Skjellerup. The most obvious differences between the two comets lie in the ULF waves and velocity space diffusion characteristics (e.g., Coates et al., 1993).

One of the dramatic plasma discoveries at comet Halley was the clear bifurcation of the cometary ion peak in the cometosheath region (Johnstone et al., 1986; Thomsen et al., 1987). The explanation for the bifurcation has already been alluded to, namely the different velocity either side of the bow shock which gives different pickup shell radii and thus different peak energies. However, this does not explain the very suddenly enhanced splitting of the water group ion population which occurs approximately half-way from the nucleus caused by a change in solar wind velocity there. This boundary, called the 'mystery' boundary as its origin is still not understood, is also characterized by the sudden end of significant fluxes of energetic (keV) electrons (e.g., Rème et al., 1987; Rème, 1991). The mystery boundary also ends a region of higher solar wind density and velocity, and following the boundary the number of ions in the ram direction increases sharply. There is surprisingly no strong effect in the magnetic field to match these sharp and significant changes in the plasma parameters. The boundary is still present in the ion data on the *Giotto* outbound pass (although suitable electron data are not available) and is also reported at comet P/Grigg–Skjellerup (Johnstone et al., 1993; Mazelle et al., 1995; Jones and Coates, 1996) with its unexpected bursts of high energy (keV for Halley, hundreds of eV for P/Grigg–Skjellerup) electrons observed upstream the boundary, again about half way between the shock and the nucleus, on both sides.

Rème (1991) also argued that comparable boundaries were also observed on sometimes different plasma parameters in the Vega, Suisei and ICE data sets. Because of the similar behavior observed by the spacecraft in the cometosheath of the three comets it is possible to compare the position of the mystery boundary as seen by Giotto at Halley with the other measurements including the transition region-sheath boundary identified at comet P/Giacobini–Zinner (Bame et al., 1986). To do so a linear scaling factor has been determined from the bow shock wave crossing locations at the three comets. The Giotto transitions at Halley and at P/Grigg–Skjellerup and the P/Giacobini–Zinner transition region-sheath boundary are constructed by fitting a paraboloid to the three inbound boundary crossing points (Figure 4.1.5). The positions of the mystery boundary lie remarkably close to the transition-sheath surface inferred from the ICE data at P/Giacobini–Zinner. In addition the positions found at Halley by Suisei (end of the 'turbulent' regime of the flow), *Vega-1* and *Vega-2* (drop in electron temperature and signatures in the wave spectra) are included in Figure 4.1.5 showing that the measurements of all the spacecraft are surprisingly consistent, as for the shock position, taking into

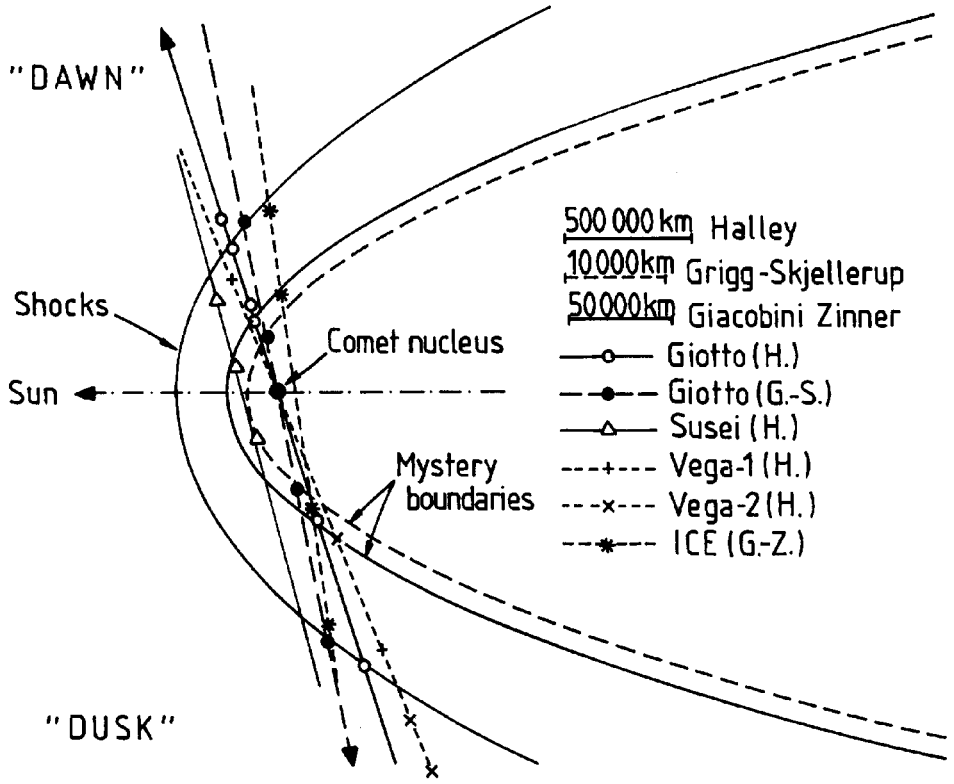

Figure 4.1.5. Comparison of the size of P/Halley, P/Giacobini–Zinner and P/Grigg–Skjellerup solar wind interaction regions. The bow shocks (or bow waves), the mystery transitions, and the distance scale appropriate to each comet are shown. The plane of projection is defined by the spacecraft trajectories and the sun comet direction. For Halley, inbound *Giotto* results (Shock and mystery boundary) and for P/Grigg–Skjellerup Giotto results (mystery boundary) were taken to put the boundary positions. Positions from the other spacecraft are added when available. 'Dusk' side is on the bottom part of the Figure and 'dawn' side on the upper part. For P/Halley the *Giotto* trajectory is from dusk to dawn while it is from dawn to dusk for P/Grigg–Skjellerup (after Glassmeier et al., 1997).

account the limits of the fluctuations due to the solar wind variations. It is then possible to conclude that a transition, about half way between the shock and the comet nucleus, appears as a unexpected permanent global feature of the active comet's plasma environment near 1 AU from the Sun. Unfortunately a satisfactory explanation of this feature of the cometosheath is still an open issue and deserves more theoretical work.

Schmidt and Wegmannn (1982) gave not only the prediction of the interfaces of bow shock and contact surface but also the interpretation of their physical nature and how they scale with the gas production rate. Galeev (1986), and Schmidt-Voigt (1989) has generalized the scaling law for the boundaries. For comets with

a gas production rate of about 10^{29} particles s^{-1} (the so-called linear comets, this includes comet Halley) the shock stand-off distance RB is given by:

$$R_B = \frac{G m_c \sigma (\gamma^2 - 1)}{4\pi v_c \rho_{sw} v_{sw}} . \tag{4.1.196}$$

Here, m_c is the mean mass of the cometary ions, σ the ionization cross-section of the corresponding neutral parent, γ the ratio of the specific heats, v_c the outflow speed of the neutral parent and $\rho_{sw} v_{sw}$ the solar wind flux density. For the linear comets R_B provides a natural length scale and R_B / v_{sw} natural temporal scale. Therefore, because the solar wind conditions were not too different during the cometary encounters, all discontinuities in all encountered comets should scale with the gas production rate. This provides a justification and an internal check for the linear scaling of Figure 4.1.5.

4.1.6. *The 'Magnetic Pileup Boundary'*

The second unexpected plasma feature around active comets is the 'magnetic pileup boundary' (MPB) in the inner cometosheath. This strong magnetic discontinuity, was first observed by *Giotto* at comet Halley; it appeared as a thin and sharp boundary at a distance of 1.35×10^5 km from the nucleus on the inbound leg of the trajectory (see Figure 4.1.2, at 23:30 SCET) where a strong jump of the magnetic field strength was observed (Neubauer, 1987) correlated with dramatic changes in the electron plasma properties (Mazelle et al., 1989). Also a proton density decrease was reported from both the ion plasma analyzer and the ion mass spectrometer. However, no clear effect on the heavy cometary ions has been observed (e.g., Coates, 1997; Neugebauer et al., 1991). The magnetic pileup boundary, while being the stronger magnetic field signature reported around an active comet as is obvious in Figure 4.1.2 is not present in any MHD simulation so far.

The magnetic field observations at P/Grigg–Skjellerup are very similar (Mazelle et al., 1995) particularly on the 'dusk' side of the encounter (15:20 SCET) with a strong decrease of the magnetic field strength (Neubauer et al., 1993) and a sharp decrease of the mean value of electron fluxes at all energies, at about 550 km from the nucleus (Rème et al., 1993). The 'dawn' crossing of the MPB is also clearly observed at comet P/Grigg–Skjellerup but less well defined or questionable for the outbound part at comet Halley. Strictly the same 'dawn/dusk' asymmetry was reported for the 'magnetotail' boundary crossed by ICE (e.g., Slavin et al., 1986). Inspection of Figure 4.1.2 enforces the suggestion first made by Neubauer (1987) that the MPB on the dayside could be connected to the magnetotail boundary. Moreover for P/Giacobini–Zinner, Slavin et al. (1986) have shown that a significant Alfvén draping of the magnetic field is observed only inside this magnetotail boundary with clearly defined magnetic lobes of opposite polarities around the dense plasma sheet. In the induced magnetosphere of a comet, IMF draping leads to a correlation between the local radial component of the field and the component parallel to the flow. Studies of the draping at comet Halley from the *Giotto* magnetic

field data (e.g., Israelevitch et al., 1994) have shown that there was no correlation at all between the radial component and the parallel components of the field outside the MPB whereas a strong linear correlation is obtained inside the pileup region. Thus the MPB can also represent a boundary inside which the magnetic field drapes strongly around the contact surface which was not predicted by models and could be alternatively named the 'draping boundary'. More, the relative distances of the boundary crossings for the three comets scales very well with the gas production rate, as can easily been checked from Figure 4.1.2, showing definitively the cometary nature of the boundary seen at Halley. It must be mentioned however, that the *Vega-1* and *Vega-2* magnetic field profiles reported at Halley were very different and curiously represent now the only data set that more or less reproduces the predicted magnetic pileup profile before any cometary encounter from single MHD calculations. No sharp increase of the magnitude comparable to the MPB was reported but only a gradual increase (Riedler et al., 1986). However a significant draping feature has also been reported by Schwingenschuh et al. (1987) during the *Vega-1* encounter. Also, the *Vega-2* magnetometer data are incomplete due to a damage of the triaxial sensor before closest approach. Also, modifications of the properties of the low-frequency waves were reported in this region from all data sets as, e.g., very similar compressive wave patterns observed close to the MPB at Halley and P/Grigg–Skjellerup (Glassmeier et al., 1993; Mazelle et al., 1995).

The similar planetary case is discussed in Section 4.3.

4.1.7. *The Cometopause*

The cometopause denotes a sudden change in ion composition observed by the *Vega-2* spacecraft at a distance of 1.6×10^5 km from the nucleus (Gringauz and Verigin, 1991). Before this 10^4 km thick layer the protons, behind it heavy ions of cometary origin were the dominant ions. No change was observed in the electron component, neither in the magnetic field, the cometopause is not a MHD type boundary, it was termed 'chemical boundary'. There were, however, significant electric field oscillations in the lower hybrid frequency range (8–14 Hz); this was attributed to fire hose instability by Galeev et al. (1988). During the Giotto flyby of comet Halley there was a much more gradual change between the proton and the heavy ion dominated regions, *Vega-1* was not operational there. The *Giotto* probe did not observe cometopause-like boundaries during the other cometary encounters.

The *Vega-2* observation could easily be classified as a temporal variation due to the solar wind conditions. There are, however, a few factors making us more cautious. The first one is that the cometopause is very similar to the upper boundary of the dayside mantle of non-magnetic planets (cf., Section 4.3) in many respects. The second one is related to the intense cometary X-ray radiation observed in the dayside cometary magnetospheres.

The model of Shapiro et al. (1999) shows that sufficiently close to the cometopause approximately 10% of the solar wind electrons are accelerated to the en-

ergies exceeding 100 eV due to the lower hybrid waves. These energetic electrons penetrating into dense cometary atmosphere are capable of producing a strong soft X-ray emission by combination by bremsstrahlung and K-shell line radiation. This model is one of the possible explanations of the strong cometary X-ray emissions recently observed, first from the comet P/Hyakutake, and later on from the whole bunch of other active comets. Therefore, it is possible that the cometopause is a general phenomenon at comets, however, the sharpness of the boundary depends on solar wind conditions. There were no electric field measurements on *Giotto* what probably could have settled the issue.

4.1.8. *Pick Up Ion Distributions*

The study of mass loading processes was very much intensified after the cometary flybys. In this part we shall discuss how well can the theory presented in the previous sections account for the observations. The three cometary encounters represent different conditions in cometary emission, in the solar wind conditions, and in the size of the interaction volume available for pickup. We shall address below a number of questions emphasizing the discrepancies rather then the agreements between observations and theory.

4.1.8.1. *The isotropy of ion emission.* Cometary activity is anisotropic; the activity depends on surface characteristics, solar illumination angle, rotation state, etc. There are known variations in the neutral gas escape velocity: the majority of atoms leave the cometary atmosphere with an expansion velocity of the order of 1 km s^{-1}, but H atoms coming from the photodissociation of OH radicals leave with a velocity of about 8 km s^{-1}. The chemistry of CO_2 may also lead to C and O atom escape velocities in the 6 to 10 km s^{-1} range. However, the results of the plasma experiments in general do not reveal any anisotropy, and this is sort of a mystery.

4.1.8.2. *Observation of shell distributions.* The naive approach is that no matter where the actual measurement is made, ions, picked up before and swept back by the solar wind, should mask the place of the local injection point in the ion distribution. In reality, however, to assess the shape of the distribution one has to compare the time τ_c (what the ions spend in the solar wind after their birth) to the time τ_{pd} necessary for pitch angle diffusion, as given by Equation (3.4.180). This analysis was done among others by Galeev et al. (1991); using the formula

$$\tau_c = \frac{\int \mathrm{d}l \; l \exp(-r(l)/L)/r^2(l)}{v_g \int \mathrm{d}l \; \exp(-r(l)/L)/r^2(l)} \,, \tag{4.1.197}$$

where $r(l)$ is the distance form the nucleus, v_g is the gas expansion velocity, τ is the ionization time, and $L = \tau v_g$. The integration is along the path of incoming ions.

For heavy ions during the Halley flybys $\tau_{pd} = \tau_c$ at about 3×10^6 km from the nucleus, and $\tau_{pd} < \tau_c$ for smaller distances. This means that in the latter case the pickup ion distributions are shell-like, whereas farther away the freshly injected ions dominate. This is in harmony with the observations.

Whereas the overall characteristics of the wave perturbations during the cometary encounters are identical, the actual wave forms observed were different, as well as the strength of the magnetic perturbation. This yielded a reduced pitch angle scattering for the P/Giacobini–Zinner and the P/Grigg–Skjellerup encounters.

The situation is more controversial for pick up protons. The diffusion time τ_{pd} is proportional to the mass, so protons should scatter faster in pitch angle than heavy ions. It is true that protons may have different sources, and for those coming from the 'fast H' population v_g is also higher. However, as presented by Neugebauer et al. (1989) the *Giotto* measurements seem to indicate a different tendency. Ziebell et al. (1990) suggested that for protons a partially filled shell can be a time-asymptotic state. The clear-cut resolution of these controversies, however, is still missing.

4.1.8.3. *Observation of bispherical shells.* An indicator of the presence of a bispherical distribution is the bulk velocity of the pickup ions in the solar wind frame of reference. If this is equal to the injection velocity, that indicates a ring distribution, if it is zero, it indicates a shell, whereas if it is between zero and v_A, corresponding to Figure 3.3.1, it indicates the presence of a bispherical shell.

This analysis has been performed by Coates et al. (1990) using the Giotto data. The conclusion was that well upstream the distribution retains ring like features, the water group ions became more isotropic inside of approximately 2.5×10^6 km, and inside the bow shock the distribution is bispherical to a good approximation.

A similar analysis has been done by Tatrallyai et al. (1999) using the data of the PLAZMAG instrument carried onboard of the *Vega-1* and *-2*. The ion spectra collected downstream of the shock by these sensors clearly show the combined effects of solar wind particles and cometary pickup ions, because there was no mass selection. A simple model calculation was performed by Tatrallyay et al. (1999) for the separation of the different ion components, assuming a drifting Maxwellian for the solar wind protons and alpha-particles, while the pickup ions were described by a bispherical shell distribution. These combined distributions were fitted to the data. During the two encounters the solar wind conditions were different both in velocity, density, and the direction of the magnetic field relative to the flow direction (accordingly the Alfvén velocity was different as well). The fits are reasonable good, clearly showing the importance of the Alfvén velocity vector when fitting a bispherical shell distribution.

4.1.8.4. *The bulk velocity of the shells.* Data presented above seem to indicate that the heavy ion pickup distributions are in harmony with theoretical expectations, the shell accommodates to the solar wind. There is, however, a striking ex-

ception: the IIS time-of-flight sensor of JPA instrument onboard of *Giotto* detected a bifurcation in the ion energy spectra in the cometosheath region (Thompson et al., 1987). The current interpretation is that the upper branch is comprised of pickup ions accommodated to the solar wind upstream and retaining their velocity, whereas the lower branch corresponds heavy ions picked up downstream, accommodating to the local solar wind velocity. This, however, means that the ion shell velocity may differ from the solar wind velocity under certain conditions. There is no theoretical explanation to this as of today.

It is also interesting to note that downstream, where V_A is comparable to the shocked solar wind velocity, there is no clear 'wind direction'. Portions of the heavy ions moves with the upstream solar wind velocity, two other portions 'blow' with $v_{sw} \pm v_A$, whereas the shocked solar wind protons move with v_{sw}, and all these mean different directions as well. This complicated wind structure invalidates MHD models, and might also complicate the calculation of pressure balance at discontinuities. This complex wind structure may be present also in the magnetosphere of giant planets.

4.1.8.5. *Observation of diffusion in energy.* It was discussed in Section 3 that diffusion in energy takes $(v_{sw}/V_A)^2$ times longer than pitch angle diffusion in the quasilinear model. However, measurements made by the EPAS instrument on the ICE spacecraft during the flyby of comet Giacobini–Zinner do not support this (Cowley et al., 1991). Well upstream of the comet EPAS measured ion fluxes with energies well above the upper limit of both the ring and the shell distributions; clearly indicating diffusion in energy. On the other hand, the ion fluxes correlated well with the angle subtended by the solar wind and magnetic field directions, as if shell distributions have not yet been formed.

This contradicts to the simple quasilinear pickup picture, and might be indicative of the fact that nongyrotropic distributions may have important but yet undiscovered properties. Shevchenko et al. (1995), however, have pointed out that in certain non linear models energy diffusion is possible even in the case of nearly monochromatic wave spectrum what was observed during the P/Grigg–Skjellerup encounter. Energy diffusion requires that particles could jump between diffusion lines; in the quasilinear approach this is made possible by the excitation of a broad wave spectrum. In the model of Shevchenko et al. the diffusion is made possible by waves excited via bounce oscillations of resonant particles. The actual speed of energy diffusion relative to pitch angle scattering, however, requires further study.

4.2. NONLINEAR WAVES AT COMETS

In collisionless plasmas the incorporation of pickup ions into the host gas is done via the generation of plasma waves and subsequent scattering and diffusion due to wave-particle interaction. The unstable waves in the cometary case rapidly grow nonlinear and are of large amplitude. A detailed review of the properties of non-

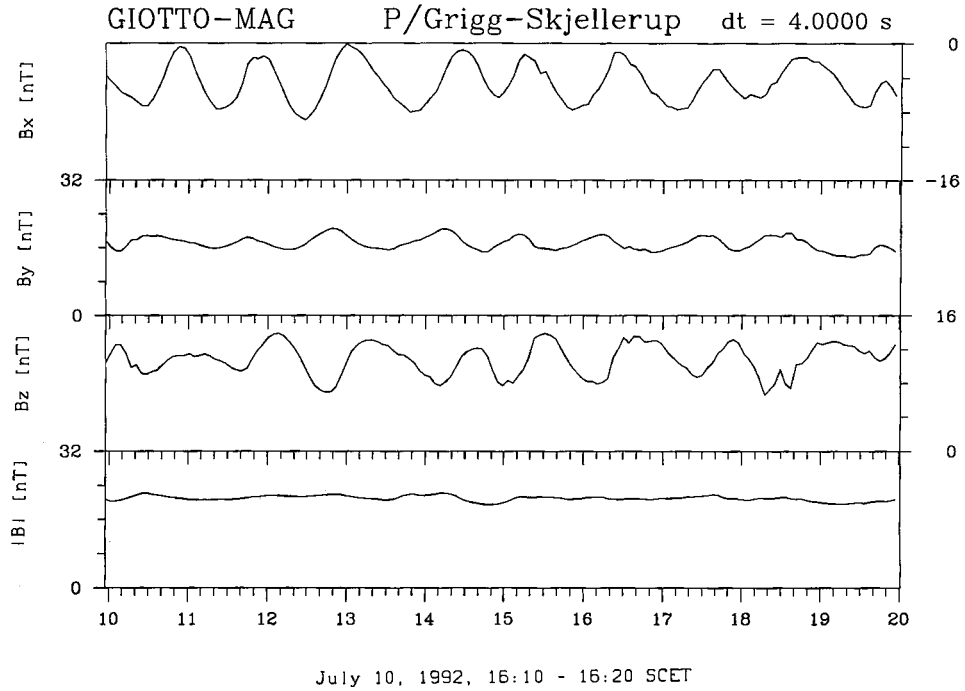

Figure 4.2.1. Magnetic field observations in the upstream region proper at P/Grigg–Skjellerup. Field values are given in nT.

linear waves is given by, e.g., Glassmeier et al. (1997). Here we briefly review the results.

The nonlinear nature of the H_2O group ion cyclotron waves at the three comets visited thus far are significantly different from each other. Comet P/Halley which had the highest neutral production rate at the time of encounter (two orders of magnitude higher than for P/Grigg–Skjellerup) had the lowest levels of nonlinearity but the highest level of turbulence (lowest coherency, close to zero). Comet Giacobini–Zinner (P/Giacobini–Zinner) which was intermediate in activity, showed systematic wave evolution as a function of inverse distance from the comet. This has been interpreted as a temporal evolution of the waves assuming that they are generated far from the comet ($\approx 10^6$ km) and develop as they are convected downstream by the solar wind. Comet P/Grigg–Skjellerup displayed large amplitude waves only quite close to the nucleus. The nonlinear aspects of these waves were only slight.

4.2.1. *P/Grigg–Skjellerup*

During the P/Grigg–Skjellerup encounter, the interplanetary magnetic field was nearly orthogonal to the solar wind flow direction and left-hand ion cyclotron waves were generated by a resonant instability involving the H_2O group pickup ions. Most of these waves far from the comet were propagating parallel to the

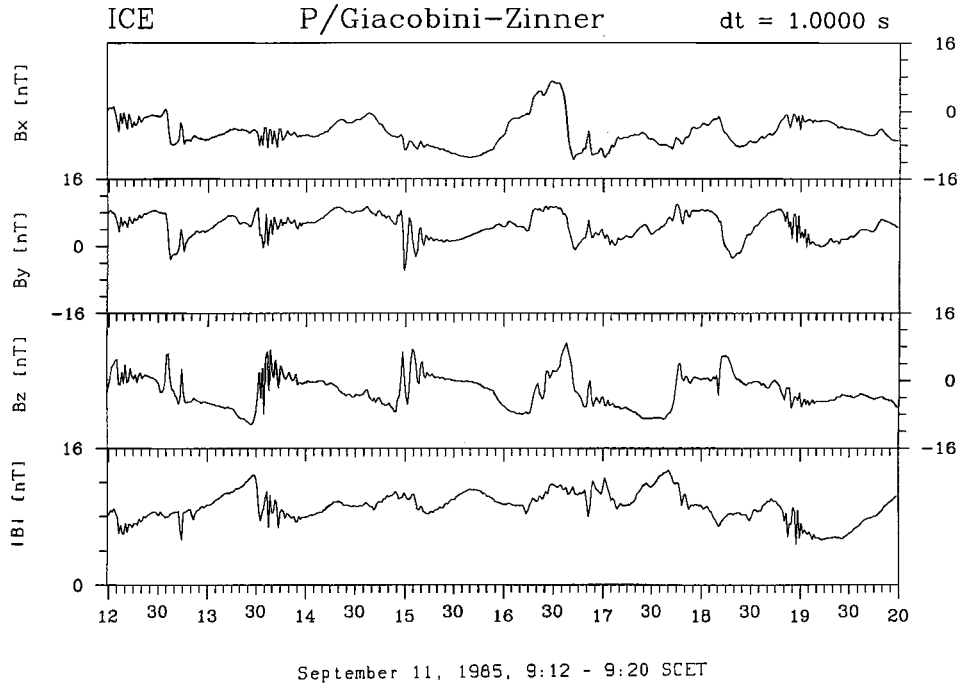

Figure 4.2.2. Magnetic field observations in the upstream region at P/Giacobini–Zinner. Field values are given in nT.

magnetic field, were sinusoidal and small-to-medium amplitude (Glassmeier et al., 1993; Neubauer et al., 1993). The largest wave amplitudes were detected just upstream of the bowshock. An example is shown in Figure 4.2.1. The peak-to-peak transverse variations are about 10 nT in an about 20 nT field. The waves are phase-steepened with the steepened edge at the trailing portion. If the waves are not Doppler shifted and are propagating past the spacecraft, this would correspond to the trailing edges of the waves being phase- steepened. For the left-hand mode waves, higher frequencies have lower phase velocities. Thus assuming nonlinear and dispersive effects are causing the generation of other frequency components away from the pump frequency, this explanation qualitatively explains the wave phase features.

It should be noted that the left-hand waves are slightly compressional. $\delta|B| \approx$ 2 nT in an about 20 nT field, or $\delta B/B \approx 0.1$.

4.2.2. *P/Giacobini–Zinner*

During the comet P/Giacobini–Zinner encounter, the magnetic field was in the Parker spiral direction (about 45°). Thus, the pickup ions generated right-hand (magnetosonic/whistler) mode waves through the resonant instability. When right-hand waves propagate obliquely to the ambient field, they are compressive. Such was the case for the nonlinear waves at P/Giacobini–Zinner. An example of P/Gia-

cobini–Zinner waves upstream of the bow-wave is shown in Figure 4.2.2. The H_2O group ion cyclotron period is approximately 100 s. At the trailing portion of the wave (in time), there is significant magnetic field compression ($\delta B/B \approx 0.5$), plus there are high frequency (about 3 s) oscillations. The latter are dispersive whistlers propagating away from the magnetosonic wave. The whistlers are circularly polarized and are not propagating in exactly the same direction as the magnetosonic wave. The magnetosonic waves and the attached whistler packets are propagating in the upstream (towards the Sun) direction, but are being blown back across the spacecraft by the solar wind. Thus, the magnetic field compressions and the whistler packets are detected last in time.

These H_2O group ion cyclotron waves are highly phase-steepened. Almost all (75–90%) of the phase rotation of the circular polarized wave occurs within the front-most 10% of the wave. This is in stark contrast to the waves at P/Grigg–Skjellerup (which were slightly phase-steepened). The wave phase-steepening occurred at the trailing edge of the left-hand P/Grigg–Skjellerup waves and not the leading edge as for the P/Giacobini–Zinner waves.

As the P/Giacobini–Zinner magnetosonic waves evolve further, other interesting features are noted. Figure 4.2.3 gives one example. The magnetosonic wave develops a double peak in magnitude and has the appearance that it is splitting into two parts. The hodogram at the bottom (from points 1 to 3) shows that there is an oppositely polarized wave present. This may indicate the onset of a decay instability (Spangler, 1998 and references therein) where the oppositely polarized wave is the backward propagating whistler mode component. Computer simulations by Omidi and Winske (1990) show similar wave splitting features. This is shown in Figure 4.2.4.

Two other nonlinear waves detected at P/Giacobini–Zinner were mirror mode structures and short duration large amplitude magnetosonic waves (SLAMS) (Schwartz et al., 1985). The former were detected near the high field magnetotail (well within the sheath) and the latter near the outbound bow shock/wave.

The mirror mode structures are shown in Figure 4.2.5. Four cycles are identified to the right of the vertical dashed line. The plasma pressure (taken to be $6n_e k_B T_e$) is out of phase with the magnetic field magnitude (and therefore magnetic pressure). The variations of the magnetic field strength are about 10 to 1, thus the magnetic pressure measure variations are as high as 100:1.

An example of a compressive SLAM, a short-duration, large amplitude magnetosonic wave, is shown in Figure 4.2.6. The compressive wave is more-or-less symmetric and is highly compressive. The peak magnetic field intensity is 4 times the background field intensity on either side. The waves are right-hand (in the spacecraft frame) circularly plane polarized and are propagating in a highly oblique direction relative to the ambient magnetic field. P/Giacobini–Zinner was the only comet where such waves were detected. Because the interplanetary magnetic field changed direction shortly before the SLAMS were detected, it has been speculated

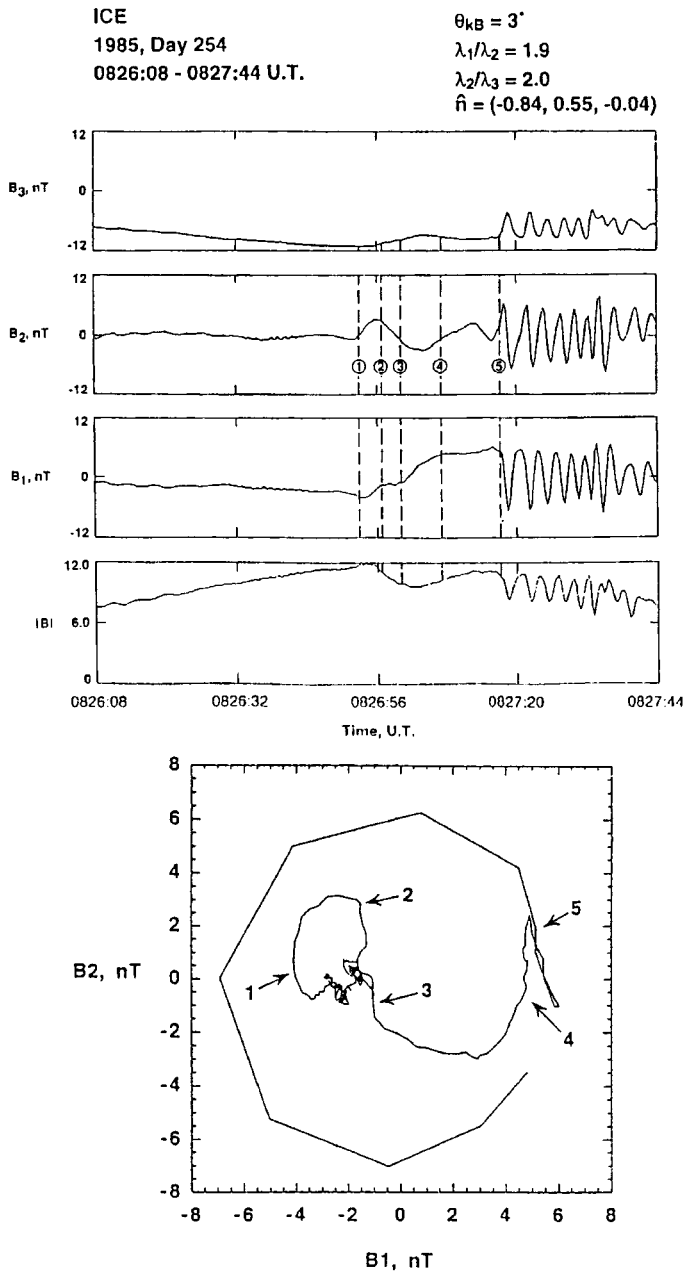

Figure 4.2.3. A complex magnetosonic wave with spitting characteristics. *Top*: wave form, *bottom*: hodogram.

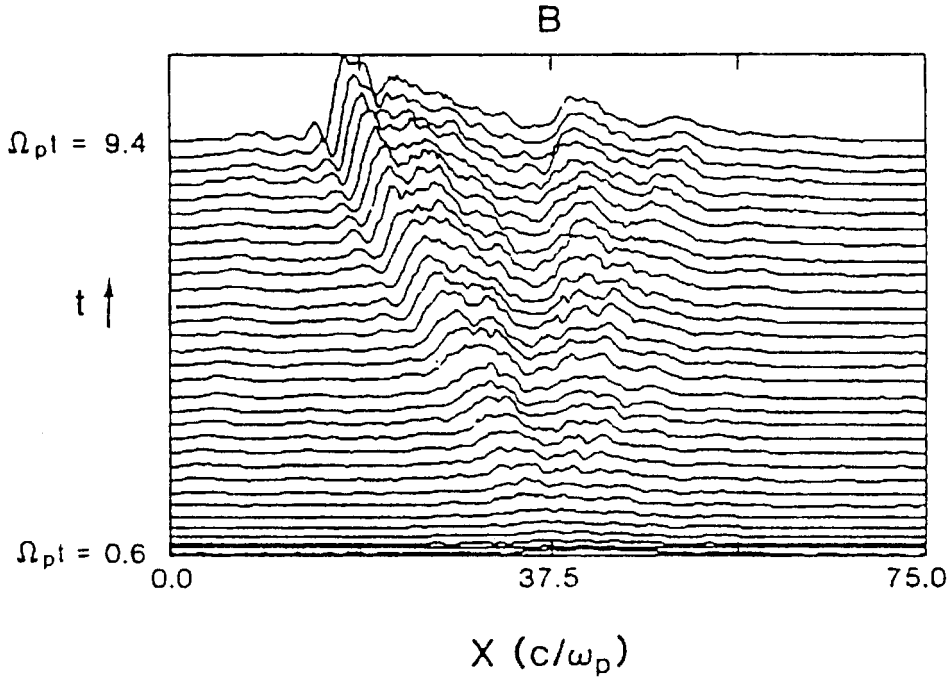

Figure 4.2.4. Wave splitting observed from computer simulation results (after Omidi and Winske, 1990).

that the SLAMS may play a role in the reformation of the cometary bow shock. They may be part of the shock itself.

4.2.3. *P/Halley*

The 'turbulence' at Halley is not understood at this time. The interplanetary magnetic field was in the Parker spiral direction, so one would expect the generation of right-hand magnetosonic waves as for P/Giacobini–Zinner. However, no such periodic waves were detected at Halley.

One can only speculate about the development of turbulence at Halley. The nonlinear wave splitting as shown at P/Giacobini–Zinner, the detachment of the whistler packets, and the interaction of the magnetosonic waves with each other are all possibilities.

Glassmeier et al. (1996) have demonstrated from Elsässer variable (e.g., Elsässer, 1950; Marsch and Mangeney, 1987) analyzes that there is definite wave power at the H_2O ion gyrofrequency pump period (about 100 s) and that the average polarization is linear. Following this clue, further analyzes were performed to attempt to see if there were 'patches' of the Halley waveforms that might give a hint of their development into turbulence. Two such wave forms and their corresponding hodograms are given in Figures 4.2.7 and 4.2.8.

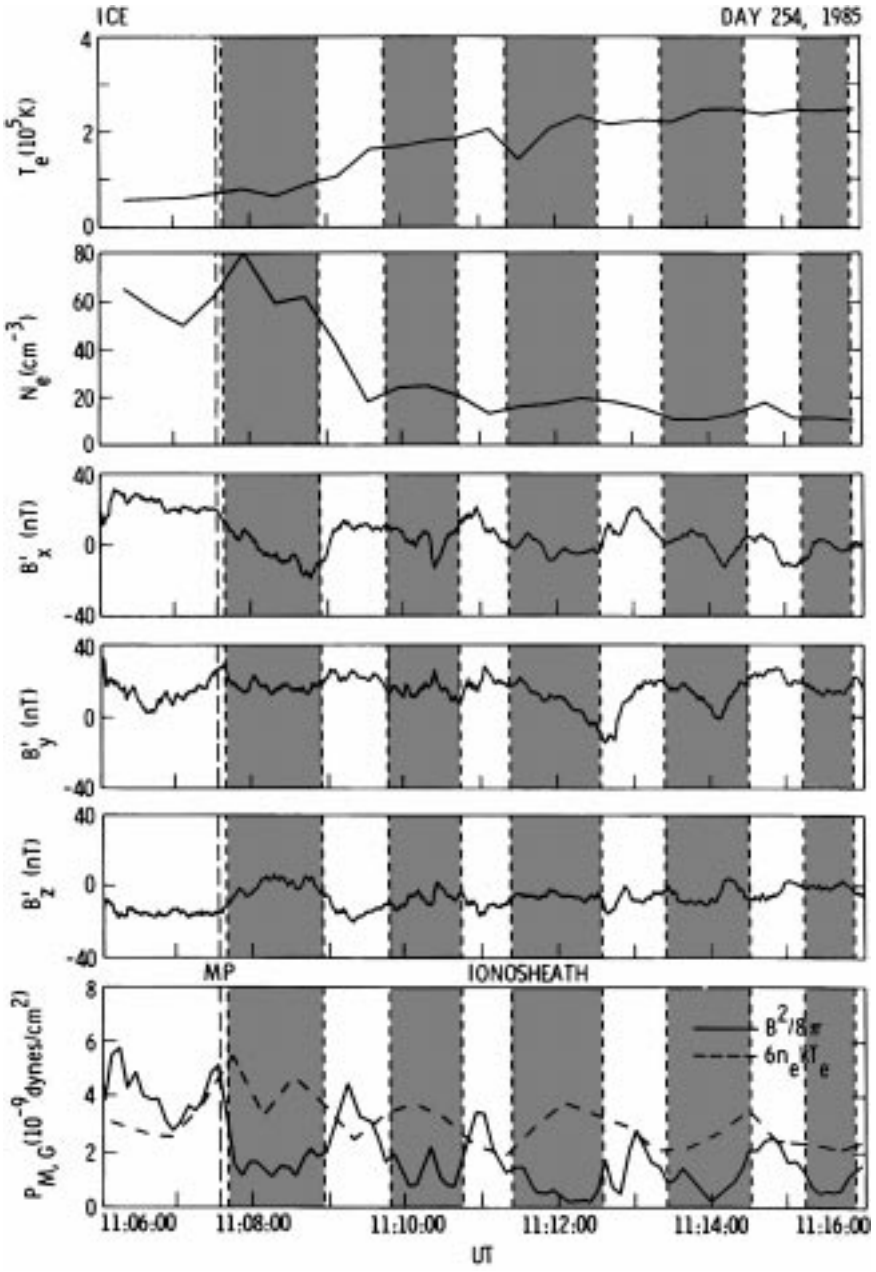

Figure 4.2.5. Mirror mode structure at P/Giacobini–Zinner.

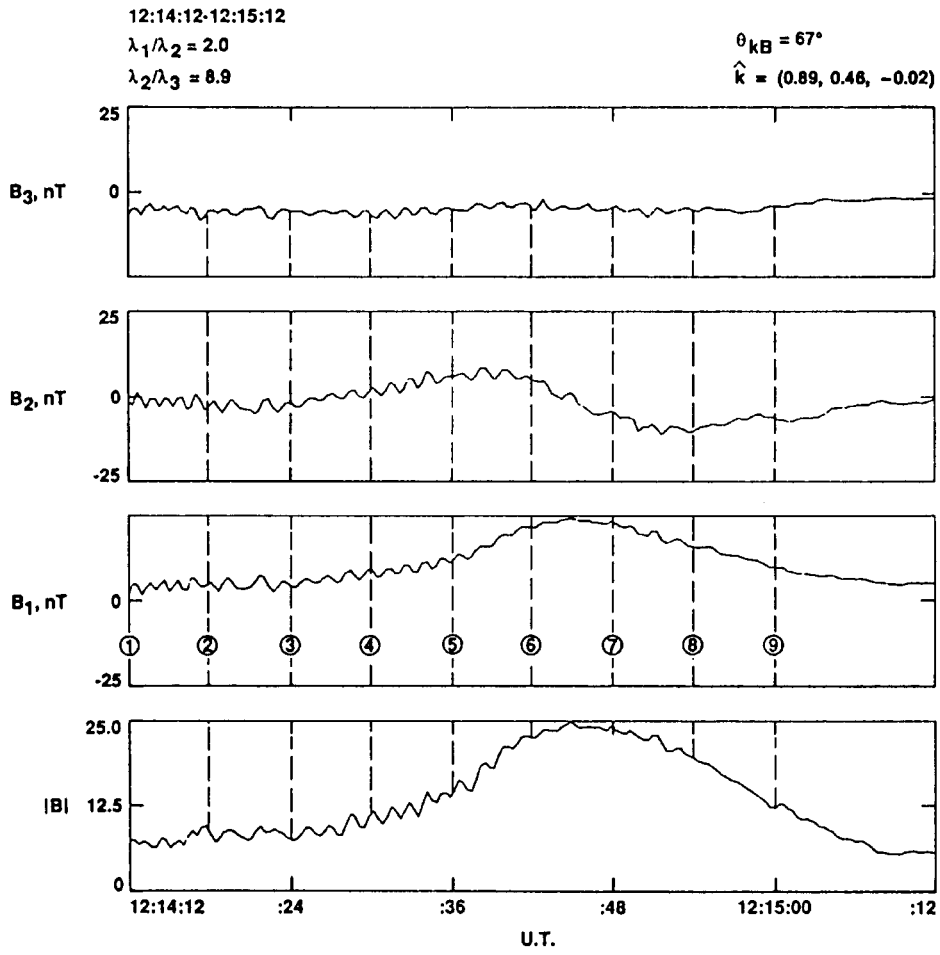

Figure 4.2.6. An example of a magnetic pulse, a compressive SLAM-structure at P/Giacobini–Zinner in principal axis coordinates (after Tsurutani et al., 1990).

Figure 4.2.7 shows a phase steepened wave where the full 360° of phase rotation occurs in a 30 s period. The polarization has an arc-polarization, a feature which will be discussed further later. The peak-to-peak (B1) wave amplitude is about 9 nT in a 7 nT field. So for this isolated case, note that there is a 2 nT compressional component at the phase steepened edge.

Another type of wave form is found further from the nucleus. This example is given in Figure 4.2.8. The peak-to-peak transverse (B1) amplitude is about 4.5 nT in a 6.5 nT magnetic field. The wave has strong compressional components. This has been interpreted as a phase steepened wave with most of the phase rotation occurring in about 25 s.

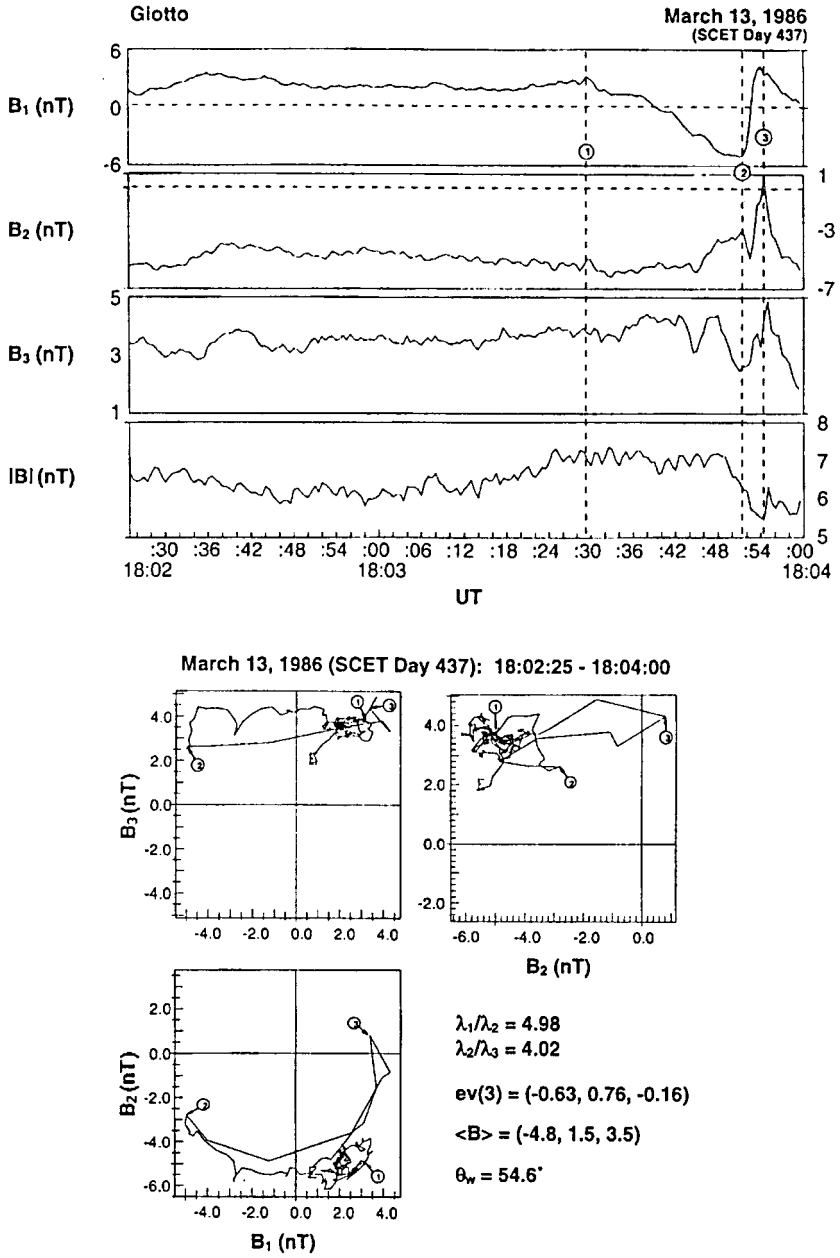

Figure 4.2.7. A low-frequency wave at P/Halley, displayed in minimum variance coordinates. The hodogram at the bottom indicates that the highly nonlinear wave is arc-polarized. Most of the phase rotation occurs at the trailing portion of the interval, between points 2 and 3 (after Tsurutani et al., 1997).

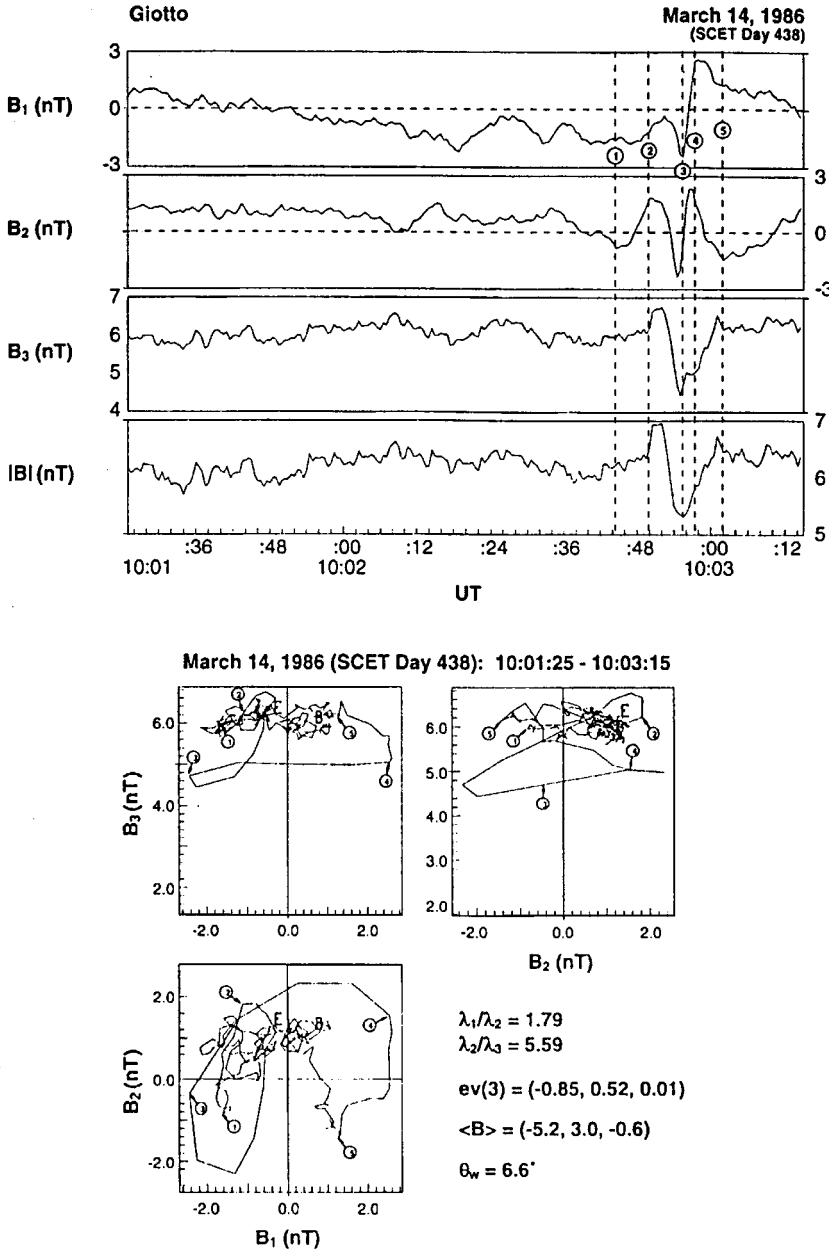

Figure 4.2.8. A low-frequency wave at P/Halley, displayed in minimum variance coordinates. The polarization is left-handed in the spacecraft frame and has some properties similar to arc-polarization. The wave is phase-steepened and nonplanar (after Tsurutani et al., 1997).

The polarization is very unusual. It appears like a 'sunglass' shape. Similar forms have been described by Hada and Mjoelhus (1996) using Derivative Nonlinear Schroedinger (DNLS) formulations. Whether this wave is evolving toward an arc polarization or not cannot be known at this time.

The next stage in understanding the development of cometary turbulence will probably not come until we have further measurements from the Rosetta mission. There, the waves and turbulence evolution can be studied as the comet becomes more active as it approaches the sun.

4.3. MASS LOADING AT PLANETS

Mass loading at planets differs both from the cometary and the interplanetary cases, and evidently depends on the size of the magnetosphere of the planet. The source of the pickup ions is generally the neutral corona, although in several cases the moons and satellites of the planets also contribute as sources. Planets with significant intrinsic magnetic fields, such as the Earth or any of the gas giant planets, have large magnetospheres which shield those planets and their neutral atmospheres from direct interaction with the solar wind. On the other hand, the solar wind is able to interact directly with the ionospheres and atmospheres of planets such as Venus, Mars, and probably Pluto, which have only weak intrinsic magnetic fields. The neutral corona is comprised of several components: cold atoms escaping from the exosphere; hot atoms coming from different chemical reactions or resulting from ion-neutral reactions in the ionosphere and momentum transfer by the solar wind to neutral gases. The probability that an ion is produced at the height h is proportional to $f_{\mathrm{tot}} n_{\mathrm{ion}}(h)$, where f_{tot} is the total ionization rate, combining the results of different processes such as photoionization by solar extreme ultraviolet radiation, impact ionization, and charge exchange processes (see, e.g., Bauske et al. (1998) concerning the relative importance of these processes).

A special type of mass loading takes place at the 'edge' of the flow in the case of non-magnetic planets (moons), where the shocked solar wind flow encounters planetary plasma near the ionosphere, and picks up planetary plasma via wave-particle processes. The solar wind (or other external plasma) slows down as a result of the momentum and energy transfer. The interaction volume is called the planetary mantle and this process is called 'laminar' pickup. Laminar pickup is always a collective plasma phenomena, which is not always true for $\mathbf{E} \times \mathbf{B}$ pickup that can sometimes lead either to collective plasma processes characterized by wave excitation, but not always to a significant extent.

In some cases the neutral corona extends far upstream, and therefore the solar wind slows down in front of the bow shock; however, other effects also contribute to this, or even dominate the observed deceleration of the solar wind. Therefore much care is needed whether or not to associate the decrease of the flow velocity to pickup processes.

TABLE 4.3.1

Solar system mass-loading environments. B = magnetic field strength, v = typical ion speed, Ω_g = gyrofrequency, r_g = gyroradius. For Venus and Mars shocked solar wind values were used for B and v, for comets the distance to the subsolar shock is used as the radius, for the heliosphere, the rough estimated distance to the heliopause/termination shock is used for the radius and for the B estimate

Planet/Object	Radius R (km)	Neutrals	B (nT)	Ω_g (s^{-1})	v (km s^{-1})	r_g (km)	r_g/R
Venus	6050	hot O	30	0.2	100	500	0.1
Mars	3400	hot O	10	0.05	100	1500	0.5
Pluto	1200	CH_4	1	0.01	400	10^5	100
Io	1800	$SO_2, \ldots$	2000	5	100	20	0.01
Titan	2575	N, ...	5	0.03	200	6000	3
P/Halley	3×10^5	$H_2O, \ldots$	10	0.05	300	6000	0.02
P/Giacobini-Zinner	5×10^4	$H_2O, \ldots$	10	0.05	300	6000	0.1
P/Grigg-Skjellerup	2×10^4	$H_2O, \ldots$	20	0.1	300	3000	0.2
Heliosphere	10^{10}	H, He	0.3	0.03	400	10^4	10^{-6}

In this section first we discuss the case when the bulk of the (shocked) solar wind flow gets loaded due to $\mathbf{E} \times \mathbf{B}$ and $\mathbf{E} \times \mathbf{B}$-induced collective pickup processes, and then we turn to laminar pickup processes.

4.3.1. $\mathbf{E} \times \mathbf{B}$ *and* $\mathbf{E} \times \mathbf{B}$*-induced Collective Pickup Processes at Planets*

The nature of the mass-loading varies from object to object, depending on the scale-size of the obstacle, type of neutral environment, and other characteristics. Table 4.3.1 compares some of the key characteristics of several objects/planets. The size of the object/obstacle is given, as is the species of the most important exospheric neutral. The speed of the external plasma flow is also given, as is the magnetic field strength in the external plasma. For the planets, the interplanetary field strength decreases with increasing heliospheric distance. Also shown are the approximate gyrofrequency of a pickup ion, the gyroradius, and the ratio of gyroradius to object size (r_g/R).

The efficiency of the initial ion pickup and assimilation process (and hence the degree of mass-loading) for an object/planet depends on the r_g/R ratio. Small values of r_g/R indicate that at least the initial $\mathbf{E} \times \mathbf{B}$ part of the pickup process is complete (i.e., a fully-formed ring-beam distribution exists) and even that wave-particle interactions have probably had time to act to further assimilate the pickup ions. In that sense r_g/R is a measure whether collective pickup processes set in, or the newborns can be considered in a test particle limit. On the other hand, large values of r_g/R (i.e., of the order unity or greater) means that a typical pickup ion

will not have undergone even a single gyration before the obstacle is encountered. In this case, pickup (and the associated mass-loading) is 'incomplete', the distribution function is non-gyrotropic, or even nonplanar in velocity space. Large values of r_g/R are found near Mars, Pluto, and Titan. Note that even when large values of r_g/R are present in the relatively unperturbed upstream flow, smaller values of this ratio will exist closer to the object where the flow has already slowed down. For the details of the pickup, however, it is important to take into account how the shocked solar wind velocity and the magnetic field varies within the magnetosheath, and whether the $\mathbf{E} \times \mathbf{B}$ force points towards or away the planets, therefore, whereas the r_g/R parameter is a good global indicator, the details of the actual pickup depend on the local geometry and plasma parameters.

Some specific examples of mass-loading at planets and satellites are provided next. In particular, we consider mass-loading at Venus, Mars, Pluto, Io, and Titan.

4.3.1.1. *Venus.* The solar wind interaction with Venus is shown schematically in Figure 4.3.1. (see review papers on this topic: Luhmann et al., 1997; Cravens et al., 1997a; Luhmann and Cravens, 1991). A very similar figure would apply to Mars. The intrinsic magnetic field of Venus is below detectable limits, and the main obstacle to the solar wind is the electrically conducting ionosphere. The boundary between the cold dense plasma of the ionosphere and the solar wind plasma is called the ionopause. A bow shock forms in the solar wind upstream of the planet. A magnetic barrier is formed above the ionopause due to the 'pile-up' of interplanetary magnetic field lines. Most of the solar wind dynamic pressure is converted into magnetic pressure in this barrier. Approximately co-incident with the magnetic barrier is a transition region called the plasma mantle. Both solar wind plasma and plasma of Venus origin are present in the plasma mantle. Mass-loading effects tend to be concentrated in this layer due to its proximity to the planet.

The most important neutral species for mass-loading at Venus (and Mars) is the non-thermal atomic oxygen populating the hot oxygen corona. Fast oxygen atoms are injected into the exosphere from the ionosphere (cf., Nagy and Cravens, 1988; Nagy et al., 1990). The exosphere is the atmospheric region where the atoms are collisionless and follow ballistic trajectories. Hot O atoms with energies of a few eV are produced by the dissociative recombination of O_2^+ ions with electrons. O_2^+ is the major ion species near the ionospheric peak on both Venus and Mars (cf., Brace and Kliore, 1991). Calculated hot O density profiles are shown in Figure 4.3.2. Hot oxygen calculations for Mars have been undertaken by a number of authors including Kim et al. (1998) and Nagy and Cravens (1988). Mass-loading of the solar wind results when these O atoms are ionized. Atomic hydrogen also is present in the exospheres of Venus and Mars, resulting in the presence of pickup protons near these planets. Wave activity, indicative of collective pickup, has not been observed in the magnetosheath.

The solar wind interaction at Venus, including mass-loading effects, was reviewed by Luhmann et al. (1997). Mass-loading is thought to increase the distance

of the bow shock from the planet and also to enhance the magnetic flux contained in the induced magnetotail. In fact, O^+ ions were observed in the magnetotail of Venus by the plasma analyzer onboard the Pioneer Venus Orbiter (PVO), indicating that planetary ions are indeed added to the solar wind flow near Venus. Test particle methods, hybrid simulations, gas dynamic global calculations, and MHD calculations have been applied to this problem. Spreiter and Stahara (1992) made global three-dimensional gas dynamic calculations, with and without mass-loading terms included, and demonstrated that the bow shock position moved outward slightly due to mass-loading. Murawski and Steinolfson (1996), Bauske et al. (1998), and Tanaka and Murawski (1997) came to similar conclusions using MHD models.

Moore et al. (1991) carried out a hybrid simulation of the solar wind interaction with Venus for the dayside region (see Figure 4.3.3.). This simulation included both solar wind protons and oxygen pickup ions. The location of the bow shock is clearly evident in the proton trajectories. The O^+ ions originate relatively close to the planet where the exospheric neutral density is highest. The gyroradius of a typical O^+ ion (also see Table 4.3.1) is comparable to the distance between the ionopause and bow shock (about 2000 km). These trajectories are asymmetric and depend on the direction of the motional electric field. For this simulation the upstream interplanetary magnetic field was directed into the page so that the motional electric field is directed upward. Consequently, newborn ions are accelerated northward and ions created below the planet have a good chance of running into the planet.

4.3.1.2. *Mars.* The solar wind interactions with Mars and Venus are thought to be similar (cf., Luhmann, 1992). Both planets have weak intrinsic fields, at least globally, so that the solar wind interacts directly with their atmospheres and ionospheres. Recent measurements made by the magnetometer onboard the Mars Global Surveyor (Acuña et al., 1998) indicate that Mars does not have a sufficiently large global-scale intrinsic magnetic field to significantly affect the solar wind interaction with that planet. However, these measurements show that Mars, unlike Venus, possesses significant, but highly localized, magnetic fields associated with the crust. Another difference between Mars and Venus is that the ratio of a typical gyroradius to obstacle size for a pickup ion is larger at Mars than at Venus (see Table 4.3.1). Consequently, finite gyroradius effects will be more important at Mars than at Venus.

Extensive plasma and field measurements were made in the vicinity of Mars during the PHOBOS-2 mission (Sagdeev and Zakharov, 1989). Particle instruments onboard PHOBOS (that is, the ASPERA, TAUS, and SLED instruments) observed planetary ions in the solar wind flow near Mars (cf., Dubinin et al., 1997). Cold heavy, planetary ions were observed to exist in the Martian tail (Lundin et al., 1990; Kotova et al., 1997) and probably originate in the ionosphere. More energetic pickup ions were also observed on both the dayside of the planet and in the tail (McKenna-Lawlor et al., 1998). The solar wind interaction with Mars has been

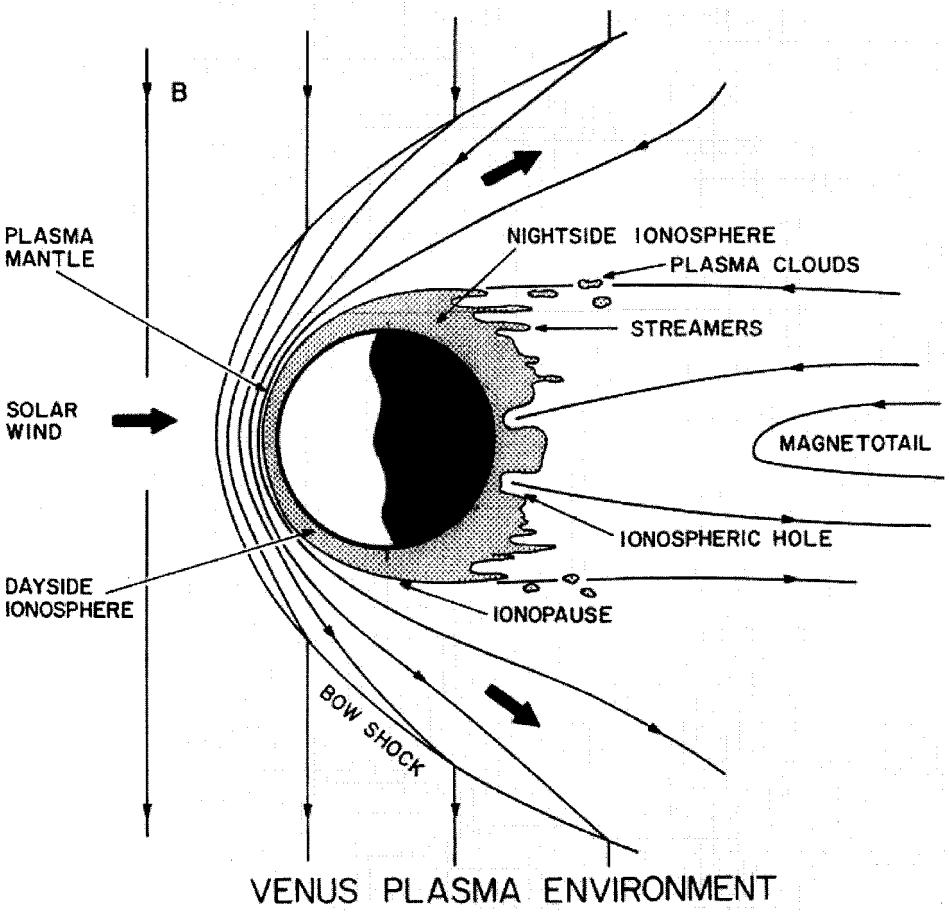

Figure 4.3.1. Schematic of the solar wind interaction with Venus (from Cravens, 1991).

studied using a variety of methods including test particle methods, fluid calculations, and hybrid calculations. For example, Sauer et al. (1997a) carried out bi-ion (protons and heavy ions) fluid modeling of the solar wind interaction with Mars, and hybrid simulations were made by Brecht and Ferrante (1991) and Brecht et al. (1993). Both the bi-ion fluid and the hybrid simulations show significant finite gyroradius effects, especially for heavy ions. For example, the bow shock is quite asymmetric.

Empirical models of the solar wind flow near Mars have also been constructed; Kallio et al. (1997) used such a model of the Martian plasma environment to estimate that about 1–3% of solar wind protons are lost to charge exchange reactions with exospheric oxygen ahead of the bow shock. The oxygen ions that replace the protons mass-load the solar wind plasma. Kallio et al. (1997) also estimated the energetic neutral atom fluxes produced by this charge exchange process. In a further study Kallio and Koshkinen (1999) analyzed in detail the possible O^+

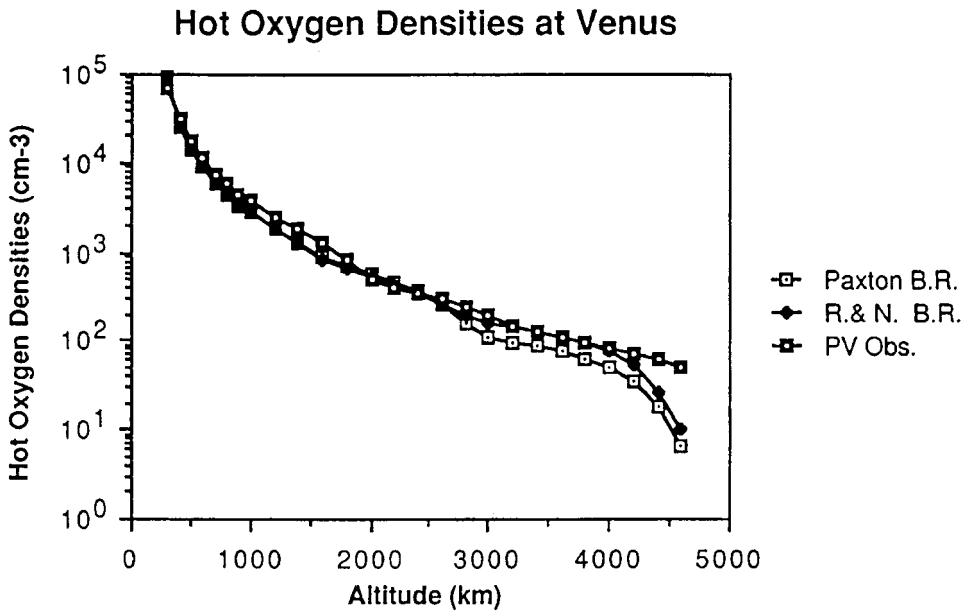

Figure 4.3.2. Hot oxygen density versus altitude for Venus (from Nagy and Cravens, 1988).

trajectories for $\mathbf{E} \times \mathbf{B}$ pickup at Mars; the orbits are reproduced here in Figure 4.3.4. It is visually evident from this that there is not enough room in the magnetosphere even for the development of a pickup ring; it is also instructive to compare this figure with the previous one for Venus, to appreciate the difference between Mars and Venus. Lichtenegger et al. (1997) made an estimate of solar wind depletion near Mars due to charge exchange.

4.3.1.3. *Pluto.* The important neutral species for the solar wind interaction with Pluto is probably methane (Stern and Tholen, 1997). The probable (but as yet unobserved) solar wind interaction with that planet is discussed in the review by Bagenal et al. (1997). The gravitational attraction of Pluto is low enough such that much of the CH_4 can escape from the planet, resulting in the production of a very extensive cometary-type atmosphere. Pluto is the only planet not visited by a spacecraft, and we have to rely on theory and analogies with other solar wind interaction scenarios to understand this interaction scenario. The exosphere of Pluto is thought to be extensive so that the solar wind interaction with that planet is probably comet-like. The striking feature of this interaction is that the ratio of a pickup ion gyroradius to the size of the planet is extremely large (Table 4.3.1). Hence, the pickup ion distribution function is expected to be highly non- gyrotropic and a purely fluid treatment of the mass-loading process cannot possibly be valid. Figure 4.3.5. shows a theoretical heavy ion distribution function calculated by numerically determining several thousand test particle trajectories (Kecskemety and Cravens, 1993). The particle distribution is clearly non-gyrotropic with more particles being present at

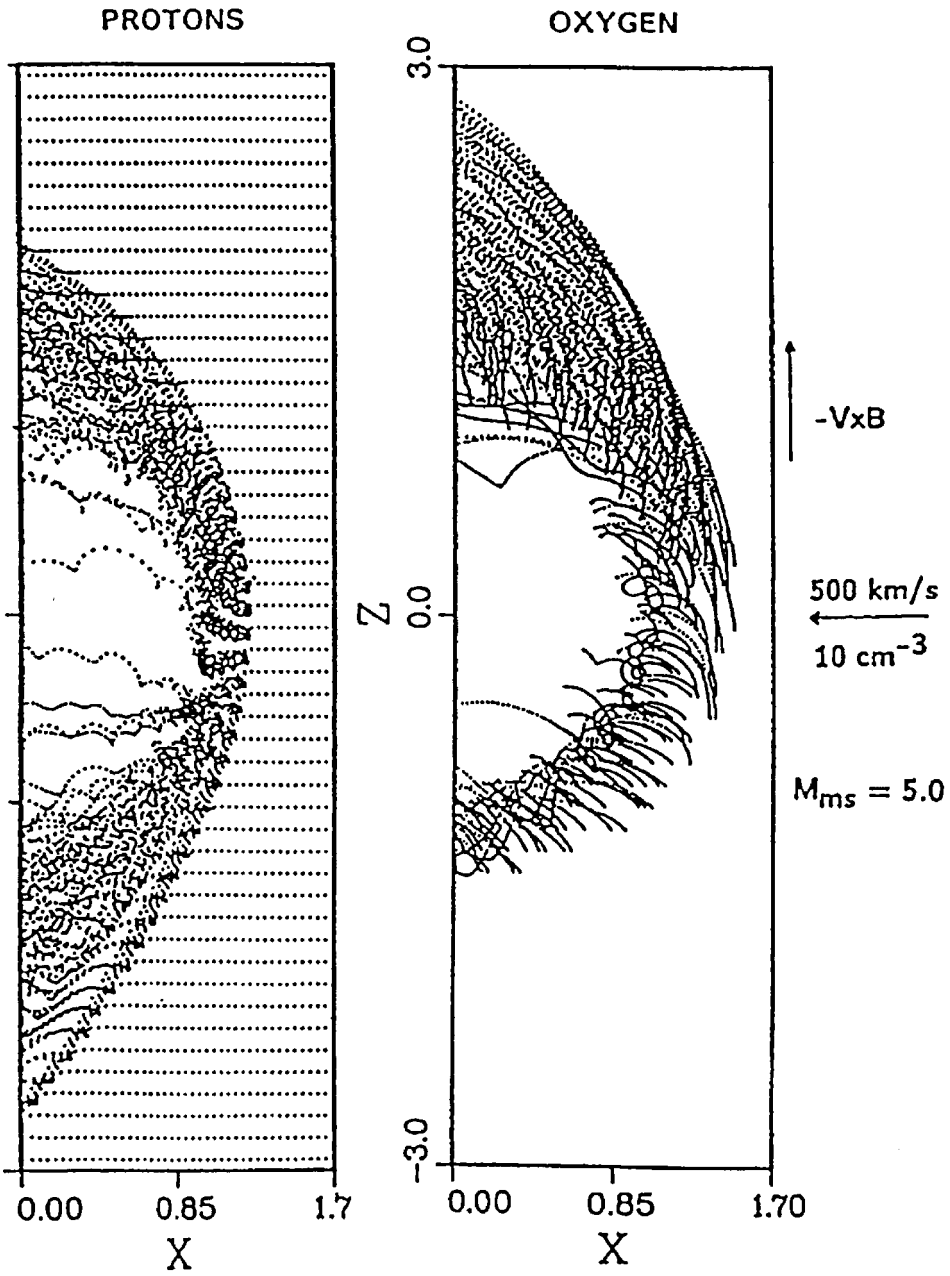

Figure 4.3.3. Proton and oxygen ion trajectories in the solar wind near Venus (from Moore et al., 1991).

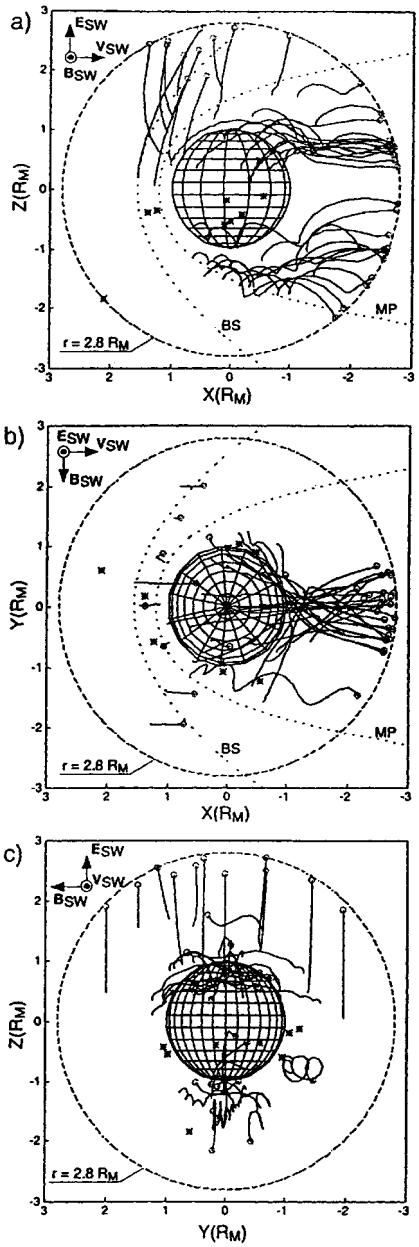

Figure 4.3.4. A few trajectories of O^+ test particles near Mars projected on (a) the $x - z$, (b) the $x - y$, and (c) on the $y - z$ plane. The dashed circle represents the projection of a spherical shell of a radius of 2.8 R_M on the $x - z$ plane where the location (open circles) and the velocities of the ions were recorded. The dotted lines show the magnetopause (MP) and the bow shock (BS). The stars show the starting points for the ions which hit the obstacle boundary. The solar wind parameters were $v_{sw} = 400$ km s^{-1} in the x-direction, and $B = 4$ nT in the y-direction (from Kallio and Koskinen, 1999).

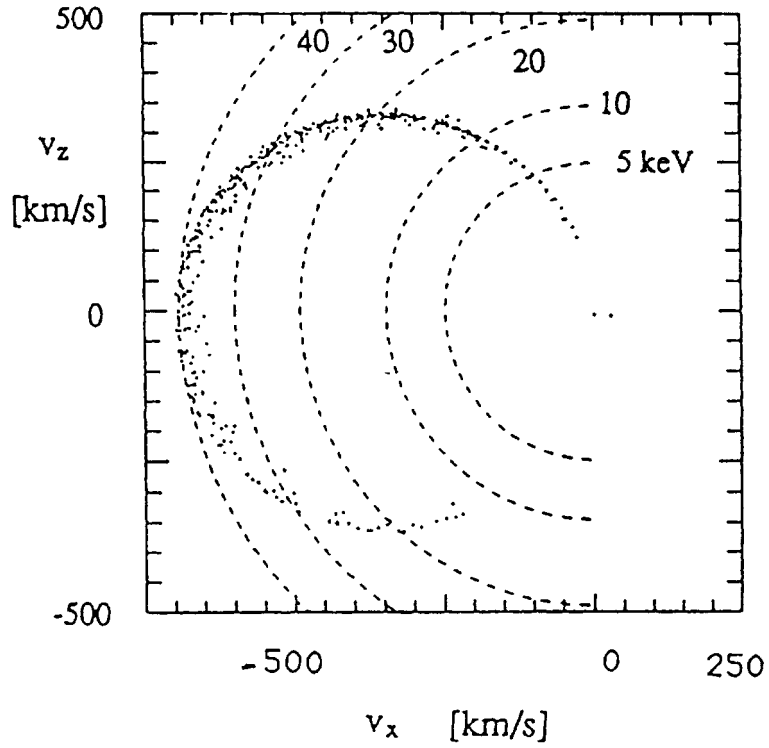

Figure 4.3.5. Velocity space distribution of pickup CH_4^+ ions upstream of Pluto (from Kecskemety and Cravens, 1993).

positive v_z (northward velocity) than at negative v_z. Low-frequency MHD waves were included in this calculation, but the distribution function was not significantly affected by these waves. Sauer et al. (1997b) carried out both a bi-ion fluid simulation and a hybrid simulation of the solar wind interaction with Pluto, and included heavy ions as well as solar wind protons. These calculations showed that the interaction region is highly asymmetric.

4.3.1.4. *Io.* The plasma flow within a magnetosphere can also be affected by mass loading if new ions are created within the magnetosphere. This is happening at both Jupiter and Saturn. The satellites of these planets are sources of neutrals which are ionized in the surrounding planetary magnetosphere. First, we will consider the effect of Jupiter's satellite Io on the Jovian magnetosphere.

The plasma in the inner Jovian magnetosphere to a very high degree co-rotates with the planet (Dessler, 1983), the plasma corotation velocity is approximately 74 km/s, which is greater than Io's orbital velocity (17 km s^{-1}), thus the torus plasma nominally flows by Io at a velocity of about 57 km s^{-1}. A region of enhanced plasma density (i.e., densities of about 2000 cm^{-3}) has been observed by several spacecraft (*Pioneer, Voyager, Ulysses*, and *Galileo*) to be present in the approximate

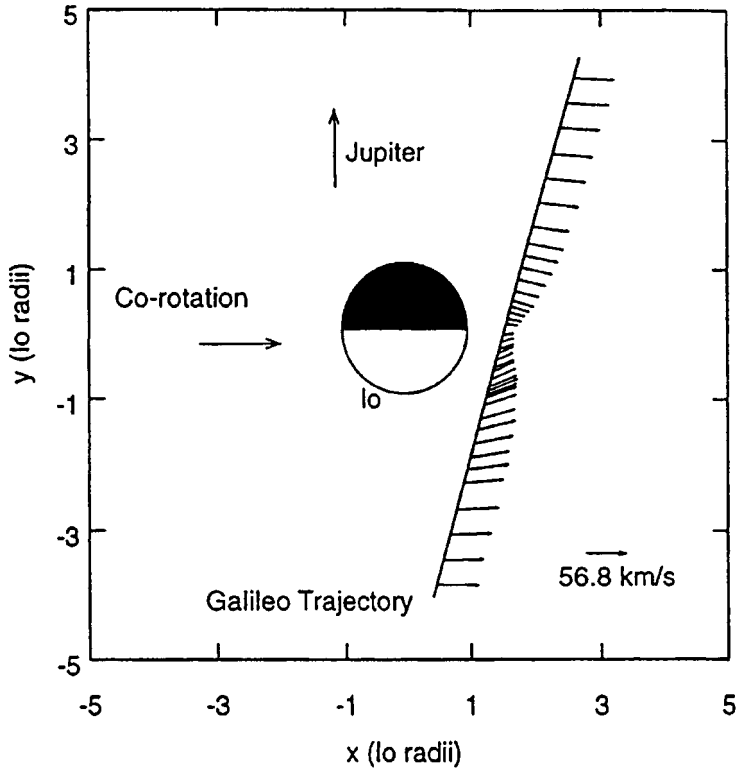

Figure 4.3.6. Velocity flow vectors downstream of Io from the MHD model of Combi et al. (1998).

vicinity of Io's orbit (Bagenal, 1985). The plasma in this region, known as the Io plasma torus, is known to largely consist of sulfur and oxygen ions (Bagenal, 1985).

The innermost Galilean satellite of Jupiter, Io, is known to have an atmosphere consisting of SO_2 and SO_2 dissociation products. Mass-loading of the inner magnetosphere takes place due to ionization of the neutral species, mainly due to electron impact collisions associated with hot magnetospheric electrons (Johnson, 1990). The mass addition associated with this ionization should lead to mass-loading effects not only in the Io torus as a whole but even more dramatically in the immediate vicinity of Io where the neutral densities are highest. In fact, *Galileo* mission plasma ion measurements showed that the plasma in Io's wake is significantly slower than in the surrounding magnetosphere (Frank et al., 1996).

Fluid methods are appropriate for studying mass-loading effects near Io since the gyroradius is rather small (Table 4.3.1). Both Linker et al. (1991) and Combi et al. (1998) have used MHD models to study the plasma-Io interaction problem. Figure 4.3.6. shows some calculated ion flow vectors in the wake of Io from the Combi et al. model. The slowing of the plasma in the wake, due to mass-loading, is clearly evident and agrees with the Galileo plasma measurements.

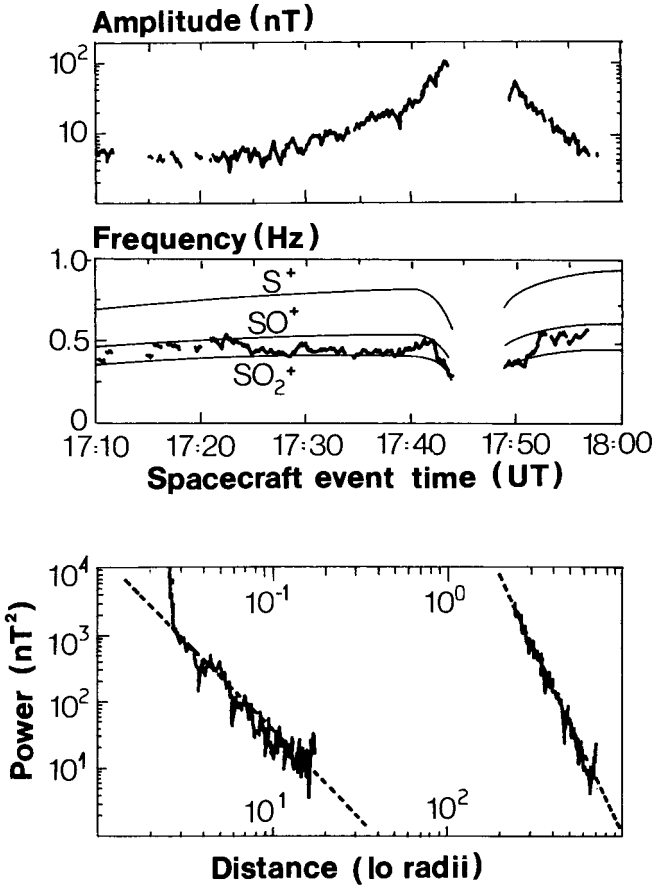

Figure 4.3.7. Ion cyclotron waves in the vicinity of Io. (A) The upper trace shows the magnetic field amplitude near the peak frequency, the lower trace shows the frequency of the spectral peak of a dynamic power spectrum, for frequencies above 0.3 Hz, and where the fractional polarization of the signal exceeds 0.5. Reference lines are plotted at gyrofrequencies of ions with mass per unit charge of 32, 48, and 64. (B) Power of the polarized signal versus distance in Io radii for the inbound (lower scale) and outbound (upper scale) portions of the flyby.

One complication that arises for mass-loading associated with satellites in planetary atmospheres is that the ionosphere of the planet itself can affect the mass-loading by means of the field-aligned currents linking the ionosphere and magnetosphere (Hill et al., 1983). The magnetic footprint of Io has been observed as a bright spot in near-IR images of Jupiter (Connerney et al., 1993) and has been explained as being due to particle precipitation associated with field-aligned currents flowing from the near vicinity of Io.

Recently the magnetometer onboard the Galileo probe measured clear signatures of wave activity due to pickup ions in the wake of Io (Kivelson et al., 1996). The spectral analysis of the ion cyclotron waves indicate the presence of gyrofre-

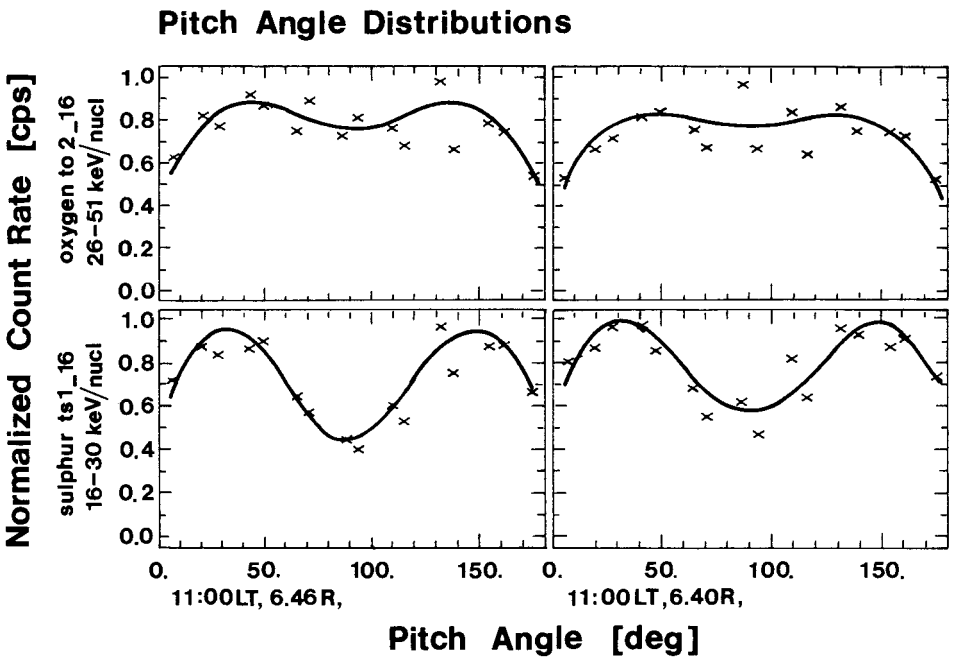

Figure 4.3.8. Pitch angle distribution for oxygen (top panel) and sulfur ions (bottom panel) for two successive time periods. The solid line indicates the fit to measured data (crosses) (from Lagg et al., 1998).

quencies of ions with mass per unit charge of 32, 48, and 64, corresponding, e.g., to SO_2^+, SO^+, and S^+ (Figure 4.3.7). The wave generation was analyzed by Huddleston et al. (1998) in the special corotation plasma environment, in which the background particle distribution was a warm Maxwellian, and the newborn ions a ring distribution, with appropriate velocity and temperature values. Otherwise the method described in Section 3.3. was used, and this model reproduced well the observations. The idealized pickup ion distributions were also calculated. These distributions were measured by the Energetic Particle Detector carried onboard *Galileo* (Lagg et al., 1998); the results are reproduced here in Figure 4.3.8. These distributions differ from a shell that is the distribution was not isotropic, the minima of the counts at low pitch angles are attributed to the interaction of the particles with the Jovian atmosphere via a pitch angle diffusion mechanism. The observed minimum at 90° pitch angle is interpreted as the result of a charge exchange interaction with the neutrals in the Io torus. This interpretation provides an estimate of the neutral density of the torus (about 35 particles cm^{-3}).

4.3.1.5. *Titan.* Titan is one of the largest satellites in the solar system. This satellite has a dense atmosphere (the surface pressure exceeds that of Earth) consisting mostly of N_2 but also with a few percent CH_4 (cf., Hunten et al., 1984). Titan is

also known to have a significant exosphere (e.g., Lammer and Bauer, 1991; Cravens et al., 1997b).

Titan orbits Saturn at a radial distance of 20.3 Saturn radii, close, but probably outside the region of simple corotating plasma. This makes it difficult to model the plasma impinging on the ionosphere, especially taking into account the effect of mass loading. At least at the time of the *Voyager* encounter, *Titan* was located in the outer magnetosphere of Saturn. *Titan* can also be located at times in the solar wind or in Saturn's magnetosheath. The *Voyager* spacecraft passed through the wake of *Titan* at a radial distance from *Titan* of about 2.7 Titan radii (see review by Neubauer et al., 1984). The plasma density was observed to be greatly enhanced in the wake and the magnetic field was observed to be strongly draped. The plasma flow speed was also observed to be much lower in the wake than in the surrounding magnetosphere. The ions in the wake/tail structure were observed to be primarily heavy ions (perhaps N^+) (Hartle et al., 1982), and the ion enhancements probably can be associated with the location of ions accelerated in the mantle by laminar pickup (see next section). All of these measurements point to the existence of significant mass addition to the flow by Titan. In fact, heavy ions were detected throughout most of the outer magnetosphere and not just in the immediate vicinity of the satellite.

A number of calculations of the external plasma interaction with *Titan* have been carried out recently, motivated by the recent launch of the *Cassini* spacecraft, now on its way to Saturn (and to *Titan*). For example, Keller and Cravens (1994) made one-dimensional, multispecies hydrodynamic calculations of ionospheric outflow into *Titan*'s wake. Ledvina and Cravens (1998), and Cravens et al. (1998), all carried out two- or three-dimensional global MHD calculations of the external flow interaction with *Titan*. The addition of new plasma to the flow was critical in all these calculations. Even though these calculations did reproduce some of the features of the plasma wake observed by *Voyager*, as Table 4.3.1 indicates, the gyroradius of a pickup ion is larger than the radius of *Titan* so that these fluid simulations are severely limited in their applicability to this problem, at least at larger distances from the satellite.

Luhmann et al. (1998) made test particle calculations of pickup ions near *Titan*, demonstrating that the size of a pickup ion gyro-orbit is large in comparison with the satellite and demonstrating that large asymmetries should be present in the particle fluxes around *Titan*. Ledvina and Cravens (1998) also carried out test particle calculations both for 'ambient' magnetospheric ions and for pickup ions born near *Titan*. Figure 4.3.9 shows the trajectory of a pickup N^+ ion first in an unperturbed uniform magnetic field and second in the motional electric field and the magnetic field taken from the three-dimensional MHD model of Ledvina and Cravens (1998). The ion trajectories are strongly affected by the field perturbations only in the immediate vicinity of *Titan* and in the immediate wake region (Ledvina et al., 1998).

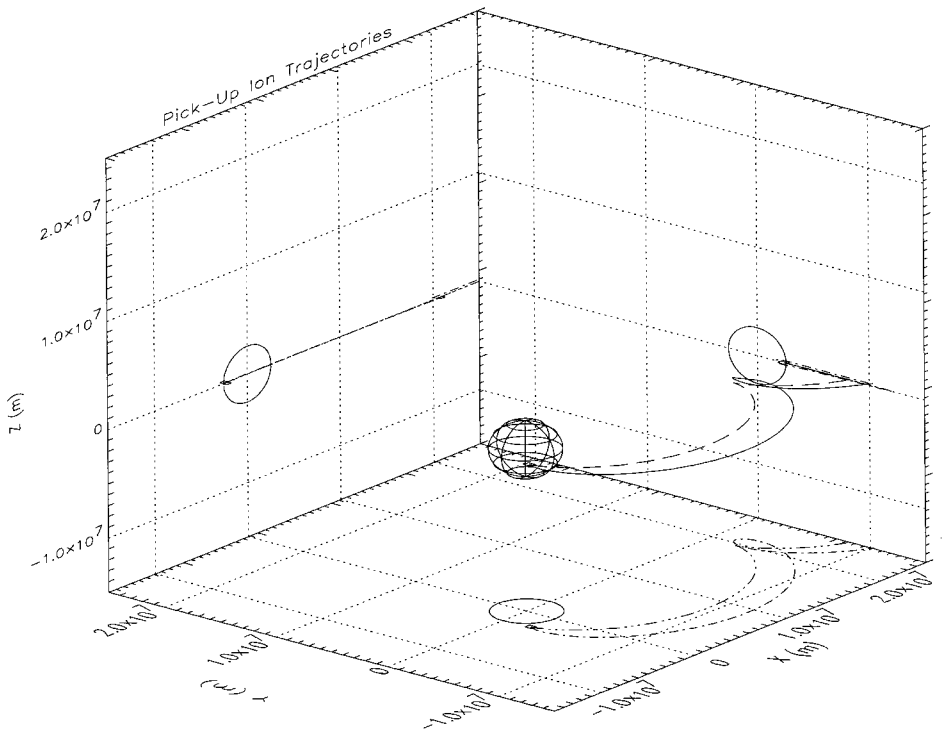

Figure 4.3.9. Two calculated N^+ trajectories in the vicinity of Titan are shown. The unperturbed magnetic field is vertical in this plot, and the co-rotating magnetospheric flow is from the left. The solid line shows a trajectory in the unperturbed flow field and magnetic field (both uniform in the calculation). The dashed line shows a trajectory that was calculated for the flow field and magnetic field from the three-dimensional MHD model of Ledvina and Cravens (1998). The fields from this model differ significantly from the uniform fields mainly in a wake region approximately the size of Titan.

4.3.2. *Laminar pickup*

4.3.2.1. *The mantle.* In the case of non-magnetic planets, the solar wind contacts directly the ionosphere, and the region where this direct contact takes place, is particularly interesting from the point of view of energy and momentum transfer. The properties and physics of this region, the so-called dayside mantle, is the subject of this section.

The lower boundary of the dayside mantle is the ionopause. In the literature there are several definitions available for this, such as the pressure balance ionopause (where the kinetic pressure of the ionosphere balances the incoming solar wind); the 'Brace-ionopause', where the ionospheric electron density drops to a value of 100 ions cm^{-3}; a definition that derives the ionopause from magnetic signatures, etc. Here we stick to the first definition, we identify the lower boundary with the pressure balance ionopause.

The upper boundary is less sharp and well-defined, and we take as the upper boundary the location where the shocked solar wind gets depleted and is deflected above the ionosphere. Along the Sun-planet line, the width of the region is a few hundred kilometers, and it is wider as we approach the terminator line.

The existence of the dayside mantle was first established by Spenner et al. (1980) based on the electron measurements of the retarding potential analyzer on board the Pioneer Venus Orbiter (PVO). It was shown that between the magnetosheath and the ionosphere there is a separate layer where both the shocked solar wind and the planetary superthermal electron populations are present. Early Venera and Mariner missions also detected a special region behind the terminator line and named it a 'rarefaction wave' or 'penumbra'; these are now believed to be the nightside continuation of the mantle. At Venus, the dayside mantle was explored during the first two epochs, and on a few orbits even during the third epoch of the PVO mission. At Mars, instruments carried onboard the *Phobos 2* mission measured the structure of the dayside mantle on three orbits. The retarding potential analyzer onboard the *Viking* landers also provided data on the mantle electrons. It is hoped that the *Cassini* mission will explore the dayside mantle of *Titan* after the year 2004. Exploration of comets (and ion releases) also enriches our knowledge about the mantle, though due to the much faster ion outflow and the much larger size of the cometary interaction volume the relationship to planetary mantles needs further study (Szegö et al., 1992).

The dayside mantle is rich in different plasma phenomena. A significant feature is the magnetic barrier; the magnetic field in the solar wind piles up, and reaches its maximum strength at altitudes higher than the ionopause altitude. As has been pointed out by Zhang et al. (1991), this is the effective obstacle for the solar wind. (In some publications the mantle region is called the magnetic barrier region.) The formation of the magnetic barrier is seemingly a global phenomena of the solar wind flow around non magnetic obstacles. Behind the barrier the magnetic field drops fast and significantly, indicating the presence of a current layer associated with the change of the field. Law and Cloutier (1997) pointed out that not only the field magnitude changes, but the field direction as well, and in such a way, that the resulting direction of the magnetic field will be parallel to the solar wind flow at the ionopause.

Another significant feature of the mantle is the excited waves in the few tens – few hundreds Hertz frequency range. These waves were detected by the electric field detector onboard PVO in its 100-Hz channel (the next channel was centered at 730 Hz), and by the plasma wave spectrometer on board *Phobos 2*, in several channels in the 50–200 Hz range. Neither the polarization, nor the wavelength of the waves could be established. The spinning antenna on PVO in principle could allow a measurement of the projection of the polarization vector; however, noise associated with the changing ambient plasma at the ionopause made these efforts ambiguous (Strangeway, priv. comm.). The statistical analysis (Strangeway and Russell, 1996) clearly proved that wave activity always takes place higher

in altitude above the planet than the location of the magnetic barrier. This is an important result, because in the very inhomogeneous mantle plasma environment one might well assume that the wave excitation is due to electron drift connected to the gradients of the magnetic fields at the ionopause. However, as the wave activity is localized to higher altitudes, this excludes the possibility that the electron drift drives significant wave excitation. The same holds for possible density gradient drifts as well.

Both at Venus and Mars accelerated heavy ions and electrons were observed in the dayside mantle (Taylor et al., 1981; Grebowsky et al., 1993; Lundin et al., 1989; Rosenbauer et al., 1989; Szegö et al., 1998), and also behind the terminator at locations accessible to these particles. Details will be discussed in the next chapter. We believe that most of these particles are accelerated and heated due to their interaction with the waves excited. Within the dayside mantle, with the exception of a few special regions, no acceleration mechanisms other than wave-particle can operate due to the limited physical volume available; the measurements behind the terminator line can be interpreted as a result of a non collective $\mathbf{E}\times\mathbf{B}$ pickup (Kallio and Koskinen, 1999). Using the retarding potential analyzer's data on board PVO it was shown (Szegö et al., 1997) that accelerated electrons are present in the Venus mantle, and the idea was also put forward by the same authors that these electrons can significantly contribute to the change of the field direction discussed above.

The shape of the mantle around the planet resembles the structure of an onion. It is evident that the observed features have both a solar zenith angle dependence and a dependence on altitude. This latter is related to the mixing ratio of the shocked solar wind and planetary plasma, which clearly depends on altitude. The solar zenith angle dependence is connected with the decreasing strength of the magnetic barrier, the changing relative velocity of the two plasma populations (as the solar wind decelerates), and also with the time required for the instabilities to build up and to act on the planetary population. It is evident from these that the sun-planet line and its close vicinity is a peculiar region, and also that some of these processes are not in operation behind the terminator; consequently, the dayside and the nightside mantle should differ.

Behind the terminator, in the continuation of the dayside mantle, many interesting plasma features were observed, such as plasma clouds, troughs, etc. We do not think that these are just the heritage of some dayside phenomena.

It is known that the ionosphere of Venus reacts strongly to solar conditions; during solar maximum the ionopause is higher than during solar minimum conditions. The periapsis altitude of PVO was low enough to study the mantle only during solar maximum conditions (during the first two epochs, in 1979–1980), and sometimes the question arises whether the dayside mantle exists at all during solar minimum. The *Phobos-2* investigation of Mars also took place during rising solar activity, in 1989. Whereas we agree that the mantle structure might depend on the solar conditions, it is evident to us that in both cases the solar wind and the planetary

plasma interact much in the same way; the existence of a region with both plasma populations present is unavoidable.

It is well established that the solar wind flow scavenges and erodes the ionosphere. It is less clear whether or not there is a direct heat flux directed into the ionosphere from the mantle due to the wave-particle interactions. In early models at Venus a topside ionosphere heating was required; later, however, Nagy et al. (1990) pointed out the thermal equilibrium of the ionosphere could be understood without a topside heating, by assuming different heat conductivity along and perpendicular to the magnetic field. Whereas at Venus these authors could not reach an unambiguous conclusion about the necessity of a topside heating, at Mars the topside heating seems to be unavoidable (Choi et al, 1998). The MTSI scenario can provide at least a portion of the missing heat, as the waves always carry a group velocity component perpendicular to the ionosphere, even if the dominant group velocity is parallel to the boundary. To settle this problem, further analysis is needed.

4.3.2.2. *Energetic particle observations in the mantle region.* We review the experimental data on energetic particles in the vicinity of the mantle of Venus and Mars, to clarify when it is likely that instruments measured the products of $\mathbf{E} \times \mathbf{B}$ pickup, or when it is more likely that other mechanisms, such as the collective pickup, is in operation.

Theoretical calculations of Kallio and Koskinen (1999) for non collective $\mathbf{E} \times \mathbf{B}$ pickup at Mars clearly show that ion pickup in the mantle is effective only close to the 'magnetic polar regions'; that is, where the magnetic field frozen in the shocked solar wind slips over the obstacle. This is the region where the flow velocity subtends the biggest angle with the magnetic field. Around the 'North' pole the $-\mathbf{V}\times\mathbf{B}$ motional electric field points away from the planet (towards ecliptic North); around the 'South' pole it points in the same direction, but now towards the planet. Accordingly, the pickup orbits are different: (a) around the North pole r_L is large, and the pickup ion trajectories follow more or less the ionopause, (b) around the South pole r_L is small, and the ions gyrate several times within the dayside mantle (see Figure 4.3.4). However, with the exception of about a $\pm 10^\circ$ wide region close to the poles, the $\mathbf{E} \times \mathbf{B}$ pickup is ineffective inside the mantle. Though no similar detailed calculation exists for Venus, it is fairly likely that within the dayside mantle only the magnetic polar regions are effective for pickup. This is actually verified both by PVO plasma analyzer data and by *Mariner-V* measurements, as discussed recently by Perez-de-Tejada (1998).

The presence of pickup ions changes the MHD flow picture as was shown recently by Bauske et al. (1998), and in several previous works referenced there. It shall be noted, however, that in general MHD models do not take into account the collective aspect of the pickup.

The presence of pickup ions in the magnetosphere is widespread. On board the Pioneer-Venus Orbiter, there were three instruments capable to measure energetic

ions, the ion mass spectrometer (OIMS) (Grebowski et al., 1993), the neutral mass spectrometer (ONMS) (Niemann and Kasprzak, 1992) and the plasma analyzer (Moore and McComas, 1992). The PVO plasma analyzer can detect energetic ions in the 50 eV–8 keV energy range, and it observed such ions mostly in the tail region. These results are in harmony with the picture described above for pickup ions.

The OIMS measured superthermal ions in the dayside mantle in the 15 to 90 eV energy range (though they could not be distinguished from protons accelerated to 90–95 eV). The ONMS measured those ions in the 40–90 eV range; the data of the two instruments correlate well. Here we concentrate on the OIMS data, because all its data were analyzed that were measured on orbits which penetrated the dayside ionosphere (Grebowsky et al., 1993). In Figures 2 and 3 of that paper the location of the complete set of OIMS observations of superthermal ions were plotted between 150 km and 6500 km for the first three years of the PVO mission, as a function of local time versus altitude. The most important conclusions of that analysis are: (1) such ions on the dayside are predominantly seen in the ionopause region; (2) the dayside measurements show an obvious grouping of the events near local noon, extending from 7 to 18 local hours; (3) the events are predominantly on the inbound orbital legs, leading to the conclusion that the ions are moving in the solar wind direction; (4) the measurements have a sharp boundary at low altitudes, coinciding with the position of the magnetic barrier between 8 and 16 hours local time; (5) the low altitude termination of the data is below the so called 'Brace-ionopause', that is where the electron density is 100 cm^{-3}, as measured by Orbiter electron temperature probe on PVO.

Whereas the observations in the vicinity of local noon can be accounted for by $\mathbf{E} \times \mathbf{B}$ pickup, it is evident that the extent of the data set in local hours (even allowing for the magnetic field variations) requires other acceleration mechanisms. As we shall show in this paper, laminar pickup due to wave particle interactions is really the proper candidate to account for these observations.

Measurements at Mars are sparse relative to Venus. The *Phobos-2* spacecraft penetrated the dayside mantle, but only along three orbits. The plasma data measured between the bowshock and the terminator along the above mentioned three orbital sections are summarized in Szegö et al. (1998). Currently the Mars Global Surveyor Mission makes observations around Mars, but its data are not public yet. On the *Phobos-2* spacecraft that explored Mars in 1989 two instruments registered energetic ions in the mantle (Szegö et al., 1998).

4.3.2.3. *The wave-particle interaction for laminar pickup.* It was discussed in Section 3 that in the mantle, if the effect of the magnetic field is not negligible, the modified two-stream instability (MTSI) plays the dominant role. The quasi-electrostatic lower hybrid waves are excited by counter-streaming plasma components. These waves are basically ion plasma oscillations across the magnetic field, but in an environment where the dielectric constant is dominantly defined by

magnetized cold electrons. The lower hybrid waves propagate obliquely, almost perpendicular to the magnetic field, and consequently their phase velocity along the magnetic field, $\omega/k_{\|}$ exceeds significantly the phase velocity perpendicular to **B**, ω/k. As a result, these waves can resonate simultaneously with the slow ions propagating across **B**, and the magnetized fast electrons, moving along the field lines. If the electrons are unmagnetized (or do not feel the magnetic field because of the short wavelength), ion acoustic waves are excited.

Originally Sagdeev et al. (1990) proposed a model that was elaborated further to a MTSI scenario described by Szegö et al. (1991), and Shapiro et al. (1995); Bingham (1991) discussed this model in the context of artificial comets. It was Huba (1993) who suggested investigating the situation where the electrons stay unmagnetized (this yields ion acoustic wave excitation). In earlier publications Scarf et al. (1980) proposed that the waves in the dayside mantle of Venus might be whistlers, but data analysis shows that we are in a different regime of the parameter ω_{pe}/kc, as in the mantle this parameter is less than one. All these models assume that the linear dispersion relation describing the interaction has the form

$$D(\mathbf{k}, \omega) = 1 + \chi_{\text{solar wind}} + \chi_{\text{planetary ions}} + \chi_{\text{electrons}} , \tag{4.3.198}$$

where

$$\chi_{\text{solar wind}} = \frac{1}{k^2\lambda_{D,p}^2}(1 + \eta_p Z(\eta_p)) \tag{4.3.199}$$

and

$$\chi_{\text{planetary ions}} = \frac{1}{k^2\lambda_{D,i}^2}(1 + \eta_i Z(\eta_i)) \approx \frac{\omega_{pi}^2}{\omega^2} \tag{4.3.200}$$

with $\eta_p = \omega - \mathbf{ku_{sw}}/\mathbf{kv_{th\ p}}$ and $\eta_i = \omega/kv_{th\ i}$.

In the upper regions of the mantle, Huba (1993) assumed that the electron component is a uniform, warm, drifting Maxwellian; because it was believed that in this upper region the cold electrons coming from the ionopause already have a negligible density. Only the short wavelength mode was considered ($k\lambda_{D,e} \approx 1$), and this means that the electrons do not feel the magnetic fields (i.e., they behave unmagnetized). However, as we move closer to the ionopause, two electron components should be taken into account, warm solar wind electrons and cold planetary electrons. The excited ion acoustic waves occur near the frequency $\omega/\omega_{pi} \approx 0.5$, but as the relative density of cold electrons increases, the instability quenches.

It is possible to calculate the energy density of the waves. This is the energy transferred from the solar wind:

$$\delta W = \frac{1}{8\pi}\mathbf{E}_k^* \left(\frac{\partial}{\partial\omega}(\omega\mathcal{E}_r)\right)\mathbf{E}_k , \tag{4.3.201}$$

where $\mathcal{E}_r$ is the real part of the dielectric permittivity tensor. For electrostatic waves this simplifies to

$$\delta W = \frac{1}{8\pi}|\mathbf{E}_k^2|\left(\frac{\partial}{\partial\omega}(\omega D)\right) , \tag{4.3.202}$$

$D = 0$ is the dispersion relation. In the case discussed above the wave energy density is of the order of

$$\delta W \approx \frac{1}{4\pi}\frac{\omega_{pi}^2}{\omega^2}\mathbf{E}_k^*\mathbf{E}_k \approx \frac{1}{\pi}\mathbf{E}_k^*\mathbf{E}_k . \tag{4.3.203}$$

Closer to the ionopause the plasma components have different characteristics; the cold electron density is comparable to the shocked solar wind density, as in the model of Shapiro et al. (1995). When the long wave length mode, $kv_{th}/\omega_{LH} \approx 1$ is considered, the effect of the magnetic field cannot be neglected. One of the electron components is a warm Maxwellian drifting with the solar wind, the second cold component is at rest in the planetary frame, because in the close vicinity of the ionopause the flow velocity and **B** are almost parallel. In higher regions the cold component can be picked up by the $\mathbf{E} \times \mathbf{B}$ force generated by the streaming solar wind. As was shown by Shapiro et al. (1995), the waves accelerate both electrons and ions.

When the cold electrons are at rest, two branches of waves are excited. Introducing the variable $\rho^* = (T_p/m_p)^{1/2}\omega_{LH}^{-1}$, the first branch corresponds to $k\rho^* < 1$ (the frequency is below the lower hybrid frequency) the second branch corresponds to $k\rho^* > 1$, and the frequency is a few times larger than the lower hybrid frequency. The first branch is a hydrodynamic type instability and the second is a kinetic one (Shapiro et al., 1995). The energy density of the MTSI waves can be calculated in the same way as above, and we find that the wave energy density is of the order of

$$\delta W \approx \frac{1}{8\pi}\mathbf{E}_k^*\mathbf{E}_k\frac{\omega_{pe}^2}{\Omega_{He}^2} .$$

This is about 10^3 larger than in the previous case, for comparable electric fields (ω_{pe} and Ω_{He} are the electron plasma and gyrofrequency, respectively). We note, however, that the total wave energy is an integration over k space, and the k-space for the ion acoustic mode is bigger than for the MTSI mode, because the dependence of the ion acoustic mode on the angle between **k** and **B** is rather flat, whereas for the MTSI mode it is peaked. The quasilinear approximation for electrons yielded an electron population in the 100 to 300 eV range; ions, as a nonlinear analysis showed, could reach about 100 eV energy.

Despite the difficulty of numerically solving the linear dispersion relation for moving electrons, the study of the linear dispersion relation clearly shows that a new branch, similar to an electron-ion instability develops, and the new branch dominates. This result seems to be curious, but it can be understood in the following way: though the free energy of the plasma is in the solar wind protons, this energy is transmitted to the electrons by the motional electric field $\mathbf{v} \times \mathbf{B}$, and the electrons excite the waves, despite the fact that without their continuous electrostatic coupling to the protons their energy would be negligible.

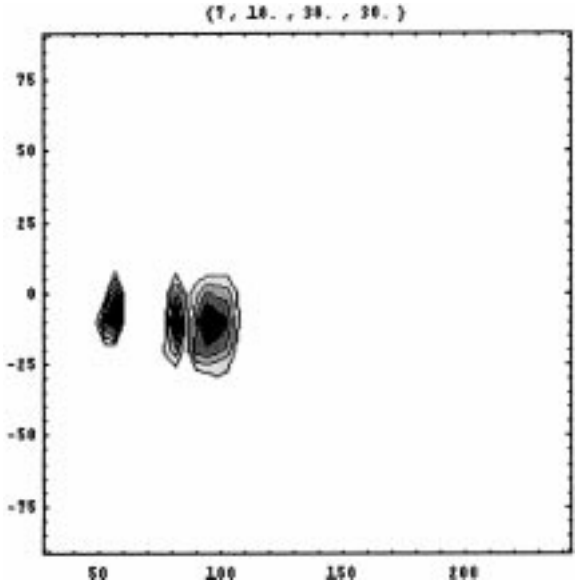

Figure 4.3.10. Two-dimensional spectra of ions are shown as TAUS ion spectrometer measured them in the mantle of Mars on 1 February, 1989. The coordinate axes are v_x (horizontal) and v_y (vertical) in km s^{-1}, the altitude of the spacecraft and the magnetic field data are shown on the right. The v_x points anti-sunward, v_y is perpendicular to it, but due to the slow spacecraft rotation, it does not have a specific direction in the ecliptic frame. Above the frames, in brackets are the frame number, and the time in h min s of the data.

To study this situation further Dobe et al. (1999) initiated a numerical simulation to analyze both the wave excitation and the subsequent ion acceleration. The assumptions for the hybrid simulation were that electrons can be treated as fluid, though retaining finite electron mass, the warm protons and cold (1 eV) ions were described kinetically. Waves could propagate in two directions, parallel and perpendicular to the magnetic field; the physical quantities varied along one dimension, as it is realistic for the mantle. The numerical technique used maintains current conservation and requires periodic boundary conditions.

The equations of motion were:

$$\frac{\partial n_m}{\partial t} + \frac{\partial n_m u_m}{\partial x} = 0 \quad m = e,\ p,\ O^+ , \tag{4.3.204}$$

$$n_e m_e \left(\frac{\partial u_e}{\partial t} + u_e \frac{\partial u_e}{\partial x} \right) = -e n_e \left(\mathbf{E} + \frac{1}{c} \mathbf{u}_e \times \mathbf{B} \right) - \frac{\partial P_e}{\partial x} , \tag{4.3.205}$$

$$n_s m_s \left(\frac{\partial u_s}{\partial t} + u_s \frac{\partial u_s}{\partial x} \right) = -e n_s \mathbf{E} - \frac{\partial P_s}{\partial x} \quad s = p,\ \mathrm{O}^+ , \tag{4.3.206}$$

$$\nabla \cdot \mathbf{B} = 0 , \tag{4.3.207}$$

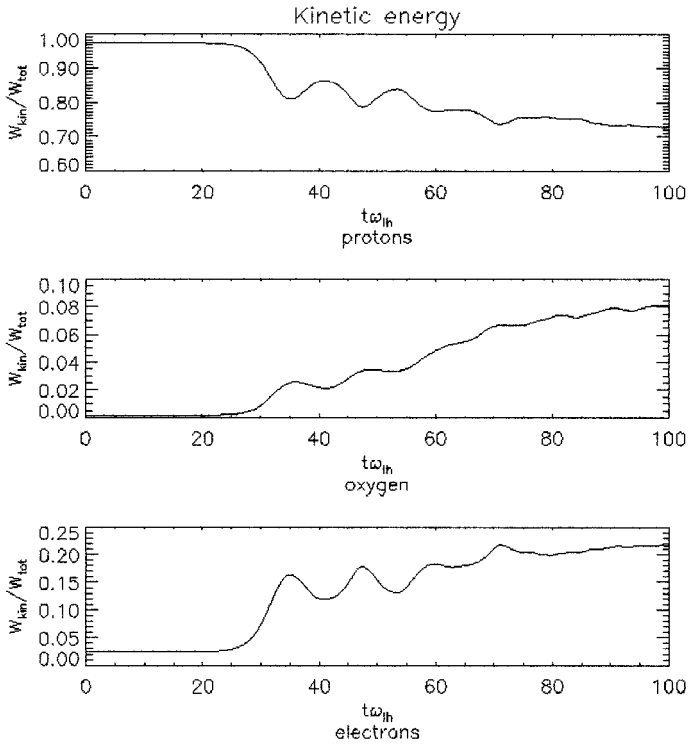

Figure 4.3.11. Results of a hybrid code simulations, from Dobe et al. (1999). The plots show the energy of the different plasma components relative to the total energy, as a function of time, in $t\omega_{LH}$ units, in the mantle region.

$$\nabla \times \mathbf{B} = \mu_o \mathbf{j} \,, \tag{4.3.208}$$

$$\nabla \times \mathbf{E} = -\frac{\partial \mathbf{B}}{\partial t} \,. \tag{4.3.209}$$

The system was followed through 150 gyrofrequency periods (this is about 5 s), this is adequate for the interaction to reach the nonlinear phase, though probably it is still far from equilibrium. The most important results are summarized in Figure 4.3.11, this shows that if the waves are propagating almost in the perpendicular direction, when $\kappa = (m_p/m_e)^{1/2}(k_\parallel/k) = 1$, about 10% of the kinetic energy is still in the waves, and about 50% of the solar wind momentum has already been transferred to the ions. The calculation of the phase space density of the ions shows that the ions are mostly heated, their bulk velocity is only about 10% of the proton bulk velocity.

A limitation of this model due to computational difficulties is that only cold ions were considered, and pre-accelerated ions did not participate in the interaction. We believe that taking into account the full ion population and allowing interaction time till all the wave energy is deposited into ions, this hybrid code

will also simulate the presence of an anomalous friction that corresponds well with observations.

4.4. MASS LOADING PROCESSES IN THE INTERPLANETARY REGION

In addition to the effects of spatially confined sources, such as comets and planets, large-scale sources of neutral particles provide mass-loading of the solar wind throughout interplanetary space. The primary source of these particles is the inflow of the neutral component of the local interstellar medium (LISM). Over the last 10 years, these interstellar pickup ions have become a valuable tool to probe the interstellar gas distribution, in order to derive the density, composition, flow velocity and temperature of the surrounding interstellar environment. Of course, the interstellar parameters outside the solar system have to be inferred from data taken in the inner heliosphere using a detailed modeling of the transport of the interstellar gas into the heliosphere. Solar EUV radiation, charge exchange by solar wind ions, and electron collisions ionize the incoming interstellar neutrals, thus creating a cavity in the interstellar gas cloud. Except in the case of hydrogen, where radiation pressure is important, the Sun acts as a huge gravitational lens creating a focusing cone with a substantial density increase of the interstellar gas on the downwind side. The density concentration in the center and the width of the cone depend sensitively on the temperature and relative velocity of the interstellar gas cloud as well as on the mass of the species. It is this structure which provides the main experimental handle on the interstellar gas temperature and the relative velocity. For overviews on this topic the reader is referred to the reviews of, e.g., Axford (1972) and Holzer (1989).

Currently accepted values for the properties of the neutral interstellar gas have been compiled by Geiss and Witte (1996): The relative speed of the heliosphere through the LISM is on the order of 25 km s^{-1}, and the temperature of the surrounding medium is approximately 7000 K. The composition is dominated by hydrogen and helium, and the local density of neutral helium is $n_{He} \approx 0.015$ cm^{-3}. The determination of the interstellar hydrogen density is complicated by the strong charge-exchange interaction experienced by these atoms in their passage through the heliosheath, which filters a substantial fraction of these particles (Fahr and Ripken, 1984). For this discussion of mass-loading, however, the interesting quantity is the density of the hydrogen which survives and enters the supersonic plasma flow through the solar wind termination shock. Current estimates of this value are on the order of $n_{He} \approx 0.12$ cm^{-3}. Observational details, error bars, and additional abundances are given by Geiss and Witte (1996).

The nature of the interaction changes with the expansion of the solar wind. The solar wind ram pressure declines with the square of the distance from the Sun, while the neutral gas density is practically constant beyond a few AU. This radial variation can be characterized by three distinctly different regimes inside the heliospheric termination shock, as indicated in Figure 4.4.1. In the inner solar

system, where almost all of the pickup ion measurements have been carried out so far, pickup ions behave like test particles. They do not modify the solar wind parameters, and the effect of the solar wind and interplanetary magnetic field on the pickup ions can be studied without modifications of the original environment. Beyond approximately 5 AU from the sun the interstellar H density becomes high enough and the solar wind density is sufficiently decreased so that wave generation by pickup ions has to be taken into account. Between 20 and 30 AU the pressure of pickup ions becomes comparable to the thermal pressure of the solar wind because of the high intrinsic energy of the pickup ions in the solar wind rest frame. This leads to pickup ion related pressure balance effects that become visible in the inhomogeneous solar wind (e.g., Burlaga et al., 1994). Finally, beyond 30–40 AU the density of the implanted interstellar ions becomes significant enough to slow down the solar wind noticeably (Richardson et al., 1995).

The other major source of interplanetary ions is the so-called 'inner source', neutral particles produced in association with circumsolar dust. Pickup ions were identified recently close to the Sun (Geiss et al., 1995; Gloeckler and Geiss, 1999), the composition of the inner source ions is like that of the solar wind, with H^+, C^+, N^+, O^+, Ne^+, Mg^+ and Si^+ all having been identified as components of the inner source (see Gloeckler et al., 1999) for a full discussion of the inner source abundances relative to that of the solar wind). Note in particular the presence of Ne^+. Small dust grains in the heliosphere are not expected to contain volatile elements such as Ne, and may be depleted in H unless these particles are bound in molecular form. The presence of Ne and H in the inner source suggests strongly, and perhaps conclusively, that these particles originate as solar wind ions which are embedded and subsequently released from dust grains, eventually then becoming pickup ions. The physics involved in the embedding and release of solar wind ions is discussed in Gruntman (1996).

In addition to providing information on the LISM and circumsolar dust grains, the study of interplanetary pickup ions is presenting fascinating new clues on the transport of charged particles in the solar wind. Since these pickup ions are distributed over scales on the order of 1 AU or greater, it was long expected that these particles would have ample time to isotropize in pitch angle and follow the solar wind motion before being substantially affected by additional pickup or transport through the solar wind. However, pickup ion observations in the last few years have strongly contradicted that picture, particularly in that the variability of the anti-sunward flux of these particles could not be explained. It is now evident that these effects are caused by incomplete pitch-angle scattering of these ions. In quasi-radial IMF conditions, newly ionized particles appear in the sunward region of phase space and can only reach the anti-sunward region by pitch-angle scattering. Apparently, the time scale for scattering to isotropy is greater than the time scale for ionization of new particles, leading to an accumulation of pickup ions in the sunward region of phase space and a corresponding depletion of ions in the anti-sunward region.

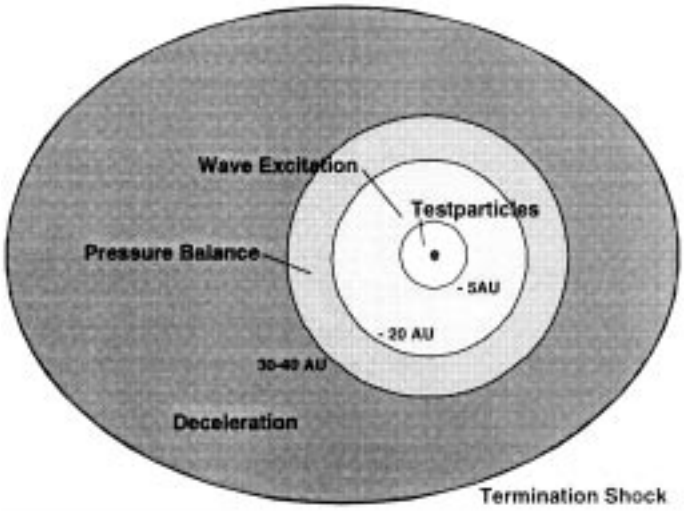

Figure 4.4.1. Different regimes of solar wind massloading by interstellar ions as a function of distance from the Sun.

4.4.1. *Basic Observations and Modeling of Interstellar Pickup Ions*

Although their existence had been predicted in the early 1970s on the basis of observations of backscattered solar ultraviolet lines (Blum and Fahr, 1970; Bertaux and Blamont, 1971; Holzer, 1972), the direct detection of interstellar pickup ions had to wait for the development of time-of-flight detectors which can separately measure the energy/charge, mass, and mass/charge of a particle with extremely low background. Interstellar pickup He^+ was first detected in 1984 by the SULEICA instrument on the Earth-orbiting AMPTE/IRM spacecraft (Möbius et al., 1985a). Interstellar pickup protons were not measured until the launch of the *Ulysses* spacecraft, carrying the SWICS instrument (Gloeckler et al., 1992).

The initial measurements of these ions (Möbius et al., 1985b; Gloeckler et al., 1993) showed fluxes with the characteristic spectrum of a relatively flat plateau ending in a sharp cutoff at an energy $E_c = 4E_{sw}$ where $E_{sw} = 0.5Mu_{sw}^2$ and M is the mass of the ion (see Figure 4.4.2).

These spectra were consistent with the theoretical expectations of the isotropic model of Vasyliunas and Siscoe (1976). This simple model is worth describing in some detail, since it provides the context for much of the subsequent observations and modeling work on interstellar pickup ions.

In steady-state, interstellar pickup ions at a heliocentric position $\mathbf{r}$ are produced at a rate given by the product of the neutral gas density $N(\mathbf{r})$ and the local ionization rate of all relevant processes $\beta(\mathbf{r})$. Within a gyroperiod, these ions are picked up by the electromagnetic fields in the solar wind and pulled into a ring-beam distribution perpendicular to the local magnetic field. They were then expected to quickly pitch-angle scatter to isotropy in the solar wind reference frame, through the cyclotron interaction with ambient and self-generated electromagnetic fluctuations (Lee and

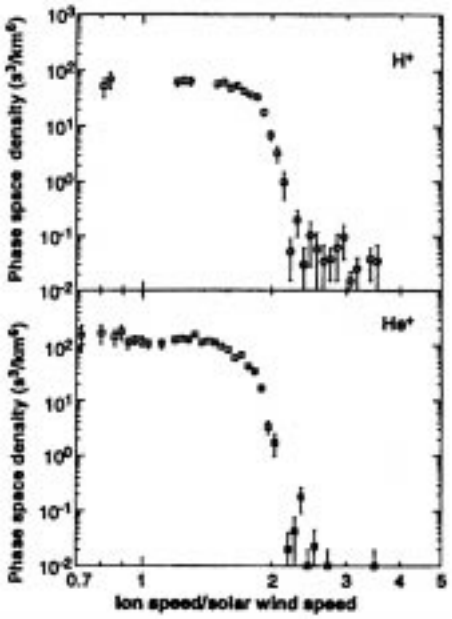

Figure 4.4.2. Phase space density of interstellar pickup hydrogen (upper panel) and pickup helium (lower panel), measured in the Ulysses spacecraft frame with SWICS at a heliocentric distance of 4.82 AU, during the time period 24 November to 9 December 1991 (from Gloeckler et al., 1993).

Ip, 1987; Bogdan et al., 1991). The scattering transforms the initial ring distribution into a spherical shell in velocity space, with a radius of the solar wind speed and centered on the solar wind flow. While the shell is convected away from the Sun, the pickup ion distribution is subject to adiabatic cooling in the expanding solar wind. As shown by Möbius et al. (1988) on the basis of the observed steepness of the cut-off, adiabatic cooling acts much faster than diffusion in energy space. Continued ionization into the same parcel of solar wind results in a distribution of nested shells in velocity space whose phase space density $f(v)$ is determined by the ion production rate $S^+(r)$ of these ions as a function of the heliocentric distance r along the Sun-spacecraft line. The adiabatic cooling of a shell from the point of ionization to the spacecraft location provides a direct mapping of the variation of this local production rate $S^+(r)$ into the velocity distribution function $f(v)$ centered on the solar wind according to:

$$\frac{v}{u_{sw}} = \left(\frac{r_o}{r}\right)^{-2/3} , \tag{4.4.210}$$

where r_o is the distance of the spacecraft from the Sun. This mapping is shown schematically in Figure 4.4.3.

In a spherically-symmetric, constant speed solar wind, the isotropic distribution of these pickup ions can be described by an equation balancing convection in the

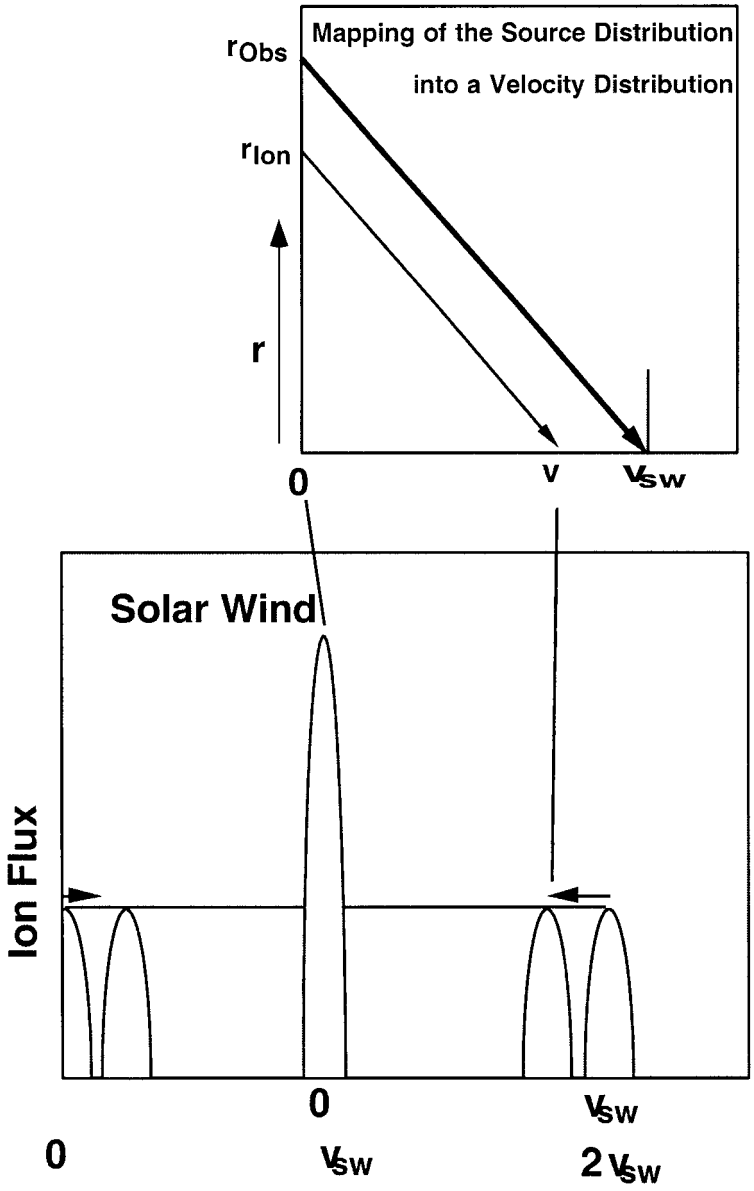

Figure 4.4.3. Mapping of a neutral gas source into a velocity distribution, assuming adiabatic deceleration in the expanding solar wind. Mapping relation (upper panel), resulting cut through the distribution function in the direction of the solar wind (lower panel).

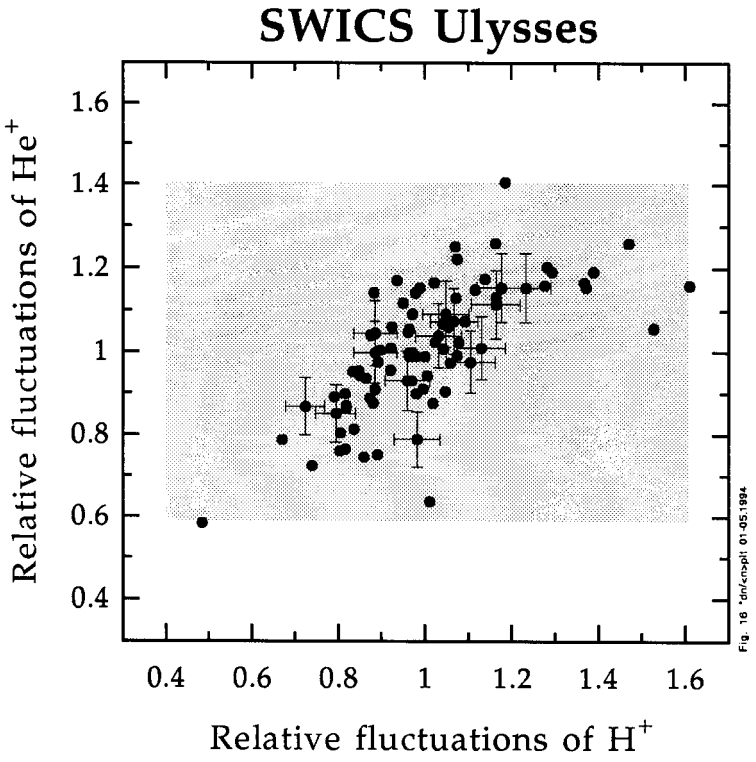

Figure 4.4.4. The relative fluctuations of interstellar pickup hydrogen vs. interstellar pickup helium. The data are formed by integrating over 48 hours and over the speed range $1.6 < w < 2$.

solar wind with adiabatic deceleration, and including the addition of new particles at the production rate appearing with a speed equal to the solar wind speed:

$$u_{sw}\frac{\partial f}{\partial r} - \frac{2v}{3r}\frac{\partial f}{\partial v} = \frac{S^+(r)}{4\pi v^2}\delta(v - u_{sw}) \; . \tag{4.4.211}$$

Generally the ionization rate falls off uniformly with distance from the Sun, so $\beta = \beta_o(r_o/r)^2$, where β_o is the ionization rate at some reference distance r_o. In this case, Equation (4.4.211) has a simple solution

$$f(v) = \frac{3\beta_o r_o^2}{8\pi r^2 u_{sw}^4} N\left(r\frac{v}{u_{sw}}\right)^{3/2} \; . \tag{4.4.212}$$

With this relation the spatial distribution of the neutral source $N(r)$ can be inferred. For the interstellar gas it can be used to constrain the average ionization rate (e.g., Möbius et al., 1988; Gloeckler, 1996). The radial density profile of the interstellar gas in the inner solar system is solely determined by the average ionization rate over the past few months prior to the observation (Möbius et al., 1995).

The first indication of a discrepancy with the Vasyliunas and Siscoe model was the detection of factor of 2–3 variations in the fluxes of pickup protons and He^+

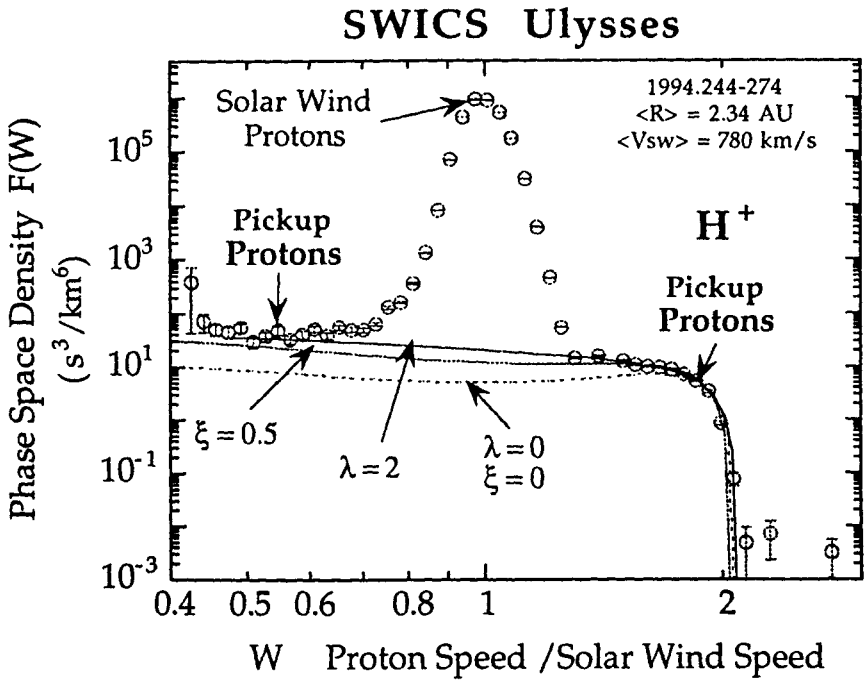

Figure 4.4.5. Pickup spectra in the phase space density for H^+ (upper panel) and He^+ (lower panel) as compared with model distributions. The thick full line represent distributions that include anisotropies in the sun-spacecraft direction, the thin dashed lines represent isotropic distributions for comparison (from Gloeckler et al., 1995).

in the spacecraft-frame speed range between 1.6–2.0 u_{sw} at the *Ulysses* spacecraft (Fisk, et al., 1997; Gloeckler, et al., 1994). Even more surprising was the ubiquitous finding that the proton variations were directly correlated with those of He^+. An example of this correlation is shown in Figure 4.4.4 from Fisk et al. (1997). The two sets of reported variations come from distinct regions of the solar wind: Gloeckler et al. (1994) present 19.5-hour average fluxes over 16 days when *Ulysses* was at 4.8 AU in the ecliptic plane. During this time the interplanetary magnetic field (IMF) was essentially in the azimuthal direction. Fisk et al. (1997) analyze six months of data, showing 48-hour average fluxes between 2.8 AU and 3.6 AU, when Ulysses was at heliolatitudes $>45°$. In this region, the IMF is directed radially on average.

The correlation between the ion species immediately rules out variable ionization rates as a cause of the variable ion fluxes, since the two species are predominantly ionized by separate, uncorrelated processes (charge-exchange with solar wind ions for protons, and photoionization by solar EUV for helium). Thus, the flux variations indicate the operation of some form of particle transport, resulting in an accumulation of ions somewhere and a corresponding depletion somewhere else.

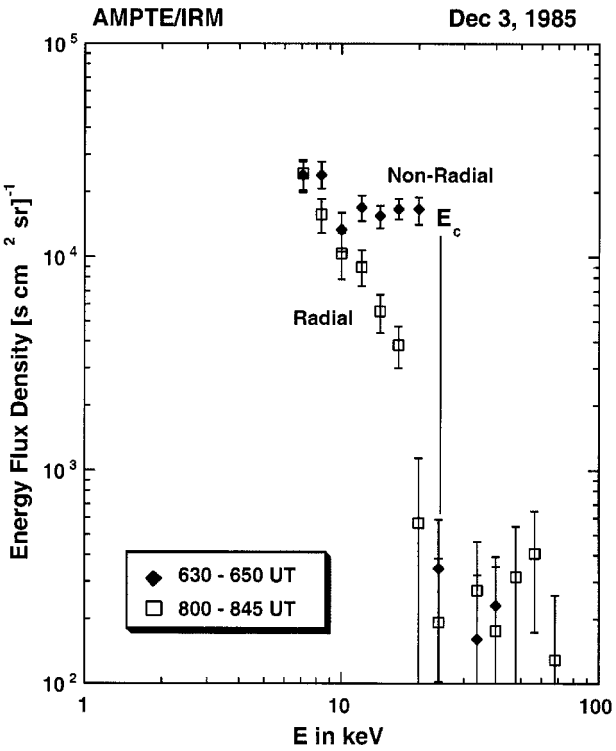

Figure 4.4.6. Pickup ion spectra in the antisunward portion with radial and nonradial magnetic fields.

Strong anisotropies were first reported in the distributions of pickup H^+ in high latitude regions of the solar wind with predominantly radial magnetic field orientation using the *Ulysses* SWICS instrument (Gloeckler et al., 1995). Sample pickup ion spectra of H^+ for radial IMF are shown in Figure 4.4.5. The isotropic distributions fall short by a factor of about 4 for H^+ in the sunward portion of the distributions. These observations are interpreted in terms of incomplete pitch-angle scattering in the frame of the solar wind due to mean free scattering lengths that are comparable with or even exceed the typical spatial scales over which the interstellar ions are picked up between the sun and the spacecraft.

The direct connection between the orientation of the IMF and the development of anisotropic distributions was demonstrated by Möbius et al. (1998). They reported reduced pickup ion fluxes in the anti-sunward portion of the distribution, i.e., at speeds higher than the solar wind speed, and a more gradual transition near the cut-off, when the IMF turns into the radial direction. Figure 4.4.6 shows an example of two consecutive time periods with almost perpendicular and almost radial IMF conditions. The fluxes are substantially reduced during the radial period and the plateau turns into a relatively steep spectrum.

The ionization rates are crucial for both the shaping of the spatial distribution of the gas in the vicinity of the sun and the local ion production rates, as was pointed

out by Möbius et al. (1996). For species that are mainly ionized by solar EUV, such as He^+, they are still not known to the accuracy needed for quantitative interstellar gas studies. This situation has changed only recently through the presence of an EUV monitor within the CELIAS package on SOHO (Judge et al., 1997). With the use of He_2^+ pickup ions, which are produced through double charge exchange by solar wind alpha particles (e.g., Rucinski and Fahr, 1989), Gloeckler (1996) has derived the most accurate interstellar He density, because both pickup and solar wind ions are measured simultaneously by the same instrument. The ionization rates relevant for interstellar pickup ions have recently been reviewed by Rucinski et al. (1996).

4.4.2. *Anisotropic Models of Interplanetary Pickup*

4.4.2.1. *The role of long scattering length.* It is now evident that the observed anisotropic effects are caused by incomplete pitch-angle scattering of the ions. In quasi-radial IMF conditions, newly ionized particles appear in the sunward region of phase space and can only reach the anti-sunward region by pitch-angle scattering. Apparently, the time scale for scattering to isotropy is greater than the time scale for ionization of new particles, leading to an accumulation of pickup ions in the sunward region of phase space and a corresponding depletion of ions in the anti-sunward region.

Fisk et al. (1997), in an analysis of the high-latitude Ulysses data, showed that if the observed pickup ion flux variations are caused by fluctuations in the pitch-angle scattering rate, a scattering mean free path $\lambda_\parallel \approx 1$ AU is implied. In addition, they showed that the anti-sunward pickup ion distributions were substantially filled in by adiabatic deceleration, which is clearly operative even when the pitch-angle scattering is slow. Finally, they demonstrated that the shape of the anti-sunward spectra appeared independent of the daily averaged IMF angle, though one should be cautious in interpreting this last point, since the long time averages of the field data may hide important information on the angular distribution.

4.4.2.2. *The hemispherical approximation.* These findings on the interstellar pickup process suggest the application of the hemispherical approximation to model the pickup ion distribution (Isenberg, 1997; Schwadron, 1998). Under this approximation, one assumes that the slow pitch-angle scattering indicated by the observations is confined to pitch angles near 90° and that the scattering at all other angles is still much faster than all other processes. In this case, the pickup ion distributions are nested hemispheres separated by the 90° pitch-angle surface, with densities independent of pitch angle within each hemisphere.

This behavior is a reasonable manifestation of the well-known resonance gap in the cyclotron interaction of ions with parallel-propagating MHD waves (e.g., Rowlands et al., 1966; Dusenbery and Hollweg, 1981). This gap comes about because ions with pitch angles near 90° resonate with very high wave number waves, but these waves should have been heavily damped by the solar wind protons so

are unable to provide the scattering. This absence of resonant waves means that the actual scattering through 90° in the solar wind may be due to other processes, such as mirroring by compressive fluctuations, and it has been difficult to make theoretical predictions of this scattering rate. Thus, modeling the observations of anisotropic pickup ions could give us valuable clues on this long-standing problem.

The equations describing these hemispherical distributions are derived by starting with the standard guiding-center equation for a gyrotropic plasma (Skilling, 1971; Kulsrud, 1983). In a background plasma of constant speed U, such an ion distribution $f(\mathbf{x},\ v,\ \mu,\ t)$ will follow the equation

$$\begin{aligned}&\frac{\partial f}{\partial t}+(\mathbf{U}+v\mu\hat{\mathbf{e}}_B)\cdot\nabla f+\left(\frac{1-3\mu^2}{2}\hat{\mathbf{e}}_B\cdot(\hat{\mathbf{e}}_B\cdot\nabla)\mathbf{U}-\frac{1-\mu^2}{2}\nabla\cdot\mathbf{U}\right)v\frac{\partial f}{\partial v}+\\&+\frac{1-\mu^2}{2}(v\nabla\cdot\hat{\mathbf{e}}_B+\mu\nabla\cdot\mathbf{U}-3\mu\hat{\mathbf{e}}_B\cdot(\hat{\mathbf{e}}_B\cdot\nabla)\mathbf{U}\frac{\partial f}{\partial v}=\\&=\frac{\partial}{\partial\mu}\left(\Phi(\mu)(1-\mu^2)\frac{\partial f}{\partial\mu}\right)+Q(\mathbf{x},\ v,\ \mu,\ t)\ ,\end{aligned}\tag{4.4.213}$$

where the speed and pitch-angle variables, v and μ, are referred to the plasma reference frame and $\mathbf{e_B}$ is the unit vector parallel to the magnetic field. The first term on the right-hand side of this equation produces pitch-angle scattering of ions toward isotropy in the plasma frame, at a rate given by the diffusion coefficient Φ. The second term Q allows for a source of new ions.

We now assume that the pitch-angle diffusion is much faster than any other process, except in a region around $\mu = 0$ representing the effects of the resonance gap at 90°. It follows that, to lowest order, the pickup ion distribution will take the hemispherical form

$$f(\mathbf{x},\ v,\ \mu,\ t)=f_-(\mathbf{x},\ v,\ t)S(-\mu)+f_+(\mathbf{x},\ v,\ t)S(\mu)\ ,\tag{4.4.214}$$

where $S(x)$ is the step function. Without loss of generality, we take the magnetic field to be pointing away from the Sun, so that f_+ (f_-) refers to the anti-sunward (sunward) hemisphere of the distribution. This construction is an extension of the 2-stream approximation of Fisk and Axford (1969) with the inclusion of dependence on particle speed. Then, integrating (4.4.213) over μ separately from -1 to 0, and from 0 to 1, we obtain the coupled equations for $f_\pm$ as

$$\begin{aligned}&\frac{\partial f_\pm}{\partial t}+U\frac{\partial f_\pm}{\partial r}\pm\frac{v}{2}(\hat{\mathbf{e}}_B\cdot\nabla)f_\pm-\frac{2Uv}{3r}\frac{\partial f_\pm}{\partial v}+\frac{v}{4}\nabla\cdot\hat{\mathbf{e}}_B(f_+-f_-)=\\&\quad=\mp\Gamma(f_+-f_-)+Q_\pm\end{aligned}\tag{4.4.215}$$

where here we have identified the background plasma as the radially flowing solar wind. The terms on the left-hand side of (4.4.215) correspond to changes in time, convection with the solar wind, streaming along the field, adiabatic deceleration,

and adiabatic focusing, respectively. On the right-hand side, the pitch-angle scattering across the gap at 90° is given by the pitch-angle gradient there times the scattering rate $\Gamma = \Phi(0)/\delta$, where δ is an effective width in μ of the transition between f_+ and f_-. Ionization of interstellar neutrals acts as a source to each hemisphere at the rate $Q_\pm$.

This hemispherical approximation yields an enormous simplification of the transport equation for pickup ions. In particular, spatial transport along the magnetic field is controlled completely by the rate of scattering through 90°. Thus, the mean free path of a particle in a hemispherical distribution is simply $\lambda_\parallel = 3v/8\Gamma$.

4.4.2.3. *Steady-state IMF angle.* Consider, first, the case of a steady, radial IMF to correspond approximately to the high-latitude conditions during the measurement of Gloeckler et al. (1995). New ions will appear in the sunward hemisphere only, so we take $Q_+ = 0$. The sunward ionization source has the usual form of a product of an ionization rate which falls as r^{-2}, a spatially varying neutral particle density $N(r)$, and a delta function which causes the new ions to appear at speed U in the solar wind frame

$$Q_- = Q_o = \frac{\beta_o r_o^2}{2\pi r^2 v^2} N(r)\delta(v - U) \; . \tag{4.4.216}$$

We then take the scattering rate Γ to scale as v/r, which plausibly implies a decrease of the scattering process with increasing distance from the Sun as well as a scattering mean free path independent of particle energy. The analytic solution of this system for an arbitrary neutral particle density was presented by Isenberg (1997). If $N(r)$ is known, the solution has only one free parameter, the mean free path. The anisotropic source term $Q_\pm$ requires the anti-sunward distribution $f_+ = 0$ at $v = U$, while the sunward value there is twice the level found for an isotropic distribution. Adiabatic focusing in the diverging field results in transport of some ions into the anti-sunward hemisphere even for $\Gamma = 0$, or infinite mean free path. Naturally, for $v < U$ there is a systematic increase in the anti-sunward density as the mean free path decreases, matched by a corresponding decrease in the sunward density.

The steady hemispherical model was compared to the high-latitude distributions observed at *Ulysses* by Schwadron (1998), using a numerical solution of Equations (4.4.215) and (4.4.216) with a spiral IMF and a constant scattering mean free path. The density of the inflowing neutral particles was given by the 'hot' model (Thomas, 1978; Wu and Judge, 1979), with the parameter values shown in Table 4.4.1. Figures 4.4.7 and 4.4.8 show the observed distributions of pickup protons and He^+, respectively, averaged over the period from day 220 to 280, 1994 when the *Ulysses* spacecraft was near 2.3 AU and 80° latitude. The solid lines show the predicted distributions from the hemispherical model, taking a scattering mean free path $\lambda_\parallel = 2$ AU for protons and $\lambda_\parallel = 0.8$ AU for He^+. The dashed lines show the equivalent results using $\lambda_\parallel = 0.01$ AU, which essentially yields

TABLE 4.4.1

Production rates and parameters used in the hot model for the interstellar neutral density. See Geiss and Witte (1996) for a detailed discussion of these values

Species	T (K)	β_L 10^{-7} s^{-1}	n_∞ (cm^{-1})	$\beta_p(r_1)$ 10^{-7} s^{-1}	v_0 (km s^{-1})	μ_0
Hydrogen	8000	5.5	0.115	≈1.0	20	0.8
Helium	7000	0.6	0.0155	≈0.42	26	0

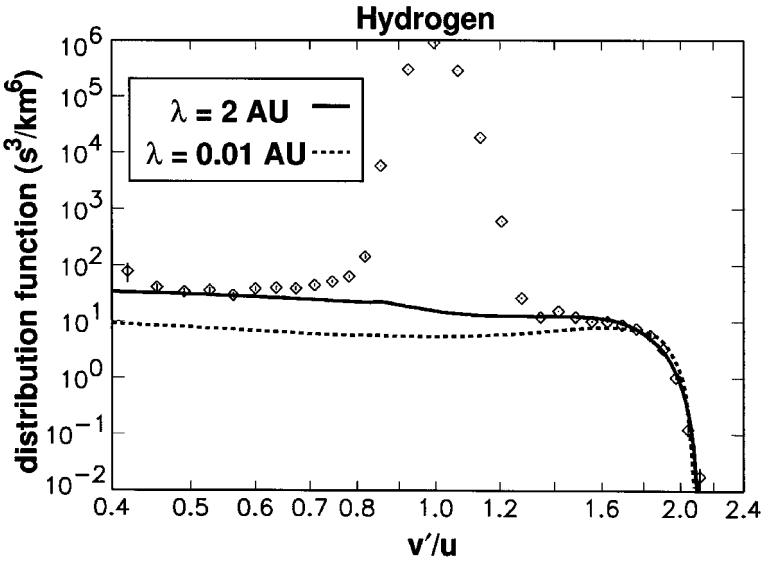

Figure 4.4.7. Comparison between the numerical model and data from Ulysses/SWICS (diamond symbols) for interstellar pickup hydrogen. The solid (dashed) curve was plotted for a 2 AU (0.01 AU) mean free path. Parameters of the model are described in section. See also text for further details.

an isotropic distribution. The agreement between the hemispherical model and the observations is quite good.

The reader may note that the spectra in these figures do not cut off sharply at twice the solar wind speed in the spacecraft frame. This more gradual cutoff is caused by two effects: first, the ions are actually scattered in the wave frame with velocity $u\mathbf{e}_r + V_A\mathbf{e}_B$ measured from the spacecraft reference; second, the solar wind speed fluctuates over the observation period. Both these effects were included in the numerical modeling, taking an Alfvén speed $V_A = 50$ km s^{-1}, and a distribution of wind speeds, centered on the observed mean speed.

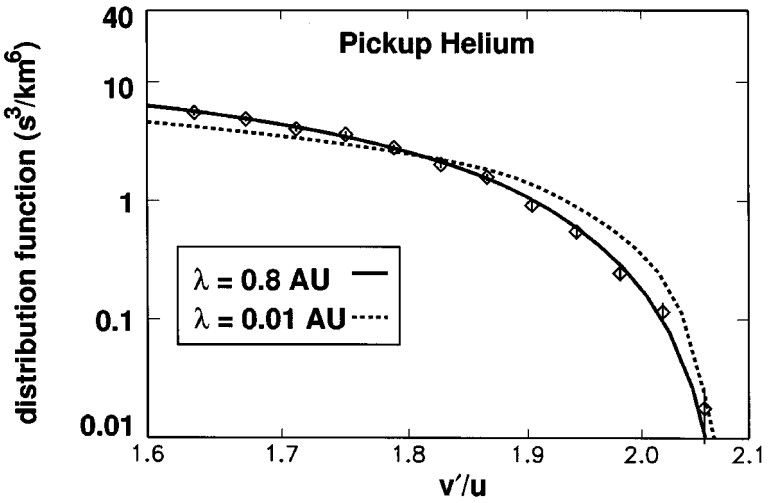

Figure 4.4.8. Comparison between the numerical model and data from Ulysses/SWICS (diamond symbols) for interstellar pickup helium. The solid (dashed) curve was plotted for a 0.8 AU (0.01 AU) mean free path. Parameters of the model are described in section. See also text for further details.

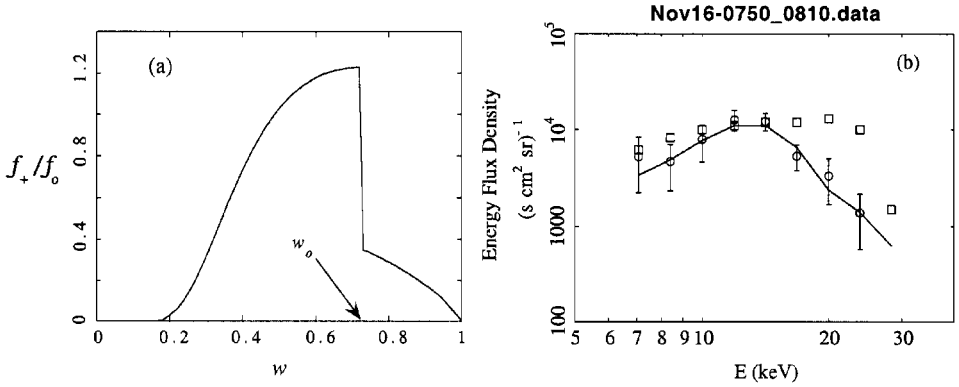

Figure 4.4.9. Left: anti-sunward distribution of pickup ions at an observation point within a radial flux tube segment, from the hemispherical bent-flux-tube model of Isenberg and Lee (1998). *Right*: comparison of a bent-flux-tube model spectrum with AMPTE/SULEICA data. The circles with error bars are the measurements of He^+ energy flux density during 07:50–08:10 on November 16, 1985. The squares are the predictions for an isotropic distribution on that date from the model of Möbius et al. (1995). The solid line is shows the spectrum that the SULEICA instrument would measure if it observed the model distribution.

4.4.2.4. *Changing IMF angle.* On a shorter time scale, the IMF angle is not steady even at high latitude, and the AMPTE data reported in Möbius et al. (1998) has sufficient time resolution to distinguish the pickup He^+ behavior between radial and non-radial conditions. To investigate the transport of pickup ions under conditions of changing IMF angle, Isenberg and Lee (1998) considered a flux tube which is azimuthal except for a single radial segment of length L. The flux

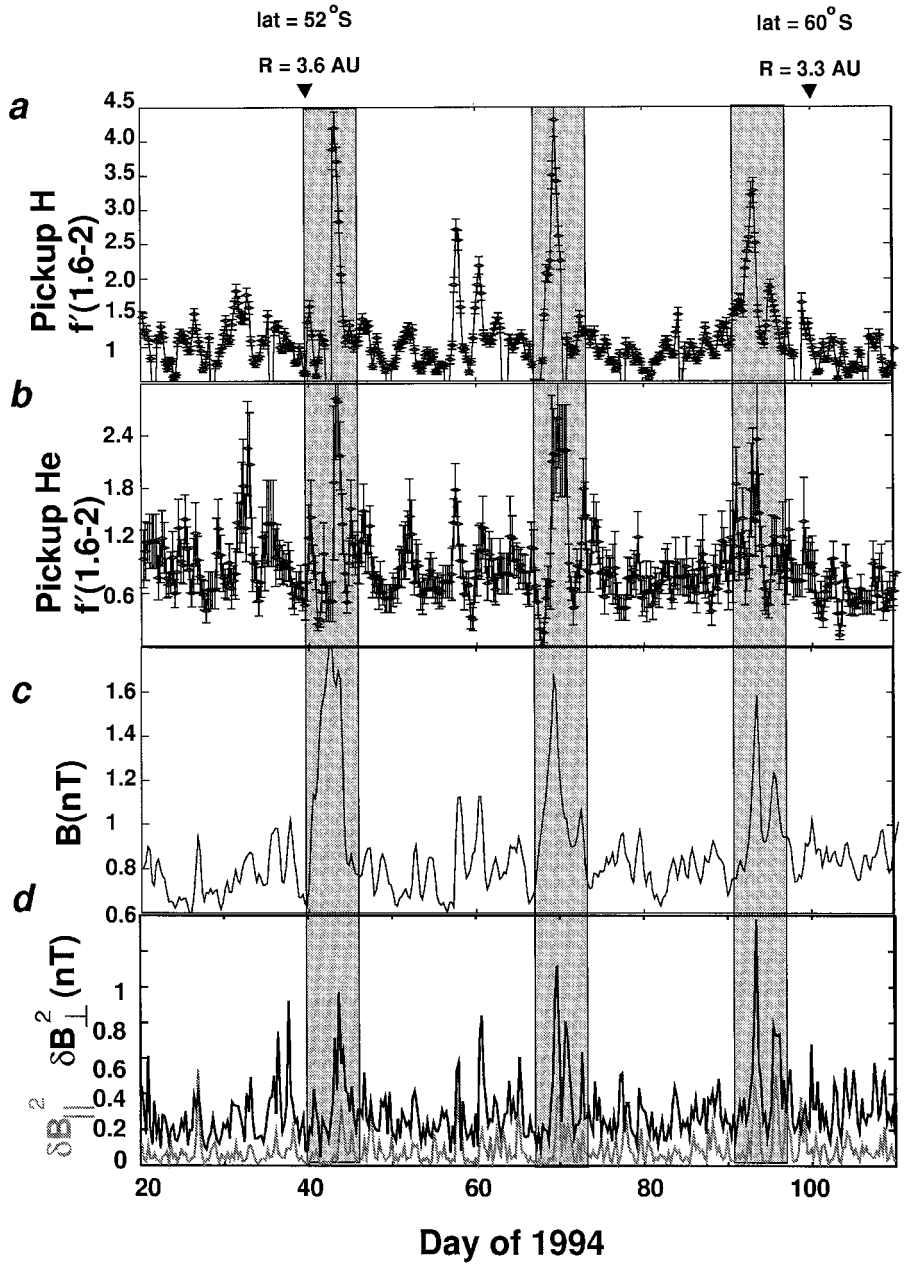

Figure 4.4.10. Observed pickup ion enhancements correlated with signatures of compression in the magnetic field data, including (a, b) the parameter $f(1.6-2)$, (c) magnetic intensity B, and (d) fluctuations in the magnetic field parallel to and perpendicular to the magnetic field, $\delta B_{\parallel}^2$ and $\delta B_{\perp}^2$, respectively. All data were obtained using running one-half day averages.

tube moves away from the Sun at constant speed U and accumulates pickup ions at the total ionization rate Q_0, given in (4.4.216). Consistent with the equatorial conditions at AMPTE, L is taken to be small compared to both the scale for pickup of new ions and the scale for the radial decrease of the magnetic field magnitude. The first of these assumptions means that the total ionization rate can be taken constant along the flux tube, though it still varies with r. The second assumption allows the neglect of adiabatic focusing on the radial segment. Further, the bends in the flux tube between the radial and azimuthal segments are taken to be gradual compared to a pickup ion gyroradius, so the parallel transport is not be affected by the bends. When the hemispherical approximation is applied to this system, it is found that the equations describing the ion transport in the radial flux tube segment are identical to those for the azimuthal regions. In this case, the only distinction between the segments comes from the source term. When the flux tube is azimuthal, new ions populate the two hemispheres equally, so $Q_+ = Q_- = Q_0/2$. In the radial segment, new ions only appear in the sunward hemisphere, so $Q_+ = 0$ and $Q_- = Q_0$, as in the earlier model. Again an analytical solution is available, this time for constant $\lambda_\parallel$.

A detailed discussion of this solution is given in Isenberg and Lee (1998). Briefly, the behavior of the anti-sunward distribution, defined as f_+ in the radial region or $(f_+ + f_-)/2$ in the azimuthal regions, is essentially understood as the result of the combined actions of pickup in the sunward hemisphere, streaming along the flux tube between regions, and adiabatic deceleration which relates the energy of a pickup ion to the distance it has traveled since it was ionized. For the long scattering mean free paths indicated by the observations, the effect of scattering between the hemispheres is secondary to these other processes.

This model exhibits a depletion of the anti-sunward pickup ion density in the radial segment, as found by Möbius et al. (1998). However, the streaming of isotropically picked up ions from the adjacent azimuthal segment requires a large value of L and an observation point fairly distant from the sunward end of the radial segment to yield density decreases of the observed magnitude. This result is emphasized by comparison of the distribution of anti-sunward ions in the radial segment with the measured spectra.

Figure 4.4.9(a) shows the shape of the f_+ distribution at an observation point in the radial segment of the model flux tube. This shape is determined by two free parameters, the mean free path $\lambda_\parallel$ and the distance from the observation point to the sunward end of the radial segment $x < L$. The distribution is split into two parts by the sharp decrease at an intermediate speed w_0, where $w = v/u_{sw}$. The ions with $w < w_0$ were picked up in the azimuthal region sunward of the radial segment and have streamed to the observation point with nearly the shape expected for an isotropic distribution. The ions with $w > w_0$ were picked up into the sunward hemisphere within the radial segment and appear in f_+ only by scattering through 90°. Thus, the position of the sharp decrease at w_0 gives the distance x, and the shape of the $w > w_0$ distribution can be fit by setting $\lambda_\parallel$.

Figure 4.4.9(b) shows a comparison of this model spectrum with AMPTE/SULEICA data. The circles with error bars depict the measured energy flux density of He^+ for the time 07:50–08:10 on November 16, 1985, at the beginning of a nearly four hour period of quasi-radial IMF. The squares show the fluxes predicted for that date from the analysis of Möbius et al. (1995) , which assumes immediately isotropized pickup ions. The line in the figure is obtained by calculating a model f_+ distribution from the same neutral helium density used for Möbius et al. (1995) with $\lambda_\parallel = 0.75$ AU and $x = 0.2$ AU, and feeding it through the software package which simulates the SULEICA response. The model fits the data quite well. Similar fits to the spectra for five of the 20-min time periods yield model parameter values of $\lambda_\parallel = 0.5–0.75$ AU and $x = 0.18–0.21$ AU. These values of $\lambda_\parallel$ are comparable to those obtained by Fisk et al. (1997) and Schwadron (1998) from analysis of Ulysses data, but the required length of the radial flux tube segment is far too large, corresponding to radial conditions at the spacecraft for a period of 12.7–14.8 hours in the 590 km s^{-1} solar wind. The model requires similarly unrealistic values of x to generate the anti-sunward density depletions reported by Möbius et al. (1998).

The likely cause of this discrepancy is the efficient pitch-angle scattering within each hemisphere which is implemented by the hemispherical approximation. In the model, ions picked up in the sunward azimuthal region populate both hemispheres of phase space and are instantaneously transported from 90° pitch angle into the parallel direction. The f_+ ions in the azimuthal region can then easily stream into the radial segment, where they show up as undepleted anti-sunward ions. In this case, substantial anti-sunward depletions can only appear in the radial segment if the observation point is far enough from the sunward end that these streaming ions are decelerated to speeds below those exhibiting depleted fluxes. As we have seen, these required distances are unrealistically long.

This discrepancy is not corrected by adjusting the value of $\lambda_\parallel$. Nor is it possible to plausibly inhibit the streaming through the bends in the flux tube without making the problem worse. One can insist that the observations do not match the conditions assumed in the model: The radial segment may in fact be longer than observed since the spacecraft does not remain on the same flux tube. It may also be true that the large values of L obtained by these comparisons are somehow manifestations of the spiral field which is more radial than azimuthal inside 1 AU and not included in the model.

However, it seems most likely that we have simply pushed the hemispherical model beyond its applicable limits. If the scattering into the parallel direction were not immediate, the streaming into the radial segment would not be so extreme and more reasonable values of L would result for a given anti-sunward depletion. It is not hard to believe that, in systems which change on scales smaller than the typical streaming distance, the fact that the pitch-angle scattering is really not instantaneous would become important. Consequently, Isenberg and Möbius (1998) have set out to test the hemispherical approximation by investigating the isotropy of anti-sunward pickup He^+ in radial IMF as seen at AMPTE. Preliminary results

show stronger flux decreases for pitch angles around the anti-sunward direction than for pitch angles closer to 90°. This investigation is not yet conclusive, but may indicate a substantially slower scattering rate within the anti-sunward hemisphere than has been assumed. Unfortunately, such a result will likely make construction of quantitative models of these pickup ion distributions more difficult.

4.4.3. *Pickup Ions in Compressive Regions*

Strong enhancements in pickup hydrogen and helium at high latitudes inside regions of strong compression have been observed by *Ulysses*. The enhancements can be explained using a pickup ion transport model which includes compression, but which still requires a long mean free path. That is, despite the strong compression, and the accompanying turbulence, the low-rigidity pickup ions still do not scatter appreciably through 90°.

The SWICS instrument is most sensitive to pickup ions in the speed range $1.6 < v/u < 2.0$. Therefore, we use the quantity $f'(1.6{-}2.0)$ as an indicator of the intensity of pickup ions, where

$$f'(1.6{-}2.0) = \frac{5}{2} \int_{1.6u}^{2.0u} \frac{\mathrm{d}v'}{u} f'(v') \; . \tag{4.4.217}$$

It should be noted however, that changes in the quantity $f'(1.6{-}2.0)$ are simply indicative of changes in the number of ions with pitch-angles of less than 90°. Therefore, both changes in the scattering rate and changes in the net flux of pickup ions would influence the quantity $f'(1.6{-}2.0)$.

An overview of the compressional events is provided in Figure 4.4.10. Plotted is $f'(1.6{-}2.0)$ for hydrogen and helium, and the magnetic intensity between day 20 and 110 of 1994. Strong enhancements of hydrogen, helium, and the magnetic intensity are observed near days 40, 70 and 95 of 1994. The intensity peaks in pickup hydrogen and helium are in fact the most dramatic increases observed during all of 1994. During this period, *Ulysses* was near 55° S latitude and 3.5 AU.

The solar wind speed drops by about 100 km s^{-1} in each of the compressional events, which are separated by almost 27 days which immediately suggests that the events are corotating phenomena. In fact, the compressional events have a heliospheric longitude, which when projected back to the solar wind source surface, correlates with a strong deformation in the coronal hole boundary. This, in turn, suggests that the drop in the solar wind speed results from the coronal deformation. This is not surprising since the deformation of the coronal hole causes a local decrease in the area from which field lines diverge below the source surface. Hence, the field lines caught up in the coronal hole deformation would be forced to expand more strongly beneath the source surface, leading to a locally slower wind. This inverse correlation between solar wind speed and flux tube expansion has been pointed out by Levine et al. (1977), and Wang et al. (1997). The fact then that the

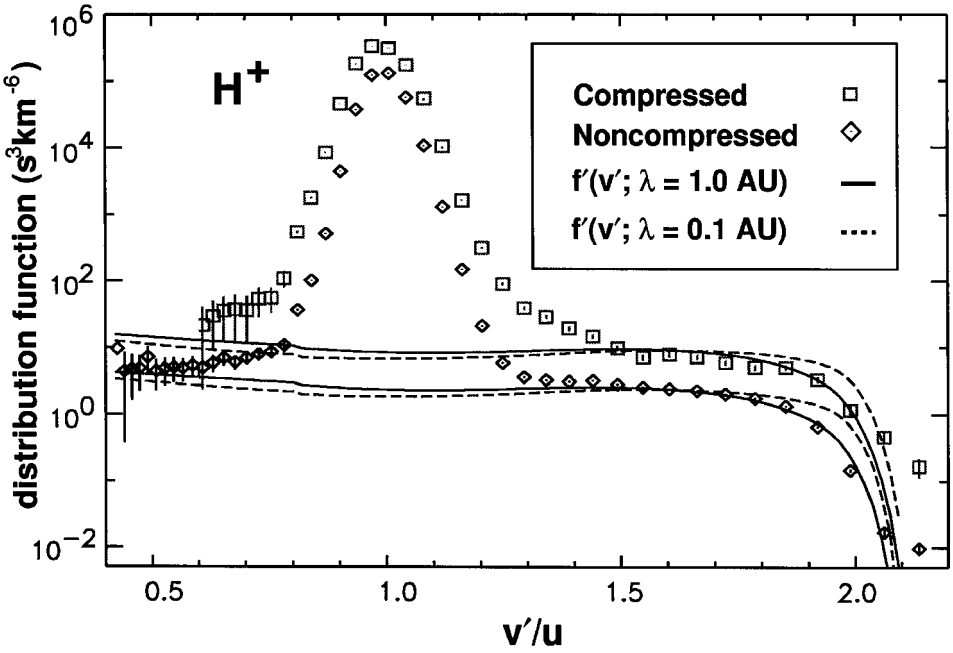

Figure 4.4.11. The observed hydrogen distribution within and outside the compressed corotating regions. Models for the pickup hydrogen distribution suggest a 1 AU scattering mean free path. The accuracy of the mean free path determination is within 10%.

flow speed decreases within the corotating events suggests immediately that the compressed region is formed as faster wind locally overtakes slower wind.

A simple model was developed for the solar wind and mean magnetic field within the compressive regions which assumed quite simply that the flow underwent a less-that-radial, or subradial, expansion. The model equations are described in detail in Schwadron et al. (1999b). For the interstellar neutral density, $n_n(r,\ \theta,\ \beta_L,\ T,\ n_\infty,\ v_o,\ \mu_o)$, we again use the 'hot' model (Fahr, 1971; Thomas, 1978; Wu and Judge, 1979). In Table 4.4.1 we list the values of the hot model parameters used for the calculations in this paper. The production rates used here are slightly different than those indicated in the table: for the pickup protons, we take $\beta_p \approx 1.4 \times 10^{-7}\ \mathrm{s}^{-1}$ and for pickup He^+ we take $\beta_p \approx 1.1 \times 10^{-7}\ \mathrm{s}^{-1}$.

The numerical model yields a pickup ion distribution function in the solar wind reference frame, which is then integrated through the response function of the SWICS instrument, yielding the distribution in the spacecraft reference frame $f'(v')$. In Figure 4.4.11 we show the predicted and observed hydrogen distribution function for hydrogen in the spacecraft reference frame. The lower spectrum was obtained by superposing the distributions observed between days 20 and 38, between days 46 and 64, between days 73 and 90, and between days 98 and 120 of 1994. Hence the lower distribution represents a pickup hydrogen spectrum

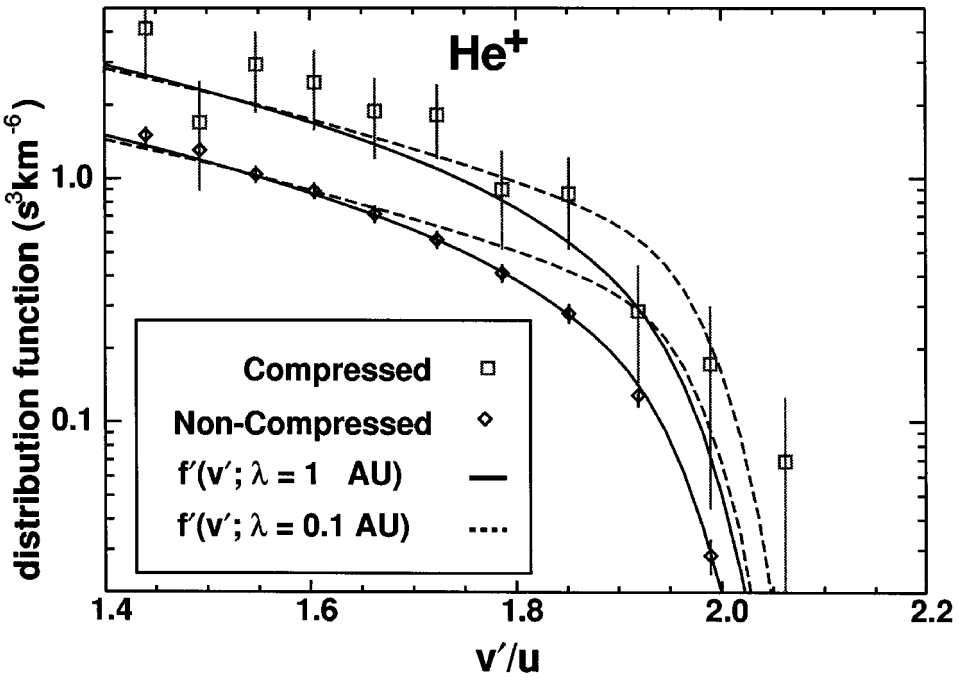

Figure 4.4.12. The observed helium distribution outside the compressed corotating regions. Models for the pickup helium distribution suggest a 1 AU scattering mean free path. The accuracy of the mean free path determination is within 10%.

observed between days 20 and 120, 1994, and it excludes the periods of strong compressional enhancements. The lower solid (dashed) curve represents the modeled distribution in the uncompressed region with a mean free path of $\lambda = 1$ AU ($\lambda = 0.1$ AU). In fact, by varying parameters we have found that the accuracy of the mean free path determination is within 10%. The knee of the spectrum has a shape which suggests the longer mean free path, and the normalization requires a production rate of $\beta_p \approx 1.4 \times 10^{-7}$ s^{-1}.

The upper spectrum in Figure 4.4.14 was obtained by superposing the distributions observed between days 43.1 and 43.9, and between days 69 and 70 of 1994. Hence the upper distribution represents a pickup hydrogen spectrum observed during the first two compressional events. The upper solid (dashed) curve represents the modeled distribution in the compressed region with a mean free path of $\lambda = 1$ AU ($\lambda = 0.1$ AU). Again, the accuracy of the mean free path determination is within 10%. The knee of the spectrum has a shape which is again consistent with the longer mean free path.

In Figure 4.4.12 we show the observed and modeled helium distribution functions in the spacecraft reference frame. The helium distribution was observed between days 20 and 120 of 1994, and superposes epochs so as to exclude the com-

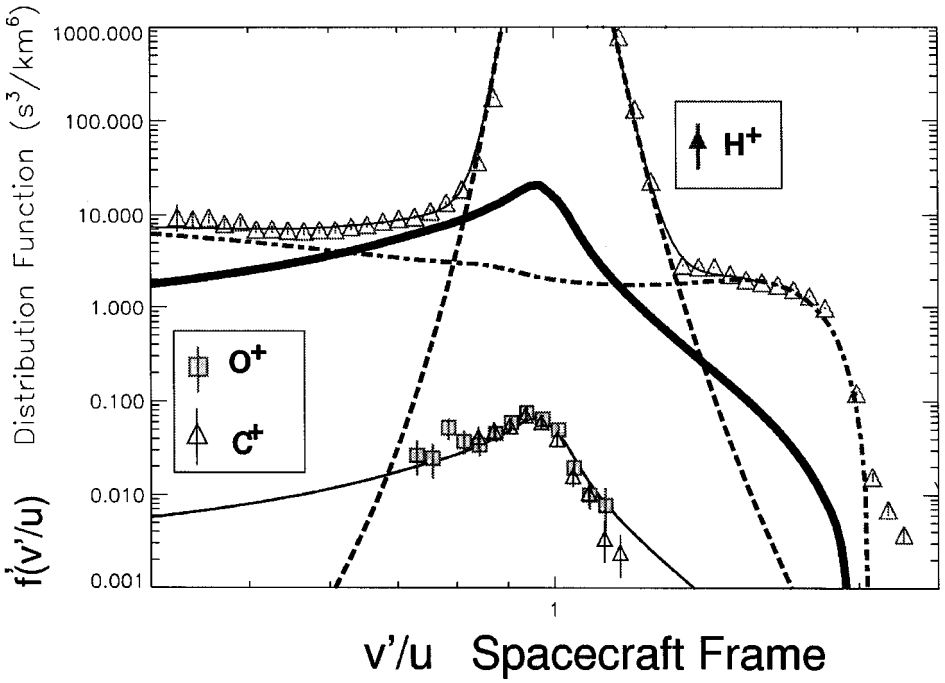

Figure 4.4.13. The inner source C^+, O^+, and H^+ distribution functions observed during all of 1994 as compared with modeled distributions. See also text for further details.

pressional events, as was done for the hydrogen spectrum. The solid (dashed) curve represents the modeled distribution in the uncompressed region with a mean free path of $\lambda = 1$ AU ($\lambda = 0.1$ AU). The knee of the spectrum has a shape which suggests the longer mean free path, and the normalization requires a production rate of $\beta_p \approx 1.1 \times 10^{-7}$ s^{-1}.

The upper distribution represents a pickup helium spectrum observed during the first two compressional events, superposing the same periods as those described for hydrogen. The upper solid (dashed) curve represents the modeled distribution in the compressed region with a mean free path of $\lambda = 1$ AU ($\lambda = 0.1$ AU). The statistics are clearly too poor in this case to distinguish between a long or short mean free path for helium.

4.4.4. *Observations of the Inner Source*

In this section, we discuss the implications of inner source C^+ and O^+ distribution functions for the radial and latitudinal profiles of the inner pickup ion sources, and establish the presence and potential energetic importance of inner source H_+.

The observed distribution functions of H^+ (upper triangles), C^+ (lower triangles), and O^+ (lower squares) are shown in Figure 4.4.13 for all of 1994. The observed distribution function, $f'(v')$ can be related to the distribution function

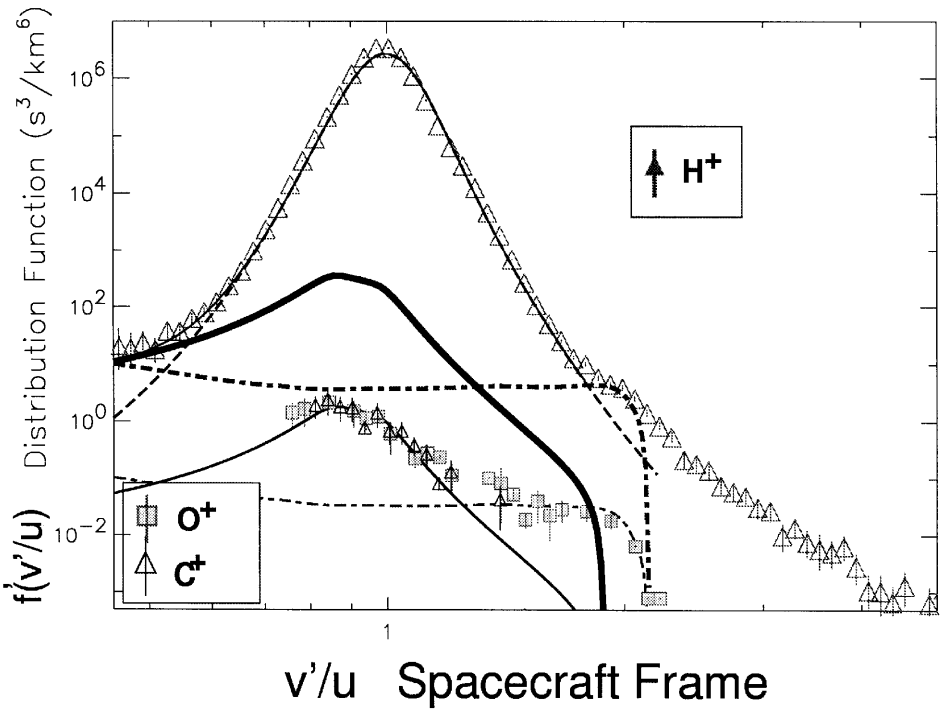

Figure 4.4.14. The inner source C^+, O^+, and H^+ distribution functions observed between day 30 and 90 of 1995 as compared with modeled distributions. See also text for further details.

in the solar wind frame, $f(v)$, through an angular integration over the instrument acceptance angles (1). During the observation period used in Figure 4.4.13, all of 1994, *Ulysses* moved between 48° S latitude to 80° S and then back to 45° S. *Ulysses* also traveled from 3.8 AU to 1.6 AU. The solar wind speed was extremely steady with a speed of about 780 km s^{-1}.

The second set of observations are shown in Figure 4.4.14 representing a period from day 30 to day 90 of 1995 while *Ulysses* moved rapidly between 25° S latitude to 20° N latitude climbing about 1° in latitude each day, as it remained near 1.4 AU. Some smoothing of the C^+ (lower triangles) and O^+ (lower squares) data was performed. This was a unique opportunity to observe the inner source ions since *Ulysses* was closer to the Sun than at other points in its orbit. *Ulysses* experienced at least half a dozen fast and slow streams during this period as the solar wind varied between 300 km s^{-1} and 750 km s^{-1}.

The conclusion of the investigation of Schwadron et al. (2000) are:

Transport Implications: the observed distributions are highly anisotropic consistent with mean free paths $\lambda > 2$ AU, suggesting that ions are essentially unscattered through 90° pitch angle. This shows clearly that the large mean free path observed for interstellar pickup ions at $r > 1$ AU is still quite large at the much smaller radial distances (10 $R_s < r < 0.5$ AU) at which inner source ions are picked up.

TABLE 4.4.2
Modeling parameters and mass production rates

Lat.	λ	$\beta_p\, n_o\, [H^+]$	L	χ	$[H^+]/[O^+]$	$\frac{dm}{dt}(r_1, +)$ C	$\frac{dm}{dt}(r_1, +)$ H
	(AU)	($cm^{-3}\ s^{-3}$)	(AU)		(kg^{-1} $nucl^{-1}$ sr^{-1})	(kg^{-1} $nucl^{-1}$ sr^{-1})	
$<25°$	>2	16.7	0.3	2.5	2000	22	43 200
$>45°$	>2	6.2	0.05	1.2	310	37	11 300

Moreover, inner source ions cool adiabatically as they propagate due to the usual betatron effect. Hence the mean free path must remain large, $\lambda > 2$ AU over a wide range of rigidities, $R_0/10 < R < R_0$, where R is the ion rigidity and R_0 is the rigidity of the initially picked up ion ($R_0 \approx 2$ MV).

Radial Profile: At high latitudes we observed a distribution function consistent with a source density which scales as $n_n(r) \approx n_o(r_1/r)^\nu \exp(-L/r)$ where $L \approx 10R_s$ and $\nu \approx 1.2$. This distribution is quite similar to an interstellar grain distribution, having $\nu \approx 1$ (e.g., Fahr, 1981). The distribution at low latitudes is somewhat different: the maximum is pushed out to $L \approx 0.3$ AU and the radial falloff is steeper $\nu \approx 2.5$.

Latitudinal Distribution: The mass production rate per nucleon within a steradian solid angle element, dm/dt is listed in Table 4.4.2 for inner source H^+ and C^+ (note that dm/dt is nearly identical for C^+ and O^+). This parameter together with the relative abundances also listed in Table 4.4.2 at two different latitude ranges reveals some interesting features. There is apparently a factor of 4 more inner source H^+ at low latitudes. This excess of inner source material at low latitudes is consistent with a grain distribution which has a factor of about 8 more material at low compared to high latitudes (e.g., Dumont, 1976). This excess in material at low latitudes is not consistent with the C^+ and O^+ distributions. Moreover, the relative abundance $[H^+]/[C^+]$ is near the universal value at low latitudes but is smaller at high latitudes. This observation suggests that inner source material is processed differently at low vs. high latitudes.

The energetic importance of inner source H^+ : The inner source H^+ density constrained by the fit in Figure 4.4.13 is $n_{\text{inner}}(H^+) \approx 1.7 \times 10^{-4}$ cm^{-3} and is similar to the constrained density of interstellar pickup ions, $n_{\text{int}}(H^+) \approx 1.2 \times 10^{-4}$ cm^{-3} observed in this case at about 3 AU. During this 1994 period, the solar wind density was about a factor 1000 larger than the inner source and interstellar densities. Hence, it is plausible that the inner source ions have a large pressure closer to the Sun, particularly if they are more anisotropic near their source.

To quantify the potential energetic importance of this new population, consider the following illustrative calculation. The density of inner source O^+ at $r = 3$ AU was derived from our fit to the distribution function in Figure 4.4.13 $n_{\text{inner}}(r =$

$r_{\rm obs},\ {\rm O}^+) \approx 5.5 \times 10^{-7}\ {\rm cm}^{-3}$. Consider the density of inner source O^+ at $r_{\rm in} = 0.3$ AU:

$$\frac{n_{\rm inner}(r = r_{\rm in},\ {\rm O}^+)}{n_{\rm inner}(r = r_{\rm obs},\ {\rm O}^+)} = \left(\frac{r_{\rm obs}}{r_{\rm in}}\right)^2 \frac{u - v_o(r_{\rm obs})}{u - v_o(r_{\rm in})}\ . \tag{4.4.218}$$

Here, $v_0(r)$ is the average speed at which O^+ ions stream against the solar wind in the radial direction. We find that $v_0(r_{\rm obs}) = 80\ {\rm km\ s}^{-1}$. In the case of a highly anisotropic distribution close to the inner source, $u - v_0(r_{\rm in})$ may be much smaller than the solar wind speed u. In this illustrative example, we take $u - v_0(r_{\rm in}) \approx 10\ {\rm km\ s}^{-1}$, yielding $n_{\rm inner}(r = r_{\rm in},\ {\rm O}^+) \approx 4 \times 10^{-3}\ {\rm cm}^{-3}$. Factoring in the relative abundance $[H^+]/[O^+]$ about 310 we find a density of inner source H^+, $n_{\rm inner}(r = r_{\rm in},\ {\rm H}^+) \approx 1.2\ {\rm cm}^{-3}$, and a pressure given by $P_{\rm inner}(r = r_{\rm in},\ {\rm H}^+) \approx m_p n_{\rm inner}(r = r_{\rm in},\ {\rm H}^+)u^2 \approx 1.2 \times 10^{-8}$ erg cm^{-3}. As a comparison, a 4 nT magnetic field at 1 AU has a magnetic pressure given by $B(r = r_{\rm in})^2/8\pi \approx 4 \times 10^{-9}$ erg cm^{-3}, and a typical solar thermal pressure at $r = r_{\rm in}$ is given by $P_{sw}(r = r_{\rm in}) \approx 6 \times 10^{-9}$ erg cm^{-3}. In other words, if the inner source ions are highly anisotropic close to the Sun, their pressure $P_{\rm inner}(r = r_{\rm in})$ may exceed both the solar wind magnetic and thermal pressures.

4.4.5. *Effects of Mass Loading in the Outer Heliosphere*

Mass loading of the solar wind occurs on the largest scale in the outer heliosphere, through the cumulative effect of the pickup of inflowing interstellar hydrogen. The resulting energy and momentum input to the solar wind has been investigated in many works (e.g., Blum and Fahr, 1970; Holzer, 1972; Holzer and Leer, 1973; Isenberg, 1986; Lee, 1997; Whang, 1998), and should yield substantial heating and deceleration of the flow. However, experimental confirmation of these effects has proven difficult. The *Pioneer* and *Voyager* probes, the only spacecraft to travel beyond 10 AU, are not equipped with instrumentation that can detect pickup ions unambiguously. In addition, accurate solar wind measurements become more of a problem as the densities and fluxes shrink with distance from the Sun, and the instrument capabilities and data coverage also decline with the age of these venerable missions. However, several attempts to detect these effects have been encouraging, if not completely conclusive.

4.4.5.1. *Pressure-balanced structures.* Near 1 AU, structures are often found in the solar wind in which the thermal pressure of the solar wind varies opposite to the magnetic pressure such the total pressure remains constant according to:

$$\frac{B^2(x)}{8\pi} + n_p(x)k[T_p(x) + T_e(x)] \approx \text{constant}\ , \tag{4.4.219}$$

where n_p is the solar wind proton density, T_p and T_e are the proton and electron temperatures, and x is the position within the structure. In a series of papers,

Burlaga et al. (1990, 1994, 1996) used *Voyager* observations of structures with anti-correlated proton and magnetic field pressures between 20 and 40 AU to investigate the pickup proton heating of the solar wind.

The inclusion of a pickup proton component to (4.4.219) yields an outer heliosphere pressure balance equation

$$\frac{B^2(x)}{8\pi} + n_p(x)k\left[T_p(x) + T_e(x) + \frac{n_i(x)}{n_p(x)}T_i(x)\right] \approx \text{constant}\ , \qquad (4.4.220)$$

where n_i and T_i are the density and temperature, respectively, of the pickup protons. Since T_i, the effective temperature of an isotropic pickup proton distribution, is directly related to the nearly constant solar wind speed, it is assumed to be constant within the structure. Furthermore, the bulk of the pickup protons are generated by charge exchange with the solar wind protons, so n_i/n_p is also expected to be constant. Then the value of the constant $n_i T_i/n_p$ is obtained as that value which minimizes the variation of the total pressure through the structure according to (4.4.220).

This technique is insensitive to the fraction of the pickup proton pressure which is constant across the structure, so photoionized pickup protons and any portion of the distribution which gets smeared out over the about 0.01 AU scale size of the structure will not be detected. Still, for those structures beyond 34 AU, Burlaga et al. (1996) have found that hot pickup protons were required to give pressure balance, and the derived lower limits on the densities were quite reasonable when compared with theoretical expectations.

4.4.5.2. *Solar wind deceleration.* The solar wind mass- and momentum-loading from interstellar pickup protons should also slow the wind measurably. However, the solar wind speed is extremely variable in both latitude and time which complicates the detection of this effect. Richardson et al. (1995) compared the running yearly average speed between IMP 8 at 1 AU and *Voyager 2* approaching 40 AU in an attempt to quantify the net loading of the plasma. After correcting for an apparent offset between the averaged speed measurements at the two spacecraft, Richardson et al. concluded that the average flow at 40 AU was 30 km s^{-1} slower than that at 1 AU. From this value, they inferred an inflowing hydrogen density at the termination shock of $n_H \approx 0.05$ cm^{-3}.

We now think that n_H is considerably larger than this, but Isenberg and Lee (1999) have suggested that the Richardson et al. data may not be inconsistent with inflowing hydrogen densities as large as $n_H = 0.14$ cm^{-3}. *Voyager 2* has been traveling to higher heliolatitudes since 1990, and the higher speeds found away from the equatorial region will mask any deceleration, yielding smaller differences between *Voyager* and IMP. Richardson et al. felt that at 40 AU, Voyager had reached the maximal latitude to allow this comparison, but the average speed there may have already been modified by the high-speed mid-latitude flow. Isenberg points out that similar speed comparisons when Voyager was closer to the Sun result in

larger values of nH. In addition, the analysis in Richardson et al. (1995) was taken from the outer heliosphere model of Lee (1997), which should not be extrapolated in as far as 1 AU.

4.4.5.3. *Consequences for the solar wind termination shock.* The combination of solar wind deceleration and heating resulting from the pickup of interstellar hydrogen leads to a considerable reduction in the Mach number of the flow. In the absence of such mass loading, the expanding solar wind would cool continuously ($T_p \approx r^{-4/3}$ in a steady adiabatic solar wind) and the Mach number would reach very high values in the outer heliosphere. A termination shock placed at 80–100 AU would consequently need to be a very strong shock with a sonic Mach number on the order of 100 or more. However, the mass loading due to an inflowing hydrogen density of $n_{\mathrm{H}} \approx 0.1$ cm^{-3} reduces the Mach number in this radial range to less than 3 (e.g., Holzer, 1972).

Although the termination shock has yet to be observed directly as of this writing, the strength of the shock influences the spectrum of energetic particles accelerated there. These particles, the 'anomalous cosmic rays', have been used analyzed by Stone et al. (1996) to estimate the position and strength of the shock. Their findings, though dependent on a number of model assumptions, are consistent with the expectations of significant mass loading of the solar wind by interstellar hydrogen (Isenberg, 1997).

4.5. MASS LOADING AND ION RELEASES

Mass loading onto a streaming plasma may be realized in a variety of ways. The mass source may be extended and diffuse or concentrated. Examples are the interstellar gas pervading the heliosphere and, for concentrated sources, comets and unmagnetized planets, all of them loading ions onto the solar wind plasma. These situations differ by the way they affect the plasma flow. They range from slight perturbations to severe slow-down and rerouting of the flow around the mass source. The artificial comet experiments of the AMPTE mission, performed in 1984–1985, were extreme realizations of the latter. In addition, special circumstances prevailed in these experiments because of the small dimensions of the mass source in comparison with the gyroradii of the pickup ions. This gave rise to the appearance of very surprising effects, which put the experiments in contrast to most of the natural mass loading situations and make it worthwhile to revisit them.

This subchapter will deal solely with those aspects of the artificial comet releases which are relevant to mass loading, and will neglect several other interesting features. The first step, before ion implantation into the ambient plasma flow can proceed, is the magnetization of the initially fully diamagnetic plasma cloud, because it is the magnetic field that couples momentum from the flow to the plasma source. The central topic is that of momentum transfer. It is intimately connected with ion extraction from the plasma cloud and offers the most surprising findings

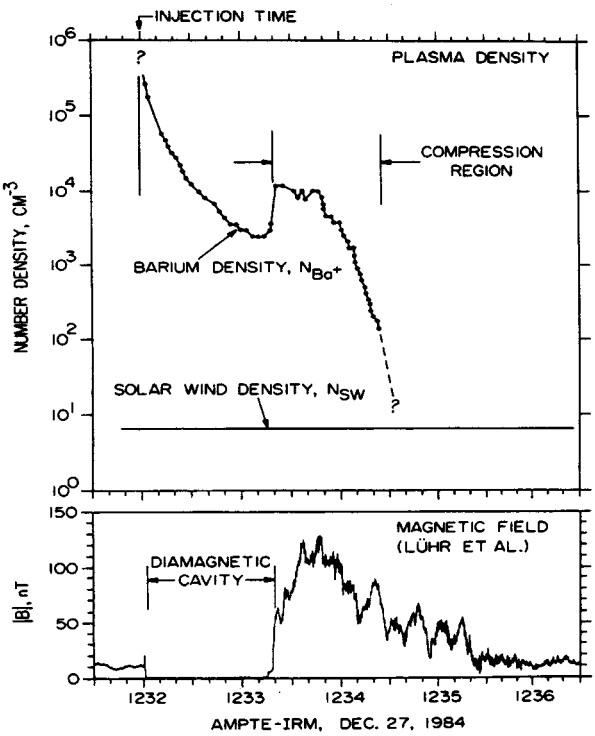

Figure 4.5.1. Plasma density (upper diagram) and magnetic field strength during the first artificial comet experiment on 27 December 1984 at 12:32 UT (Gurnett et al., 1986).

of these experiments. Comparison with natural mass loading situations asks for the definition and differentiation between light and heavy mass loading, which will be presented in the third section. Finally, we will comment on the fact that such a plasma cloud, quite alike to comets, is not a continuous plasma source, but that detachment of plasma packets or clumps from the main body is another mode of mass loading. A clumping instability as origin of that will be suggested. A more detailed discussion of the latter in the context of cometary simulations can be found in Section 4.6.

4.5.1. *Magnetization*

Figure 4.5.1, taken from Gurnett et al. (1985), shows the total plasma (electron) density and magnetic field strength as measured at the center of the barium plasma cloud created on December 27, 1984, in front of the bow shock by the Ion Release Module (IRM) of the AMPTE project. The released mass was about 2.0 kg ($\cong 9 \times 10^{24}$ ions). It was sufficient to create a magnetic cavity in the ambient 12 nT field of about 80 km radius (Valenzuela et al., 1986). This maximum extent of the cavity was reached after 60 s, and already 20 s thereafter, the magnetic

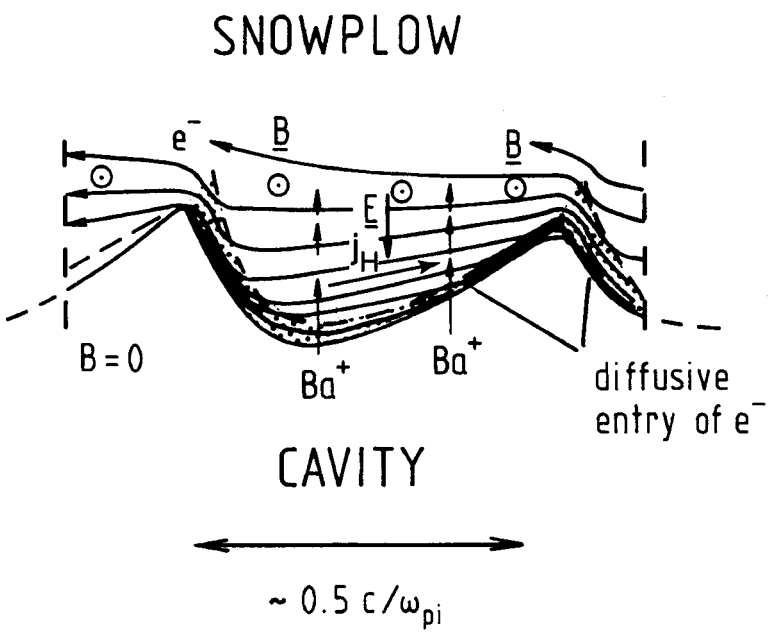

Figure 4.5.2. Ion and electron trajectories at the striated front of the magnetic snow plow which propagates into the initial diamagnetic cavity. The ions are unmagnetized and slowed down by a polarization field, **E**. The electrons perform an $\mathbf{E} \times \mathbf{B}$-drift and constitute a Hall current screening the magnetic field form the cavity.

field returned to the position of the IRM in the cloud's center, accompanied by compressions of both, magnetic field and plasma density (see Figure 4.5.1).

Haerendel et al. (1986) interpreted the quick magnetization of the initially diamagnetic cloud as caused by a snow plow effect, by which the compressed magnetic field acts against the inertia of the ions entering the field and depositing most of their momentum relative to the magnetic front. It progresses with the speed:

$$v_{sp} \cong \frac{B_c}{\sqrt{8\pi\rho_o}}\,, \tag{4.5.221}$$

whereby B_c is the compressed field (by a factor of 10 in the experiment) and ρ_0 the mass density in front of the snow plow. With $n_0 = 2.5 \times 10^3$ cm^{-3} and $B_c = 130$ nT and further refinements of Equation (4.5.221), one obtains $v_{sp} \approx 3.8$ km s^{-1} and the right timing for the field return. The cause of the magnetic field compression is, of course, the ram pressure of the solar wind. Its magnitude, $\kappa = B_c/B_o$, will be discussed next.

The snow plow mechanism is rather subtle. Whereas the ions can enter directly from the cavity into the compressed field, because of a negligible Lorentz force, and are slowed down behind the magnetic front by a retarding electric potential, the electrons experience the magnetic field as a not easily penetrable barrier. Formation of striations, however, offers a help, as sketched in Figure 4.5.2 (Haerendel, 1986).

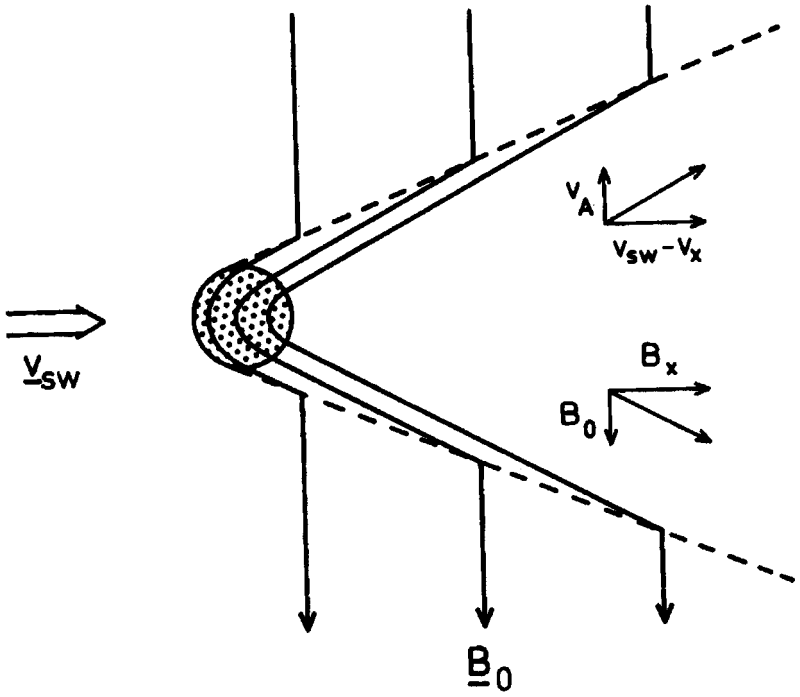

Figure 4.5.3. Momentum transfer form solar wind to the barium plasma cloud via a compressed field with Alfvén wings.

After initial magnetization in a thin layer of order c/ω_{pe} owing to some wave activity (Gurnett et al., 1985), the electrons perform an $\mathbf{E} \times \mathbf{B}$-drift in the retarding electric field, transverse to the motion of the ions.

This generates a Hall current, the very current screening the snow plow field from the cavity. Charge neutrality inside the snow plow requires equality of the integrated Hall current, J_{H}, and of the entry flux of ions in one striation of width, $\lambda_\perp$. This leads to the estimate

$$J_{\mathrm{H}} \approx e n_o v_{sp} \lambda_\perp = \frac{c}{4\pi} B_c \tag{4.5.222}$$

and, with Equation (4.5.221), to

$$\lambda_\perp \cong \frac{c}{\omega_{pi}} \,. \tag{4.5.223}$$

Equation (4.5.223) is indeed consistent with the observed width of such striations (Bernhardt et al., 1987).

4.5.2. *Transfer of Momentum*

One should think that the propagation velocity of the snow plow is directed in solar wind direction, since the magnetic barrier should built up on the subsolar side of

the cloud, but this is not the case. The reasons will become clear when considering the transfer of momentum. sketched in Figure 4.5.3. The momentum lost by the solar wind is coupled to the plasma cloud via a compressed and sheared magnetic field. If the cloud behaved like a rigid body, it should be accelerated in the direction of the solar wind as

$$\frac{\mathrm{d}v_{c\parallel}}{\mathrm{d}t} = \frac{1}{\tau_{\mathrm{acc}}}(u_{sw} - u_{c\parallel}) \tag{4.5.224}$$

with the acceleration time (Haerendel, 1987)

$$\tau_{\mathrm{acc}} = \frac{\tau_o}{2\kappa} \tag{4.5.225}$$

and the momentum exchange time, τ_o, (Scholer, 1970)

$$\tau_o = \frac{\rho_c \ell_c}{2\rho_o v_{\mathrm{A}o}} \,. \tag{4.5.226}$$

Subscript c refers to the plasma cloud and o to the unperturbed ambient plasma. $V_{\mathrm{A}o}$ is the ambient Alfvén velocity and ℓ_c the width of the cloud. The compression factor, κ, can be derived by observing that the magnetic pressure gradient in the front part of the cloud must not lead to an upstream ion motion. This means that magnetic pressure and tension force must cancel each other in front and add their effects in the center and rear of the cloud. Thus one finds (Haerendel, 1987):

$$\kappa = \frac{B_c}{B_o} = 2M_A = \frac{2u_{sw}}{v_{\mathrm{A}o}} \,. \tag{4.5.227}$$

In the first artificial comet experiment, $M_A \approx 5$ and $\kappa \approx 10$.

The initial acceleration that should be experienced by the cloud, $g_\parallel$, can be found from Equations (4.5.224) to (4.5.227):

$$g_\parallel = \frac{u_{sw}}{\tau_{\mathrm{acc}}} = 8\frac{\rho_o u_{sw}^2}{\rho_c \ell_c} \approx \frac{4\rho_o u_{sw}^2 A_c}{M_c} \,, \tag{4.5.228}$$

where M_c is the total mass and A_c the cross-section of the cloud. Via the Alfvén wings about four times the momentum carried by the solar wind directly onto the cloud's cross-section is transferred to the cloud.

In reality, however, the cloud does not behave like a rigid body. The magnetic field affects essentially only the electrons and, to some extent, the solar wind ions, but the heavy barium ions with $m_i/m_e = 2.6 \times 10^5$, are almost fully unmagnetized. They respond only to electric polarization fields. These fields are the ultimate agent in the momentum transfer process.

Observation of the evolution of the ion distribution from the initial cloud provides the clue to the polarization fields which consist essentially of three components. Figure 4.5.4 shows the barium cloud (in colours indicating the brightness distribution) after 4.4 min, viewed nearly along the direction of the undisturbed

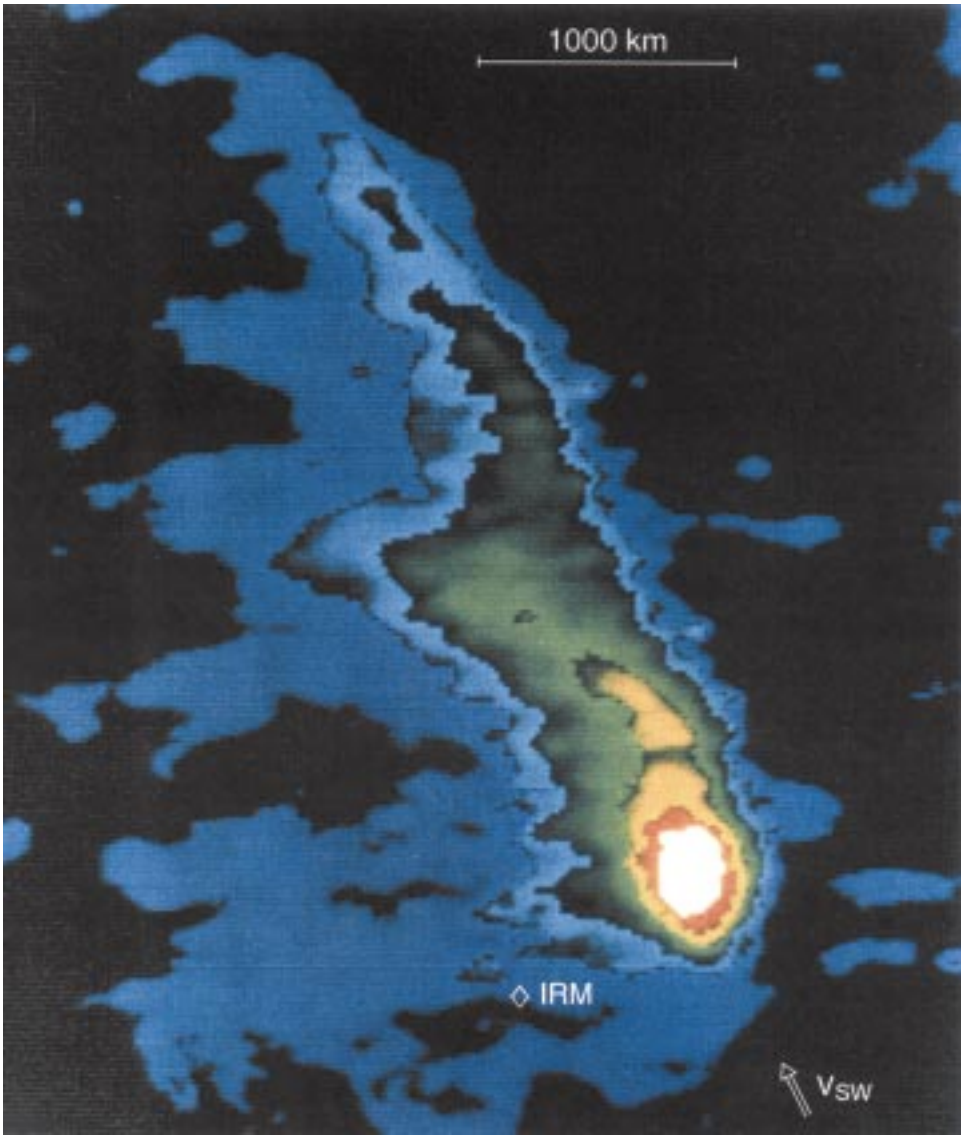

Figure 4.5.4. Barium cloud of 27 December 1984 at 4.4 min after release (false colours indicating brightness). The flow direction of the solar wind and the position of the IRM are indicated.

magnetic field. The position of the spacecraft is shown as a diamond. The most striking facts are (1) the formation of a tail, (2) the absence of a motion of the comet head in the solar wind direction, (3) the displacement of the comet transverse to the solar wind direction, and (4) an asymmetric diffuse ion distribution in lateral directions. (1) and (2) show that during the first phase all momentum in flow direction is transferred to the rear end of the cloud from where the ions forming the tail are extracted by means of a tailward-pointing polarization field. Figure 4.5.5(a)

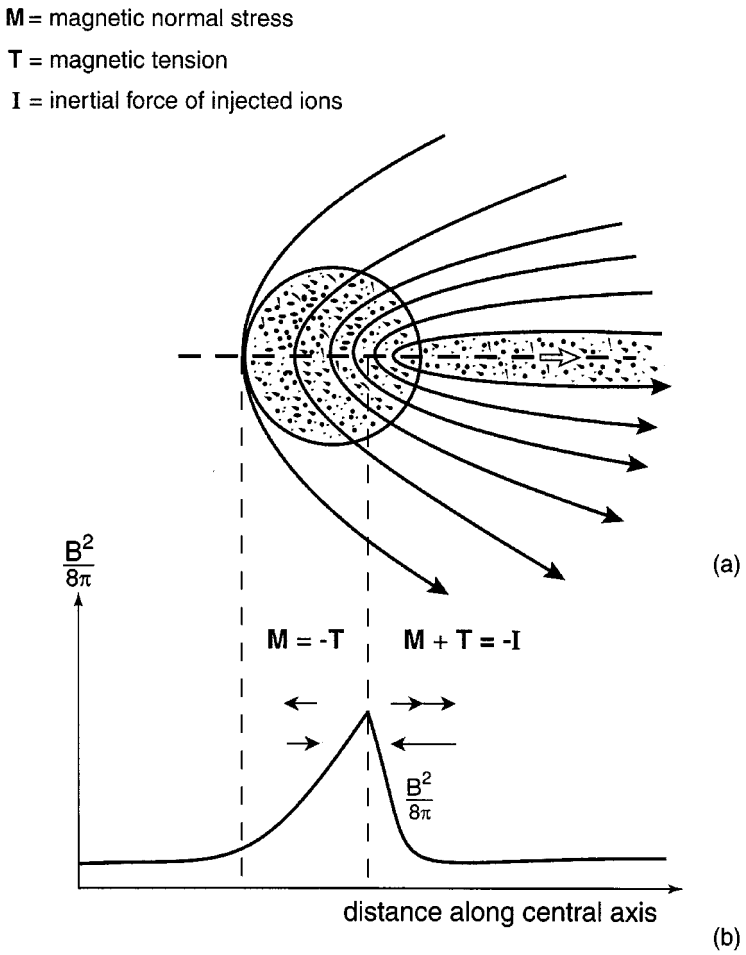

Figure 4.5.5. Stress balance in the flow direction of the solar wind (x-direction); (a) magnetic field draping and ion injection from the rear of the cloud by an electric polarization field. (b) Magnetic pressure as function of x with indication of the force balance between magnetic stresses (**M** and **T**) and the ion inertial force (**I**).

sketches the situation, and Figure 4.5.5(b) suggests that throughout most of the cloud the upstream pointing normal pressure force is balanced by the downstream pointing magnetic tension (see above). The slow transverse displacement (3) indicates the existence of a weak electric polarization field pervading most of the cloud and pointing oppositely to the ambient electric field. At the opposite side of the cloud, i.e. in th direction of the solar wind electric field, $\mathbf{E}_0$, the ambient electric field is enhanced and extracts ions from this flank at high speed into the solar wind and thus creates the asymmetric ion distribution and brightness (4). Ion extraction in $\mathbf{E}_0$-direction and transverse cloud displacement must be consistent with a vanishing total transverse momentum flow, since there is no net transverse force.

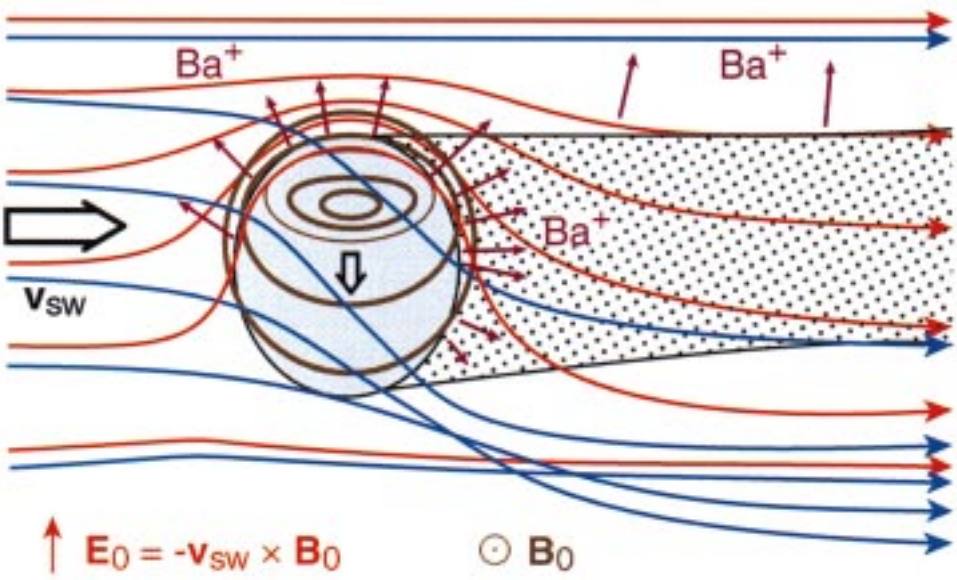

Figure 4.5.6. Ion and electron trajectories through and around the plasma cloud with its magnetic field concentration (brown contours). The initial trajectories of the barium ions extracted from the upper and rear boundaries are also shown.

Thus there are three electric polarization fields with rather different functions. The one on the rear side transfers the solar wind momentum to the tail ions, the one on the $\mathbf{E}_0$-flank guides the solar wind electrons around the magnetic obstacle and extracts ions sideways into the solar wind, and the weak one in most of the cloud's interior is needed for transverse momentum balance by pushing the whole cloud to the opposite side. Figure 4.5.6 summarizes the situation. It also indicates the separation of solar wind ion and electron trajectories. Whereas the ions are slowed down, but penetrate the cloud under deflection in $\mathbf{u}_o \times \mathbf{B}$ direction (see Haerendel et al., 1996), the electrons are guided around the obstacle into the central plane of the tail. They are neutralized by the extracted barium ions. This solar wind electron flow also constitutes the Hall current screening the compressed field in front, on the $\mathbf{E}_0$ side, and on the rear.

The observed lateral acceleration of $g_\perp \cong 2\times 10^3$ cm s^{-2} can also be understood as the action of the compressed magnetic field on the main body of the cloud. Hence, by virtue of Equations (4.5.227) and (4.5.228):

$$g_\perp = \frac{B_c^2}{8\pi\rho_c\ell_c} = 2\frac{\rho_o u_{sw}^2}{\rho_c\ell_c} = \frac{1}{4}g_\parallel \,. \tag{4.5.229}$$

With the measured values, $n_o = 5$ cm^{-3}, $u_{sw} = 540$ km s^{-1}, $\rho_c = 1.3\times 10^4$ cm^{-3}, $\ell_c \approx 110$ km we find $g_\perp = 1.5\times 10^3$ cm s^{-2}, a value close to the observations. This calculation neglects, however, the contribution of the electron pressure which enhances the polarization fields and thus $g_\parallel$.

In total one can summarize the momentum balance between solar wind and plasma cloud in the following way. The plasma cloud is an obstacle to the solar wind flow leading to a local slow down of the flow, a temporary trapping of the magnetic field in the cloud under compression and stretching into a magnetic tail and accompanying momentum transfer. The magnetic forces pointing in the downstream direction act on the ions at the rear end of the cloud and accelerate them to form a long visible tail, leaving the main body of the cloud unmoved. Since there are no natural walls to confine the enhanced magnetic (and electron) pressure inside the cloud in the transverse direction, only ion inertia is able to balance the lateral forces. This problem is solved in an asymmetric fashion. Whereas few ions are extracted out of the cloud and injected with high speed into the solar wind on the flank into which $\mathbf{E}_0$ is pointing, the opposite force pushes slowly on the main body of the cloud leading to its transverse displacement with $g_\perp$.

From the above it is obvious that all momentum and most of the energy transferred to the plasma cloud is consumed by extracting ions out of the cloud and injecting them finally into the solar wind flow. Those ions extracted from the flanks enter the undisturbed flow almost immediately and perform cycloidal trajectories with scales of ~70 000 km, whereas the ions injected into the tail or separating in form of finite plasma clumps (see below) form for a while a disturbed wake flow behind the cloud extending far beyond the visible extent of the tail (~10 000 km).

Ion extraction limits the lifetime of the plasma cloud. In order to obtain an estimate, we must know the ion extraction speed, $u_{\text{extr.}}$. It follows naturally from the momentum balance, if one makes an assumption on the density of the extracted ions once they have traversed the accelerating potential on rear or flank of the cloud. The assumption made by Haerendel (1987) was that this terminal density is equal to the undisturbed ambient density, $n_\circ$. A simple 1-D model yields

$$u_{\perp\text{extr}} = \sqrt{\frac{2}{\mu_i}} u_{sw} \tag{4.5.230}$$

and

$$u_{\parallel\text{extr}} = 2\sqrt{\frac{2}{\mu_i}} u_{sw} \, . \tag{4.5.231}$$

This reflects the 4-times greater force in parallel (to $\mathbf{u}_{sw}$) than transverse direction. The total mass loss by ion extraction is then

$$\begin{aligned} \dot{N}_c &= n_o A_c (u_{\perp\text{extr}} + u_{\perp\text{extr}}) = 3 n_o u_{\perp\text{extr}} A_c \\ &= 3 N_e \frac{3}{4 r_c} \sqrt{\frac{2}{\mu_i}} u_{sw} \frac{n_o}{n_c} \, , \\ \tau_{\text{extr}} &= \frac{N_c}{\dot{N}_c} = \frac{4}{9} \sqrt{\frac{\mu_i}{2}} \frac{n_c r_c}{n_o u_{sw}} \, . \end{aligned} \tag{4.5.232}$$

u_{extr} ranges between 12 and 24 % of u_{sw}. τ_{extr} is of order 15 min, if n_c is chosen to be the maximum density observed in the cloud and r_c is taken to be the visible initial radius. There are, however, two neglected items which shorten the ion extraction time, (1) an enhanced total pressure due to heated electrons, which enhances the electric polarization fields, and (2) the observed separation of entire plasma clumps from the rear of the cloud. Thus the observed lifetime of about 4 min after magnetization does not conflict with the above estimate.

Finally, there is one open question left. Why is all the longitudinal momentum imparted to the rear end of the cloud and not, at least partially, to the main body? Why does the artificial comet's head acquire a downstream velocity component only shortly before its complete depletion of ions (Valenzuela et al., 1986)? The reason lies in a nonlinear steepening of the density and magnetic field profiles at the rear end of the cloud. Here, as shown in Figure 4.5.5, magnetic normal and tangential stresses, **M** and **T**, point in the same (downstream) direction and pull the ions my means of an electric polarization field, **E**. Since the current is a pure Hall current and all the momentum is taken up by the accelerated ions, one can write:

$$en\mathbf{E} = \mathbf{M} + \mathbf{T} \,, \tag{4.5.233}$$

whereby the gas pressure has been neglected. So, the sharper the magnetic gradients in the rear and the lower the density, the stronger becomes **E** and the acceleration. This will have the consequence that n falls off rapidly in the rear, where the magnetic forces concentrate. Upstream of this region, but still inside the cloud, the magnetic field arranges itself to make E_x (flow direction) essentially vanish. One can also say that the ion acceleration in the rear acts like a jet engine whose recoil holds the plasma cloud in place ($E_x \equiv 0$) until the ion reservoir is nearly exhausted.

4.5.3. *Light and Heavy Mass Loading*

Now, what do we understand under 'heavy mass loading'? It is a situation in which the injected mass is so dense that the ambient flow is completely stopped inside a certain volume, that it is rerouted around the obstacle and extracts mass only in a boundary layer via electric polarization fields. So, we have to compare the mass extraction rate, $\dot{M}_{\text{extr}}$, with the mass deposition rate, $\dot{M}_i$. If V_{inj} is the mass injection volume,

$$\dot{M}_i = \dot{\rho}_i \cdot V_{\text{inj}} \,, \tag{4.5.234}$$

$$\dot{\rho} = m_i \alpha_{\text{ion}} n_n \,, \tag{4.5.235}$$

where n_n is the neutral density and α_{ion} the ionization rate. The mass extraction rate is:

$$\dot{M}_{\text{extr}} = m_i n_o S_{\text{inj}} v_{\text{extr}} \,, \tag{4.5.236}$$

where S_{inj} is the surface area through which ions are extracted and n_o the ambient density. If we set $S_{\text{inj}} = A_c$, the cloud's cross-section, we can take from Equation (4.5.231):

$$\dot{M}_{\text{extr}} = m_i n_o A_c 3 \sqrt{\frac{2}{\mu_i}} u_{sw} \, . \tag{4.5.237}$$

Thus,

$$\frac{\dot{M}_i}{\dot{M}_{\text{extr}}} = \frac{2\sqrt{2} R_c}{9\sqrt{\mu_i} u_{sw}} \frac{\dot{\rho}_i}{\rho_o} \, . \tag{4.5.238}$$

If this ratio exceeds unity, we have the case of heavy mass loading. For the AMPTE artificial comet experiment, the ratio was about 30. For the lithium releases, the situation was reserved. Practically all ions were directly deposited in the ambient flow causing little perturbation.

4.5.4. *Clumping Instability*

We have identified the recoil of the ions accelerated into the tail as the force balancing the combined action of magnetic normal and shear stresses on the cloud. Thereby, not only the plasma cloud is kept in station, but with it also the magnetic flux trapped in the initial magnetization process. Most of the magnetic flux subsequently carried by the solar wind towards the cloud is circumventing the cloud on the $\mathbf{E}_0$-flank and picks up the ions injected from the rear as sketched in Figure 4.5.6. However, this is not the full story.

As the tail grew, one could also observe the separation of plasma packets. Unfortunately, no in-situ diagnostics were available downstream of the cloud. Only the motion of the packets or clumps could be tracked optically. It revealed a rather quick acceleration (within a few tens of seconds) to a velocity which stayed well below the solar wind speed (typically $\sim$100 km s^{-1}). We can only guess what creates these plasma clumps. Our suspicion is that it shows the peeling off of some of the trapped magnetic flux rom the rear end in a fashion indicated in Figure 4.5.7. The figure demonstrates the growth of a small perturbation of the magnetic field profile (in x-direction) near the point of $B_{\max}$. A small indentation of $B(x)$ would have little effect on the tailward directed magnetic tension, $\mathbf{T}$, but create oppositely directed contributions of the pressure force, $\mathbf{M}$, on either side of the indentation. Thus ions would become accelerated on the upstream side of the indentation and slowed down soon again on the downstream side, thereby pushing on the magnetic field and widening the indentation, until part of the magnetic flux has separated entirely from the cloud. As these plasma and field clumps proceed, they continue to be pushed from the upstream side and slowed down at the downstream side because of the recoil of the accelerated ions. So, the clumps do not show the true ion flow speed. They are just transitory plasma and field concentrations in the tail flow. In a simulation of cometary plasma tails, the creation of such plasma clumps have been demonstrated and analyzed the plasma flow through them (see Section 4.6).

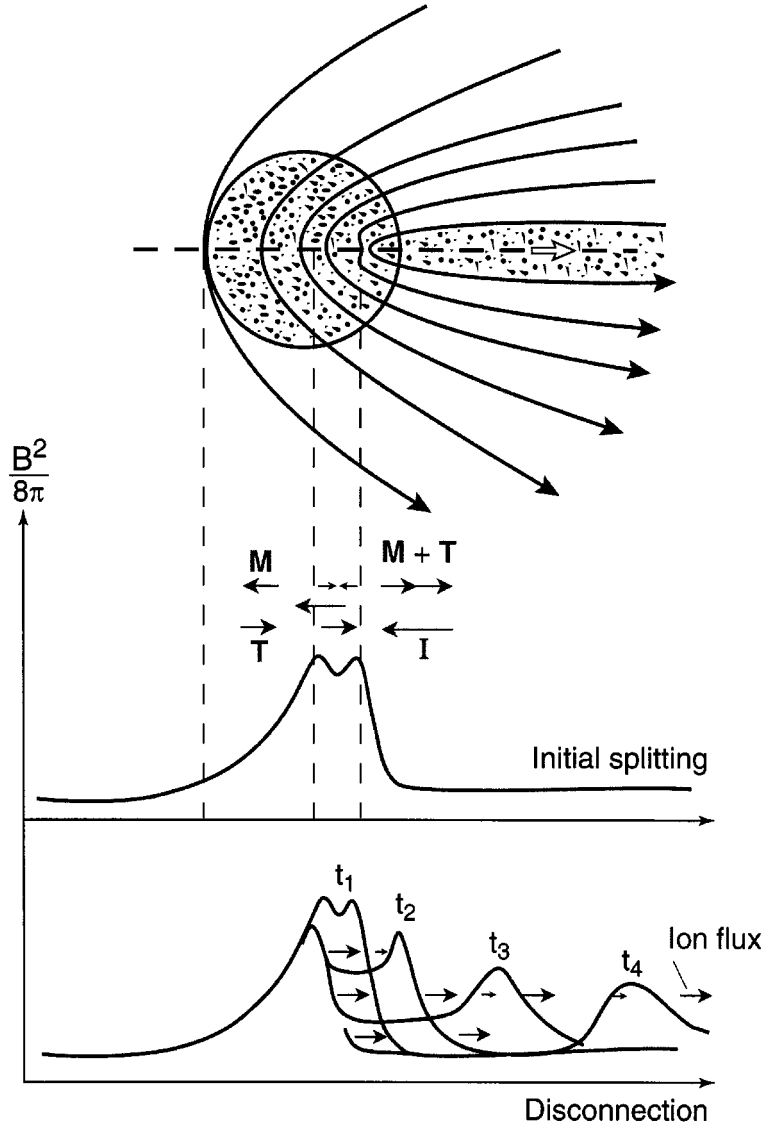

Figure 4.5.7. Suggested splitting mechanism of the concentrated magnetic field leading to the disconnection of plasma clumps.

The description of the physical processes acting on the plasma cloud in the solar wind, in particular of the ion extraction, was given without reference to follow-up attempts of theoretical interpretation and numerical simulation. This is not a small amount of literature, some of which presents alternate views and more detailed analysis. Two references may ease the entry into this literature (Lui, 1989; Harold and Hassam, 1994).

4.6. NUMERICAL SIMULATIONS OF MASS LOADING: COMPARISON WITH AMPTE RELEASES

Numerical modeling of mass-loading effects in space plasmas is particularly challenging because of the widely differing spatial and time scales involved with different ion species and electrons. In order to simulate the pickup process of newly born cometary ions in the solar wind or the interaction of the solar wind with active experiments such as the AMPTE release experiments which formed an artificial comet or the interaction of the solar wind with planetary magnetospheres with little or no intrinsic magnetic field like Mars or Venus it is important to be able to resolve disturbances on the scale of the ion gyroradius and cyclotron frequencies. Conventional magnetohydrodynamic codes serve well in investigating low frequency plasma behaviour, i.e. frequencies much less than the ion cyclotron frequency $\omega \ll \omega_{ci}$. The electrons and ions in these codes behave mainly as a charge neutral fluid. Magnetic fields in the ideal case (e.g. where no resistivity or other dissipation exists) become frozen into the fluid and move along with it. In the magnetohydrodynamic regime the time scales are set by ion inertia and magnetic restoring forces, the electrons move to maintain charge neutrality and are eliminated from the problem.

For shorter time scales ($\omega \sim \omega_{ci}$) the ions begin to slip across the magnetic field relative to the electrons which are still constrained to move along $\mathbf{B}$ to maintain charge neutrality. In this regime a two fluid treatment is required. If their exists multiple ion species with a few number of ions representing one of the species then a multiple fluid treatment is not sufficient and a full kinetic description of the ions together with a fluid description of the electrons is necessary, we can also consider massless electrons. The codes describing kinetic ions and fluid or massless electrons are called hybrid codes and are ideal for the study of mass-loading or ion pickup. For even shorter time scales ($\omega \geq \omega_{ce}$) then a full particle treatment is necessary. High frequency short scalelength turbulence can only be investigated fully using full particle in cell codes, where both electron and ion dynamics are considered self-consistently.

4.6.1. *The Simulation Model*

The simulations were done using particle in cell codes which treat the electrons as a massless fluid and the ions as fully kinetic and known as hybrid Vlasov-fluid Code or hybrid code for short. A hybrid code is intermediate between a full particle and an MHD code. It can resolve disturbances on the scale of the ion gyroradius, its basic time scale is the ion gyroperiod.

The equations describing each ion are

$$\frac{\mathrm{d}\mathbf{x}_i}{\mathrm{d}t} = \mathbf{v}_i \ , \tag{4.6.239}$$

$$\frac{\mathrm{d}\mathbf{x}_i}{\mathrm{d}t} = \frac{e}{M_i}\left(\mathbf{E} + \frac{v_i \times \mathbf{B}}{c}\right) \ , \tag{4.6.240}$$

where subscript i refers to each ion, $\mathbf{x}_i(\mathbf{v}_i)$ is the ion position (velocity), M_i is its mass.

The massless electrons however satisfy the following equation:

$$\mathbf{E} + \frac{\mathbf{v}_e \times \mathbf{B}}{c} = 0 \,, \tag{4.6.241}$$

where $\mathbf{v}_e$ is the electron fluid velocity. In writing Equation (4.6.241) we assume perfect conductivity along $\mathbf{B}$; e.g.,

$$\mathbf{E} \cdot \mathbf{B} = 0 \,. \tag{4.6.242}$$

Quasi-neutrality is also assumed

$$n_e = n_i = \int f_i \, \mathrm{d}\mathbf{v} = n \,, \tag{4.6.243}$$

n_e, n_i are the electron and ion densities and f_i is the ion distribution function.

The current $\mathbf{j}$ is therefore:

$$\mathbf{j} = en\mathbf{v}_e + e \int \mathbf{v} f_i \, \mathrm{d}\mathbf{v} \,. \tag{4.6.244}$$

This current $\mathbf{j}$, according to Equation (4.6.243) (quasi-neutrality assumption) must be divergence free. Thus

$$\nabla \cdot \mathbf{j} = 0 \,. \tag{4.6.245}$$

This is equivalent to

$$\mathbf{j}_L = 0 \,, \tag{4.6.246}$$

where $\mathbf{j}_L$ is the longitudinal current ($\mathbf{j}_L \parallel \mathbf{k}$). The relevant Maxwell equations are Faraday's law and Ampere's law without the displacement current, i.e.,

$$\nabla \times \mathbf{E} = -\frac{1}{c} \frac{\partial \mathbf{B}}{\partial t} \,, \tag{4.6.247}$$

$$\nabla \times \mathbf{B} = -\frac{4\pi}{c} \mathbf{j} \,. \tag{4.6.248}$$

Substituting 4.6.244 into 4.6.248 gives:

$$\mathbf{j} = \frac{c}{4\pi} \nabla \times \mathbf{B} = -en\mathbf{v}_e + e \int f_i \mathbf{v} \, \mathrm{d}\mathbf{v} \,. \tag{4.6.249}$$

Which then implies:

$$\mathbf{v}_e = \frac{e \int \mathbf{v} f_i \, \mathrm{d}\mathbf{v} - \dfrac{c}{4\pi} \nabla \times \mathbf{B}}{ne} \,. \tag{4.6.250}$$

As a result using (4.6.241) and (4.6.250) we have:

$$\mathbf{E}, = -\frac{\mathbf{v}_e \nabla \times \mathbf{B}}{c} = -\frac{\mathbf{B} \times (\nabla \times \mathbf{B})}{4\pi ne} + \frac{\mathbf{B} \times \int \mathbf{v} f_i \, \mathrm{d}\mathbf{v}}{nc} \, . \tag{4.6.251}$$

Finally using (4.6.247) and (4.6.251) we get:

$$\frac{\partial \mathbf{B}}{\partial t} = c\nabla \times \left\{ \frac{\mathbf{B} \times (\nabla \times \mathbf{B})}{4\pi ne} - \frac{\mathbf{B} \times \int \mathbf{v} f_i \, \mathrm{d}\mathbf{v}}{nc} \right\} \, . \tag{4.6.252}$$

Using $\mathbf{v}' \left(= \int \mathbf{v} f_i \, \mathrm{d}\mathbf{v}/n_e\right)$ as the average ion velocity in a given cell Equation (4.6.251) can be written as

$$\mathbf{E}, = -\frac{\mathbf{B} \times (\nabla \times \mathbf{B})}{4\pi ne} + \frac{\mathbf{B} \times \mathbf{v}'}{c} \tag{4.6.253}$$

and using Equation (4.6.240) and (4.6.253) we can obtain

$$\frac{\mathrm{d}\mathbf{v}_i}{\mathrm{d}t} = \frac{e}{M_i} \frac{(\mathbf{v}_i - \mathbf{v}') \times \mathbf{B}}{c} - \frac{e}{M_i} \frac{\mathbf{B} \times (\nabla \times \mathbf{B})}{4\pi ne} \tag{4.6.254}$$

and from (4.6.252) we get the expression for the magnetic field

$$\frac{\partial \mathbf{B}}{\partial t} = c\nabla \times \left\{ \frac{\mathbf{B} \times (\nabla \times \mathbf{B})}{4\pi ne} - \frac{\mathbf{B} \times \mathbf{v}'}{c} \right\} \, . \tag{4.6.255}$$

Equations (4.6.254) and (4.6.255) form the analytic basis of our model. They involve only $\mathbf{v}_i$, $\mathbf{v}'$ and $\mathbf{B}$ ($\mathbf{E}$ does not appear explicitly). Equation (4.6.254) is the velocity push equation for the ions. The other push equation is the relation between the velocity of any particle and its position

$$\frac{\mathrm{d}\mathbf{x}_i}{\mathrm{d}t} = \mathbf{v}_i \, . \tag{4.6.256}$$

Equations (4.6.254), (4.6.255), and (4.6.256), the three push equations, are the basis of hybrid simulation models. As written above, only one ion species is included. However, for two or more ion species (the solar wind and cometary ions or the solar wind and planetary ions), a distribution function for each species is introduced and separate equations of the form (4.6.254) for each ion species with the appropriate charge to mass ratio are used.

In the particular hybrid model described above the electric field is never calculated explicitly, the magnetic field is calculated using Equation (4.6.255). The zero mass electrons mean that their inertia is neglected, the electrons in this case are tied to the magnetic field lines and respond instantaneously to changes in the magnetic field. Electron pressure can be included in the code however, their temperature will be fixed, ideally a particle description for both electrons and ions would be for better but with the different spatial and time scales responses of electrons and ions makes requires vast amounts of computer resources. To model an experiment the size of the AMPTE releases using a full particle code is beyond the capability

of present day supercomputers. The ideal code in this case is a hybrid code, even a fluid code is not sufficient for AMPTE releases because the Larmor orbits for the solar wind protons are almost as large as the plasma clouds diameter for the Barium releases. The observations also provide evidence of structures such as jets that go beyond fluid models. These type of hybrid codes, ion kinetics and massless electrons have been used successfully by Brecht et al. (1988, 1993) to model the interaction of the solar wind with Mars, for artificial releases (Brecht et al., 1987; Bingham et al., 1991a; Kazeminezhad et al., 1993) and have also been used to investigate shocks.

The simulations that we describe are of the AMPTE barium and lithium releases in the solar wind (Bingham et al., 1991a; Kazeminezhad et al., 1993; Bollens et al., 1999). The experimental details can be easily found in Section 4.5.

In the simulations, initially the solar wind particles were positioned on a lattice for the 2-D runs and a cell for the 3-D runs in a regular array moving to the right in the simulation box. The system size was 256×256 grids for the 2-D case and $256 \times 256 \times 256$ for the 3-D case, each grid corresponding to one ion skin-depth c/ω_{pi}, where ω_{pi} is the ion plasma frequency and time is measured in proton gyroperiods. New solar wind particles were continually introduced at the left while solar wind particles leaving the box at the right were removed. The comet particles on the other hand, occupied a circular area centred at the grid point 70–128 with a diameter of $8c/\omega_{pi}$.

4.6.2. *The Appropriate Model*

Electrostatic noise, magnetic wave field, and general plasma wave measurement have revealed the following characteristics about the Ba, as well as the Li releases:

1. The plasma wave phenomena observed in the AMPTE measurements were most intense between the solar wind ion cyclotron and ion plasma frequencies and sharply dropped at higher frequencies. Using the background solar wind condition as $B_0 = 10$ nT, $n_o = 5$ cm^{-3} for the Ba release, (Valenzuela et al., 1986) and $B_0 = 4$ nT, $n_o = 5$ cm^{-3} for the Li release (Häusler et al., 1986), the following respective ranges of values for the ion and electron plasma frequencies, the lower hybrid frequency, the ion and electron cyclotron frequencies, and the Alfv́en speed are obtained:
   $\omega_{pi} \simeq 3$ kHz, $\omega_{pe} \simeq 134$ kHz, $\omega_{lh} \in (16,\ 41)$ Hz
   $\omega_{ci} \in (0.4,\ 1)$, $\omega_{ce} \in (0.7,\ 1.7)$ kHz, $V_{\mathrm{A}} \in (40,\ 100)$ km s^{-1} .
2. For the problem in which the magnetic field is at right angles to the solar wind flow (second Li release), variations along the field line (field draping) can be neglected if they do not qualitatively alter the cloud dynamics, i.e., if the magnetic tensile forces due to the field draping only act in the solar wind direction.
   In the Li releases, no significant alteration from the above was observed, presumably due to the clouds rapid expansion and its large radius. For the Ba releases also, Lühr et al. (1986b) report that the magnetic tensile forces act

along the solar wind flow; i.e., in the same direction as the magnetic pressure forces. So the field draping did not qualitatively alter such fine features as the sideways deflection, and according to Lühr et al. (1986b, p. 711), '... the field stresses are still seen to act on a gross scale in the manner expected for larger objects...'. Consequently, neglecting variations along the field (using a two-dimensional model) should not qualitatively affect the results. The 3-D results show similar behaviour justifying this conclusion.

3. Neglecting the displacement current in Maxwell's equations will cause errors of $O(V_A^2/c^3)$ in which $V_A \in (40,\ 100)$ km s^{-1} in the background and which shows only increases of ≤ 10 km s^{-1} in the compressed region, such errors thus minor.

To sum up, we note that a model of kinetic ions and zero mass fluid electrons, neglecting the displacement current, should be sufficient for a qualitative investigation of the AMPTE observations.

4.6.3. *The Simulation Procedure*

To model these observations, the model had to incorporate the following features: (1) include the gradual cloud neutral gas ionization in a realistic way; (2) include multiple ion species; (3) include the streaming of the solar wind through the cloud plasma; (4) include the collective behaviour of the plasma particles in their self-consistent electromagnetic fields; (5) include kinetic effects of the ions; because of their large Larmor orbit size compared to the cloud they must be treated in a kinetic manner; and (6) handle a very large system because of the complexity and the scale of the interaction.

In the simulations, initially solar wind particles were positioned on a lattice in a regular array moving to the right of the simulation box. The system size was 256×256 grids for 2-D simulations and $256 \times 256 \times 256$ for 3-D simulations with each grid corresponding to one proton skin depth. New solar wind particles were continually introduced at the left with drift velocities along positive x, while solar wind particle leaving the box at the right were removed. The cloud particles (mass 6), on the other hand, occupied a circular area centred at the grid point (70, 128); they are initially neutral and expanding radially and are gradually ionized over one gyroperiod. More specifically, a neutral particle undergoes free streaming at its initial speed, and upon ionization it begins to feel the electromagnetic forces and its motion is then governed by Equation (4.6.254). Random samples of the cloud particles are ionized in this way from the neutral bunch once every $\frac{1}{40}$th of a gyroperiod. The solar wind magnetic field is in the $\hat{z}$ direction $\mathbf{B}_0 = \mathbf{B}_0\hat{z}$.

In the model, $\mathbf{B}$ and $\mathbf{v}$ are normalized according to (c_s is the ion acoustic speed)

$$\tilde{\mathbf{B}} = \frac{\mathbf{B}}{\sqrt{4\pi\rho_o}c_s}, \quad \tilde{\mathbf{v}} = \frac{\mathbf{v}}{c_s}\,. \tag{4.6.257}$$

Setting $T_i = 20$ eV and $T_e = 15$ eV as the temperatures of the two species in the solar wind ($c_s = \sqrt{(T_i + T_e)/M}$) gives $c_s = 57.9$ km s^{-1}. Using c_s then, we

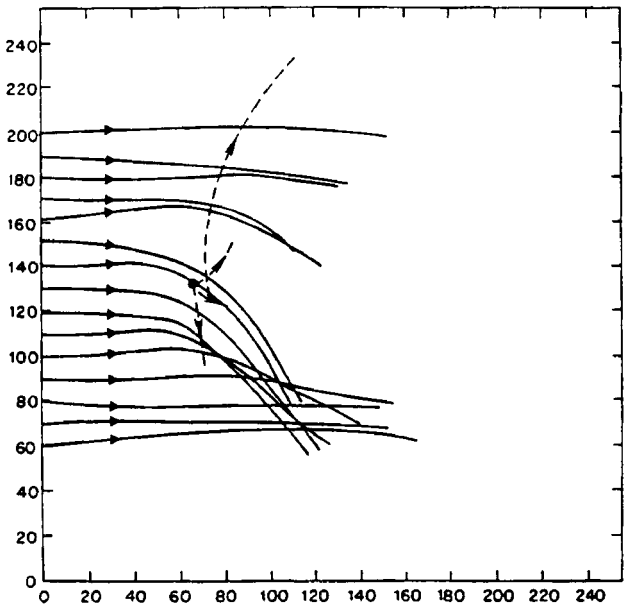

Figure 4.6.1. Trajectory of some solar wind particles – and barium particles – chosen at random after two and a half proton gyroperiods.

obtain the following correspondence of our simulation values of v_{sw} (solar wind particle speed), v_{gas} (the cloud particle speed), and V_{A} (the Alfvén speed) in MKS units as follows:

$$v_{sw} = 1.5c_s \cong 86.85 \text{ km s}^{-1} ,$$

$$v_{\text{gas}} = 0.3c_s \cong 17.37 \text{ km s}^{-1} ,$$

$$V_{\text{A}} = 0.15c_s \cong 8.685 \text{ km s}^{-1} .$$

This last value of V_{A} also gives rise to an external magnetic field of 0.889 nT.

The corresponding experimental values are $v_{sw} = 455$ km s^{-1}, $v_{\text{gas}} = 3.05$ km s^{-1}, (Coates et al., 1986) with the background B_0 and 4 nT and proton density of 5 cm^{-3} (Häusler et al., 1986). These last two values give rise to the measured Alfvén speed of 39.04 km s^{-1}, in contrast to our simulation values of 8.7 km s^{-1}, and the collisionless skin depth of $\Delta = c/\omega_{pi} \cong 101$ km, which is the unit grid spacing used in the simulations. As will be shown in what follows, these differences between the experimental and the simulation parameters which were imposed by the computational limitations (Courant–Friedrichs–Lewy condition) will have no qualitative effects on the simulation results as one attempts to make comparisons with the measurements.

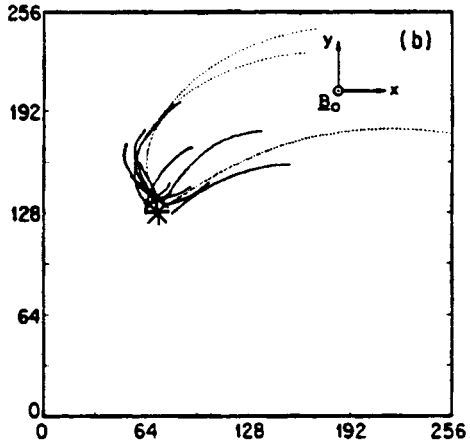

Figure 4.6.2. Cometary pickup particles showing part of their cycloidal orbits.

4.6.4. *AMPTE Simulations*

4.6.4.1. *Particle trajectories.* The first and most significant result was obtained by real space plots of the trajectories of cloud particles in time using the MHD model with the Hall term and the hybrid model, respectively. The MHD model with the Hall term shows only isotropic expansion while the hybrid model shows an anisotropic expansion with sharp upward acceleration at the top with a deflection of the magnetic field and deflection of the solar wind ions in the opposite sense together with an asymmetric acceleration of the barium ions resembling ion pickup Figure 4.6.1. The later is much closer to the observations (Coates et al., 1986, Li; Coates et al., 1988, Ba; and Haerendel et al., 1986, Ba), which rules out the treatment of this problem by an MHD approach, even one with the Hall term. The corresponding density contours closely resemble the experimental contours (Haerendel et al., 1986, Figure 4), further emphasizing this point.

Computer simulations using the hybrid code have also yielded excellent depictions of both species of the ion (solar wind and cloud) trajectories. Figure 4.6.1, representing a selection of solar wind particles flowing in from the left of the simulation box, indicates a downward deflection of the particles at the bottom of the box due to the sharp magnetic field gradient in front of the cloud, the reflection of some ions at the center indicating the shocklike structure in agreement with the measurements by Gurnett et al. (1986, Li), and Gurnett et al. (1985, Ba), and almost unperturbed trajectories at the very top; on the show, though, they do not indicate immediate downward deflection. Cloud particles (Figure 4.6.2) show cycloid type (partial cycloids) trajectories owing to their pickup by the solar wind's convective electric field and their large Larmor radii in agreement with the trajectory measurements of Coates et al. (1986, Li), and similar findings by Coates et al. (1988, Ba), and Haerendel et al. (1986, Ba).

The magnetic field contours indicate little symmetry change within one gyroperiod, and it is not until two gyroperiods that they show any significant symmetry changes, i.e., the magnetic field drapes and moves over the cloud. The electric field in the cloud rest frame does not indicate a unidirectional field throughout the cloud location; i.e., for $x\varepsilon(40,\ 140)$ and $y\varepsilon(40,\ 180)$ the **E** does not point consistently along the positive x to definitely cause an $\mathbf{E} \times \mathbf{B}$ deflection along the negative y.

As a result, the cloud particle pickup in the solar wind appears to precede the generation of asymmetry in the magnetic field topology and the overall solar wind deflection behind the shocklike region (snowplough boundary), and therefore the particle pickup appears to be the main cause of the cloud's sideways deflection via momentum conservation (rock effect) as first proposed by Haerendel et al. (1986) and Cheng (1987). Microscale investigation of the AMPTE results through the study of ion dynamics (e.g., trajectories) thus proved vital, for any global field changes and cloud motion appear to follow their patterns.

The model, however, being a hybrid one which treats electrons as a fluid, does not give electron trajectories or heating. However, the presence of the high-energy electrons observed by the spacecraft has been probed by investigating the lower hybrid wave activity (i.e., waves which could render electron heating) at the locations both upstream and downstream of the cloud-solar wind boundary. We will elaborate on this issue next.

4.6.4.2. *Wave activity.* While the convective electric field of the solar wind in the cloud's rest frame plays a significant role in the momentum coupling to the solar wind at the cloud edge, the intense magnetic wave activity induced by the cloud-solar wind interaction plays an equally important role. Indeed, from the UKS electron measurements, Hall et al. (1986, Li) and Rodgers et al. (1986, Ba) concluded that there was electron wave beating, and Hall et al. (1986, Li) 1 showed the wave heating to dominate the adiabatic compression and electrostatic shock potential difference. The IRM detectors, on the other hand, detected wave activity in the range of lower hybrid frequencies in the transition region upstream of the cloud (Häusler et al., 1986, Li; Woolliscroft et al., 1986; and Klöcker et al., 1988, Ba) report similar findings.

Two mechanisms may be responsible for the lower hybrid activity. First, the measurements indicate the generation of a diamagnetic current which is set up to exclude the solar wind magnetic field from the highly conducting expanding cloud (Lühr et al., 1986a, b, Li and Ba). These currents can induce what is called the lower hybrid drift instability (Bingham et al., 1991). This instability can occupy the whole turbulent region, it exists in the region of high ion density, and it is not suppressed with increasing density. Its only constraint is a threshold velocity for the current-carrying electrons which must exceed the ion thermal speed. These lower hybrid drift waves can in turn be absorbed by electrons resulting from Landau damping, providing an anomalous resistance and electron heating (Bingham et al., 1988). Second, it is believed that an instability arising from a two-beam (solar

wind cloud particle) situation plays a role in exciting the lower hybrid modes (Papadopoulos et al., 1987; Bingham et al., 1991a). Since the cloud is photoionized by solar radiation and the unionized neutrals freely penetrate into the solar wind, a two-stream type situation is produced. We have full dynamic (electron and ion) simulations that show strong electron heating by this mechanism (Bingham et al., 1988).

Our hybrid model is rich in its capability of simulating various waves, both fluidlike as well as kinetic like (Bernstein modes). Using the model, we were able to investigate the generation of lower hybrid waves at arbitrary locations in the simulation box. Since the shock generated at the solar wind/cloud interaction region is believed to be responsible for both the above instabilities and the resulting wave activity, the simulation model could well investigate this point.

The simulations illustrate the generation of the diamagnetic cavity within the cloud location (cloud's left boundary falls at the enhanced B field see Figure 4.6.1 from Bingham et al., 1991b), i.e., one observes a very weak field which is located within the cloud, and a sudden enhancement afterward (shock region). To sum up then, these simulations reveal, first, that the plasma flow does have a component of flow through the cloud, that the solar wind velocity does decrease intensity, as it flows past the cloud and, third, the existence of the reflected ions, which could also cause a streaming instability by flowing through the solar wind. These effects are in agreement with the findings by Gurnett et al. (1986, Li) and Gurnett et al. (1985, Ba) and are signatures of a shocklike activity at the cloud/solar wind boundary.

A simple jump condition across the shock boundary can be derived using the two-fluid and Maxwell's equations

$$[Mn\mathbf{v}_x^2]_{s.r} = -\frac{1}{8\pi}(|B_z|^2_{s.r} - |B_z|^2_{sw}) + [Mn\mathbf{v}_x^2]_{s.w} \; . \tag{4.6.258}$$

To check Equation (4.6.258) against the simulation results, one needs to use the normalizations employed in the model.

Using (4.6.257) in (4.6.258) gives

$$n_{\text{s.r.}}\tilde{v}^2_{\text{s.r.}} = -\tfrac{1}{2}\left(n_{0\text{s.r}}\tilde{B}^2_{\text{s.r.}} - n_{0\text{s.w}}\tilde{B}^2_{sw}\right) + n_{sw}\tilde{v}^2_{sw} \; , \tag{4.6.259}$$

where $\tilde{v}$ and $\tilde{B}$ which appear in this equation correspond to the simulation values. We shall drop the tilde from now on. Also $n_{0\text{s.r}}$ and $n_{0\text{s.w}}$ correspond to the initial particle numbers (recall that $\rho_0 = n_0 M$, with ρ_0 the density and n_0 the particle number) in the cloud (shock region) and the solar wind regions, respectively, and the B is the z component of the magnetic field. We note the values for B, v, and n from the simulations and compute the shock jump relation, i.e., Equation (4.6.259):

$$[nv^2] = -\tfrac{1}{2}[n_0 B_z^2] \; , \tag{4.6.260}$$

where

$$[nv^2] = (nv_x^2)_{140} - (nv_x^2)_{170} = -2.20 \tag{4.6.261}$$

and

$$-\tfrac{1}{2}[n_0 B_z^2] = -\tfrac{1}{2}(n_0 B_z^2)_{140} - (n_0 B_z^2)_{170} = -2.23 \; . \tag{4.6.262}$$

Note that the initial particle numbers quoted in 4.6.262 arise from the initial conditions, i.e., $n_{0\text{s.w}}$ corresponds to 1 particle per cell for the background solar wind particles, and $n_{0\text{s.r.}}$ to 10 000 cloud particles in a circle of radius 8 grid points used in the simulations. The results (4.6.261) and (4.6.262) differ by 1.5%, which is very good agreement indeed and supports the theory that a shocklike structure is formed and is responsible for the observed wave activity.

In conclusion, the wave analysis confirms the generation of the lower hybrid waves in the transition region between the diamagnetic cavity and the upstream solar wind in agreement with the measurements by Häusler et al. (1986, Li) and Woolliscroft et al. (1986) and Klöcker et al. (1988, Ba). The simulations also indicate a shocklike formation at the cloud boundary, presumably as a source for the waves. These waves thus act as a source of energy for the electrons via Landau damping, as first suggested by Hall et al. (1986, Li) and Rodgers et al. (1986, Ba), and explain the observed electron heating in their measurements (Bingham et al., 1988).

4.6.4.3. *Cloud motion.* Ground-based optical observations of the (Ba) cloud revealed some astounding features of the AMPTE cloud (Valenzuela et al., 1986), the most important of which were the cloud's transverse movement across the solar wind flow, the presence of macroscopic protrusions at the top of the cloud, and a tail along the solar wind flow.

In the lithium releases, due to lithium's show ionization time ($\approx$1 h) (D. A. Bryant et al., Energization of electrons following ion releases in the solar wind, private communications, 1986) and the cloud's resulting low radiation intensity, no ground-based cloud observations (category 3 above) were performed; e.g., no sideways cloud deflection was observed. In our simulations, we do observe this feature the effect is more pronounced in the 3-D simulation. This suggests the same underlying mechanism (rocket effect) to be responsible in both cases. Any reference to the Ba measurements therefore serves only to outline this important feature. Valenzuela et al. (1986) observed that the cloud head did not move in the direction of the solar wind for the first 4.6 min. Instead it made a sideways deflection in the negative y direction at a much lower speed than the solar wind.

Figure 4.6.3 shows the time history of the y component of the center of intensity of the heavy part of the 'cloud' using this scheme. The pattern shown is similar to what the experimentalists have observed. The cloud does not move for a while (computer time 60, which is roughly 1.5 gyroperiods in the simulations), presumably because not enough particles have been ejected from the top of it to allow a significant recoil of the remaining heavy material. Then suddenly it starts moving down in a relatively short period. Furthermore, protrusions at the top of Figure 4.6.4 resemble those of the observations.

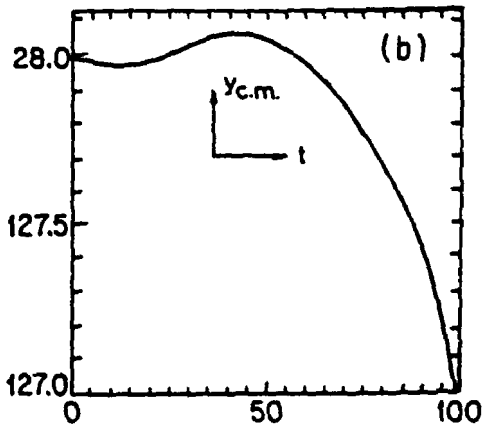

Figure 4.6.3. The experimental density contours, adopted from Figure 4 of *Haerendel et al.* (1986).

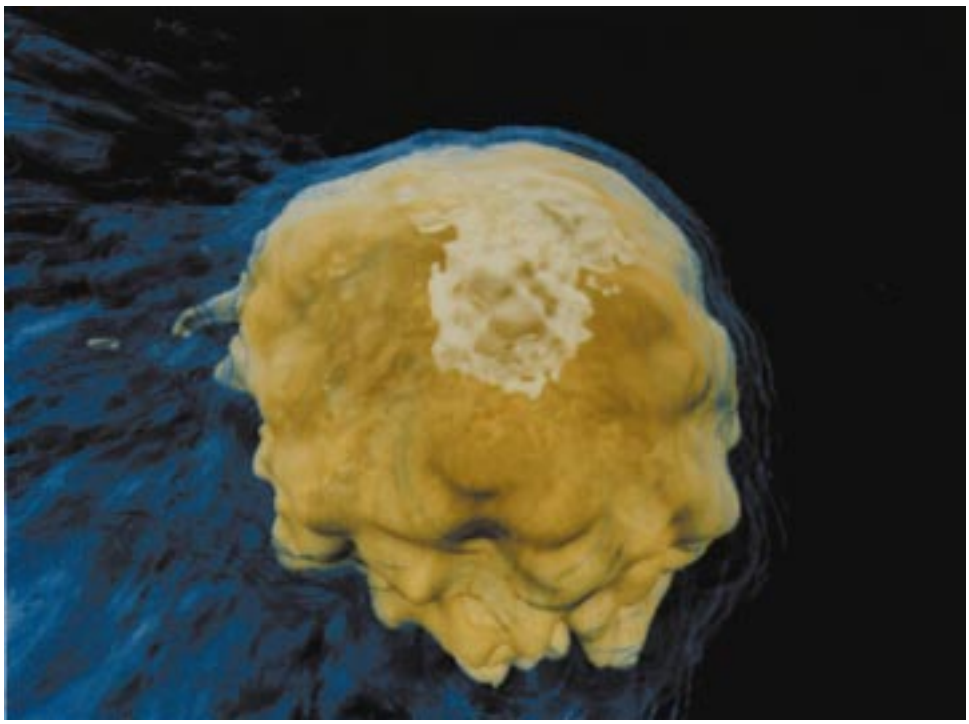

Figure 4.6.4. Density image from the 3-D simulations showing the density ripples at the top, attributed to the Rayleigh–Taylor instability, formation of tail and smooth profile on the bottom. the solar wind flows from left to right and the magnetic field is perpendicular to plane of figure.

It has been suggested (Hassam and Huba, 1987; Huba et al., 1987) that the macroscopic protrusions were from a Rayleigh-Taylor type instability driven by the cloud's transverse acceleration. The transverse acceleration (across the solar wind flow) in turn was induced by a rocket effect due to the upward ejection of the cloud particles by the solar wind driven convective electric field. The cloud deflection results from momentum conservation as first suggested by Haerendel et al. (1986) and Cheng (1987), Figure 4.6.3, parabolic shape indicates an acceleration. This accelerating motion could thus account for the generation of the instability and the resulting protrusions; i.e., as the low-density cloud particles are ejected by $\mathbf{E}_c$, the dense part recoils (accelerates) in the opposite direction to conserve momentum.

One can think of the heavy fluid composed of the main cloud particles as being accelerated by a lighter fluid which is composed of the solar wind particles and a few cloud ions; one then has the classic Rayleigh-Taylor instability taking place. Since the top region is a relatively sharp boundary of the two fluids, one can obtain the growth rate to be approximately

$$\Gamma = \sqrt{k_z a}\ . \tag{4.6.263}$$

Here k_z is just the wave number along the head boundary, i.e., along the x axis, while a is the magnitude of the acceleration which points along the negative y direction.

We shall next use Figure 4.6.3 to check Equation (4.6.263). From Figure 4.6.3 one sees that the center of mass begins to accelerate at the time $t - 45$, and between $t = 55$ and $t = 100$ it travels one grid point in the negative y direction. Thus upon fitting a parabola to that diagram, for a displacement of one grid point in the time period $\Delta t = 45$, one obtains an acceleration $s = 1.06 \times 10^{-3}$ in the normalized computer units. Given this a and $\lambda = 15$, one obtains the growth rate from (4.6.263) to be

$$\Gamma_1 = \sqrt{\frac{2\pi}{\lambda} \times a} = 2.10 \times 10^{-2}\ . \tag{4.6.264}$$

Also for the period of acceleration $\Delta t = 45$ of the dense part, one obtains the following growth rate:

$$\Gamma_2 = \frac{1}{\Delta t} = \frac{1}{45} = 2.22 \times 10^{-2}\ . \tag{4.6.265}$$

Equations (4.6.264) and (4.6.265) agree to within 5.1%, which is as good as we can expect from the accuracy of the calculations and supports our physical interpretation. All the effects of the 2-D simulations show up in the 3-D simulations with some such as the field draping only existing in the 3-D simulations. In 3-D we see that more magnetic flux is carried over the top of the cloud. The additional pressure and tension on the top side of the cloud helps to push the cloud sideways more effectively than in the 2-D case. We still have the rocket type effect reported by Haerendel et al. (1986) of the released ions being accelerated by the convective

electric field out of the top and starting to undergo cycloidal orbits. Figure 4.6.4 shows the resultant modulated top structure which is more obvious in the 3-D simulations. This feature is reminiscent of the Rayleigh–Taylor type instability described in the previous section. The richness of the 3-D simulations still needs to be fully examined but still confirms the present understanding of the mass-loading and pickup processes involved with new born ions in the solar wind. The hybrid simulation of the AMPTE releases is an ideal example of how computations can address the complex issues arising of mass pickup by the solar wind and can be used to investigate planetary atmospheric pickup from Mars, etc.

4.7. Observation and simulation of tail condensations

Cometary plasma tails display a large variety of different structures, such as streamers, kinks, helical waves, knots and disconnection events. The appearance of these features depends strongly on the activity of the comet and the interplanetary solar wind and IMF conditions which vary from comet to comet. A wealth of ground based observational data concerning the dynamics of tail structures exists, to mention only some of the results, for comets P/Morehouse (Lüst, 1967), P/Halley (Celnik and Schmidt-Kaler, 1987) and P/Swift–Tuttle (Jockers and Bonev, 1997). Published data cover the determination of velocities of various tail structures for a large range of distances from the nucleus. Structures in the ion tail near the nucleus have initial velocities of about 10 km s^{-1} at distances of several 10^5 km; they get accelerated at a rate of about 100 cm s^{-2} and end up with velocities up to 100 km s^{-1} or higher (at distances of several 10^7 km from the nucleus) but never reach the velocity of the free flowing solar wind. In most cases the structure velocities are anticorrelated to the total mass content of the particular structure.

Regular structures like streamers, helical waves and knots or density enhancements (for an overview see Mendis et al., 1985) are by no means singular events at comets and thus should not be explained by singular external causes. Ershkovich (1980) considered a model of a comet tail as a plasma cylinder separated by a tangential discontinuity surface from the solar wind and solved the stability problem. He showed that under typical conditions the Kelvin-Helmholtz instability can be the cause for the helical wave phenomena. However, one could also think that regular knots or density enhancements in the plasma tail are simply the result of a modulation of the cometary environment.

Different numerical models have been used to simulate the cometary environment. As already mentioned, a one-fluid MHD approach has been used to simulate the cometary plasma processes (for example, Biermann et al., 1967; Schmidt and Wegmann, 1982). A bi-ion fluid MHD approach shows the existence of an ion composition boundary at comets (Sauer et al., 1994) that was related to the pile-up boundary (or: cometopause, planetopause) observed at comets or planets like Mars. The bi-ion fluid MHD model has also been used to simulate plasma structures at weak comets (Bogdanov et al., 1996), and tail structuring has been found to be

TABLE 4.7.1
Characteristic parameters for comet Austin during observation from May 1 to May 3 1990

Gas production rate	2×10^{29} s^{-1}
Distance to Sun	0.7 AU
Distance to Earth	0.5 AU
Magnitude	5.5 mag$_V$
Projection angle of plasma tail θ	72°

the result of solitary waves originating in the heavy ion source and propagating downstream.

The formation of a plasma tail was well observed during the artificial comet experiments where also in-situ measurements were made (Haerendel, 1987). Of course, the parameter range is very different from that of an ordinary comet tail, but similarities can be found: In the experiments, knots in the tail were formed. This also suggests a mechanism for knot production independent from external causes.

We made the attempt to find a mechanism for knot formation under stable external conditions. As already mentioned, tail structures under stable conditions have been found in a 2D bi-ion fluid MHD simulation of a weak comet (Bogdanov et al., 1996). We have extended this model to 3D.

In this work we analyze observations of comet Austin which show substantial structuring in the tail in the form of knots appearing regularly in time. The dynamics of the knots in the tail is analyzed and the results are shown. Similar knot structures are found in a 3D bi-ion fluid MHD simulation. The origin and the dynamics of the simulated structures are discussed qualitatively.

4.7.1. *Observations of Comet Austin*

Table 4.7.1 contains the characteristic parameters of comet Austin during the observations. The comet has been observed with a 30 cm telescope from Skinakas/Crete during May 1990 (perihelion). The gas production rate was determined to 2×10^{29} s^{-1} (see, for example, Bonev and Jockers, 1994). Assuming average interplanetary conditions the cometary parameters were such that a bow shock should have formed (Bogdanov et al., 1996). The projection angle of 72° and the low gas production rate provided almost perfect conditions for deriving the dynamics of individual tail structures from consecutive images. Advantageously comet Austin had only a low dust release so even structures very close to the nucleus were still observable.

Figure 4.7.1 shows comet Austin on May 3. The plasma tail is split into several rays and in the 'main tail' several structures (knots) can be detected. Series of consecutive images of the comet were taken and the evolution of the tail structures

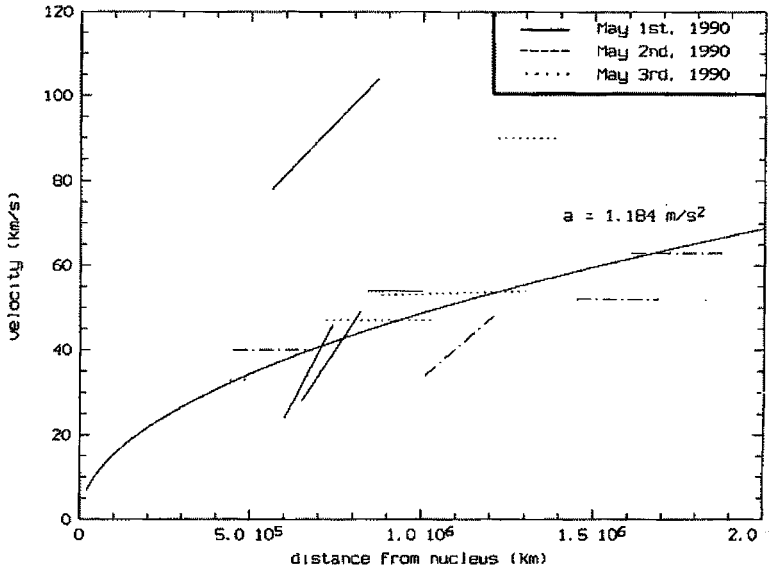

Figure 4.7.1. Comet Austin observed from Skinakas/Crete on May 3 1990. The right image is the extension of the left one. A CO^+-Filter has been used with a central wavelength of 4273 Å and a width of 76 Å. Several tail rays and pretty regular knot structuring in the main tail can be noticed.

is traced to determine their propagation velocity. In Figure 4.7.2 all traced structures are shown. Most of the structures exhibit only very low acceleration. If one fits the velocity versus separation of most of the structures by assuming constant acceleration, a global acceleration of about 100 cm s^{-2} is found. However, there are a few exceptionally high values.

4.7.2. *3D Bi-Ion Fluid Simulation*

In order to simulate the cometary plasma tail, we use the bi-ion fluid MHD model developed by Sauer et al. (1994). We assume cold ions and neglect the so-called Hall contributions. The model equations are solved by applying a finite differences scheme with flux correction (Book, 1981). In the case shown, the solar wind flows along the x-axis of a 3D simulation box and the magnetic field lies in the xz-plane at an angle of 45° with respect to the flow direction of the solar wind. At time $t = 0$, the cometary source is 'switched on' to produce heavy ions. After a transition period, a state of dynamical equilibrium between the heavy ions and the inflowing solar wind protons is reached. A criterion for the onset of equilibrium condition is that the bow shock remains at a constant upstream position.

As a representative example we show simulation results with the parameter configuration contained in Table 4.7.2. All times that are given in the following are in units of the inverse gyrofrequency of the heavy ions $\Omega_h^{-1} = 9.5$ s. All velocities are given in units of $v_A = 144$ km s^{-1}.

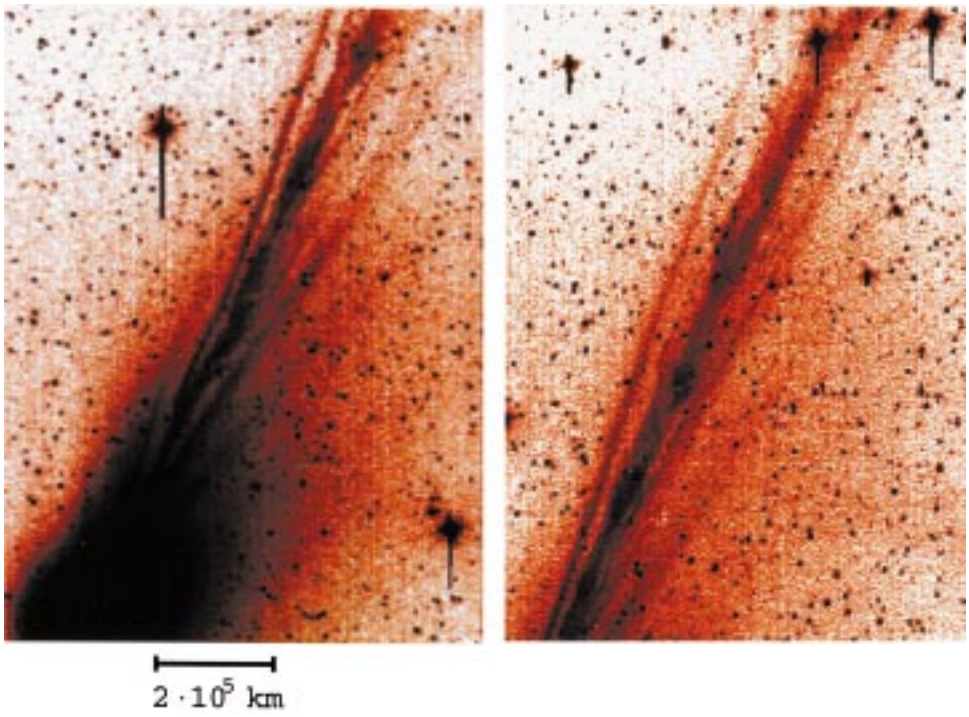

Figure 4.7.2. Velocity evolution of all traced knots and a global fit for constant acceleration. One line stands for the evolution of one particular knot.

TABLE 4.7.2
Parameters used for bi-ion fluid simulation

Gas production rate	10^{28} s^{-1}
Initial magnetic field strength	16 nT
Angle of magnetic field with respect to x-axis	45°
Solar wind flow speed	575 km s^{-1}
Solar wind density	6 cm^{-3}
Alfvén Mach number	4
Heavy ion mass	15 m_p
Simulation box size (in grid points)	300 × 80 × 80
Temporal resolution Δt	Ω_p^{-1}
Resolution per pixel Δx	1800 km = 20 $L_{p,skin}$

4.7.3. *Simulation Results*

All prominent features of the cometary plasma environment can be observed in the results. The magnetic field is piling up just upstream of the nucleus and a bow shock is formed. In the case shown, a state of dynamical equilibrium is reached after a time of about 40 Ω_h^{-1}. The calculations are continued to 350 Ω_h^{-1}. Figure 4.7.3 shows the system at a time of 250 Ω_h^{-1}. Two isosurfaces for the proton and heavy ion density are represented in the figure. The isosurface of the proton density is chosen so as to depict approximately the form of the bow shock. The other surface is representative for the dynamics of the heavy ions. The heavy ion tail direction deviates slightly from the solar wind flow direction: The main tail still lies in the xz-plane and points to negative z-values. This is the result of the specific geometry of the IMF.

Figure 4.7.4 shows xz- and yz-cuts through the simulation box. The magnitude of the magnetic field, the proton velocity, the proton density and the heavy ion density have been chosen as representative for the overall behaviour of the system. Also projections of the magnetic field lines are included in two of the plots. The field line distribution in the xz-plane demonstrates the draping of the magnetic field around the obstacle, the field lines projected to the yz-plane show the expulsion of the field from the region of the obstacle. This expulsion is caused by the asymmetric magnetic pressures above and below the tail axis. The location of the current sheet (regions with a low magnetic field magnitude) in the tail are well illustrated in the figure. One can see also that the magnetic field lines near the cometary centre are more stretched while the ones farther out in the tail tend to relax to their undisturbed state. For this figure and throughout the following we define the comet tail position as the point (for every x-position) in the yz-plane where the heavy ion density has a maximum.

This simulation example shows a substantial structuring in the tail. Near the cometary centre, knots are formed and then propagate into the tail region. Some knots disappear again a short time after they have been born, some originate further down in the tail.

Figure 4.7.5 shows a plot of the temporal evolution of several parameters at a distance of 5000 km downstream from the cometary centre. The average velocity over one gyroperiod of the heavy ions defines their transport velocity. At the given distance, the y- and z-components of the heavy ion velocity and the gyration can be neglected, so the transport velocity can be well expressed by the velocity of the heavy ions in x-direction v_{hx}. The average velocity of the protons $\langle v_{px} \rangle$ is in conformity with this transport velocity as a result of the frozen-in magnetic field.

A periodic behaviour of all parameters with a strong correlation to each other is found. The period is about 20 Ω_h^{-1}. The peak of the magnetic field strength appears always a short time after the peak of the heavy ion density. Hence a region of magnetic field pile up is connected to the 'upstream side' of a newly formed knot. The interesting point is: Although dynamic equilibrium is reached at the upstream side of the comet head and the external parameters are constant there, the density

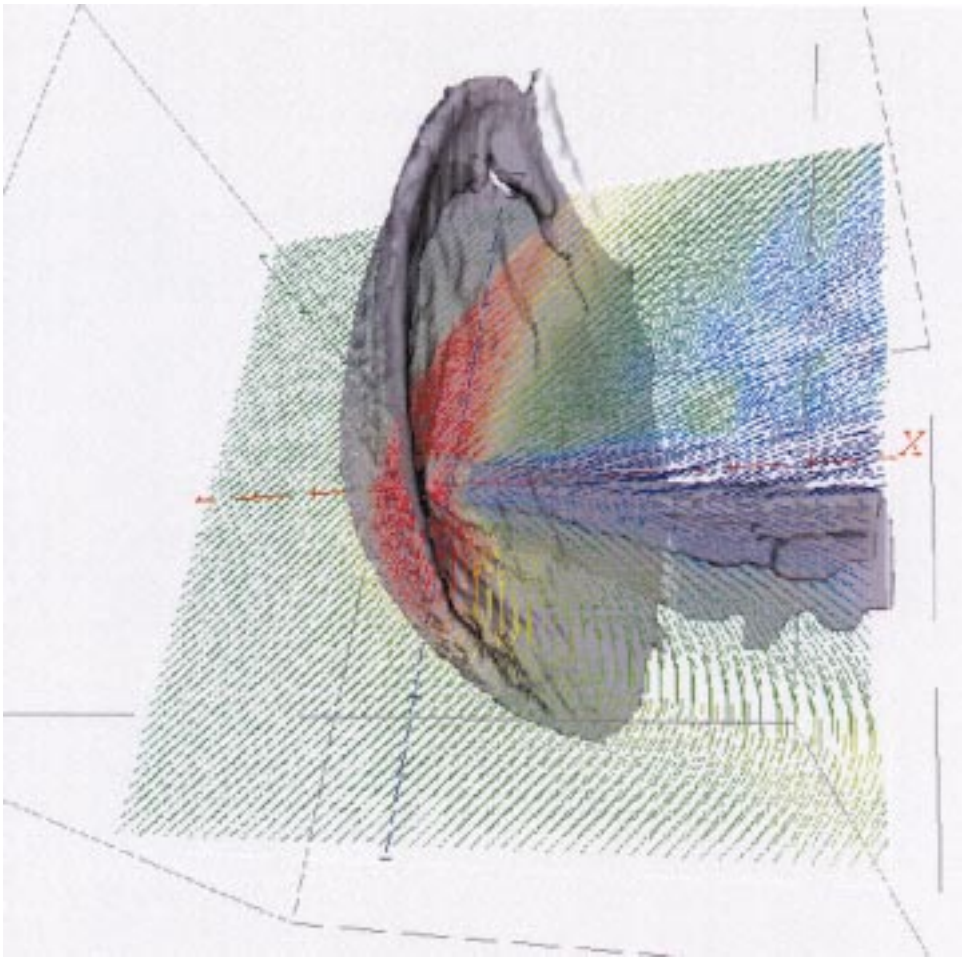

Figure 4.7.3. The simulation box configuration at a time $t = 250\ \Omega_h^{-1}$. The magnetic field lines are piling up and a bow shock is formed. The magnetic field strength is shown on a linear colour scale (red $>$ 40 nT, dark blue $=$ 0 nT).

on the downstream side of the cometary centre remains subject to fluctuations. This instability generates density knots just downstream of the cometary centre which then propagate tailwards.

In Figure 4.7.6 the temporal evolution of all detected knots is shown. Different velocity levels can be observed and also accelerated motion can be seen. Generally the knots are accelerated near the nucleus and then reach constant velocity of about 130 km s^{-1}. If a fixed point in space is examined, then a pretty regular time pattern of the reappearance of consecutive knots can be noticed.

A comparison of the heavy ion velocity and the velocity of the particular knots (Figure 4.7.7) reveals three different regions going from the nucleus out into the tail. In the first region, the heavy ions and knots are accelerated (when the knots

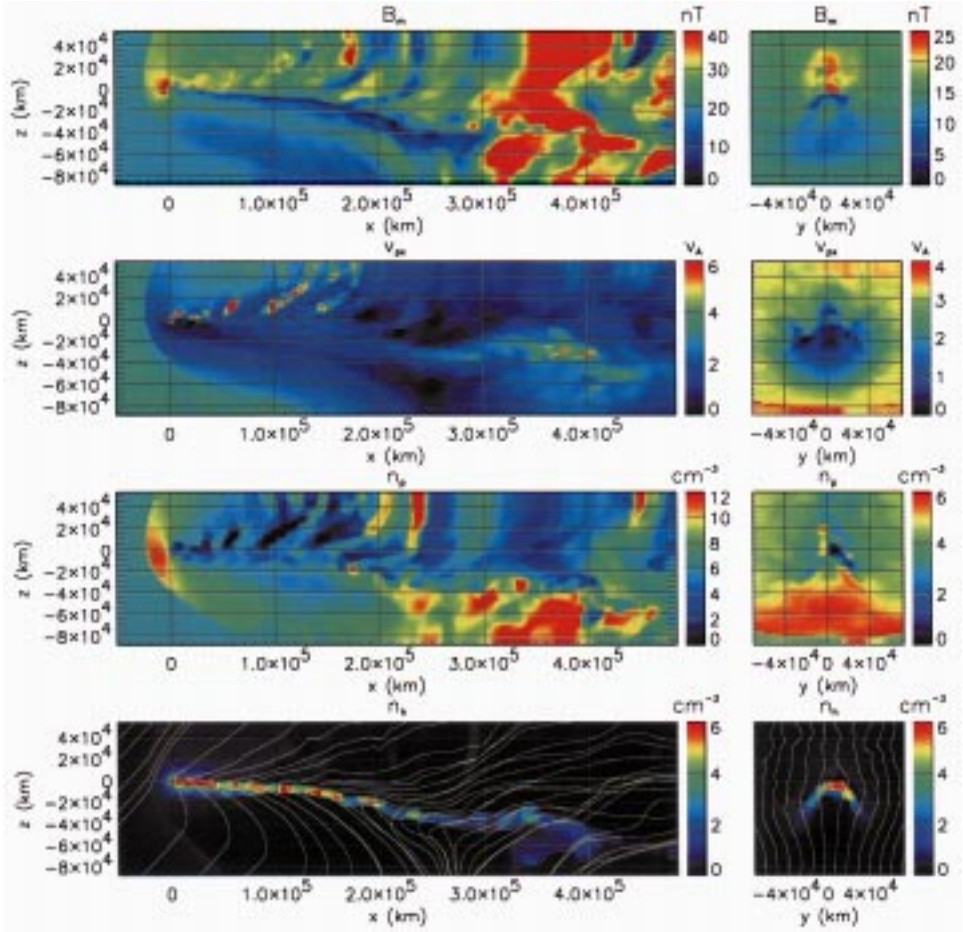

Figure 4.7.4. 2D-cuts of simulation box at a time $t = 200\ \Omega_{\mathrm{h}}^{-1}$ of magnetic field magnitude, proton velocity (x direction), proton density, heavy ion density. Left: xz-cut ($y = 0$), right: yz-cut ($x = 7 \times 10^4$ km). The field lines included in the xz-cut of the heavy ion density plot are the projection of the 3D field lines that go through the comet tail (see text); the starting points for the field lines in the yz-cut are chosen on a line on the bottom of the plot. The velocities are normalized to v_{A}. In each plot higher values than shown on the particular colour table occur and are represented by the highest colour value. Note that each cut has its own range of displayed values.

are born already ion flux through them exists). Then the knots reach their final velocity while the ions still get accelerated to values about a factor of two higher than the velocity of the knot. In the last region the ions reach their final velocity and the flux (at least the flow speed) through the knots remains constant.

Numerous observation results (in this study comet Austin) show density knots appearing pretty regularly in the tail. Their dynamics and temporal behaviour have been discussed. The remarkable regularity of the knot pattern suggests the existence of a mechanism that produces them independently from external changes in

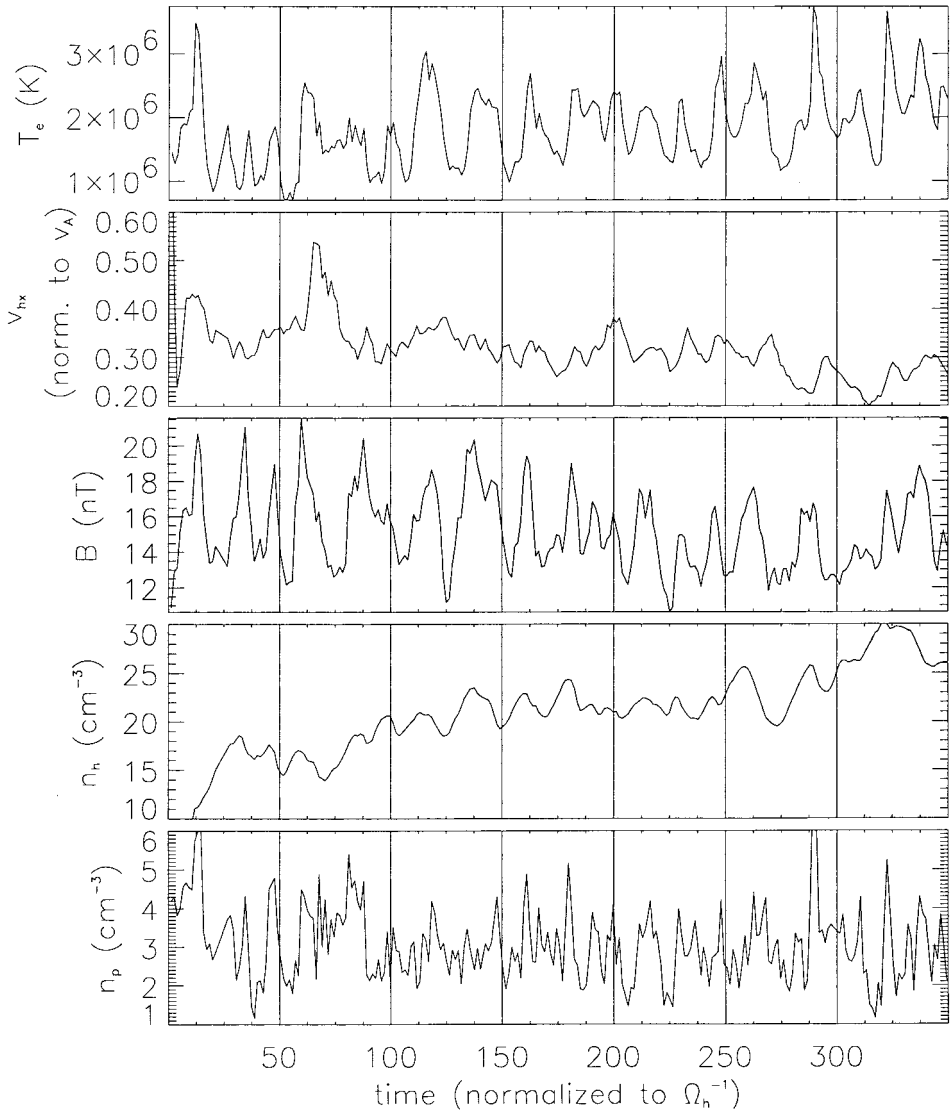

Figure 4.7.5. Temporal evolution of simulation variables at a distance of 5000 km from the comet centre. v_{hx} represents the plasma transport velocity (see text).

the solar wind plasma parameters. This observation and the attempt to understand its physics is the main point of our study.

The results from the 3D bi-ion fluid simulations show structures in the tail similar to those observed at comet Austin around perihelion. The origin and evolution of the knots in the simulation have been qualitatively discussed. An ion flux through the knots determines their evolution during their propagation down the tail. The nonlinear effects that are responsible for their origin and the steepening of the

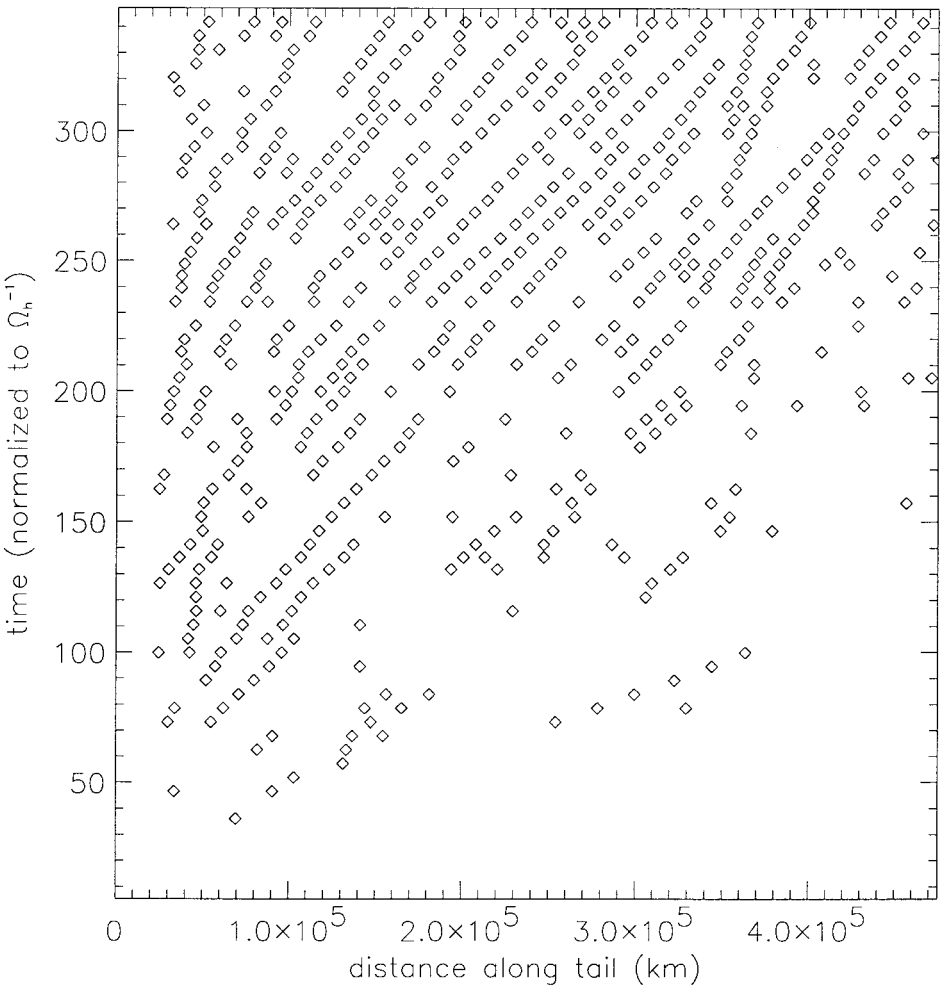

Figure 4.7.6. Temporal evolution of the knots along the tail. One diamond symbol means that a local density enhancement is found. The obvious tracks of diamonds describe the evolution of separate knots. Merging tracks mean merging of knot structures.

knots in the tail have to be studied in more detail. The described mechanism is most probably only one of the possible ways in which density enhancements in comet tails are created and propagate along the tail.

Since the gas production rates of both, observation and simulation, differ by one order of magnitude, the two cases can not be compared directly, but nevertheless our simulation results show tail structuring without changing the external solar wind plasma parameters in a wide range of parameter sets (also at higher gas production rates). So one can be confident that the effects seen in the simulation should also be relevant for comets of the strength of comet Austin.

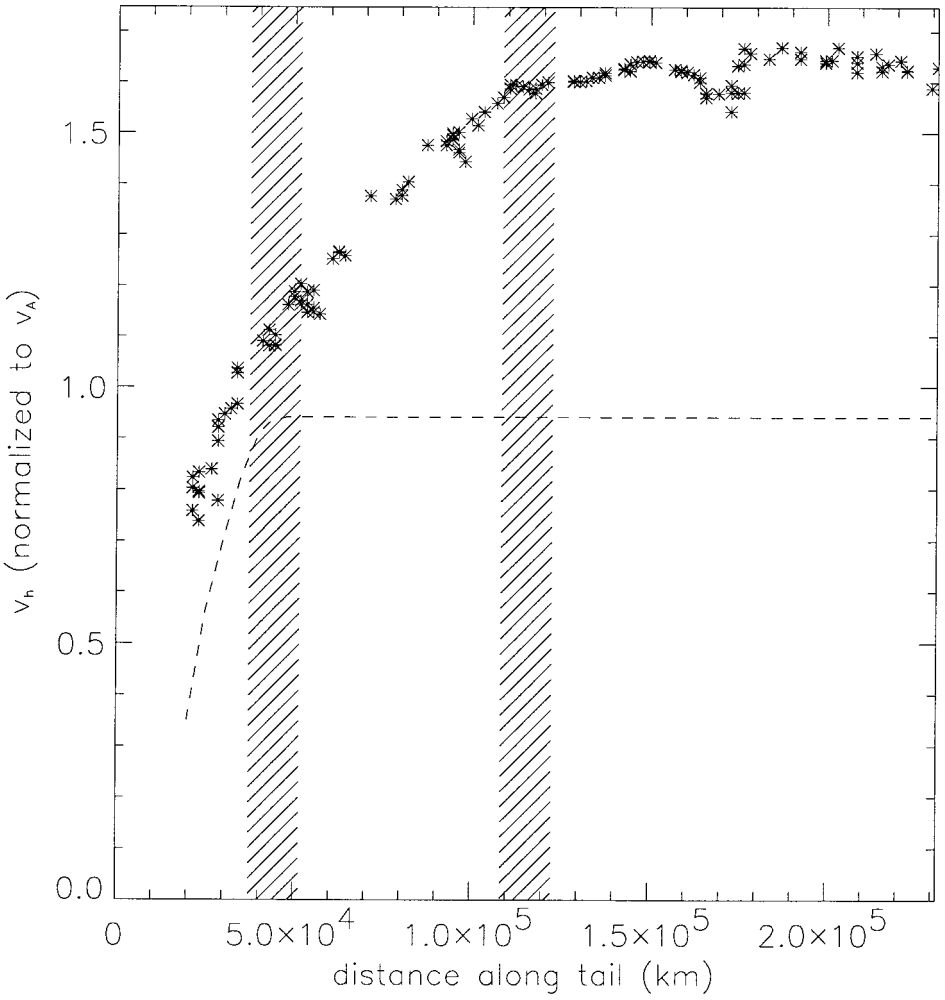

Figure 4.7.7. Comparison of knot velocity and heavy ion velocity. The dashed line is the knot velocity, the stars represent the heavy ion velocity at the centre of one knot. The gray vertical boundaries divide the x-axis into three regions: (1) Heavy ion and knot acceleration, (2) Heavy ion acceleration and constant knot velocity, (3) Constant heavy ion and knot velocity.

5. Final Comments

In this paper we have reviewed processes that lead to the loading of the solar wind flow with additional mass, momentum, and energy. This phenomena is widespread in the solar system, spectacular examples are comets, but wherever we look, at planets, moons, other solar system bodies, interstellar wind, mass loading is present, and frequently is the dominant process of the given region.

Mass loading is frequently connected with cometary activity, because an active nucleus is evidently a source of newborn ions, and around the comet a huge volume

is available for their interaction with the solar wind. During the flybys the activity varied by a few orders of magnitude from 10^{27} to 10^{30} ions s^{-1}, and we observed artificial ion emissions loading about 10^{25} ions into the solar wind. In all cases the most significant features were very similar: the newborn ions got entangled into a forest of magnetic field lines and were coiled up, the interaction of the new and host plasma liberated free (kinetic) energy from the host plasma turning it to electromagnetic energy (waves), finally the electromagnetic energy was slowly absorbed by the newborns, making them accommodated to the host plasma. Details of this process are fascinating, and depend on the source strength, as well as on other upstream parameters.

Mass loading at (non-magnetic) planets is similar as far as this simple picture is concerned. However, because the available space is limited, it is not that the forest of field lines is the important player, rather the electron components of the two (planetary and solar wind) plasmas, reacting quickly to the locally generated electric field, tap the free energy available and changes it to wave energy. It is not well established yet whether this process has an analogy at comets, though there are indications that this is the case. The analogy of the cometary pick up at planets is manifested as the simple $\mathbf{E} \times \mathbf{B}$ pickup, but the quickly varying conditions and the limited volume does not allow it to blossom out.

Interplanetary pickup shows distinct features, because during this pickup process no free energy is liberated, probably due to the fact that this source is week (the neutral density is about 0.1 particle cc^{-1}) and extended. The newborns get accommodated with the help of already existing waves, leading to a very slow and possibly even incomplete pickup.

Adding mass, momentum and energy to a simple collision dominated gas already exhibits very interesting features, because the new material may tap the kinetic and thermal energy reservoir of the host gas at different speeds, leading to its deceleration or acceleration. It is not trivial to translate these processes to collisionless plasmas. The natural framework is MHD theory, with different level of complications. In one-fluid MHD the new material appears as source in the equations, the shape and physical extent of the source is of importance. In MHD the gyromotion of the particles is neglected, and that probably sets a natural limit to grid resolution. The pickup itself is instantaneous, it is unclear whether this distorts some of the details of the interaction, or not. MHD also means that relatively low-order velocity moments are used to characterize the complicated velocity distributions of the various plasma components. In such descriptions a large part of the underlying kinetic processes are neglected, or at most are characterized by some transport coefficients. Still, surprisingly, even this simple approach gives realistic results: accounts for the flow deceleration, shock modification, etc.

The next step of complication is to have an MHD description for all components separately. A warning is in place here, whereas conservation laws lead to the three lowest momentum equations in the case of a single flow, if we split up the equations according to components, only the mathematical analogy guides us, and

our intuition concerning the coupling between the various components. Therefore multifluid MHD has a somewhat less solid basis. Though we do not discuss here problems related to closing the MHD equation system, or problems associated with the different approximation schemes well known in the MHD context; we note that it is far not trivial what value of γ is introduced into the equation of state. The usual closure of the momentum equations via a polytropic law is not always the most appropriate approximation. If strong heat flux effects are involved using the polytropic law closure introduces an approximation where the polytropic index becomes a parameter required to describe the neglected heat flux effects. Details of this effect also need further work.

A special case that deserves attention is the very successful bi-ion-fluid MHD approach. Here electromagnetic fields couple the various fluids, and the effect of particle scattering in the highly turbulent magnetofluid is neglected. Another possible approach is when this term is present, and approximated as an additional 'friction' in the multi fluid equations. This latter method leads to extended shock waves when loading inside the shock structure has significant effects. Multifluid MHD models result in a separate boundary layer structure for each component located at different places. It is striking, however, that these locations differ less than the gyroradii involved. A definite novelty of the multifluid approach is the appearance of solutions that are oscillatory at time infinity. It is not a trivial business to associate physical meaning to those, or better to say to separate, which, if any, is a real solution. The solutions of the different MHD approaches have not yet been compared in a systematic manner, this is also a task to be done in the future.

MHD, however, cannot account properly for the wave excitations; this would require a full kinetic treatment that is much beyond the current possibilities. Linear approximations are still frequently used to describe the initial phase of wave generation, the subsequent wave particle interaction is treated in the quasi-linear approximation. Whereas the general shell (or bispherical shell) formation is seemingly well understood, the differences observed between proton and heavy ion shell structure is unclear. The stability of the bispherical shell, the way it accommodates to the flow, the structure of the flow with significantly different bulk velocities for the shell segments and the solar wind, its effects on the flow pressure are questions still to be investigated. The quasilinear picture of energy diffusion might be inadequate, other causes could also produce the same effect.

Hybrid codes are a new tool to study these processes, they develop quickly in parallel with hardware available, and have already shed light to many details of the pickup processes. It is a realistic hope that many new results will be available soon; though the physical interpretation of the calculations are never an easy task.

In summary, the physics of mass loaded plasmas is not only an exciting field, but it is an important tool to understand the basic processes in our solar system. Mass loading is a special but effective vehicle for energy and momentum transfer, therefore its significance is self evident.

Acknowledgements

This review paper is the result of a working group activity conducted at the International Space Science Institute (ISSI) in Bern. The entire working group would like to thank the ISSI directors, Johannes Geiss and Bengt Hultqvist, and their staff for their generous support and warm hospitallity that made this project possible and enjoyable.

The work by Armando Brinca was partially supported by FEDER and PRAXIS XXI. The work by Karl-Heinz Glassmeier was financially supported by the Deutsches Zentrum für Luft- und Raumfahrt under contract FK 50QP97025. The work of K. Szegö was supported by OTKA grant T 32634. The work by Konrad Sauer was supported by the Max-Planck-Society. The work by Tamas Gombosi was supported by NASA under grants NAG5–4714, NAGW–1366, and NCCS5–146 and by NSF under grants AST–9618795 and ATM–9318181. The work by Uwe Motschmann was supported by the Deutsche Forschungsgemeinschaft through a Heisenberg-Stipendium. Portions of the work of Bruce Tsurutani were performed at the Jet Propulsion Laboratory, California Institute of Technology under contract with NASA. The work by Eberhard Möbius was supported by NASA under contract NAS-31166 and NSF under Grant xxxx. The work of Phil Isenberg was supported in part by NASA grant NAG5-7097, and by the NASA Space Physics Theory program under grant NAG5-1479. The work of Martin Lee was supported in part by NASA grant NAG5-7097, and by the NASA Space Physics Theory program under grant NAG5-1479, and by NSF grant ATM-9633366. Gary P. Zank has been supported in part by an NSF Young Investigator Award ATM-9357861, a NASA grant NAG5-6469, an NSF-DOE Award ATM-97133223, JPL contract 959167 and a NASA Delaware Space Grant College award NGT5-40024.

K. Szegö and K. H. Glassmeier were supported by the OMFB-TET cooperation.

The authors are extremely grateful to Carsten Aulbert, Andreas Jung and Florian Kirstein of the Technical University of Braunschweig for LaTeX help at any time.

Appendix

Appendix to 3.2.2

When the particle species have (possibly drifting and anisotropic) Maxwellian distributions, that is,

$$F_{ol} = M_l(v_{tl}, V_{Dl}, A_l)$$

$$= \frac{1}{A_l(\sqrt{\pi}v_{tl})^3} e^{-(v_x - v_{Dl})^2/v_{tl}^2} \; e^{-v_\perp^2/(A_l v_{tl}^2)}$$

for the gyrotropic populations ($l = e, p$), and

$$F_{ob} = G_{ob}(v_x,\ v_\perp)\Phi_b(\Delta) = 2\pi M_b(v_{tb},\ V_{Db},\ A_b)\Phi_b(\Delta)\ ,$$

for the nongyrotropic particles, with anisotropies, parallel drifts and thermal velocities denoted by $A_s = T_{\perp s}/T_{xs}$, V_{Ds}, and $v_{ts} = (2T_{xs}/m_s)^{1/2}$ where $s = e,\ p,\ b$, the matrix elements m_{rs} become

$$\begin{aligned}
m_{++} &= \left(\frac{k_c}{\overline{\omega}_1}\right)^2 - 1 - \sum_{s=e,\ p,\ b}\left(\frac{\omega_{ps}}{\overline{\omega}_1}\right)^2 \times \\
&\quad \times\left[\frac{\overline{\omega_1}}{kv_{ts}}\left(1 - \frac{kV_{Ds}}{\overline{\omega_1}}\right)Z(\xi_{s+}) - \frac{1}{2}(A_s - 1)Z'(\xi_{s+})\right]\ , \\
m_{+x} &= \frac{\pi^{\frac{3}{2}}}{2}\sqrt{A_b}\left(\frac{\omega_{pb}}{\overline{\omega}_1}\right)^2\frac{\overline{\omega}_1}{kv_{tb}}\phi_1 Z'(\xi_{b+})\ , \\
m_{+-} &= \pi A_b\frac{\omega_{pb}^2}{\overline{\omega}_{-1}\omega_1}\phi_2 Z'(\xi_{b+})\ , \\
m_{x+} &= -\pi^{\frac{3}{2}}\sqrt{A_b}\frac{\omega_{pb}^2}{\overline{\omega}_1 kv_{tb}}\phi_{-1}Z'(\xi_{bx})\ , \\
m_{xx} &= 1 - \sum_{s=e,\ p,\ b}\left(\frac{\omega_{ps}}{kv_{ts}}\right)^2 Z'(\xi_{sx})\ , \\
m_{x-} &= -\pi^{\frac{3}{2}}\sqrt{A_b}\frac{\omega_{pb}^2}{\overline{\omega}_{-1}kv_{tb}}\phi_1 Z'(\xi_{bx})\ , \\
m_{-+} &= \pi A_b\frac{\omega_{pb}^2}{\overline{\omega}_{-1}\omega_1}\phi_{-2}Z'(\xi_{b-})\ , \\
m_{-x} &= \frac{\pi^{\frac{3}{2}}}{2}\sqrt{A_b}\left(\frac{\omega_{pb}}{\overline{\omega}_{-1}}\right)^2\frac{\overline{\omega}_{-1}}{kv_{tb}}\phi_{-1}Z'(\xi_{b-})\ , \\
m_{--} &= \left(\frac{kc}{\overline{\omega}_{-1}}\right)^2 - 1 - \sum_{s=e,\ p,\ b}\left(\frac{\omega_{ps}}{\overline{\omega}_1}\right)^2 \times \\
&\quad \times[\frac{\overline{\omega}_{-1}}{kv_{ts}}\left(1 - \frac{kV_{Ds}}{\overline{\omega}_{-1}}\right)Z(\xi_{s-}) - \frac{1}{2}(A_s - 1)Z'(\xi_{s-})]
\end{aligned}$$

where

$$\xi_{s\pm} = \frac{\overline{\omega}_{\pm 1} - kV_{Dj} \mp \Omega_s}{kv_{ts}}, \qquad \xi_{sx} = \frac{\omega - kV_{Ds}}{kv_{ts}}$$

and $Z(x)$ and $Z'(\xi)$ represent the plasma dispersion function and its derivative.

References

Acuña, M. H., Glassmeier, K.-H., Burlaga, L. F., Neubauer, F. M. and Ness, N. F.: 1986, 'Upstream Wave of Cometary Origin Detected by the Giotto Magnetic Field Experiment', *Proceedings of the 20th Symposium on the Exploration of Halley's Comet* **ESA SP 250**, 447–449.

Acuña, M. H., Connerney, J. E. P., Wasilewski, P., Lin, R. P., Anderson, K. A., Carlson, C. W., Mc Fadden, J., Curtis, D. W., Mitchell, D., Réme, H., Mazelle, C., Sauvaud, J. A., d'Uston, C., Cros, A., Medale, J. L., Bauer, S. J., Cloutier, P., Mayhew, M., Winterhalten, D. and Ness, N. F.: 1998, 'Magnetic Field and Plasma Observations at Mars: Initial Results of the Mars Global Surveyor Mission', *Science* **279**, 1676.

Alfvén, H.: 1960, 'Collision between a Nonionized Gas and a Magnetized Plasma', *Rev. Modern Phys.* **32**, 710.

Astudillo, H. F., Livi, S., Marsch, E. and Rosenbauer, H.: 1996, 'Evidence for Nongyrotropic Alpha Particle and Proton Distribution Functions: TAUS Solar Wind Measurements', *J. Geophys. Res.* **101**, 24423–24432.

Axford, W. I.: 1972, 'The interaction of the solar wind with the interstellar medium', in C. P. Sonnett, P. J. Coleman, Jr., and J. M. Wilcox (eds.), *The Solar Wind*, **NASA SP 308**, p. 609.

Bagenal, F.: 1985, 'Planetary Magnetospheres', in E. R. Priest (ed.), *Solar System Magnetic Fields*, D. Reidel Publ. Co., Dordrecht, Holland, p. 224.

Bagenal, F., Cravens, T. E., Luhmann, J. G., McNutt, R. L. Jr. and Cheng, A. F.: 1997, in S. A. Stern and D. J. Tholen (eds), 'Pluto's Interaction with the Solar Wind', *Pluto and Charon*, University of Arizona Press, Tucson, p. 523.

Balsiger, H., Altwegg, K., Bühler, F., Geiss, J., Ghielmetti, A. G., Goldstein, B. E., Goldstein, R., Huntress, W. T., Ip, W. H., Lazarus, A. J., Meier, A., Neugebauer, M., Rettenmund, J., Rosenbauer, H., Schwenn, R., Shelley, R. D., Ungstrup, E., and Young, D. T.: 1986, 'Ion Composition and Dynamics at Comet Halley', *Nature* **321**, 330–334.

Bame, S. J., Anderson, R. C., Asbridge, J. R., Baker, D. N., Feldman, W. C., Fuselier, S. A., Gosling, J. T., McComas, D. J., Thomsen, M. F., Young, D. T. and Zwickl, R. D.: 1990, 'The Comet Giacobini–Zinner: Plasma Description', *Science* **232**, 356.

Baumgärtel, K. and Sauer, K.: 1992, *Ann. Geophys.* **10**, 763.

Baumgärtel, K. et al.: 1998, *Earth Planets Space* **50**, 453.

Bauske, R., Nagy, A. F., Gombosi, T. I., DeZeeuw, D. L., Powell, K. G. and Luhmann, J. G.: 1998, 'A Three-Dimensional MHD Study of Solar Wind Mass Loading Processes at Venus: Effects of Photoionization, Electron Impact Ionization, and Charge Exchange', *J. Geophys. Res.* **103**, 23625.

Belmont, G. and Mazelle, Chr.: 1992, 'Polytropic Indices in Collisionless Plasmas: Theory and Measurements', *J. Geophys. Res.* **97**, 8327–8336.

Bernhard, P. A., Roussel-Dupree, R. A., Pongratz, M. B., Haerendel, G., Valenzuela, A., Gurnett, D. A. and Anderson, R. R.: 1987, 'Observations and theory of the AMPTE magnetotail barium releases', *J. Geophys. Res.* **92**, 5777–5794.

Bertaux, J. L. and Blamont, J. E.: 1971, 'Evidence for a Source of Extraterrestrial Lyman Alpha Emission: The Interstellar Wind', *Astron. Astrophys.* **11**, 200.

Bhatnagar, P. L., Gross, E. P. and Krook, M.: 1954, 'A Model for Collision Processes in Gasses', *Phys. Rev.* **94**, 511.

Bieber, J. W., Matthaeus, W. H., Smith, C. W., Wanner, W., Kallenrode, M.-B. and Wibberenz, G.: 1994, 'Proton and Electron Mean Free Paths: The Palmer Consensus Revisited', *Astrophys. J.* **420**, 294.

Biermann, I., Brosowski, B. and Schmidt, H. U.: 1967, 'The Interaction of the Solar Wind with a Comet', *Solar Phys.* **7**, 254–284.

Bingham, R., Bryant, D. A., Hall, D. S., Dawson, J. M., Kazeminejad, F. and Su, J. J.: 1988, 'AMPTE Observations and Simulation Results', *Comput. Phys. Commun.* **49**, 257–265.

Bingham, R., Shapiro, V. D., Tsytovich, V. N., de Angelis, J., Gilman, M. and Shevchenko, V. I.: 1991, 'Theory of Wave Activity Occurring in the AMPTE Artificial Comet', *Phys. Fluids* **3**, 1728–1738.

Blum, P. W. and Fahr, H. J.: 1970, 'Interaction between Interstellar Hydrogen and the Solar Wind', *Astron. Astrophys.* **4**, 280.

Bogdan, T. J., Lee, M. A. and Schneider, P.: 1991, 'Coupled Quasi-Linear Wave Damping and Stochastic Acceleration of Pickup Ions in the Solar Wind', *J. Geophys. Res.* **96**, 161.

Bogdanov, A. T., Sauer, K., Baumgärtel, K. and Srivastava, K.: 1996, 'Plasma Structures at Weakly Outgassing Comets – Results from Bi-Ion Fluid Analysis', *Planetary Space Sci.* **44**, 519–528.

Bonev, T., et al.: 1998, *Earth, Moon and Planets,* to be published.

Bonev, T. and Jockers, K.: 1994, 'H_2O^+ Ions in the Inner Plasma Tail of Comet Austin 1990V', *Icarus* **107**, 335–357.

Book, D., Boris, J. P. and Zalesak, S. T.: 1973, in D. Book (ed.), *Finite-Difference Techniques for Vectorized Fluid Dynamics Calculations*, Springer-Verlag, Berlin.

Borowski, J. E.: 1988, 'Properties and Dynamics of the Electron Beams Emanating from Magnetized Plasma Double Layers', *J. Geophys. Res.* **93**, 5713–5725.

Brace, L. H. and Kliore, A. J.: 1991, 'The Structure of the Venus Ionosphere', *Space Sci. Rev.* **55**, 81.

Brecht, S. H. and Thomas, V. A.: 1988, 'Multidimentsional simulations using hybrid particle codes', *Comput. Phys. Commun.* **48**, 135.

Brecht, S. H. and Ferrante, J. R.: 1991, 'Global Hybrid Simulation of Unmagnetized Planets: Comparison of Venus and Mars', *J. Geophys. Res.* **96**, 11209.

Brecht, S. H., Ferrante, J. R. and Luhmann, J. G.: 1993, 'Three-Dimensional Simulations of the Solar Wind Interaction with Mars', *J. Geophys. Res.* **98**, 1345.

Brinca, A. L.: 1991, in A. D. Johnstone (ed.), 'Cometary linear instabilities: from profusion to perspective', *Cometary Plasma Processes* Geophys. Monogr. Ser., 61, Amer. Geophys. Union, Washington, DC, 211.

Brinca, A. L.: 1996, 'Observation and interpretation of cometary low frequency waves', *Surveys Geophys.* **17**, 1–39.

Brinca, A. L. and Tsurutani, B. T.: 1988, 'Temperature Effects in the Pickup Process of Water Group and Hydrogen Ions', *J. Geophys. Res.* **93**, 243–246.

Brinca, A. L. and Romeiras, F. J.: 1998, 'On the stability of stationary nongyrotropic distribution functions, Coupling and purely growing waves', *J. Geophys. Res.* **103**, 9275–9284.

Brinca, A. L. and Tsurutani, B. T.: 1988, 'Survey of Low Frequency Electromagnetic Waves Stimulated by Two Coexisting Newborn Ion Species', *J. Geophys. Res.* **93**, 48–58.

Brinca, A. L. and Tsurutani, B. T.: 1989, 'Influence of Multiple Ion Species on Low Frequency Electromagnetic Wave Instabilities', *J. Geophys. Res.* **94**, 13565–13569.

Brinca, A. L. and Tsurutani, B. T.: 1989, 'The Oblique Behavior of Low Frequency Electromagnetic Wave Instabilities', *J. Geophys. Res.* **94**, 3–14.

Brinca, A. L. and Tsurutani, B. T.: 1989, 'On the Excitation of Cyclotron Harmonic Waves by Newborn Heavy Ions', *J. Geophys. Res.* **94**, 5467–5473.

Brinca, A. L., Tsurutani, B. T. and Scarf, F. L.: 1989, 'Local Generation of Electrostatic Bursts at Comet Giacobini–Zinner, Modulation by Steepened Magnetosonic Waves', *J. Geophys. Res.* **94**, 60–64.

Brinca, A. L., Moreira, A. A., Serra, F. M., Haerendel, G. and Paschmann, G.: 1986, 'Complementary Analysis and Interpretation of the Shocklike Electrostatic Noise Observed During the AMPTE Solar Wind Lithium Releases', *J. Geophys. Res.* **91**, 10167–10172.

Brinca, A. L., Borda de Agua, L., and Winske, D.: 1992, 'Nongyrotropy as a Source of Instability and Mode Coupling', *Geophys. Res. Lett.* **12**, 2445–2448.

Brinca, A. L., Borda de Agua, L. and Winske, D.: 1993, 'On the Stability of Nongyrotropic Ion Populations, A First (Analytic and Simulation) Assessment', *J. Geophys. Res.* **98**, 7549–7560.

Brinca, A. L., Omura, Y. and Matsumoto, H.: 1993, 'Linear Coupling Effects Originated in Electron Nongyrotropy', *J. Geophys. Res.* **98**, 21071–21076.

Brinca, A. L., Omura, Y. and Matsumoto, H.: 1994, 'Bernstein Modes in Nongyrotropic Space Plasmas', *International Conference on Plasma Physics* Foz do Igua cu (Brazil), Oct. 31–Nov 4.

Brinca, A. L., Omura, Y. and Matsumoto, H.: 1998, 'Stability of Perpendicular Propagation in Time-Varying Nongyrotropic Plasmas, Simulations', *J. Geophys. Res.* **103**, 29493–29503.

Burgers, J. M.: 1969, *Flow Equations for Comosite Gasses*, Academic Press, New York.

Burgess, D.: 1987, 'Simulations of Backstreaming Ion Beams Formed at Oblique Shocks by Direct Reflection', *Ann. Geophys.* **5**, 133–145.

Burlaga, L. F., Scudder, J. D., Klein, L. W. and Isenberg, P. A.: 1990, 'Pressure-Balanced Structures Between 1 AU and 24 AU and Their Implications for Solar Wind Electrons and Interstellar Pickup Ions', *J. Geophys. Res.* **95**, 2229.

Burlaga, L. F., Ness, N. F., Belcher, J. W., Szabo, A., Isenberg, P. A. and Lee, M. A.: 1994, 'Pickup Protons and Pressure-Balanced Structures: Voyager 2 Observations in Merged Interaction Regions Near 35 AU', *J. Geophys. Res.* **99**, 21511–21524.

Burlaga, L. F., Ness, N. F., Belcher, J. W. and Whang, Y. C.: 1996, 'Pickup Protons and Pressure-Balanced Structures from 39 to 43 AU: Voyager 2 Observations During 1993 and 1994', *J. Geophys. Res.* **101**, 15523–15532.

Cabannes, H.: 1970, 'Theoretical Magnetofluiddynamics', *Academic*, San Diego, Calif.

Chao, J. K.: 1973, 'Steepening of Nonlinear Waves in the Solar Wind', *J. Geophys. Res.* **78**, 5411.

Cao, J. B., Mazelle, C., Belmont, G. and Réme, H.: 1995, 'Nongyrotropy of Heavy Newborn Ions at Comet Grigg-Skjellerup and Corresponding Instability', *J. Geophys. Res.* **100**, 23379–23388.

Cao, J. B., Mazelle, C., Belmont, G. and Réme, H.: 1998, 'Oblique Ring Instability Driven by Nongyrotropic Ions: Application to Observations at Comet Grigg–Skjellerup', *J. Geophys. Res.* **103**, 2055–2067.

Cao, J. B., Mazelle, C., Belmont, G. and Réme, H.: 1995, 'Nongyrotropy of Heavy Newborn Ions at Comet Grigg-Skjellerup and Corresponding Instability', *J. Geophys. Res.* **100**, 23379–23388.

Celnik, W. E. and Schmidt-Kaler, T. H.: 1987, 'Structure and Dynamics of Plasma-Tail Condensations of Comet P/Halley 1986 and Inferences of the Structure and Activity of the Cometary Nucleus', *Astron. Astrophys.* **187**, 233–248.

Cheng, A. F.: 1987, 'Transverse Deflection and Dissipation of Small Plasma Beams and Clouds in Magnetized Media', *J. Geophys. Res.* **92**, 55–63.

Choi, Y. W., Kim, J., Min, K. W., Nagy, A. F. and Oyama, K. I.: 1998, 'Effect of the Magnetic Field on the Energetics of Mars Ionosphere', *Geophys. Res. Lett.* **25**, 2753.

Coates, A. J., Johnstone, A. D., Smith, M. F. and Rodgers, D. J.: 1986, 'AMPTE/UKS Ion Experiment Observations of Lithium in the Solar Wind', *J. Geophys. Res.* **91**, 1311–1319.

Coates, A. J., Lin, R. P., Wilken, B., Amata, E., Anderson, K. A., Borg, H., Bryant, D. A., Carlson, C. W., Curtis, D. W., Formisano, V., Jockers, K., Johnstone, A. D., Korth, A., Mendis, A. D., Réme, H., Richter, A. K., Rosenbauer, H., Sauvaud, J. A., Studemann, W., Thomsen, M. F., Duston, C., and Winningham, C. D.: 1987, 'Giotto Measurements of Cometary and Solar Wind Plasma at Comet Halley Bow Shock', *Nature* **327**, 489.

Coates, A. J., Rodgers, D. J., Johnstone, A. D., Smith, M. F. and Heath, J. W.: 1988, 'Development of the First Artificial Comet: UKS Ion Measurements', *Adv. Space Res.* **8**, 15–20.

Coates, A. J., Johnstone, A. D., Wilken, B., Jockers, K., and Glassmeier, K. H.: 1989, 'Velocity Space Diffusion of Pickup Ions from the Water Group at Comet Halley', *J. Geophys. Res.* **94**, 9983.

Coates, A. J., Wilken, B., Johnstone, A. D., Jockers, K., Glassmeier, K. H. and Huddleston, D. E.: 1990, 'Bulk Properties and Velocity Distributions of Water Group Ions at Comet Halley: Giotto Measurements', *J. Geophys. Res.* **95**, 10249.

Coates, A. J., Johnstone, A. D., Kessel, R. L., Huddleston, D. E., Wilken, B., Jockers, K. and Neubauer, F. M.: 1990, 'Plasma Parameters Near the Comet Halley Bow Shock', *J. Geophys. Res.* **95**, 20, 701–20, 716.

Coates, A. J.: 1991, in A. D. Johnstone (ed.), 'Observation of the Velocity Distribution of Pickup Ions', *Geophys. Monograph* **61**, 301, AGU.

Coates, A. J., Johnstone, A. D., Kessel, R. L., Huddleston, D. E., Wilken, B., Jockers, K., Neubauer, F. M. and Réme, H.: 1991, *Adv. Space Res.* **11**(9), 227.

Coates, A. J.: 1997, *Adv. Space Res.* **20**, 255–266.

Coates, A. J., Mazelle, C. and Neubauer, F. M.: 1997, 'Bow Shock Analysis at Comets Halley and Grigg-Skjellerup', *J. Geophys. Res.* **102**, 7105–7113.

Coates, A. J., Johnstone, A. D., Wilken, B. and Neubauer, F. M.: 1993, 'Velocity Space Diffusion and Nongyrotropy of Pickup Water Group Ions at Comet Grigg-Skjellerup', *J. Geophys. Res.* **98**, 20985–20994.

Combi, M. R., Kabin, K., Gombosi, T. I. and DeZeeuw, D. L.: 1998, 'Io's Plasma Environment During the Galileo Flyby: Global Three-Dimensional MHD Modeling with Adaptive Mesh Refinement', *J. Geophys. Res.* **103**, 9071.

Connerney, J. E. P., Baron, R., Satoh, J. and Owen, J.: 1993, 'Images of Excited H_3^+ at the Foot of the Io Flux Tube in Jupiter's Atmosphere', *Science* **262**, 1035.

Cowley, S. W. H., Balogh, A., Hynds, R. J., Staines, K., Yates, T. S., Daly, P. W., Richardson, I. G., Sanderson, T. R., Tranquille, C. and Wenzel, K. P.: 1991, in A. D. Johnstone (ed.), 'Energetic Water Group Ions at Comet Giacobini-Zinner: An Overview of Observations by the EPAS Instrument', *Geophys. Monograph* **61**, AGU, p. 319.

Cravens, T. E., Kozyra, J. U., Nagy, A. F., Gombosi, T. I. and Kurtz, M.: 1987, 'Electron Impact Ionization in the Vicinity of Comets', *J. Geophys. Res.* **92**, 7341.

Cravens, T. E.: 1991, in J. G. Luhmann, M. Tatrallyay, and R. O. Pepin (eds), 'Ionospheric Models for Venus and Mars, in Venus and Mars: Atmospheres, Ionospheres, and Solar Wind Interactions', *Geophys. Monog. Ser.* **66**, p. 277, AGU, Washington, D.C.

Cravens, T. E.: 1991a, in R. L. Newburn (ed.), 'Plasma Processes in the Inner Coma', in *Comets in the Post-Halley era*, Vol. 2, pp. 1211–1255, Kluwer Academic Publishers, Dordrecht, Holland.

Cravens, T. E. and Shinagawa, H.: 1991, 'The Ionopause Current Layer at Venus', *J. Geophys. Res.* **96**, 11119.

Cravens, T. E., Shinagawa, H. and Luhmann, J. G.: 1997a, in S. W. Bougher, D. M. Hunten, and R. J. Phillips (eds), 'Magnetohydrodynamic Processes: Magnetic Fields in the Ionosphere of Venus, in Venus II – Geology, Geophysics, Atmosphere, and Solar Wind Environment', University of Arizona Press, Tucson, p. 61.

Cravens, T. E., Keller, C. N. and Ray, B.: 1997b, 'Photochemical Sources of Non-Thermal Neutrals for the Exosphere of Titan', *Planet. Space Sci.* **45**, 889.

Cravens, T. E., Lindgren, C. J. and Ledvina, S. A.: 1998, 'A Two-Dimensional Multifluid MHD Model of Titan's Plasma Environment', *Planet. Space Sci.* **46**, 1193.

Davidson, R. C.: 1983, in M. N. Rosenbluth and R. Z. Sagdeev (eds), 'Kinetic Waves and Instabilities in a Uniform Plasma', Handbook of Plasma physics, Vol.I., p. 519, North-Holland.

Delcourt, D. C., Sauvaud, J.-A. and Moore, T. E.: 1997, 'Phase Bunching During Substorm Dipolarization', *J. Geophys. Res.* **102**, 24313–24324.

Delcourt, D. C. and Belmont, G.: 1998, 'Ion Dynamics at the Earthward Termination of the Magnetotail Current Sheet', *J. Geophys. Res.* **103**, 4605–4613.

Dennerel, K., Englhauser, J. and Trumper, J.: 1997, 'X-ray Emission from Comets Detected in the Röntgen X-Ray Satellite all Sky Survey', *Science* **277**, 1025.

Dessler, A. J., ed.: 1983, 'Physics of the Jovian Magnetosphere', Cambridge University Press, Cambridge, U.K.

Dobe, Z., Quest, K. B., Shapiro, J. D., Szegö, K. and Huba, J. D.: 1999, 'On the Interaction of the Solar Wind with Unmagnetized Planets', *Phys. Rev. Lett.*, in press.

Dubinin, E., Sauer, K., Lundin, R., Baumgärtel, K. and Bogdanov, A.: 1996, *Geophys. Res. Lett.* **23**, 785.

Dubinin, E. M., Sauer, K., Baumgartel, K. and Lundin, R.: 1997, 'The Martian Magnetosheath: Phobos 2 Observations', *Adv. Space Res.* **20**, 149.

Dubinin, E., Sauer, K., Baumgärtel, K. and Shrivastava, K.: 1998, *Earth Planets Space,* **50**, 279.

Dumont, R. F. and Sanchez, F.: 1976, 'Zodiacal Light Photopolarimetry. III. All-Sky Survey from Teide 1964–1975 with Emphasis on O-Ecliptic Features', *Astron. Astrophys.* **51**, 393.

Dungey, J. W.: 1994, 'Memories, Maxims, and Motives', *J. Geophys. Res.* **99**, 19189–19197.

Dusenbery, P. B. and Hollweg, J. V.: 1981, 'Ion-Cyclotron Heating and Acceleration of Solar Wind Minor Ions', *J. Geophys. Res.* **86**, 153.

Eastman, T. E., Anderson, R. R. and Frank, L. A.: 1981, 'Upstream Particles Observed in the Earth's Foreshock Region', *J. Geophys. Res.* **86**, 4379–4395.

Eberhardt, P. and Krankowsky, D.: 1995, 'The Electron Temperature in the Inner Coma of Comet P/Halley', *Astron. Astrophys.* **295**, 795.

Elsässer, W. M.: 1950, 'The Hydromagnetic Equations', *Phys. Rev. A* **79**, 183.

Ershkovich, A. I.: 1980, 'Kelvin-Helmholtz Instability in Type-1 Comet Tails and Associated Phenomena', *Space Science Reviews* **25**, 3–34.

Fahr, H. J.: 1971, 'The Interplanetary Hydrogen Cone and its Solar Cycle Variations', *Astron. and Astrophys.* **14**, 263.

Fahr, H. J., Ripkin, H. W. and Lay, G.: 1981, 'Plasma-Dust Interaction in the Solar Vicinity and Their Observational Consequences', *Astron. Astrophys.* **102**, 359.

Fahr, H. J. and Ripken, H. W.: 1984, 'The Physics of the Heliospheric Interface and its Implications for LISM Diagnostics', *Astron. Astrophys.* **139**, 551.

Fisk, L. A. and Axford, W. I.: 1969, 'Anisotropies of Solar Cosmic Rays', *Solar Phys.* **7**, 486.

Fisk, L. A., Kozlovsky, B. and Ramaty, R.: 1974, 'An Interpretation of the Observed Oxygen and Nitrogen Enhancements in Low Energy Cosmic Rays', *Astrophys. J.* **190**, L35–L38.

Fisk, L. A., Schwadron, N. A. and Gloeckler, G.: 1997, 'Implications of Fluctuations in the Distribution Functions of Interstellar Pickup Ions for the Scattering of Low Rigidity Particles', *Geophys. Res. Lett.* **24**, 93.

Forman, M. A. and Webb, G. M.: 1995, in R. Stone and B. T. Tsurutani (eds), 'Acceleration of Energetic Particles' in Collisionless Shocks in the Heliosphere', *Geophys. Monograph*, **34**, p. 91.

Frank, L. A., Paterson, W. R., Ackerson, K. L., Vasyliunas, V. M., Coroniti, F. V. and Bolton, S. J.: 1996, 'Plasma Observations at Io with the Galileo Spacecraft', *Science* **274**, 394.

Freund, H. P. and Wu, C. S.: 1988, 'Stability of a Spherical Shell Distribution of Pickup Ions', *J. Geophys. Res.* **93**, 14, 277.

Galeev, A. A., Sagdeev, R. Z. and Formissano, V.: 1982, 'The Role of the Critical Ionization Velocity Phenomena in the Production of Inner Coma Cometary Plasma', *Planet. Space Sci.* **30**, 491.

Galeev, A. A.: 1986, 'Theory and Observations of Solar Wind/Cometary Plasma Interaction Processes', *Proceedings of the 20th ESLAB Symposium on the Exploration of Comet Halley* Eur. Space Agency Spec. Publ., 250, Vol. I, 3–18.

Galeev, A. A., Sagdeev, R. Z., Shapiro, V. D., Shevchenko, V. I., Poluydov, A. N., and Szegö, K.: 1987, 'MHD Turbulence in a Solar Wind Flow Interacting with Comets', *JETP* **192**, 2090.

Galeev, A. A. and Sagdeev, R. Z.: 1988, 'Alfvén Waves in a Space Plasma and its Role in the Solar Wind Interaction with Comets', *Astrophys. Space Sci.* **144**, 427.

Galeev, A. A., Gringauz, K. I., Klilmov, S. I., Remizov, A. P., Sagdeev, R. Z., Savin, S. P., Sokolov, A. Y., Verigin, M. I., Szegö, K., Tatrallyai, M., Grard, R., Eroshenko, Y. G., Mogilevsky, M. J., Riedler, W. and Schwingenschuch, K.: 1988, 'Physical Processes in the Vicinity of the Cometopause Interpreted on the Basis of Plasma, Magnetic Field, and Plasma Wave Data Measured on Board the Vega 2 Spacecraft', *J. Geophys. Res.* **93**, 7527.

Galeev, A. A.: 1991, in R. L. Newburn, M. Neugebauer, and J. Rahe (eds), 'Comets in the Post-Halley Era', 1145, Kluwer Academic Publishers, Boston, Mass.

Galeev, A. A., Sagdeev, R. Z., Shapiro, V. V. D., Shevchenko, V. I. and Szegö, K.: 1991, in A. D. Johnstone (ed.), 'Quasilinear Theory of the Ion Cyclotron Instability and its Application to the Cometary Plasma', *Geophys. Monograph* **61**, AGU, p. 223.

Galeev, A. A. and Khabibrakhmanov, I. K.: 1992, *Adv. Space Res.* **12**, 323.

Galeev, A. A. and Khabibrakhmanov, I. Kh.: 1993, in T. I. Gombosi (ed.), 'Critical Problems in the Plasma Environments of Comets and other Non-Magnetized and Weakly Magnetized Bodies', *COSPAR Colloq.* **vol. 4**, Pergamon, New York.

Gan, L., Cravens, T. E. and Horanyi, M.: 1990, 'Electrons in the Ionopause Boundary Layer of Venus', *J. Geophys. Res.* **95**, 19023.

Gan-Baruch, Z. et al.: 1998, *J. Geophys. Res.,* **103**, 23,639.

Gary, S. P., Smith, C. W., Lee, M. A., Goldstein, M. L. and Forslund, D. W.: 1984, 'Electromagnetic Ion Beam Instabilities', *Phys. Fluids* **27**, 1852.

Gary, S. P., Akimoto, K. and Winske, D.: 1989, 'Computer Simulations of Cometary Ion/Ion Instabilities and Wave Growth', *J. Geophys. Res.* **94**, 3513–3525.

Gary, S. P.: 1991, 'Electromagnetic Ion/Ion Instabilities and their Consequences in Space Plasma: A Review', *Space Sci. Rev.* **56**, 373–415.

Gary, S. P., Miller, R. M. and Winske, D.: 1991, 'Pitch Angle Scattering of Cometary Ions: Computer Simulations', *Geophys. Res. Lett.* **18**, 1067.

Geiss, J., Gloeckler, G., Mall, U., von Steiger, R., Galvin, A. B. and Ogilvie, K. W.: 1994, 'Interstellar Oxygen, Nitrogen and Neon in the Heliosphere', *Astron. Astrophys.* **282**, 924.

Geiss, J., Gloeckler, G., Fisk, L. A., and von Steiger, R.: 1995, 'C^+ Pickup Ions in the Heliosphere and Their Origin', *J. Geophys. Res.* **100**, 23373–23377.

Geiss, J., Gloeckler, G. and von Steiger, R.: 1996, 'The Origin of C^+ Pickup Ions in the Heliosphere', *Space Sc. Rev.* **78**, 1, 43–52.

Geiss, J. and Witte, M.: 1996, 'Properties of the Interstellar Gas Inside the Heliosphere', *Space Sci. Rev.* **78**, 229.

Gendrin, R.: 1981, 'General Relationships Between Wave Amplification and Particle Diffusion in a Magnetoplasma', *Rev. Geophys.* **19**, 171–184.

Glassmeier, K. H., Neubauer, F. M., Acuña, M. H. and Mariani, F.: 1986, 'Strong Hydromagnetic Fluctuations, in the Comet P/Halley Magnetosphere Observed by the Giotto Magnetic Field Experiment', *Proceeding of the 20th ESLAB Symposium on the Exploration of Comet Halley* vol. III, **ESA-SP 250**, 447–449.

Glassmeier, K.-H., Coates, A. J., Acuña, M. H., Goldstein, M. L., Neubauer, F. M., Johnstone, A. D. and Rème, H.: 1989, 'Spectral Characteristics of Low-Frequency Plasma Turbulence Upstream of Comet P/Halley', *J. Geophys. Res.* **94**, 37–48.

Glassmeier, K. H., Motschmann, U., Mazelle, Chr., Neubauer, F. M., Sauer, K., Fuselier, S. A., and Acuña, M. H.: 1993, 'Mirror Modes and Fast Mode Waves Near the Magnetic Pile-Up Boundary of Comet P/Halley', *J. Geophys. Res.* **98**, 20955.

Glassmeier, K. H., and Neubauer, F. M.: 1993, 'Low Frequency Electromagnetic Plasma Waves at Comet P/Grigg-Skjellerup: Overview and Spectral Characteristics', *J. Geophys. Res.* **98**, 20921–20935.

Glassmeier, K.-H., Tsurutani, B. T. and Neubauer, F. M.: 1997, in T. Hada and H. Matsumoto (eds), 'Adventures in Parameter Space, A Comparison of Low-Frequency Plasma Waves at Comets', in: *Nonlinear Waves and Chaos in Space Plasmas* Terra Scientific Publishing Company, Tokyo, 77–119.

Gloeckler, G., et al.: 1992, 'The Solar Wind Ion Composition Spectrometer', *Astron. Astrophys. (Supp.)* **92**, 267.

Gloeckler, G., Geiss, J., Balsiger, H., Fisk, L. A., Galvin, A. B., Ipavich, F. M., Ogilvie, K. W., von Steiger, R. and Wilken, B.: 1993, 'Detection of Interstellar Pickup Hydrogen in the Solar System', *Science* **261**, 70.

Gloeckler, G., Jokipii, J. R., Giacalone, J. and Geiss, J.: 1994, 'Concentration of Interstellar Pickup H^+ and He^+ in the Solar Wind', *Geophys. Res. Lett.* **21**, 1565.

Gloeckler, G., Schwadron, N. A., Fisk, L. A. and Geiss, J.: 1995, 'Weak Pitch Angle Scattering of Few MV Rigidity Ions from Measurements of Anisotropies in the Distribution Function of Interstellar Pickup H^+', *Geophys. Res. Lett.* **22**, 2665.

Gloeckler, G., Fisk, L. A. and Schwadron, N.: 1995, 'Anisotropies of Interstellar Pickup Protons – Implications for Scattering of Low Rigidity (∼1 to 3 MV) Particles', *Geophys. Res. Lett.* **24**, 93 –96.

Gloeckler, G.: 1996, 'The Abundance of Atomic 1H, 4He and 3He in the Local Interstellar Cloud from Pickup Ion Observations with SWICS on Ulysses', *Space Science Reviews* **78**, 1, 335–347.

Gloeckler, G. and Geiss, J.: 1996, *Nature*, **381**, 210.

Gloeckler, G., Fisk, L. A., Geiss, J., Schwadron, N. A. and Zurbuchen, T. H.: 1999, 'An Important New Source for Energetic Particles Accelerated in the Heliosphere', Submitted to *Geophys. Res. Lett.*

Gloeckler, G. and Geiss, J.: 1999, 'Interstellar and Inner Source Pickup Ions Observed with SWICS on Ulysses', in press *Space Science Reviews.*.

Godunov, S. K.: 1972, 'Symmetric Form of the Equations of Magnetohydrodynamics', *Numerical Methods for Mechanics of Continuum Medium* **1**, 26–34.

Goldstein, M. L., Wong, H. K., and Glassmeier, K. H.: 1990, 'Generation of Low Frequency Waves at Comet Halley', *J. Geophys. Res.* **95**, 947.

Goldstein, M. L., Roberts, D. A. and Matthaeus, W. H.: 1995, 'Magnetohydrodynamic Turbulence in the Solar Wind', *Ann. Rev. Astron. Astrophys.* **33**, 283.

Gombosi, T. I., Lorencz, K. and Jokipii, J. R.: 1989, 'Combined First- and Second-Order Fermi Acceleration in Cometary Environments', *J. Geophys. Res.* **94**, 15011.

Gombosi, T. I., Neugebauer, M., Johnstone, A. D., Coates, A. J. and Huddleston, D. E.: 1991, 'Comparison of Observed and Calculated Implanted Ion Distributions Outside Comet Halley's Bow Shock', *J. Geophys. Res.* **96**, 9467.

Gombosi, T. I.: 1994, 'Gaskinetic Theory', Cambridge University Press, Cambridge.

Gombosi, T. I., de Zeeuw, D. L., Häberli, R. M. and Powell, K. G.: 1996, 'Three-Dimensional Multiscale MHD Model of Cometary Plasma Environments', *J. Geophys. Res.* **101**, 15233–15253.

Grebowsky, J. M., Kasprzak, W. T., Hartle, R. E., Majahan, K. K. and Wagner, T. C. G.: 1993, 'Superthermal Ions Detected in Venus' Dayside Ionosheath, Ionopause and Magnetic Barrier Regions', *Journ. Geophys. Res.* **98**, 9055.

Gringauz, K. I. and Verigin, M. I.: 1991, in A. D. Johnstone (ed.), 'Permanent and Nonstationary Plasma Phenomena in Comet Halley's Head', *Geophys. Monograph* **61**, AGU, p. 107.

Gruntman, M.: 1996, 'H_2^+ Pickup Ions in the Solar Wind: Outgassing of Interplanetary Dust', *J. Geophys. Res.* **101**, 15555.

Gurgiolo, C., Parks, G. K., Mauk, B. H., Lin, C. S., Anderson, K. P., Lin, R. P. and Réme, H.: 1981, 'Non-E-B Ordered Ion Beams Upstream of the Earth's Bow Shock', *J. Geophys. Res.* **86**, 4415–4424.

Gurnett, D. A., Anderson, R. R., Häusler, B., Haerendel, G., Bauer, O. H., Treumann, R. A., Koons, H. C., Holzworth, R. H. and Lühr, H.: 1985, 'Plasma Waves Associated with the AMPTE Artificial Comet', *Geophys. Res. Lett.* **12**, 851–854.

Gurnett, D. A., Anderson, R. R., Bernhardt, P. A., Luehr, H., Haerendel, G., Bauer, O. H., Koons, H. C. and Holzworth, R. H.: 1986, 'Plasma Waves Associated with the First AMPTE Magnetotail Barium Release', *Geophys. Res. Lett.* **13**, 644–647.

Gurnett, D. A., T. Z. M. A., Anderson, R. R., Bauer, O. H., Haerendel, G., Häusler, B., Paschmann, G., Treumann, R. A., Koons, H. C., Holzworth, R. and Lühr, H.: 1986, 'Analysis and Interpretation of the Shock-Like Electrostatic Noise Observed During the AMPTE Solar Wind Lithium Releases', *J. Geophys. Res.,* **91**, 1301–1310.

Hada, T., Kennel, C. F., and Terasawa, T.: 1987, 'Excitation of Compressible Waves and the Formation of Shocklets in the Earth's Foreshock', *J. Geophys. Res.* **92**, 4423.

Häberli, R., Altwegg, K., Balsiger, H. and Geiss, J.: 1995, 'Physics and Chemistry of Ions in the Pile-Up Region of Comet P/Halley', *Astron. Astrophys.* **297**, 881.

Haerendel, G.: 1986, 'Künstliche Kometen', *Phys. Bl.* **42**, 134–137.

Haerendel, G., Paschmann, G., Baumjohann, W. and Carlson, C. W.: 1986, 'Dynamics of the AMPTE Artificial Comet', *Nature* **320**, 720–723.

Haerendel, G.: 1987, in A. T. Y. Lui (ed.), 'Tail Exploration and Tail Formation With Artificial Plasma Clouds', in *Magnetotail Physics*, pp. 337–351, The John Hopkins University Press, Baltimore and London.

Hall, D. S., Bryant, D. A., Chaloner, C. P., Bingham, R. and Lepine, D. R.: 1986, 'AMPTE/UKS Electron Measurements During the Lithium Releases of September 11 and 20, 1984', *J. Geophys. Res.* **91**, 1320–1324.

Harold, J. B. and Hassam, A. B.: 1994, 'Two Ion Fluid Numerical Investigations of Solar Wind Gas Releases', *J. Geophys. Res.* **99**, 19, 325–340.

Hartle, R. E., Sittler, E. C. Jr., Ogilvie, K. W., Scudder, J. D., Lazarus, A. J. and Atreya, S. K.: 1982, 'Titan's Ion Exosphere Observed from Voyager 1', *J. Geophys. Res.* **87**, 1382.

Hassam, B. and Huba, J. D.: 1987, 'Structure of the Magnetotail Barium Releases', *Geophys. Res. Lett.* **14**, 60–63.

Häusler, B., et al.: 1986, 'Plasma Wave Observed by the IRM and UKS Spacecraft During the AMPTE Solar Wind Lithium Releases: Overview', *J. Geophys. Res.* **91**, 1283–1299.

Hill, T. W., Dessler, A. J. and Goertz, C. K.: 1983, in A. J. Dessler (ed.), 'Magnetospheric Models', in Physics of the Jovian Magnetosphere, Cambridge University Press, Cambridge, p. 353.

Holzer, T. E.: 1972, 'Interaction of the Solar Wind with the Neutral Component of the Interstellar Gas', *J. Geophys. Res.* **77**, 5407.

Holzer, T. E. and Leer, E.: 1973, 'Solar Wind Heating Beyond 1 AU', *Astrophys. Space Sci.* **24**, 335.

Holzer, T. E.: 1989, 'Interaction Between the Solar Wind and the Interstellar Medium', *Ann. Rev. Astron. Astrophys.* **27**, 129.

Hoshino, M. and Terasawa, T.: 1985, 'Numerical Study of the Upstream Wave Excitation Mechanism, 1, Nonlinear Phase Bunching of Beam Ions', *J. Geophys. Res.* **90**, 57–64.

Hoshino, M.: 1987, 'Evolution of Polarization in Localized Nonlinear Alfvén Waves', *Phys. Rev. Lett.* **59**, 2639–2642.

Huba, J. D., Lyon, J. G. and Hassam, A. B.: 1987, 'Theory and Simulation of the Rayleigh Taylor Instability in the Limit of Large Larmor Radius', *Phys. Res. Lett* **59**, 2971–2974.

Huba, J. D.: 1993, 'Generation of Waves in the Venus Mantle by Ion Acoustic Beam Instability', *Geophys. Res. Lett.* **20**, 1751.

Huba, J. D. and Strangeway, R. J.: 1997, in S. W. Bougher, D. M. Hunten, and R. J. Phillips (eds), 'Plasma Wave Phenomena at Venus, in Venus II – Geology, Geophysics, Atmosphere, and Solar Wind Environment', University of Arizona Press, Tucson, p. 95.

Huddleston, D. E., Johnstone, A. D. and Coates, A. J.: 1990, 'Determination of Comet Halley Gas Emission Characteristics From Mass Loading of the Solar Wind', *J. Geophys. Res.* **95**, 21.

Huddleston, D. E. and Johnstone, A. D.: 1992, 'Relationship Between Wave Energy and Free Energy from Pickup Ions in the Comet Halley Environment', *J. Geophys. Res.* **97**, 12217–12230.

Huddleston, D. E., Coates, A. J., Johnstone, A. D., and Neubauer, F. M.: 1993, 'Mass Loading and Velocity Diffusion Models for Heavy Pickup Ions at Comet Grigg-Skjellerup', *J. Geophys. Res.* **98**, 20995.

Huddleston, D. E., Strangeway, R. J., Warnecke, J., Russell, C. T. and Kivelson, M. G.: 1998, 'Ion Cyclotron Waves in the Io Torus: Wave Dispersion, Free Energy Analysis, and $SO2^{+}$ Source Rate Estimates', *J. Geophys. Res.* **103**, 19, 997.

Hunten, D. M., Tomasko, M. G., Flasar, F. M., Samuelson, R. E., Strobel, D. F. and Stevenson, D. J.: 1984, in T. Gehrels and M. S. Matthews (eds), 'Titan', in *Saturn* University of Arizona Press, Tucson, p. 671.

Ip, W.-H. and Axford, W. I.: 1982, in L. L. Wilkening (ed.), 'Theories of Physical Processes in the Cometary Comae and Ion Tails', in *Comets*, University of Arizona Press, Tuscon, Arizona, pp. 588–634.

Ip, W.-H.: 1988, 'On a Hot Oxygen Corona at Mars', *Icarus* **76**, 135.

Ip, W.-H. and Axford, W. I.: 1990, in W. F. Huebner (ed.), 'The plasma', in *Physics and chemistry of comets*, Springer-Verlag, Berlin, pp. 177–233.

Isenberg, P. A.: 1986, 'Interaction of the Solar Wind with Interstellar Neutral Hydrogen: Three-Fluid Model', *J. Geophys. Res.* **91**, 9965.

Isenberg, P. A.: 1997, 'A Weaker Solar Wind Termination Shock', *Geophys. Res. Lett.* **24**, 623.

Isenberg, P. A.: 1999, in S. R. Habbal, R. Esser, J. V. Hollweg and P. A. Isenberg (eds), 'Interstellar Pickup Ions in the Solar Wind', in Solar Wind Nine, p. 189, AIP, Woodbury, NY.

Isenberg, P. A. and Jokipii, J. R.: 1979, 'Gradient and Curvature Drifts in Magnetic Fields with Arbitrary Spatial Variation', *Astrophys. J.* **234**, 746.

Isenberg, P. A.: 1987, 'Energy Diffusion of Pickup Ions Upstream of Comets', *J. Geophys. Res.* **97**, 8795.

Isenberg, P. A. and Lee, M. A.: 1996, 'A Dispersive Analysis of Bispherical Pickup Ion Distributions', *J. Geophys. Res.* **101**, 11055.

Isenberg, P. A.: 1996, in D. Winterhalter, J. T. Gosling, S. R. Habbal, W. S. Kurth, and M. Neugebauer (eds), 'Effects of Spatial Transport and Ambient Wave Intensity on the Generation of MHD Waves by Interstellar Pickup Protons, in *Solar Wind Eight*, p. 626, AIP, Woodbury, New York.

Isenberg, P. A.: 1997, 'A Hemispherical Model of Anisotropic Interstellar Pickup Ions', *J. Geophys. Res.* **102**, 4719.

Isenberg, P. A. and Möbius, E.: 1998, 'Are Interstellar Pickup Ion Distributions Really Hemispherical?', *EOS Trans. AGU* **79**(17), Spring Meet. Suppl., p. 294.

Isenberg, P. A. and Lee, M. A.: 1998, 'Transport of Anisotropic Interstellar Pickup Ions on Bent Flux Tubes', *J. Geophys. Res.* **103**, 12, 037.

Isenberg, P. A. and Lee, M. A.: 1999, in S. R. Habbal, et al. (eds.), 'Solar Wind Speed Dependence of Pickup Ion Fluxes by Cross-Field Diffusion', *Solar Wind Nine*, In Press, AIP, Woodbury, NY.

Israelevitch, P. L., Neubauer, F. M. and Ershkovich, A. I.: 1994, 'The Induced Magnetoshpere of Comet Halley: Interplanetary Magnetic Field During Giotto Encounter', *J. Geophys. Res.* **99**, 6575–6584.

Jackson, J. D.: 1975, 'Classical Electrodynamics', John Wiley and Sons, New York.

Jockers, K. and Bonev, T.: 1997, 'H_2O^+, CO^+, and Dust in Comet P/Swift-Tuttle', *Astron. Astrophys.* **319**, 617–629.

Johnson, R. E.: 1990, 'Energetic Charged-Particle Interactions with Atmospheres and Surfaces', Springer-Verlag, Berlin.

Johnstone, A. D., et al.: 1986, *Nature* **321**, 344–347.

Johnstone, A. D., et al.: 'Waves in the Magnetic Field and Solar Wind Flow Outside the Bow Shock at Comet Halley', *Astron. Astrophys.* **187**, 47–54.

Johnstone, A. D., Huddleston, D. E. and Coates, A. J.: 1991, in A. D. Johnstone (ed.), *Cometary Plasma Processes*, *Geophys. Monogr. Ser.* **61**, p. 259, AGU, Washington, D.C.

Johnstone, A. D., Coates, A. J., Huddleston, D. E., Jockers, K., Wilken, B., Borg, H., Gurgiolo, C., Winningham, J. D. and Amata, E.: 1993, 'Observations of the Solar Wind and Cometary Ions During the Encounter Between Giotto and Comet P/Grigg-Skjellerup', *Astron. Astrophys.* **273**, L1–L4.

Jokipii, J., Giacalone, J. and Geiss, J.: 1994, 'Concentration of Interstellar Pickup H and He in the Solar Wind', *Geophys. Res. Lett.* **21**, 1565.

Jones, G. H. and Coates, A. J.: 1997, *Adv. Space Res.* **20**, 271–274.

Judge, D., McMullin, D. R., Ogawa, H. S., Hovestadt, D., Klecker, B., Hilchenbach, M., Möbius, E., Canfield, L. R., Vest, R. E., Watts, R., Tarrio, C., Kühne, M. and Wurz, P.: 1997, 'First Solar EUV Irradiances Obtained from SOHO by the CELIAS/SEM', *Solar Physics* **177**, 161–173.

Kallio, E., Luhmann, J. G. and Barabash, S.: 1997, 'Charge Exchange Near Mars: The Solar Wind Absorption and Energetic Neutral Atom Production', *J. Geophys. Res.* **102**, 22183.

Kallio, E. and Koskinen, H.: 1999, 'A Test Particle Simulation of the Motion of Oxygen Ions and Solar Wind Protons Near Mars', *Journ. Geophys. Res.* **104**, p. 557.

Kantrowitz, A. R. and Petschek, H. E.: 1966, in W. B. Kunkel (ed.), 'MHD Characteristics and Shock Waves', *Plasma Physics in Theory and Application*, McGraw-Hill, New York.

Kecskemety, K. and Cravens, T. E.: 1993, 'Pick-Up Ions at Pluto', *Geophys. Res. Lett.* **20**, 543.

Keller, C. N. and Cravens, T. E.: 1994, 'One-Dimensional Multispecies Hydrodynamic Models of the Wakeside Ionosphere of Titan', *J. Geophys. Res.* **99**, 6527.

Kennel, C. F. and Engelmann, F.: 1966, 'Velocity Space Diffusion from Weak Plasma Turbulence in a Magnetic Field', *Phys. Fluids* **9**, 2377.

Kessel, R. L., Coates, A. J., Motschmann, U. and Neubauer, F. M.: 1994, 'Shock Normal Determination for Multiple-Ion Shocks', *J. Geophys. Res.* **99**, 19, 359.

Khabibrakhmanov, I. Kh. and Zank, G. P.: 1993, in T. I. Gombosi (ed.), 'Critical Problems in the Plasma Environments of Comets and other Non-Magnetized and Weakly Magnetized Bodies', *COSPAR Colloq.* **4**, 105, Pergamon, New York.

Kim, J., Nagy, A. F., Fox, J. L. and Cravens, T. E.: 1998, 'Solar Cycle Variation of Hot Oxygen Atoms at Mars', *J. Geophys. Res.*, **103**, 29339.

Kintner, P. M., Vago, J., Chesney, S. et al.: 1992, *Phys. Rev. Lett.* **68**, 2448.

Kivelson, M. G., Wang, Z., Joy, S., Khurana, K. K., Polanskey, C., Southwood, D. J. and Walker, R. J.: 1995, 'Solar Wind Interaction with Small Bodies: 2. What can Galileo's Detection of Magnetic Rotations tell us about Gaspra and Ida', *Adv. Space Res.* **16**, 59–68.

Kivelson, M. G., Khurana, K. K., Walker, R. J., Wernecke, J., Russell, C. T., Linker, J. A., Soothwood, D. J. and Polansky, C.: 1996, 'Io's Interaction with the Plasma Torus: Galileo Magnetometer Report', *Science* **274**, 396.

Klimov, S., Savin, S., Aleksevich, Y. et al.: 1986, 'Extremely Low Frequency Plasma Waves in the Environment of Comet Halley.', *Nature* **321**, 292.

Kliore, A. J., Hinson, D. P., Flasar, F. M., Nagy, A. F. and Cravens, T. E.: 1997, 'The Ionosphere of Europa from Galileo Radio Occultations', *Science* **277**, 355.

Klöcker, N, Lühr, H., Southwood, D. J. and Acuña, M.: 1988, 'Magnetic ULF Fluctuations in the Compressional Zone of AMPTE's Artificial Comets', *Adv. Space Res.* **8**, 23–26.

Kotelnikov, A. D., Poluydov, A. N., Malkov, M. A., Sagdeev, R. Z. and Shapiro, V. D.: 1991, 'High Amplitude Magnetosonic Waves in the Upstream Region of the Cometary Bow-Shock', *Astron. and Astrophysics* **243**, 546.

Kotova, G. A., Verigin, M. I., Shutte, N. M., Remizov, A. P., Rosenbauer, H., Riedler, W., Schwingenschuh, K., Delva, M., Szegö, K. and Tatrallyay, M.: 1997, 'Planetary Heavy Ions in the Magnetotail of Mars: Results of the TAUS and MAGMA Experiments Aboard Phobos', *Adv. Space Res.* **20**, 173.

Kulsrud, R. M.: 1983, in A. A. Galeev and R. N. Sudan (eds), 'MHD Description of Plasma', *Basic Plasma Physics I*, p. 115–145, North-Holland, New York.

Lagg, A., Krupp, N., Woch, J., Livi, S., Wilken, B. and Williams, D. J.: 1998, 'Determination of the Neutral Number Density in the Io Torus from Galileo-EPD Measurements', *Geophys. Res. Lett.* **21**, 4039.

Lammer, H. and Bauer, S. J.: 1991, 'Nonthermal Atmospheric Escape from Mars and Titan', *J. Geophys. Res.* **96**, 1819.

Law, C. C. and Cloutier, P. A.: 1997, 'Currents and Magnetic Field Structures in the Dayside Solar Wind Interaction with Venus', *J. Geophys. Res.* **102**, 22, 199.

Lax, P. D.: 1973, 'Hyperbolic Systems of Conservation Laws and the Mathematical Theory of Shock Waves', *Reg. Conf. Ser. Appl. Math.* **SIAM**, Philadelphia, Pa.

Ledvina, S. A. and Cravens, T. E.: 1998, 'A Three-Dimensional MHD Model of Plasma Flow Around Titan', *Planet. Space Sci.* **46**, 1175.

Ledvina, S. A., Cravens, T. E., Salman, A. and Kecskemety, K.: 1998, 'Ion Trajectories in Saturn's Magnetosphere Near Titan', *Nagoya COSPAR Proceedings* submitted.

Lee, M. A.: 1971, 'Self-Consistent Kinetic Equations and the Evolution of a Relativistic Plasma in an Ambient Magnetic Field', *Plasma Phys.* **13**, 1079.

Lee, M. A. and Ip, W.-H.: 1987, 'Hydromagnetic Wave Excitation by Ionized Interstellar Hydrogen and Helium in the Solar Wind', *J. Geophys. Res.* **92**, 11, 041.

Lee, M. A.: 1989, in B. T. Tsurutani and H. Oya (eds), 'Ultra-Low Frequency Waves at Comets', *Plasma Waves and Instabilities at Comets and in Magnetospheres*, pp. 13–29, *Geophys. Monogr. Ser.*, Vol. 53, Washington D.C..

Lee, M. A. and Gary, S. P.: 1991, 'Quasi-Linear Evolution of ULF Waves Excited by Cometary Ion Pickup', *J. Geophys. Res.* **96**, 21319–21327.

Lee, M. A., Shapiro, V. D. and Sagdeev, R. Z.: 1996, 'Pickup Ions Energization by Shock Surfing', *J. Geophys. Res.* **101**, 4777.

Lee, M. A.: 1997, in J. R. Jokipii, C. P. Sonett, and M. S. Giampapa (eds), 'Effects of Cosmic Rays and the Interstellar Gas on the Dynamics of the Solar Wind', *Cosmic Winds and the Heliosphere*, p. 857, University of Arizona, Tucson.

Levine, R. H., Altschuler, M. D. and Harvey, J. W.: 1977, 'Solar Sources of the Interplanetary Magnetic field and Solar Wind', *J. Geophys. Res.* **82**, 1061.

Lichtenegger, H., Dubinin, E. and Ip, W.-H: 1997, 'The Depletion of the Solar Wind Near Mars', *Adv. Space Res.* **20**, 143.

Linker, J. A., Kivelson, M. G. and Walker, R. J.: 1991, 'A Three-Dimensional MHD Simulation of Plasma Flow Past Io', *J. Geophys. Res.* **96**, 21037.

Linsky, J.: 1996, 'GHRS Observations of the LISM', *Space Sci. Rev.* **78**, 157–164.

Lisse, S. M., Dennerel, K., Englhauser, J. et al.: 1996, 'Discovery of X-Ray and Extreme Ultra-Violet Emission from Comet C/Hyakutake 1996 B2', *Science* **274**, 205.

Luhmann, J. G. and Cravens, T. E.: 1991, 'Magnetic Fields in the Ionosphere of Venus', *Space Sci. Rev.* **55**, 201.

Luhmann, J. G.: 1992, in J. G. Luhmann, M. Tatrallyay, and R. O. Pepin (eds), 'The Solar Wind Interaction with Unmagnetized Planets: A Tutorial, in Venus and Mars: Atmospheres, Ionospheres, and Solar Wind Interactions', *Geophys. Monog. Ser.* **66**, AGU, Washington, D. C., p. 401.

Luhmann, J. G.: 1996, 'Titan's Ions Exospheric Wake: A Natural Ion Mass Spectrometer?', *J. Geophys. Res.-Planets* **101**, 29387.

Luhmann, J. G., Brecht, S. H., Spreiter, J. R., Stahara, S. S., Steinolfson, R. S. and Nagy, A. F.: 1997, in S. W. Bougher, D. M. Hunten, and R. J. Phillips (eds), 'Global Models of the Solar Wind Interaction with Venus', *in Venus II – Geology, Geophysics, Atmosphere, and Solar Wind Environment*, University of Arizona Press, Tucson, p. 33.

Lundin, R., et al.: 1989, 'First Measurements of the Ionospheric Plasma Escape from Mars', *Nature* **341**, 609.

Lundin, R., et al.: 1990, 'Plasma Composition Measurements of the Martian Magnetosphere Morphology', *Geophys. Res. Lett.* **17**, 877.

Lundin, R., Zacharov, A., Pellinen, R., Barabash, S. V., Borg, H., Dubinin, E., Hultqvist, B., Koskinen, H., Liede, I. and Pissarenko, M.: 1990, 'ASPERA/Phobos Measurements of the Ion Outflow from the Martian Ionosphere', *Geophys. Res. Lett.* **17**, 873.

Lühr, H., Southwood, D. J., Klöcher, N., Acuña, M., Háusler, B., Dunlop, M. W., Mier-Jedrzejowicz, W. A. C., Rijnbeek, R. P. and Six, M.: 1986, 'In Situ Magnetic Field Measurements during AMPTE Solar Wind Li^+ Release', *J. Geophys. Res.* **91**, 1261–1270.

Lühr, H., Southwood, D. J., Klöcher, N., Dunlop, M. W., Mier-Jedrzejowicz, W. A. C., Rijnbeek, R. P., Six, M., Háusler, B. and Acuña, M.: 1986, 'In Situ Magnetic Field Observations of the AMPTE Artificial Comet', *Nature* **320**, (6064), 708–711.

Lüst, R.: 1967, 'Bewegung von Strukturen in der Koma und im Schweif des Kometen Morehouse', *Zeitschrift für Astrophysik* **65**, 236–250.

Lui, A. T. Y.: 1989, 'Collisionless Coupling Processes in AMPTE Releases', *Physics of Space Plasmas* SPI Conference Proceedings and Reprint Series, No. 9, 227–299.

Mann, G.: 1996, 'On Simple Magnetohydrodynamic Waves', *J. Plasm. Phys.* in press.

Marsch, E. and Mangeney, A.: 1987, 'Ideal MHD Equations in Terms of Compressive Elsässer Variables', *J. Geophys. Res.* **92**, 7363.

Marsch, E.: 1995, 'Analysis of MHD Turbulence: Spectra of Ideal Invariants, Structure Functions and Intermittence Scalings', *Proc. of the CLUSTER Workshop on Data Analysis Tools* Braunschweig, **ESA SP 371**, 107–118.

Matsumoto, H. and Usui, H.: 1997, 'Intense Bursts of Electron Cyclotron Harmonic Waves Near the Dayside Magnetopause Observed by GEOTAIL', *Geophys. Res. Lett.* **24**, 49–52.

Matthaeus, W. H. and Goldstein, M. L.: 1982, 'Measurements of the Rugged Invariants of Magnetohydromagnetic Turbulence in the Solar Wind', *J. Geophys. Res.* **87**, 6011–6028.

Mazelle, C., Rème, H., Sauvand, J. A., d'Uston, C., Carlson, C. W., Anderson, K. A., Curtis, D. W., Lin, R. P., Korth, A., Mendis, D. A., Neubauer, F. M., Glassmeier, K. H. and Raeder, J.: 1989, 'Analysis of Suprathermal Electron Properties at the Magnetic Pile-Up Boundary of Comet P/Halley', *Geophys. Res. Lett.* **16**, 1035–1038.

Mazelle, C., Belmont, G., Lu Quéau, D., Glassmeier, K. H., and Rème, H.: 1991, 'Ultra Low Frequency Waves at the Magnetic Pile-Up Boundary of Comet P/Halley', *Adv. Space Res.* **11**, (9)73–(9)77.

Mazelle, C. and Neubauer, F. M.: 1993, 'Discrete Wave Packets at the Proton Cyclotron Frequency at Comet P/Halley', *Geophys. Res. Lett.* **20**, 153–156.

Mazelle, C., Réme, H., Neubauer, F. M. and Glassmeier, K.-H.: 1994, *Adv. Space Res.*

Mazelle, C., Rème, H., Neubauer, F. M. and Glassmeier, K. H.: 1995, 'Comparison of the Main Magnetic and Plasma Features in the Environments of Comet Grigg-Skjellerup and Halley', *Adv. Space Res.* **16**, 41–45.

Mazelle, C., Cao, J. B., Belmont, G., Neubauer, F. M. and Coates, A. J.: 1997, 'Compressive Character of Low Frequency Waves Driven by Newborn Ions at Comet Grigg-Skjellerup', *Adv. Spcae Rex.* **20**, 267–270.

McKean, M. E., Winske, D. and Gary, S. P.: 1992, 'Kinetic Properties of Mirror Waves in Magnetosheath Plasmas', *Geophys. Res. Lett.* **19**, 1331–1334.

McKenna-Lawlor, S. M. P., Afonin, V. V., Kirsch, E., Schwingenschuh, K., Slavin, J. A. and Trotignon, J. G.: 1998, 'An Overview of Energetic Particles (from 55 keV to >30 MeV) Recorded in the Close Martian Environment, and Their Energization in Local and External Processes', *Planet. Space Sci.* **46**, 83.

McKenna-Lawlor, S., Kirsch, E., O'Sullivan, D., Thompson, A. and Wenzel, K.-P., 'Energetic ions'.

McKenzie, J., Marsch, E., Baumgärtel, K. and Sauer, K.: 1993, *Ann. Geophysicae* **11**, 341.

Mendis, D. A., Houpis, H. L. F. and Marconi, M. L.: 1985, 'The Physics of Comets', *Fundamentals of cosmic physics* **10**, 1–380.

Moore, K. R., Thomas, V. A. and McComas, D. J.: 1991, 'Global Hybrid Simulation of the Solar Wind Interaction with the Dayside of Venus', *J. Geophys. Res.* **96**, 7779.

Moore, K. R. and McComas, D. J.: 1992, in J. G. Luhmann, M. Tatrallyay, and R. O. Pepin (eds), 'A Synthesis of Measured and Deduced Properties of Pickup Ions in the Venus-Solar Wind Interaction', in: *Venus and Mars: Atmospheres, Ionospheres, and Solar Wind interactions Geophys. Monograph*, **65**, p. 405, AGU.

Motschmann, U., Sauer, K., Roatsch, T. and McKenzie, J. F.: 1991, 'Subcritical Multiple-Ion Shocks', *J. Geophys. Res.* **96**, 13841–13848.

Motschmann, U. and Glassmeier, K. H.: 1993, 'Nongyrotropic Distribution of Pickup Ions at Comet P/Grigg-Skjellerup: A Possible Source of Wave Activity', *J. Geophys. Res.* **98**, 20977–20983.

Motschmann, U. and Glassmeier, K.-H.: 1997, 'Concerning Nongyrotropic Particle Distributions and Magnetic Field Reconnection', *AGU Fall Meeting*, San Francisco, December.

Motschmann, U., Kafemann, H. and Scholer, M.: 1997, 'Nongyrotropy in Magnetoplasmas: Simulation of Wave Excitation and Phase Space Diffusion', *Ann. Geophysicae* **15**, 603–613.

Motschmann, U. and Glassmeier, K. H.: 1998, 'Dispersion and Wave Excitation in Nongyrotropic Plasmas', *J. Plasma Phys* **60**, 111–132.

Motschmann, U. and Glassmeier, K. H.: 1998, 'Relation of Magnetic Field Line Reconnection and Unstable Nongyrotropic Particle Distributions', *Proc. Int. Conf. on Substorms-4*, Lake Hamana, Japan, in press.

Motschmann, U., Glassmeier, K. H. and Brinca, A. L.: 1998, 'Nongyrotropic Distribution Functions in Space Plasmas', *Annales Geophysicae*, in press.

Möbius, E., Hovestadt, D., Klecker, B., Scholer, M., Gloeckler, G. and Ipavich, F. M.: 1985a, 'Direct Observation of He^+ Pickup Ions of Interstellar Origin in the Solar Wind', *Nature* **318**, 426.

Möbius, E., Gloeckler, G., Hovestadt, D., Ipavich, F. M., Klecker, B., Scholer, M., Arbinger, H., Höfner, H., Kenneth, E., Laeverenz, P., Luhn, A., Tums, E. O. and Waldleben, H.: 1985b, The Time-of-Flight Spectrometer SULEICA for Ions of the Energy Range 5270 keV/Charge on the AMPTE IRM, *IEEE Trans. Geosci. Remote Sens.* **GE-23** 274.

Möbius, E., Hovestadt, D., Klecker, B., Scholer, M., Gloeckler, G., Ipavich, F. M. and Lühr, H.: 1986, 'Observation of Lithium Pickup Ions in the 5 to 20 keV Energy Range Following the AMPTE Solar Wind Releases', *J. Geophys. Res.* **91**, 1325–1332.

Möbius, E., Klecker, B., Hovestadt, D. and Scholer, M.: 1988, 'Interaction of Interstellar Pickup Ions with the Solar Wind', *Astrophys. Space Sci.* **144**, 487.

Möbius, E., Rucinski, D., Hovestadt, D. and Klecker, B.: 1995, 'The Helium Parameters of the Very Local Interstellar Medium as Derived from the Distribution of He^+ Pickup Ions in the Solar Wind', *Astron. Astrophys.* **304**, 505–519.

Möbius, E.: 1996, 'The Local Interstellar Medium Viewed Through Pickup Ions, Recent Results and Future Perspectives', *Space Sc. Rev.* **78**, 375–386.

Möbius, E., Rucinski, D., Isenberg, P. A. and Lee, M. A.: 1996, 'Determination of Interstellar Pickup Ion Distributions in the Solar Wind with SOHO and Cluster', *Ann Geophys.* **14**, 492.

Möbius, E., Rucinski, D., Lee, M. A. and Isenberg, P. A.: 1998, 'Decreases in the Antisunward Flux of Interstellar Pickup He^+ Associated with Radial Interplanetary Magnetic Field', *J. Geophys. Res.* **103**, 257.

Murawski, K. and Steinolfson, R. S.: 1996, 'Numerical Modeling of the Solar Wind Interaction with Venus', *J. Geophys. Res.* **101**, 2547.

Murphy, N., Smith, E. J., Tsurutani, B. T., Balogh, A. and Southwood, D. J.: 1995, 'Further Studies of Waves Accompanying the Solar Wind Pickup of Interstellar Hydrogen', *Space Sci. Rev.* **72**, 447.

Nagy, A. F. and Cravens, T. E.: 1988, 'Hot Oxygen Atoms in the Upper Atmospheres of Venus and Mars', *J. Geophys. Res.* **15**, 443.

Nagy, A. F., Gombosi, T. I., Szegö, K., Sagdeev, R. Z., Shapiro, V. D., and Shevchenko, V. I.: 1990, 'Venus Mantle – Mars Planetosphere: What are the Similarities and Differences?', *Geophys. Res. Lett.* **17**, 865.

Nagy, A. F., Kim, J. and Cravens, T. E.: 1990, 'Hot Hydrogen and Oxygen Atoms in the Upper Atmospheres of Venus and Mars', *Annales Geophysicae* **8**, 251.

Neubauer, F. M., Gurnett, D. A., Scudder, J. D. and Hartle, R. E.: 1984, in T. Gehrels and M. S. Matthews (eds), 'Titan's Magnetospheric Interaction', *Saturn*, University of Arizona Press, Tucson, p. 760.

Neubauer, F. M., Glassmeier, K. H., Pohl, M., Raeder, J., Acuña, M. H., Burluga, L. F., Ness, N. F., Musmann, G., Mariani, F., Wallis, M. K., Ungstrup, E. and Schmidt, H. U.: 1986, 'First Results from Giotto Magnetometer Experiment at Comet Halley', *Nature* **321**, 352–355.

Neubauer, F. M.: 1987, 'Giotto Magnetic-Field Results on the Boundary of the Pile-Up Region and the Magnetic Cavity', *Astron. Astrophys.* **187**, 73–79.

Neubauer, F. M., Glassmeier, K.-H., Acuña, M. H., Mariani, F., Ness, N. F. and Coates, A. J.: 1990, *Ann. Geophys.* **8**, 463.

Neubauer, F. M.: 1991, in R. L. Newburn et al. (eds), 'Magnetic Fields at Comet P/Halley', *Comets in the Post-Halley Era*, **vol. 2**, pp. 1107–1124, Kluwer Academic Publishers, Hingham, Mass.

Neubauer, F. M., Glassmeier, K. H., Coates, A. J. and Johnstone, A. D.: 1993, 'Low Frequency Electromagnetic Plasma Wave Fields at Comet P/Grigg-Skjellerup: Analysis and Interpretation', *J. Geophys. Res.* **98**, 20937–20954.

Neubauer, F. M., Marshall, H., Pohl, M., Glassmeier, K. H., Musmann, G., Mariani, F., Acuña, M. H., Burluga, L. F., Ness, N. F., Wallis, M. K., Schmidt, H. U. and Ungstrup, E.: 1993, 'First Results from the Giotto Magnetometer Experiment During the P/Grigg-Skjellerup Encounter', *Astron. Astrophys.* **268**, L5–L8.

Neugebauer, M. A., Lazarus, A. J., Balsiger, H., Fuselier, S. A., Neubauer, F. M. and Rosenbauer, H.: 1989, 'The Velocity Distribution of Cometary Protons Picked Up by the Solar Wind', *J. Geophys. Res.* **94**, 5277.

Neugebauer, M.: 1990, 'Spacecraft Observations of the Interaction of Active Comets with the Solar Wind', *Rev. Geophys.* **28**, 231.

Neugebauer, M. et al.: 1991, 'Densities and Abundances of Hot Cometary Ions on the Coma of P/Halley', *Astrophys. Journal* **372**, 291–300.

Niemann, H. B. and Kasprzak, W. T.: 1992, 'Superthermal Ions Observed by the Pioneer Venus Orbiter Neutral Mass Spectrometer (ONMS) Revisited', *Eos Trans. AGU*, 189.

Omidi, N. and Winske, D.: 1987, 'A Kinetic Study of Solar Wind Mass Loading and Cometary Bow Shocks', *J. Geophys. Res.* **92**, 13409.

Omidi, N. and Winske, D.: 1990, 'Steepening of Kinetic Magnetosonic Waves into Shocklets: Simulations and Consequences for Planetary Shocks and Comets', *J. Geophys. Res.* **95**, 2281–2300.

Palmer, I. D.: 1982, 'Transport Coefficients of Low-Energy Cosmic Rays in Interplanetary Space', *Rev. Geophys.* **20**, 335.

Papadopoulos,K., Huba, J. D. and Lui, A. T. Y.: 1987, 'Collisionless Coupling in the AMPTE Artificial Comet', *J. Geophys. Res.* **92**, 47–54.

Parker, E. N.: 1958, 'Dynamics of the Interplanetary Gas and Magnetic Elds', *Astrophys. J.* **128**, 664.

Perez-de-Tejada: 1998, 'Rarified Plasma Fluxes', *Adv. Space Res.* in press.

Powell, K. G.: 1994, 'An Approximate Riemann Solver for Magnetohydrodynamics (That Works in More than One Dimension)', Tech. Rep. 94-24, ICASE, Langley, VA.

Powell, K. G., Roe, P. L., Linde, T. J., Gombosi, T. I. and De Zeeuw, D. L.: 1999, 'A Solution-Adaptive Upwind Scheme for Ideal Magnetohydrodynamics', *J. Comput. Phys.*, submitted.

Puhl, P., Cravens, T. E. and Lindgren, J.: 1993, 'Ion Thermalization in the Inner Coma of a Comet', *Astrophys. J.* **418**, 899.

Quest, K. B. and Shapiro, V. D.: 1996, 'Evolution of the Firehose Instability: Linear Theory and Wave-Wave Coupling', *J. Geophys. Res.* **101**, 24457.

Quest, K. B., Shapiro, V. D., Szegö, K. and Dobe, Z.: 1997, 'Microphysics of the Venusian and Martian Mantles', *Geophys. Res. Lett.* **24**, 301–304.

Rème, H., Sauvard, J. A., d'Uston, C., Cotin, F., Cros, A., Anderson, K. A., Carlson, C. W., Curtis, D. W., Lin, R. P., Mendis, D. A., Korth, A. and Richter, A. K.: 1986, 'Comet Halley-Solar Wind Interaction from Electron Measurements Aboard Giotto', *Nature* **321**, 349–352.

Rème, H., Sauvard, J. A., d'Uston, C., Cros, A., Anderson, K. A., Carlson, C. W., Curtis, D. W., Lin, R. P., Korth, A., Richter, A. K. and Mendis, D. A.: 1987, 'General Features of Comet P/Halley: Solar Wind Interaction from Plasma Measurements', *Astron. Astrophys.* **187**, 33–38.

Rème, H.: 1991, in A. D. Johnstone (ed.), 'Cometary Plasma Observations Between the Shock and the Contact Surface', *Cometary Plasma Processes*, *Geophys. Monogr. Ser.*, Vol. 61, pp. 87–105, AGU, Washington, D.C.

Rème, H., Mazelle, C., Sauvaud, J. A., d'Uston, C., Froment, F., Lin, R. P., Anderson, K. A., Larson, D. E., Korth, A., Chaisy, P. and Mendis, D. A.: 1993, 'Electron Plasma Environment at Comet Grigg-Skjellerup: General Observations and Comparison with the Environment at Comet Halley', *J. Geophys. Res.* **98**, 20965.

Richardson, J. D., Paularena, K. I., Lazarus, A. J. and Belcher, J. W.: 1995, 'Evidence for a Solar Wind Slowdonw in the Outer Heliosphere?', *Geophys. Res. Lett.* **22**, 1469–1472.

Rieck, E., Tums, O., von Steiger, R., Weiss, W. and Wilken, B.: 1992, 'The Solar Wind Ion Composition Spectrometer', *Astron. Astrophys. Suppl. Ser.* **92**, 267.

Riedler, W., et al.: 1986, 'Magnetic Fields Observations in Comet Halley's Coma', *Nature* **321**, 288–289.

Rivas, D. R. and Hastings, D. E.: 1992, 'Theoretical Interpretation of the Electrostatic Waves in the Space Shuttle Induced Plasma Environment', *J. Geophys. Res.* **97**, 17097–17113.

Roberts, D. A. and Goldstein, M. L.: 1991, 'Turbulence and Waves in the Solar Wind', *Rev. Geophys., Suppl.* **29**, 373–415.

Roboz, A. and Nagy, A. F.: 1994, 'The Energetics of Titan's Ionosphere', *J. Geophys. Res.* **99**, 2087.

Rodgers, D. J., Coates, A. J., Johnstone, A. D., Smith, M. F., Bryant, D. A., Hall, D. S. and Chaloner, C. P.: 1986, 'UKS Plasma Measurements Near the AMPTE Artificial Comet', *Nature* **320**, (6064), 712–716.

Romeiras, F. J. and Brinca, A. L.: 1999, 'On the Stability of Perpendicular Electrostatic Modes in Stationary Nongyrotropic Plasmas', *J. Geophys. Res* in press.

Rosenbauer, H., Shutte, N., Apathy, I., Galeev, A., Gringauz, K., Grünwaldt, H., Hemmerich, P., Jockers, K., Kiraly, P., Kotova, G., Livi, S., Marsch, E., Richter, A. K., Riedler, W., Remizov, T., Schwenn, R., Schwingenschuh, K., Steller, M., Szegö, K., Verigin, M. and Witte, M.: 1989, 'Ions of Martian Origin and Plasma Sheet in the Martian Magnetosphere: Initial Results of the TAUS Experiment', *Nature* **341**, 612.

Rosenbluth, M. N. and Post, R. F.: 1965, 'High-Frequency Electrostatic Plasma Instability Inherent to Loss-Cone Particle Distributions', *Phys. Fluids* **8**, 457.

Rowlands, J., Shapiro, V. D. and Shevchenko, V. I.: 1966, 'Quasilinear Theory of Plasma Cyclotron Instability', *Sov. Phys. JETP* Engl. Transl. 23, 651.

Rucinski, D. and Fahr, H. J.: 1989, 'The Influence of Electron Impact Ionization on the Distribution of Interstellar Helium in the Inner Heliosphere; Possible Consequences for Determination of Interstellar Helium Parameters', *Astron. Astrophys.* **224**, 290.

Rucinski, D., Cummings, A., Gloeckler, G., Lazarus, A., Möbius, E. and Witte, M.: 1996, 'Ionization Processes in the Heliosphere – Rates and Methods of Their Determination', *Space Sci. Rev.* **78**, 73–84.

Russell, C. T., Childers, D. D. and Coleman, P. J.: 1971, 'Ogo 5 Observations of Upstream Waves in the Interplanetary Medium: Discrete Wave Packets', *J. Geophys. Res.* **76**, 865.

Russell, C. T., et al.: 1990, *Geophys. Res. Lett.* **17**, 897.

Sagdeev, R. Z. and Vedenov, A. A.: 1959, in M. A. Leontovich (ed.), 'About Certain Properties of a Plasma with the Anisotropic Velocity Distribution in Magnetic Field', in *Plasma Physics and Controlled Thermonuclear Reactions* Vol. 3, p. 287, Tarrytown, NY.

Sagdeev, R. Z. and Shafranco, V. D.: 1961, 'On the Instability of a Plasma with an Anisotropic Distribution of Velocities in a Magnetic Field.', *Sov. Phys. JETP.* **12**, 130.

Sagdeev, R. Z., Shapiro, V. D., Shevchenko, V. I. and Szegö, K.: 1986, 'MHD Turbulence in the Solar Wind-Comet Interaction Region', *Geophys. Res. Lett.* **13**, 85.

Sagdeev, R. Z. and Zakharov, A. V.: 1989, 'Brief History of the Phobos Mission', *Nature* **341**, 581.
Sagdeev, R. Z., Shapiro, V. D., Shevchenko, V. I., Zacharov, A., Király, P., Szegö, K., Nagy, A. F., and Grard, R. J. L.: 1990, 'Wave Activity in the Neighborhood of the Bow Shock of Mars', *Geophys. Res. Lett.* **17**, 893–896.
Sauer, K., Motschmann, U. and Roach, T.: 1990, *Ann. Geophys.* **8**, 243.
Sauer, K., Roatsch, T., Baumgärtel, K. and McKenzie, J.: 1992, *Geophys. Res. Lett.* **19**, 645.
Sauer, K., Bogdanov, A. T. and Baumgärtel, K.: 1994, 'Evidence of an Ion Composition Boundary (Protonopause) in Bi-Ion Fluid Simulations of Solar Wind Mass Loading', *Geophys. Res. Lett.* **21**, 2255–2258.
Sauer , K., Bogdanov, A. and Baumgärtel, K.: 1995, *Adv. Space Res.* **16**, 153.
Sauer, K., Bogdanov, A., Baumgärtel, K. and Dubinin, E.: 1996a, *Physica Scripta* **T63**, 111.
Sauer, K., Bogdanov, A., Baumgärtel, K. and Dubinin, E.: 1996b, 'Plasma Environment of Comet Wirtanen During its Low-Activity Stage', *Planet. Space Sci.* **44**, 715–729.
Sauer, K., Dubinin, E. and Baumgartel, K.: 1997a, 'Bi-Ion Structuring in the Magnetosheath of Mars: Theoretical Modeling', *Adv. Space Res.* **20**, 137.
Sauer, K., Lipatov, A., Baumgartel, K. and Dubinin, E.: 1997b, 'Solar Wind-Pluto Interaction Revised', *Adv. Space Res.* **20**, 295.
Sauer, K., Dubinin, E., Baumgärtel, K. and Tarasov, V.: 1998, *Earth Planets Space* **50**, 269.
Sauer, K., Dubinin, E. et al.: 1999a, *J. Geophys. Res.* to be published.
Sauer, K. and Dubinin, E.: 1999, 'The Nature of the Martian 'Obstacle Boundary', *Adv. Space Res.* in press.
Sauer, K. and Dubinin, E.: 1999b, *Adv. Space Res.* to be published.
Scarf, F. L., Taylor, W. W. L., Russell, C. T. and Elphic, R. C.: 1980, 'Pioneer Venus Plasma Wave Observations: The Solar Wind-Venus Interaction', *J. Geophys. Res.* **85**, 7599.
Scarf, F.: 1989, in B. T. Tsurutani and H. Oya (eds), 'Plasma Wave Observations at Comets Giacobini-Zinner and Halley', *in Plasma Waves and Instabilities at Comets and in Magnetospheres* **Geophys. Monogr. Ser.**, 53, Amer. Geophys. Union, Washington, DC, 31–40.
Scholer, M.: 1970, 'On the Motion of Artificial Ion Clouds in the Magnetosphere', *Planet. Space Sci.* **18**, 977–1004.
Schmidt, H. U. and Wegmann, R.: 1982, 'Plasma Flow and Magnetic Fields in Comets', in *Comets*, L.L., editor pp. 538–560, University of Arizona Press, Tucson, Arizona.
Schmidt-Voigt, M.: 1989, 'Time-Dependent MHD Simulations for Cometary Plasma', *Astron. Astrophys.* **210**, 433–454.
Schunk, R. W. and Nagy, A. F.: 1980, 'Ionospheres of the Terrestrial Planets', *Rev. Geophys. and Space Phys.* **18**, 813–852.
Schwingenschuh, K., et al.: 1987, 'Magnetic Field Draping in the Comet Halley Coma: Comparison of Vega Observationbs with Computer Simulations', *Geophys. Res. Lett.* **14**, 640–643.
Schwadron, N. A.: 1998, 'A Model for Pickup Ion Transport in the Heliosphere in the Limit of Uniform Hemispheric Distributions', *J. Geophys. Res.* **103**, 20, 643.
Schwadron, N. A., Gloeckler, G., Fisk, L. A., Geiss, J. and Zurbuchen, T. H.: 2000, 'The Inner Source: Theory and Implications of Observed Distributions', *J. Geophys. Res.* **105**, 7465.
Schwadron, N. A., Zurbuchen, T. H., Fisk, L. A. and Gloeckler, G.: 1999, 'Pronounced Enhancements of Pickup Hydrogen and Helium in High-Latitude Compressional Regions', *J. Geophys. Res.* **104**, 535.
Sckopke, N., Paschmann, G., Brinca, A. L., Carlson, C. W. and Lühr, H.: 1990, 'Ion Thermalisation in Quasi-Perpendicular Shocks Involving Reflected Ions', *J. Geophys. Res.* **95**, 6337–6352.
Shapiro, A. H.: 1953, The Dynamics and Thermodynamics of Compressible Flow, New York.
Shapiro, V. D., Szegö, K., Ride, S. K., and Nagy, A. F.: 1995, 'On the Interaction Between the Shocked Solar Wind and the Planetary Ions on the Dayside of Venus', *J. Geophys. Res.* **100**, 21289.

Shapiro, V. D., Bingham, R., Dawson, J. M., Dobe, Z., Kellet, B. J. and Mendis, A.: 1999, 'Energetic Electrons Produced by Lower Hybrid Waves in the Cometary Environment and Soft X-Ray Emission: Bremstrahlung and K-shell Radiation', *J. Geophys. Res.* **104**, 2573.

Shevchenko, V. I., Shapiro, V. D., Ride, S. K. and Baine, M.: 1995, 'Upstream Wave Activity at Comet P/Grigg-Skjellerup', *J. Geophys. Res.* **100**, 1735.

Shutte, N. M., Király, P., Cravens, T. E., Dyachkov, E. V., Gombosi, T. I., Gringauz, K. I., Nagy, A. F., Sharp, W. E., Sheronova, S. M., Szegö, K., Szemerey, I., T-Szucs, I., Tátrallyay, M., Tóth, A. and Verigin, M.: 1989, 'Observation of Electron and Ion Fluxes in the Vicinity of Mars with the HARP Spectrometer', *Nature* **341**, 614.

Skilling, J.: 1971, 'Cosmic Rays in the Galaxy: Convection or Diffusion?', *Astrophys. J.* **170**, 265.

Skilling, J.: 1975, 'Cosmic Ray Streaming I.: Effect of Alfvén Waves on Particles', *Monthly Notices Royal Astron. Soc.* **172**, 557.

Slavin, J. A., Smith, E. J. and Tsurutani, B. T.: 1986, *Geophys. Res. Lett.*, **13**, 283–286.

Smith, E. J., Neugebauer, M., Balogh, A., Bame, S. J., Lepping, R. P. and Tsurutani, B.: 1995, 'Ulysses Observations of Latitude Gradients in the Heliospheric Magnetic Field: Radial Component and Variances', *Space Sci. Rev.* **72**, 165.

Söding, A.: 1994, 'Der Energietransport in der Wechselwirkungszone des Kometen P/Halley mit dem Sonnenwind, Diplomarbeit, Institut für Geophysik und Meteorologie', *Technische Universität Braunschweig*, Braunschweig.

Söding, A., Glassmeier, K. H., Johnstone, A., and Neubauer, F. M.: 1995, 'Pick-Up Ions and Associated Wave Energy Transport at Comet P/Halley: A Case Study', *Geophys. Res. Lett.* **24**, 305.

Söding, A., Glassmeier, K. H., Fuselier, S., Neubauer, F. M., and Tsurutani, B. T.: 1995, 'Comparison of Wave Energy Transport at the Comets P/Halley and P/Giacobini-Zinner', *Planet. Space Sci.* **44**, 547.

Spenner, K. W., Knudsen, W. C., Miller, K. L., Novak, V., Russell, C. T. and Elphic, R. C.: 1980, 'Observations of the Venus Mantle, the Boundary Layer Between Solar Wind and Ionosphere', *J. Geophys. Res.* **85**, 7655.

Spreiter, J. R. and Stahara, S. S.: 1992, in J. G. Luhmann (ed.), 'Computer Modeling of Solar Wind Interaction with Venus and Mars, in Venus and Mars: Atmospheres, Ionospheres, and Solar Wind Interactions', *Geophys. Monogr. Ser.* **66**, 345.

Stern, S. A. and Tholen, D. J., eds.: 1997, 'Pluto and Charon', University of Arizona Press, Tucson.

Stix, T. H.: 1992, 'Waves in Plasmas', American Institute of Physics, New York, p. 43.

Strangeway, R. J. and Russell, C. T.: 1996, 'Plasma Waves and Field Aligned Currents in the Venus Plasma Mantle', *J. Geophys. Res.* **101**, 17313.

Stone, R. G., Tsurutani, B. T. eds., 'Collisionless Shocks in the Heliosphere', *Geophys. Monogr.* **34**, Amer. Geophys. Union, Washington, DC.

Stone, E. C., Cummings, A. C. and Webber, W. R.: 1996, 'The Distance to the Solar Wind Termination Shock in 1993 and 1994 from Observations of Anomalous Cosmic Rays', *J. Geophys. Res.* **101**, 11017.

Story, T. R. and Zank, G. P.: 1996, 'The Structure of Mass-Loading Shocks', 3. Magnetohydrodynamics, *J. Geophys. Res.* **101**, 17109.

Sudan, R. N.: 1965, 'Growing Waves in a Nongyrotropic Plasma', *Phys. Fluids* **8**, 1915–1918.

Szegö, K., Shapiro, V. D., Shevchenko, V. I., Sagdeev, R. Z., Kasprzak, W. T. and Nagy, A. F.: 1991, 'Physical Processes in the Plasma Mantle of Venus', *Geophys. Res. Lett.* **18**, 2305.

Szegö, K., Sagdeev, R. Z., Shapiro, V. D. and Shevchenko, V. I.: 1992, 'On the Dayside Mantle Region Around those Nonmagnetic Solar System Bodies which Have Ionospheres', *Adv. Space Res.* **12**, 291.

Szegö, K., Dobe, Z., Knudsen, W. C., Nagy, A. F. and Shapiro, V. D.: 1997, 'Energetic Electrons in the Dayside Mantle of Venus', *J. Geophys. Res.* **102**, 2175.

Szegö, K., Klimov, S., Kotova, G. A., Livi, S., Rosenbauer, H., Skalsky, A. and Verigin, M. I.: 1998, 'On the Dayside Region Between the Shocked Solar Wind and the Ionosphere of Mars', *J. Geophys. Res.* **103**, 9101–9111.

Tanaka, T. and Murawski, K.: 1997, 'Three-Dimensional MHD Simulation of the Solar Wind Interaction with the Ionosphere of Venus: Results of Two-Component Reacting Plasma Simulation', *J. Geophys. Res.* **102**, 19805.

Tatrallyay, M., Verigin, M. I., Szegö, K., Gombosi, T. I., Hansen, K. C., Schwingenschuch, K., Delva, M., Apathy, I., Remizov, A. P. and Szemerey, T.: 1999, 'On the Distribution of Pickup Ions as Observed by the Vega Spacecraft at Comet Halley', *Adv. Space Res.* in print.

Taylor, H. A., Daniell, R. E., Hartle, R. E., Brinton, H. C., Bauer, S. J. and Scarf, F. L.: 1981, 'Dynamic Variations Observed in the In Thermal and Superthermal Ion Distribution in the Dayside Ionosphere at Venus', *Adv. Space Res.* **1**, 1247.

Thomas, G. E.: 1978, 'The Interstellar Wind and its Influence on the Interplanetary Environment', *Ann. Rev. Earth Planet. Sci.* **6**, 173.

Thomas, N. and Lichtenberg, G.: 1997, 'The Latitudinal Dependence of Ion Temperature in the Io Plasma Torus', *Geophys. Res. Lett.* **24**, 1175–1178.

Thomsen, M. F., Feldman, W. C., Wilken, B., Jockers, K., Jockers, W., Stüdemann, W., Johnstone, A. D., Coates, A., Formisano, V., Amata, E., Winningham, J. D., Borg, H., Bryant, D. and Wallis, M. K.: 1987, *Astron. Astrophys.* **187**, 141–148.

Thomsen, M. F., et al.: 1987, 'In Situ Observations of a Bi-Modal Ion Distribution in the Outer Coma of Comet Halley', *Astron. Astrophys.* **187**, 141.

Thorne, R. M. and Tsurutani, B. T.: 1987, 'Resonant Interactions Between Cometary Ions and Low Frequency Electromagnetic Waves', *Planet. Space Sci.,* **35**, 1501–1508.

Ting, A. C., Matthaeus, W. H. and Montgomery, D.: 1986, 'Turbulent Relaxation Processes in Magnetohydrodynamics', *Phys. Fluids* **29**, 3261–3274.

Tsurutani, B. T. and Smith, E. J.: 1986, 'Hydromagnetic Waves and Instability Associated with Cometary Ion Pickup, ICE Observations', *Geophys. Res. Lett.* **13**, 263–266.

Tsurutani, B. T. and Smith, E. J.: 1986, 'Strong Hydromagnetic Turbulence Associated with Comet Giacobini-Zinner', *Geophys. Res. Lett.* **13**, 259–262.

Tsurutani, B., Thorne, R. M., Smith, E. J., Gosling, J. T. and Matsumoto, H., 1987, 'Steepened Magnetosonic Waves at Comet Giacobini-Zinner', *J. Geophys. Res.* **92**, 11074.

Tsurutani, B. T., Brinca, A. L., Buti, B., Smith, E. J., Thorne, R. M. and Matsumoto, H.: 1989, 'Magnetic Pulses with Durations Near the Local Proton Cyclotron Period: Comet Giacobini-Zinner', *J. Geophys. Res.* **94**, 29–35.

Tsurutani, B. T.: 1991, in A. D. Johnstone (ed.), 'Comets: A Laboratory for Plasma Waves and Instability', in *Cometary Plasma Process*, *Geophys. Monogr. Ser.* **vol 61**, pp. 189–209, AGU, Washington, D.C.

Tsurutani, B. T.: 1991, in R. L. Newburn et al. (eds), 'Cometary Plasma Waves and Instabilities', in *Comets in the Post-Halley Era,* **vol. 2**, pp. 1171–1210, Kluwer Academic Publishers, Hingham, Mass.

Tsurutani, B. T., Glassmeier, K. H. and Neubauer, F. M.: 1995, 'An Intercomparison of Plasma Turbulence at Three Comets Grigg-Skjellerup, Giacobini-Zinner, and Halley', *Geophys. Res. Lett.* **22**, 1149.

Tsurutani, B. T., Glassmeier, K. H. and Neubauer, F. M.: 1996, 'A Review of Nonlinear Low Frequency (LF) Wave Observations in Space Plasmas: On the Development of Plasma Turbulence', this book.

Tsurutani, B. T., Lakhina, G. S., Neubauer, F. M. and Glassmeier, K. H.: 1997, 'A New Look at the Nature of Comet Halley's LF Electromagnetic Waves: Giotto Observations', *Geophys. Res. Lett.* **24**, 3129–3132.

Valenzuela, A., Haerendel, G., Föppl, H., Melzner, F., Neuss, H., Rieger, E., Stöcker, J., Bauer, O., Höfner, H. and Loidl, J.: 1986, 'The AMPTE Artificial Comet Experiments', *Nature* **320**, No. 6064, 700–703.

Vaisberg, O. L., Galeev, A. A., Zastenker, G. M. et al.: 1983, 'Electron Acceleration at the Front of a Strong Collisionless Shock Wave', *Soviet Physics* **JETP**, 716.

Vasyliunas, V. and Siscoe, G. L.: 1976, 'On the Flux and the Energy Spectra of Interstellar Ions in the Solar System', *J. Geophys. Res.* **81**, 1247.

Wang, Y., Sheeley, N. R. Jr., Phillips, J. L. and Goldstein, B. E.: 1997, 'Solar Wind Stream Interactions and the Wind Speed-Expansion Factor Relationship', *Astrophys. J. Lett.* **488**, L51.

Wallis, M. K.: 1973, 'Weakly-Shocked Flows of the Solar Wind Plasma Through Atmospheres of Comets and Planets', *Planet. Space Sci.* **21**, 1647–1660.

Whang, Y. C., 1998, Solar Wind in the Distant Heliosphere, *J. Geophys. Res.* **103**, 17419.

Williams, L. L. and Zank, G. P.: 1994, 'Effect of Magnetic Field Geometry on the Wave Signature of the Pickup of Interstellar Neutrals', *J. Geophys. Res.* **99**, 19229.

Winske, D., Wu, C. S., Li, Y. Y., Mou, Z. Z. and Guo, S. Y.: 1985, 'Coupling of Newborn Ions to the Solar Wind by Electromagnetic Instabilities and Their Interaction with the Bow Shock', *J. Geophys. Res.* **90**, 2713–2726.

Woolliscroft, L. J. C., Gough, M. P., Christiansen, P. J., Darbyshire, A. G., Gough, H. G. F., Hall, D. S., Jones, D., Jones, S. R. and Norris, A. J.: 1986, 'Plasma Waves and Wave-Particle Interactions Seen at the UKS Spacecraft During the AMPTE Artificial Comet Experiments', *Nature* **320**, (6064), 716–720.

Wu, C. S. and Davidson, R. C.: 1972, 'Electromagnetic Instabilities Produced by Neutral-Particle Ionization in Interplanetary Space', *J. Geophys. Res.* **77**, 5399–5406.

Wu, F. M. and Judge, D. L.: 1979, 'Temperature and Low Velocity of the Interplanetary Gasses along Solar Radii', *Astrophys. J.* **231**, 594.

Wu, C. S. and Yoon, P. H.: 1990, 'Kinetic Hydromagnetic Instabilities Due to a Spherical Shell Distribution of Pickup Ions', *J. Geophys. Res.* **95**, 10273.

Ye, G., Cravens, T. E., and Gombosi, T. I.: 1993, 'Pickup Protons and Water Ions at Comet Halley: Comparisons with Giotto Observations', *J. Geophys. Res.* **98**, 1311.

Yoon, P. H. and Wu, C. S.: 1991, in 'Cometary Plasma Processes', p. 241, *Geophys. Monograph* **61**, AGU.

Yumoto, K., Saito, T. and Nakagawa, T.: 1986, 'Hydromagnetic Waves Near O^+ (or H_2O^+) Ion Cyclotron Frequency Observed by Sakigake at the Closest Approach to Comet Halley', *Geophys. Res. Lett.* **13**, 825–828.

Yumoto, K., Sato, T. and Nakagawa, K.: 1987, 'Long Period HM Waves Associated with Cometary C^+ (or H_20^+) Ions, Sakigake Observations', in *Explorations of Halley Comet* p. 117, Springer-Verlag.

Zank, G. P.: 1991, 'Weyl's Theorem for Magnetohydrodynamics', *J. Plasma Phys.* **46**, 11.

Zank, G. P., Khabibrakhmanov, I. Kh. and Story, T. R.: 1993, 'The Structure of Mass-Loading Shocks', *J. Geophys. Res.* **98**, 5645.

Zank, G. P., Coates, A. J., Neubauer, F. M., Réme, H. and Mazelle, C. X.: 1995, 'Structure of Theory and Observation at Comet Halley', *J. Geophys. Res.* **100**, 7899.

Zhang, T. L., Luhmann, J. G. and Russell, C. T.: 1991, 'The Magnetic Barrier at Venus', *J. Geophys. Res.* **96**, 11145.

Zank, G. P. and Oughton, S.: 1991, *J. Geophys. Res.* **96**, 9439.

Zank, G. P., Oughton, S., Neubauer, F. M. and Webb, G. M.: 1991, 'Mass-Loading and Parallel Magetized Shocks', *Geophys. Res. Lett.* **18**, 1809.

Zank, G. P., Oughton, S., Neubauer, F. M. and Webb, G. M.: 1992, 'Properties of Mass-Loading Shocks', *2. Magnetohydrodynamics J. Geophys. Res.* **97**, 17051.

Zank, G. P., Coates, A. J., Neubauer, F. M., Rème, H. and Mazelle, C.: 1995, 'The Structure of Mass-Loading Shocks', Second Comparison of Theory and Observations at Comet Halley, *J. Geophys. Res.* **100**, 7899–7906.

Zhang, M. H. G. and Luhmann, J. G.: 1992, 'Comparisons of Peak Ionosphere Pressures at Mars and Venus with Incident Solar Wind Dynamic Pressures', *J. Geophys. Res.* **97**, 1017.

Zhang, M. H. G., Luhmann, J. G., Nagy, A. F., Spreiter, J. R. and Stahara, S. S.: 1993, 'Oxygen Ionization Rates at Mars and Venus: Relative Contributions of Impact Ionization and Charge Exchange', *J. Geophys. Res.* **98**, 3311.

Zank, G. P., Story, T. R. and Neubauer, F. M.: 1994, 'The Structure of Mass-Loading Shock', *J. Geophys. Res.* **99**, 13335.

Zank, G. P., Pauls, M. I., Cairns, I. H. and Webb, G. M.: 1996, 'Interstellar Pickup Ions and Quasiperpendicular Shocks. Implication to Termination Shocks', *J. Geophys. Res.* **101**, 457.

Ziebell, L. F., Yoon, P. H., Wu, C. S. and Winske, D.: 1990, 'Pitch Angle Diffusion of Newborn Ions by Intrinsic Turbulence in the Solar Wind', *J. Geophys. Res.* **12**, 21203.